

Dynamics of runaway electrons in tokamak plasmas

Emelie Nilsson

▶ **To cite this version:**

Emelie Nilsson. Dynamics of runaway electrons in tokamak plasmas. Physics [physics]. CEA, 2015. English. NNT : . tel-01212017

HAL Id: tel-01212017
https://pastel.hal.science/tel-01212017

Submitted on 5 Oct 2015

HAL is a multi-disciplinary open access archive for the deposit and dissemination of scientific research documents, whether they are published or not. The documents may come from teaching and research institutions in France or abroad, or from public or private research centers.

L'archive ouverte pluridisciplinaire **HAL**, est destinée au dépôt et à la diffusion de documents scientifiques de niveau recherche, publiés ou non, émanant des établissements d'enseignement et de recherche français ou étrangers, des laboratoires publics ou privés.

Association Euratom-CEA
Institut de Recherche sur la Fusion par confinement Magnétique
CEA/DSM/IRFM/SCCP/GSEM
F-13118 Saint-Paul-lez-Durance
France

École Polytechnique
Graduate School
91128 Palaiseau
France

Dynamics of runaway electrons in tokamak plasmas

Thèse de doctorat présentée devant

la Graduate School de l'École Polytechnique

par

Emelie Nilsson

pour obtenir le grade de

Docteur de l'École Polytechnique

Spécialité: Physique des plasmas

soutenue le 9 September 2015 devant le jury composé de

Prof. Nathaniel Fisch	Princeton Plasma Physics Laboratory	Président du Jury
Prof. Yves Peysson	CEA, IRFM	Directeur de Thèse
Prof. Lars-Göran Eriksson	European Commission	Rapporteur
Dr. Gergo Pokol	Budapest University of Technology	Rapporteur
Prof. Jean-Marcel Rax	École Polytechnique de Paris	Examinater
Dr. Joan Decker	École Polytechnique de Lausanne	Examinateur

Année 2015 Graduate School de l'Ecole Polytechnique

Abstract

Une des propriétés clés des plasma est la décroissance de la force de friction resultant des interactions Coulombiennes avec la vitesse des électrons. Ainsi, en présence d'un champ électrique dépassant un certain seuil critique, les électrons ayant une vitesse suffisamment élevée sont susceptibles d'être accélérés continuement. Ces électrons dénommés "découplés" peuvent atteindre des énergies considérables, de l'orde de plusieurs MeV, et de ce fait sont susceptibles de causer des dégâts importants dans ITER, le prochain tokamak de grande taille. La population d'électrons découplés est susceptible d'être multipliée par les collisions à large angle de déflection, processus au cours duquel un électron découplé de grande énergie peut transfèrer une fraction significative de son énergie cinétique à un électron presque à l'arrêt, tout en restant découplé. La compréhension du processus de formation des électrons découplés est essentielle à la réduction de cette population de particules.

Dans ce contexte, la modélisation de la dynamique des électrons découplés is étudiée avec le code cinétique LUKE résolvant l'équation 3-D relativiste et linéarisée de Fokker-Planck, moyennée sur les orbites, avecun effort particulier concernant les collisions à large angle de déflection de la part des électrons rapides sur les électrons thermiques, ce qui peut conduire à une avalanche d'électrons relativistes. La théorie de ce mécanisme est d'abord décrite dans la cadre d'un développement original, et l'opérateur associé est implanté dans le code ciéntique LUKE. Les dépendances paramétriques du taux de croissance des éléctrons découplés sont étudiées, en fonction de l'intensité du champ électrique, de la densité, de la température du plasma ainsi que de sa configuration. L'importance relative entre la génération primaire et secondaire des électrons découplés, cette dernière résultant du phénomène d"avalanche est également analysée. On montre que les avalanches d'électrons découplés peuvent être importantes même pour des régimes non-disprutifs, et que cet effet peut devenir dominant dans la mise en place du faisceau d'électrons relativistes.

En raison de leur forte magnétisation, les électrons acquérant de l'énergie grâce au processus de diffusion à large angle restent en général piégés. Leur population est donc réduite hors de l'axe mégntique. Cet effet entraine une accumulation électrons découplés dans la région centrale du plasma. La dynamique de ces électrons piegés dans le cadre de la formation d'une population d'électrons découplés est étudiée.

Enfin, la formation des électrons découplés dans des décharges en régime Ohmique réalisées dans les tokamaks Tore Supra et COMPASS est modélisé avec le code LUKE, à partir des paramètres globaux du plasma comme le champ électrique ou l'équilibre MHD toroïdal déterminé par le code METIS. Les caractéristiques de la fonction de distribution en vitesse sont données, de même que la comparaison quantitative avec le rayonnement de freinage non thermique pour le tokamak Tore Supra.

Abstract

One of the key features of a plasma is that the collisional friction resulting from Coulomb interactions decreases with the electron velocity. Therefore, in the presence of a parallel electric field larger than a critical value, electrons with sufficient velocity will be continuously accelerated. These so-called runaway electrons may reach energies on the order of several MeVs and cause serious damage to plasma facing components in ITER - the next large-scale tokamak. The runaway population may be multiplied through knock-on collisions, where an existing runaway electron can transfer a significant fraction of its energy to a secondary electron nearly at rest, while remaining in the runaway region. Understanding of the runaway electron formation processes is crucial in order to develop ways to mitigate them.

In this context, modelling of runaway electron dynamics is performed using the 3-D linearized relativistic bounce-averaged electron Fokker-Planck solver LUKE, with a particular emphasis on knock-on collisions of fast electrons on thermal ones, which can lead to an avalanche of relativistic electrons. The theory of bounce-averaged knock-on collisions is derived, and the corresponding operator is implemented in the kinetic solver LUKE. The dependencies of the runaway electron growth rate on the electric field strength, density, temperature and magnetic configuration, is investigated, in order to identify the relative importance between primary and secondary runaway generation, the latter resulting from the avalanche process. It is shown that avalanches of runaway electrons can be important even in non-disruptive regimes and this effect may become dominant in the build-up of the highly relativistic electron tail.

Owing to their high magnetization, most of the knock-on electrons are born into the magnetic trapping domain in momentum space, which leads to a reduction of the runaway population off the magnetic axis. This accumulates the runaway electrons near the magnetic axis. The dynamics of the trapped electrons in the framework of runaway electron generation is investigated.

Finally, the runaway electron formation in Ohmic discharges performed in the Tore Supra and COMPASS tokamaks is modelled with the LUKE code, using global plasma parameters such as parallel electric field and the toroidal MHD equilibrium calculated with the fast integrated modelling code, METIS. Details of the fast electron velocity distribution function are provided as well as quantitative comparison with non-thermal bremsstrahlung for the Tore Supra tokamak.

Acknowledgements

I would like to thank my supervisor Yves Peysson for his invaluable guidance and encouragement through my thesis work. Thank you for your inspiring creative mind and skills in plasma physics as well as on the glacier. I am also grateful for helping me tune my slightly ancient laptop into a powerful machine worthy of heavy calculations.

I am very thankful for the support of Joan Decker, who supervised both during my master thesis and in the first half of my thesis work, before he left CEA to work in Switzerland. Thank you for your creativity. It is thanks to you that I started this thesis.

My deepest gratitude to the IRFM (Institut de Recherche sur la Fusion par confinement Magnetique) institute for the unique opportunity to work with world leading scientists on cutting edge nuclear fusion research. I thank the Tore Supra team for the fruitful work and making me feel at home in France. A special thank you to Annika Ekedahl who initiated the collaboration between Chalmers and CEA and supervised me through my master's and licentiate thesis. I also want to thank Frederic Imbeaux, Xavier Litaudon, Jean-Francois Artaud, Francois Saint-Laurent, Marc Goniche, Julien Hillairet, Tuong Hoang, Gerardo Giruzzi and Didier Mazon. Thanks for all the interesting discussions and for making research such a pleasure.

I would like to thank Tünde Fülöp, who introduced me to fusion physics and with her passion and hard work is a great inspiration. Thank you for keeping my motivation up and for always believing in me. My 'second family' at Chalmers has been a great support and inspiration to me from the start of the master's thesis throughout the PhD thesis.

I thank CEA for letting me broaden my horizons through various missions abroad. I am very grateful to our collaborators around the world; Nathaniel Fisch, Robert Granetz, Eric Hollmann, Lars-Göran Eriksson, Gergo Pokol, Vasily Kiptily and Rudi Koslowski. Thanks to Jan 'Honsa' Mlynar, Jakub 'Kuba' Urban, Richard Paprok, Milos Vlainic, Vladimir Wainzetti, Ondrej Ficker, Martin Imrísek and Nikita Varavin at IPP Prague for your warm welcome to the COMPASS experimental campaign on runaway electrons. My participation in experiments in this creative environment has been one of the most memorable experiences during my thesis.

Thanks to colleagues and friends who inspire me in work as well as in life: Claudia Norscini, Farah Hariri, Albert Mollén, Adam Stahl, Geri Papp, Istvan Pusztai, Jakob Rydén, Ola Embreus, Robert Nyqvist, Sarah Newton, Jonathan Citrin, Billal Chouli, Maxim Irishkin, Hugo Arnichand, Alberto Gallo, Alexandre Fil and Jorge Morales. For the fun times, summer schools, conferences and trips we shared.

Last but not least I would like to thank the jury members for the time and energy they put into evaluating this work.

Publications

This thesis is based on the work contained in the following papers:

- E. Nilsson, J. Decker, Y. Peysson, R.S. Granetz, F. Saint-Laurent and M. Vlainic. "Kinetic modelling of runaway electron avalanches in tokamak plasmas", *Plasma Physics and Controlled Fusion* **57**, 095006 (2015).
- E. Nilsson, J. Decker, N.J. Fisch and Y. Peysson. "Trapped-electron Runaway Effect", *Journal of Plasma Physics* **81**, 475810403 (2015).

Additional publications

- E. Nilsson, J. Decker, Y. Peysson, J.F. Artaud, A. Ekedahl, J. Hillairet, T. Aniel, V. Basiuk, M. Goniche, F. Imbeaux, D. Mazon and P. Sharma. "Comparative modelling of lower hybrid current drive with two launcher designs in the Tore Supra tokamak", *Nuclear Fusion* **53**, 083018 (2013).
- E. Nilsson, J. Decker, Y. Peysson, J.F. Artaud, T. Aniel, M. Irishkin and F. Saint-Laurent. "Kinetic modelling of runaway electrons in non-disruptive Tore Supra plasmas", P2.152, *42^{nd} EPS Conference on Plasma Physics* (2015).
- E. Nilsson, J. Decker, Y. Peysson, E. Hollmann and F. Saint-Laurent. "Kinetic modelling of runaway electron avalanches in tokamak plasmas", O2.303, *41^{st} EPS Conference on Plasma Physics* (2014).
- E. Nilsson, J. Decker, Y. Peysson, J.F. Artaud, A. Ekedahl, J. Hillairet, T. Aniel, M. Goniche, T. Hoang, F. Imbeaux, D. Mazon and P.K. Scharma. "Comparative modelling of LHCD with Passive-Active and Fully- Active Multijunction launchers in Tore Supra tokamak.", P2.081, *39^{th} EPS Conference on Plasma Physics* (2012).

Contents

Abstract iii

Publications vii

Contents ix

List of Figures xi

1 Introduction 1

2 Magnetized fusion plasmas 5
2.1 Magnetic confinement of plasma . . . 5
2.1.1 Particle trapping . . . 8
2.2 Runaway electrons . . . 8
2.2.1 Dreicer generation . . . 10
2.2.2 Avalanche generation . . . 12
2.3 Tokamak geometry . . . 13
2.3.1 Configuration space . . . 13
2.3.2 Momentum space . . . 13

3 Kinetic description of a tokamak plasma 15
3.1 The Fokker-Planck equation . . . 15
3.1.1 Coulomb collisions . . . 16
3.2 The bounce-averaged Fokker-Planck equation . . . 18
3.3 The LUKE code . . . 21
3.3.1 Normalization . . . 23
3.3.2 Important time scales . . . 23

4 Dynamics of secondary generation of runaway electron 27
4.1 Elastic electron-electron collisions . . . 27
4.2 The knock-on source term . . . 31
4.2.1 Runaways with moderate energy . . . 33
4.2.1.1 Legendre polynomial expansion . . . 35
4.2.2 Bounce average of the knock-on source term . . . 40
4.2.3 Discretization of the source term . . . 45
4.2.4 Analytic solution in circular concentric configuration . . . 46
4.2.5 Integrability of the avalanche source term . . . 47
4.2.5.1 At $\theta = 0$ and 2π . . . 48
4.2.5.2 At $\theta = \pm\pi$ . . . 48

5 The avalanche mechanism in the LUKE code 49
5.1 Implementation of knock-on collisions in the LUKE code . . . 49

5.1.1 Runaway electron growth rate . . . 51
5.1.2 Treatment of suprathermal electrons . . . 52
5.2 The relative importance of runaway avalanches . . . 56

6 Toroidal effects on runaway dynamics 63
6.1 Toroidal effects on runaway electron growth rate . . . 63
6.1.1 Verification of the bounce averaged knock-on operator . . . 71
6.2 The fate of the trapped electrons . . . 74
6.2.1 Radial detrapping condition . . . 75
6.2.2 Runaway time . . . 77
6.2.3 Collisional effects . . . 79
6.2.4 Trapped-Electron Runaway Growth Rate . . . 82
6.2.5 Discussion . . . 84

7 Modelling of runaway electrons in tokamak plasmas 87
7.1 Modelling of non-disruptive scenarios with LUKE/METIS . . . 88
7.2 Tore Supra . . . 89
7.2.1 FEB reconstruction (R5X2) . . . 91
7.2.2 Discharge #40719 . . . 91
7.2.3 Discharge #40721 . . . 95
7.2.4 Discharge #39173 . . . 96
7.3 COMPASS . . . 97
7.3.1 Discharge #8555 . . . 98
7.3.2 Discharge #10007 . . . 101
7.3.3 Plasma elongation scan . . . 102
7.4 Summary of modelling of non-disruptive scenarios . . . 105

8 Conclusion 107

Bibliography 111

A Definition of the four momentum 117

B Derivation of scattering angle 119

C Ellipse of momentum conservation 121

D Derivation of the electron-electron differential cross section 123

E Particle motion in magnetic field 129

F Flux surface average of avalanche operator 131

G Publications 133

List of Figures

1.1 The velocity averaged cross section of fusion reactions as a function of temperature, obtained numerically from equal temperature Maxwellian distributions. The D-T reaction has a maximum reaction cross section at a temperature of around 70 keV. Adapted from [1]. 2

2.1 The toroidal (ϕ) and poloidal (θ) direction. 5
2.2 Schematic view of a tokamak. The plasma is confined by magnetic field lines running helically around the toroidal axis. Picture from [2]. 7
2.3 Chain of events in a typical disruption in the DIII-D tokamak [3]. 10
2.4 The friction force as a function of electron energy, with its maximum at thermal velocity. A suprathermal electron experiences less friction and in the presence of a local electric field, electrons may run away if the accelerating force from the electric field exceeds the friction force. 11

3.1 An electron scattering of an ion with the deflection angle α depending on the impact parameter b. 18
3.2 The angle coordinates used for the bounce averaged Fokker-Planck equation. 21
3.3 Dreicer growth rate calculated by LUKE shows excellent agreement with predictions by Kulsrud [4]. 22
3.4 A prescribed central temperature evolution in a thermal quench (a). Comparison of typical time scale for thermal quench with the initial temperature near the edge $T_e = 400$ eV (Eq. 3.39) with thermal and relativistic collisional time scales (b). . . . 25

4.1 Illustration of close collisions between a relativistic electron and an electron at rest (a). Since the electron mass is proportional to the Lorentz factor γ the relativistic mass of the relativistic electron is much larger than the mass of the electron at rest (b). 29
4.2 The dependence of the scattering angle of initial energies of the target electrons (γ_2). Black line is $\gamma_0 = 1, \gamma_1 = 10^5$. For blue lines $\gamma_0 = [1 : 0.01 : 1.1]$ and $\gamma_1 = 10^5$. Red line is $\gamma_1 = 100$ and $\gamma_0 = 1$. 30
4.3 The scattering angle θ_2 at various initial energies of the primary electron (γ_1) as a function of the energy of the initially slow electron (γ_2). Here $\gamma_1 = 10 : 20 : 100$ and $\gamma_0 = 1$. 30
4.4 Scattering angle of as a function of the Lorentz factor (γ_2) and kinetic energy ($E_k = (\gamma_2 - 1)m_0c^2$) of the secondary electron. 31
4.5 The source function S_0 of Eq. 4.37 as a function of the secondary electron energy after the collision (γ_2) for various primary kinetic energies (γ_1). 35
4.6 Including $\gamma_0 > 1$ (blue) for primary kinetic energy $E_1 = 100$ MeV. Including some (perpendicular) momentum of the target particle affects the magnitude of S_0 (Eq. 4.37) for low γ_2. 36

4.7 Directions of incident electron and knocked out electron with respect to the local magnetic field direction. 40
4.8 Geometry in the toroidal plane. The guiding center velocity v_s goes along the poloidal field lines. $\hat{\phi}$ is the toroidal direction and $\hat{s}$ the poloidal direction. 41
4.9 Coordinate system (R, Z, ϕ). 44

5.1 The knock-on process in LUKE (crosses) benchmarked against analytic growth rate in Ref. [5] (dashed line), when using the same momentum space thresholds. 50
5.2 The LUKE momentum space is divided into two separate populations: the bulk electrons with momentum $p < p_{re}$ and the runaway electrons $p > p_{re}$. The knock-on collisions between the populations n_r and n_e can lead to secondary runaway electrons. Electrons that escape the domain $p < p_{re}$ either by electrons diffusing through p_{re} or by getting contribute to the runaway electron population n_r. 51
5.3 The fraction of runaway electrons ($E/E_c = 30$ and $T_e = 0.5$ keV) as a function of time normalized to thermal collision time, with and without the avalanche effect due to the knock-on collisions. 53
5.4 The growth rate in constant electric field and $T_e = 0.5$ keV for $E/E_c = 40$ (the curves with lower growth rate) and $E/E_c = 60$ (curves with higher growth rate) as a function of the runaway electron density, with and without the avalanche effect. The Dreicer contribution is in good agreement with Kulsrud's theory [4]. The growth rates are normalized to the thermal collision frequency ($\nu_{th} = 1/\tau(v_{th})$). 54
5.5 Runaway electron fraction (a) and growth rate (b) calculated with LUKE, including runaway avalanches, for electric field strength $E/E_c = [2 : 8]$ and $\beta = 0.01$. 54
5.6 The avalanche multiplication factor ($\bar{\gamma}_A$) vs electric field strength. 55
5.7 Avalanche multiplication factor as a function of the lower momentum cut off p_{min}/p_{th} for $T_e = 5$ keV, normalized to the avalanche factor at $p_{min} = p_c$. 55
5.8 The avalanche growth rate, including ($p_{min} = p_{th}$) or excluding ($p_{min} = p_c$) the suprathermal knock on electrons. 56
5.9 The fraction of runaway electrons originating from knock-on collisions (n_A/n_r) as modelled in LUKE. The analytic estimate of when 5% (cyan line), 50% (yellow line) and 90% (red line) of the runaway electrons come from avalanche is obtained from Eq. 5.11. The parametric study is related to non-disruptive scenarios where runaway electrons were generated in several tokamaks. All data points are taken from Ref. [6] except for the Tore Supra (TS) point (discharge #40719) and COMPASS points (discharge #8555 and #8630). 57
5.10 The time required for 1% of the initially Maxwellian electrons to run away, for the electron temperature $T_e = 0.5$ keV (dashed line), 2 keV (solid line and squares) and 5 keV (solid line and circles) 58
5.11 Signature of suprathermal electrons on the edge ECE chord at around $t = 14.5$ s are seen in the Tore Supra discharge #40719 (a). When the density is higher (#40721) (b), there is no sign of supra thermal electrons. 59
5.12 Photo-neutron signal in at the end of the current flattop and in the ramp down for the two Tore Supra pulses. A peak of neutrons is observed at the plasma termination for the low density shot (#40719) but none for the higher density shot (#40721). . . 60
5.13 Electron cyclotron emission in the Tore Supra discharge #40719. 60
5.14 Electron cyclotron emission in the Tore Supra discharge #40721. 61
5.15 HXR data from the vertical camera (channels 1-21) in the energy range $E_{HXR} = 20 - 200$ keV. The HXR emission produced in the current ramp down in #40719 is a signature of suprathermal electrons, whereas in the higher density discharge #40721 no HXR emission is detected. 61
5.16 Relation to E-field evolution in a DIII-D disruption (black circles), the pre-disruptive phase illustrated with a yellow diamond, plotted on to the LUKE parameter scan. . 62

6.1 The evolution of the runaway electron population, including the avalanche effect owing to knock-on collisions, depends strongly on the radial position in a non-uniform magnetic field configuration, where $\epsilon = r/R$ is the inverse aspect ratio coordinate. $E/E_c = 40$, $T_e = 0.5$ keV and the time t is normalized to the thermal collision time τ_{th}. 64
6.2 Radial dependence of Dreicer growth rate, normalized to the growth rate for cylindrical case, i.e. $\epsilon = 0$, compared to a fit $(1 - 1.2\sqrt{2\epsilon/(1+\epsilon)})$ [7]. 64
6.3 Radial dependence of the avalanche multiplication factor from bounce-averaged LUKE calculations (circles), normalized to to the avalanche multiplication factor for the cylindrical case $\epsilon = 0$. The numerical integration over the knock-on source term in Eq. 4.28 with the toroidal dependence in the momentum integration boundary is plotted in squares. The solid line shows the analytic estimate of the growth rate off the magnetic axis from Eq. 6.27. 70
6.4 Growth rate factor as a function of the inverse aspect ratio (ε) for $E/E_c = 10$ (a) and $E/E_c = 20$ (b). 71
6.5 The inward radial displacement ($\Delta\epsilon$) required for trapped electron initially at radial position ϵ and pitch angle ξ_0 to become circulating. 76
6.6 The trapped-electron runaways will appear with a distinct pitch angle (ξ_0) in the radial extent. 77
6.7 The radial distribution of the minimum perpendicular velocity of the trapped-electron runaways, normalised to the critical velocity for $\xi_0 = 1$. 78
6.8 Time (s) for trapped electrons at (ξ_0, ϵ) to reach the radial position where they become passing electrons, for $B_\theta = 0.05\,\mathrm{T}$, $E_\phi = 0.8\,\mathrm{V/m}$ and $R = 1\,\mathrm{m}$. 78
6.9 Time (s) for trapped electrons at (ξ_0, ϵ) to reach the radial position where they become passing electrons, for $B_\theta = 0.01$ T, $E_\phi = 38$ V/m and $R = 1\,\mathrm{m}$. 79
6.10 The minimum energy needed for the Ware pinch to be faster than the collision time, for the parameters $E_\phi = 10\,\mathrm{V/m}$, $38\,\mathrm{V/m}$ and $100\,\mathrm{V/m}$, $n_e = 10^{20}\,\mathrm{m}^{-3}$ and $R = 6.2\,\mathrm{m}$. The poloidal magnetic field is calculated from a current density profile with a total plasma current of $I_p = 15\,\mathrm{MA}$. 81
6.11 The radial distribution function of the trapped-electron runaways, given the initial trapped electron distribution function $f_T \approx \sqrt{\epsilon}$ for the parameters $E_\phi = 10\,\mathrm{V/m}$, $B_\theta = 0.01\,\mathrm{T}$ and $R = 1\,\mathrm{m}$. 83
6.12 The radial distribution function of the trapped-electron avalanche, with $E_\phi = 10\,\mathrm{V/m}$ and $B_\theta = 0.01\,\mathrm{T}$, calculated from the bounce-averaged knock-on operator implemented in the LUKE code. 84

7.1 Measured line averaged electron density, plasma current and parallel electric field strength in discharge #40719 (a) and #40721 (b). 90
7.2 Temperature profiles for two Tore Supra discharges (#40719 and #40721) during the current flattop. 90
7.3 Schematic view of the hard X-ray tomographic system in Tore Supra. Blue lines show the lines of sight of the detectors, also called chords. 91
7.4 Central electric field evolution calculated with the METIS code, normalized to E_c (a) and E_D (b) in discharge #40719. 92
7.5 Internal (n_{ri}) and external (n_{ri}) runaway electron population, normalized to bulk density (a) and unnormalized (b). 93
7.6 Modelling results from TS discharge #40719. 93
7.7 Reconstructed FEB profile in discharge #40719, compared to measured FEB emission from HXR cameras. 94
7.8 Sawteeth in discharge #40719 seen on ECE measurements. The dashed/circled line shows the temperature data points used for CRONOS simulations. 94

7.9 Central electric field evolution calculated with the METIS code, normalized to E_c (a) and E_D (b) in discharge #40721. 95
7.10 Modelling results from TS discharge #40721. 96
7.11 No HXR emission is predicted by LUKE, in agreement with experimental measurements. 96
7.12 Central electric field evolution as calculated by the METIS code, normalized to E_c (a) and E_D (b) in discharge #39173. 97
7.13 Modelling results from TS discharge #39173. 97
7.14 Experimental data from COMPASS shot #8555 shows clear signatures of runaway electron losses. 98
7.15 Central electric field evolution as predicted by the METIS code, normalized to E_c (a) and E_D (b) in discharge #8555. 99
7.16 Runaway electron formation (a) and electron distribution function at $\xi = 1$ (b) in COMPASS discharge #8555 in current flattop during 0.1 s. 100
7.17 LUKE predicts a significant runaway electron population through discharge #8555. 100
7.18 Current profile carried by external runaway electrons without radial transport (a) and with radial transport ($D_{r0} = 0.8\ m^2/s$) (b) for discharge #8555. 100
7.19 Experimental data from COMPASS shot #10007. 101
7.20 Evolution of external and internal runaway electron population, normalized to reference density. 102
7.21 Simulation results at three radial positions; $\rho = 0.028, 0.16, 0.35$. 102
7.22 Evolution of current carried by runaway electrons with $E_k > 1$ MeV. 103
7.23 Runaway losses for discharges with different elongation during the current flattop. . 103
7.24 Magnetic geometry calculated by METIS for κ=1.2,1.4 and 1.6. 104
7.25 There is slightly more runaway electrons generated centrally for the higher elongation case but less off-axis than for the less elongated magnetic geometry. 104

D.1 Feynman diagrams. 124
D.2 t-channel Feynman diagram with Feynmann rules. 125

Chapter 1

Introduction

The increasing global energy demand driven by population growth and rising standards of living is causing environmental problems on Earth. The main energy sources currently in use are finite and give rise to the greenhouse effect and pollution. To satisfy the energy demand of a growing global population, sustainable energy production with much lower environmental impact than conventional technologies must be developed. Controlled nuclear fusion has some very valuable properties as an energy source. It can be made inherently safe and fuel resources are well accessible all over the planet, ensuring that the method is available for us as well as future generations. With no direct contribution to the greenhouse effect and absence of very long duration waste that would burden future generations, fusion energy is an attractive candidate for delivering clean, reliable and virtually inexhaustible energy.

Though still a somewhat exotic topic on Earth, nuclear fusion is the main energy source of our universe. In the Sun and other stars, hydrogen nuclei fuse and release enormous amounts of energy. Confined by strong gravitational pressure, the Sun is a gigantic fusion reactor that sustains our existence on Earth. By combining light nuclei into heavier elements, energy is released through the difference in binding energy of nuclei according to the formula $E = mc^2$. The goal of fusion energy research is to develop a reactor on Earth based on this principle.

There are several candidates for the fuel in a fusion reactor. The reaction between the hydrogen isotopes deuterium (^{2}H or D) and tritium (^{3}H or T) has by far the largest cross-section at the lowest energies (see Fig. 1.1) [8]. This makes the D-T fusion process

$$\mathrm{D} + \mathrm{T} \rightarrow {}^4\mathrm{He} + \mathrm{n} + 17.6\,\mathrm{MeV}, \tag{1.1}$$

the most promising reaction for an energy producing system.

In the pursuit of a sustainable energy producing system, the fusion fuel also has to be sufficiently abundant. Deuterium occurs naturally with a weight fraction of 3.3×10^{-5} in water. Thus the fuel is abundant and accessible worldwide and on along term, given the water available in the oceans. Tritium is a radioactive isotope of hydrogen with a half-life of 12.3 years. It decays into ^{3}He

$$\mathrm{T} \rightarrow {}^3\mathrm{He} + \mathrm{e}^- + \bar{\nu}_\mathrm{e}. \tag{1.2}$$

Owing to its unstable character, no significant amount of tritium exists in nature, but it can be produced with nuclear reactions of the neutrons from the D-T reaction and lithium:

$$\mathrm{n} + {}^6\mathrm{Li} \rightarrow {}^4\mathrm{He} + \mathrm{T} + 4.8\ \mathrm{MeV}, \tag{1.3}$$

$$\mathrm{n} + {}^7\mathrm{Li} + 2.5\ \mathrm{MeV} \rightarrow {}^4\mathrm{He} + \mathrm{T} + \mathrm{n}. \tag{1.4}$$

As two nuclei approach, they repel each other because of their positive charge. In order to fuse, they must be brought very close to each other, to a range on the order of 10^{-15} meters,

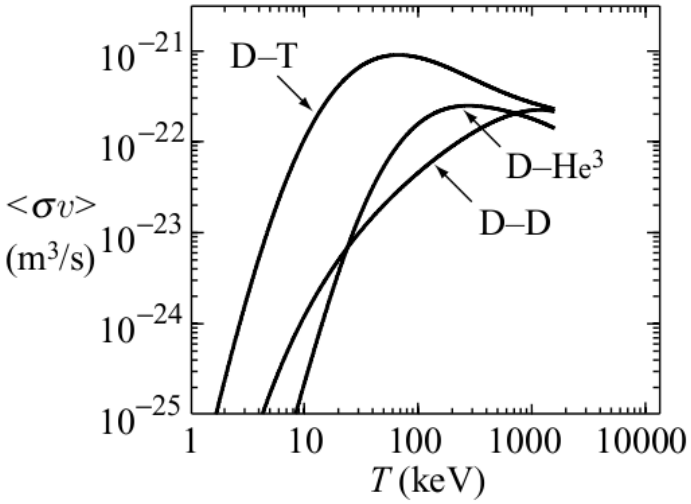


Figure 1.1: The velocity averaged cross section of fusion reactions as a function of temperature, obtained numerically from equal temperature Maxwellian distributions. The D-T reaction has a maximum reaction cross section at a temperature of around 70 keV. Adapted from [1].

where the attractive nuclear force is strong enough to overcome the electrostatic potential barrier. In the center of a star the enormous gravitational pressure provides the nuclei with enough energy to exceed the Coulomb repulsion and fuse. For the nuclei to overcome the electrostatic potential barrier they have to collide at very high speeds. This means that the temperature of the fuel has to be extremely high, on the order of 100 million degrees. At these temperatures, which are ten times higher than the core of the Sun, the nuclei of the fuel are stripped from their electrons. This state of matter is called a *plasma* and is an ionized gas, i.e. a mix of positively charged ions and free electrons. On Earth where we can not rely on gravitational pressure to confine the plasma, other confinement methods must be applied to keep the fuel in plasma state long enough for a significant part of it to fuse. The charged particles in a plasma gyrate around magnetic field lines. This is the principle behind magnetic confinement fusion, where strong magnetic fields direct the motion of the plasma particles through the Lorentz force.

The aim of fusion research is to create a so called burning plasma, in which the heating power released in fusion reactions keeps the plasma hot enough to require no external heating. A fireplace is a chemical example of ignition. One uses a match to heat the fuel and once the burning of the wood releases heat faster than the air can carry it away the fire ignites and keeps burning. In a fusion reactor, one wants to initially heat up the fuel, and then let it burn without having to add much external power.

At this point we have succeeded in achieving fusion reactions, but it has proven difficult to confine the fuel well enough at high temperature to make nuclear fusion a practical source for electrical power [9]. Fusion research is therefore focused on confining heat inside the plasma so that the reactor can ignite. Recreating the controlled fusion process on Earth is a great scientific and technological challenge. Mastering the complex technology of a fusion reactor has an amazing reward: clean, safe and accessible energy that can meet the energy needs of a growing population.

One of the most researched types of magnetic confinement devices for controlled fusion is the tokamak. The name tokamak is an acronym for the Russian ***to****roidal'naya* ***ka****mera* ***ma****gnitnymi* ***k****atushkami* (toroidal chamber with magnetic coils). The next large-scale tokamak experiment, ITER, is currently under construction in Cadarache in southern France [10]. It is an international experiment with the aim to demonstrate the technological and scientific

feasibility of magnetic confinement fusion as a future energy source. This thesis deals with one of the most important challenges for ITER; the formation of runaway electrons in tokamak plasmas. Electrons in the plasma may under certain conditions get continuously accelerated. These highly energetic electrons ($\gtrsim$ MeV), known as runaway electrons, pose a serious threat in tokamaks as they strike the inner wall of the reactor. The mitigation or avoidance of these relativistic electrons in the plasma first of all requires an understanding of the mechanisms behind the runaway electron formation. Understanding and describing these mechanisms is the motivation behind this work.

Given the complex non-linear processes that govern the generation of runaway electrons, simpler theoretical estimates may be supplemented with more advanced numerical predictions. In this thesis work such numerical predictions as well as interpretative modelling of runaway electrons in tokamak scenarios are presented. The following chapters aim to present the results of the runaway electron generation study. The principles of magnetic confinement fusion are introduced in Chapter 2. In Chapter 3 the kinetic equation is presented along with the tool used to model the evolution of the electron distribution function (the LUKE code) [7]. The dynamics of so called secondary generation through knock-on collisions between a bulk electron and a runaway electron is presented in Chapter 4 and the implementation of this mechanism in the LUKE code and its consequence, the runaway avalanche mechanism, is further described in Chapter 5. The effects on the runaway dynamics owing to the toroidal geometry of tokamaks are investigated in Chapter 6. In Chapter 7, the formation of runaway electrons is modelled with the LUKE code for tokamak scenarios and the results are compared to experimental observations. Finally, in Chapter 8 the work is summarized and concluded.

Chapter 2

Magnetized fusion plasmas

The aim of this chapter is to introduce fundamental concepts of toroidally shaped fusion plasmas relevant for runaway electron studies.

2.1 Magnetic confinement of plasma

Since any material would melt in contact with the hot fuel necessary for fusion reactions to occur, the plasma must be prevented from touching the walls of its confinement chamber. The most promising solution is magnetic confinement fusion where the motion of charged particles of the plasma is constrained by strong magnetic fields. The two main magnetic confinement fusion concepts are the *tokamak* and the *stellarator*. Both devices confine the plasma in a torus shaped magnetic cage, with a magnetic field consisting of toroidal and poloidal components (ϕ and θ in Fig. 2.1). The main difference between the two confinement concepts is that in a stellarator the magnetic field is created by complexly shaped external coils, whereas the tokamak is axisymmetric and the poloidal magnetic field component is generated by a strong electric current I_p flowing in the plasma. In reality a tokamak is not fully axisymmetric as the finite number of magnetic coils give rise to magnetic field ripples.

A plasma consists mainly of free electrons, ions and usually neutrals. These charged particles can move freely along magnetic field lines, but their movement perpendicular to the field lines

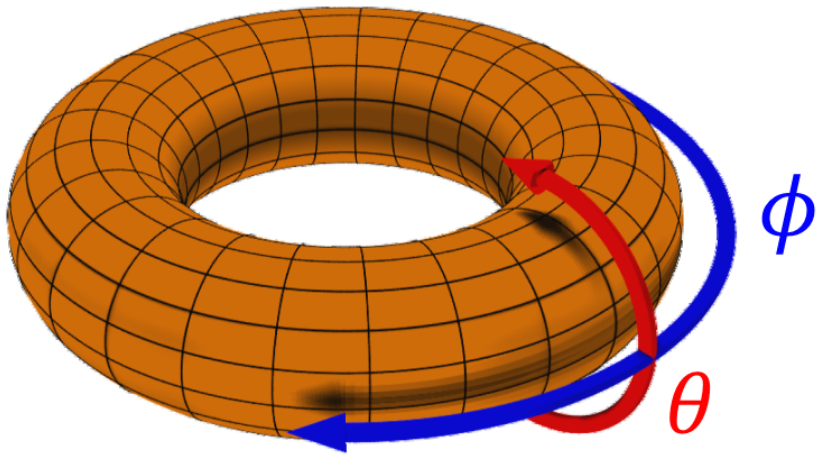


Figure 2.1: The toroidal (ϕ) and poloidal (θ) direction.

is restricted by the Lorentz force ($\mathbf{F} = q\mathbf{v} \times \mathbf{B}$, where q is the charge of the particle, $\mathbf{v}$ the particle velocity and $\mathbf{B}$ the magnetic field) acting on the positively charged nuclei and negatively charged electrons. The Lorentz force guides the particles to move perpendicularly to magnetic field lines in a circular motion resulting in gyrating particle orbits.

In a cylindrical magnetic confinement device the plasma particles would be confined perpendicularly to the field lines, but escape parallel to them at the ends of the cylinder. By bending the cylinder into a torus these end losses are eliminated. A stable plasma equilibrium can be obtained through twisted magnetic field lines by superimposing toroidal and poloidal field components. Magnetic field lines wrap around the torus axis in a helix and constrain the path of the charged particles, to counteract drift effects present in the plasma. In a tokamak the toroidal component is generated by poloidal magnetic coils wound around the torus. The poloidal magnetic field contribution is induced by driving a current in the plasma. Figure 2.2 shows a schematic view of the tokamak concept. The field lines trace out magnetic surfaces referred to as flux surfaces of constant particle pressure which the currents flow within. Both the poloidal and the toroidal magnetic field in a tokamak scale roughly as the inverse of the major radius R and the poloidal field is significantly smaller than the toroidal magnetic field.

The particle velocity can be expressed in components parallel and perpendicular to the magnetic field, $\mathbf{v} = v_{\parallel}\mathbf{b} + v_{\perp}\mathbf{b}$, where $\mathbf{b} = \mathbf{B}/B$ is the unit vector along the magnetic field $\mathbf{B}$. The radius of gyration, also known as the Larmor radius, is given by the balance of the centripetal force and the Lorenz force:

$$\frac{mv^2}{r_g} = qv_{\perp}B \;\rightarrow\; r_g = \frac{mv_{\perp}}{|q|B}, \tag{2.1}$$

where m is the particle mass, $v_{\perp}$ is the component of the velocity perpendicular to the direction of the magnetic field and B is the strength of the magnetic field. The Larmor radius is minimum on the high field side (the inner side of the torus) and maximum on the low field side (the outside). From $v_{\perp} = \omega_c r_g$ the gyration frequency, or cyclotron frequency, becomes

$$\omega_c = \frac{|q|B}{m}. \tag{2.2}$$

The electron collision time characterizing electron collisions with ions is

$$\tau = \frac{4\pi\epsilon_0^2 m_e^2 v^3}{Z^2 e^4 n_i \ln\Lambda}, \tag{2.3}$$

where $\ln\Lambda$ is the Coulomb logarithm which is the factor by which small-angle collisions are more effective than large-angle collisions. The collisional mean free path between two collisions in a plasma is given by the product of the thermal velocity (v_{th}) and the electron collision time in Eq. 2.3:

$$\lambda_{coll} = v_{th}\tau, \tag{2.4}$$

which for $Z = 1$ becomes

$$\lambda_{coll} = 1.44 \cdot 10^{23}(T_e^2/n_e \ln\Lambda)\; m \;\; (T_e\;[keV]).$$

In a hot plasma ($T_e \sim 10$ keV and $n_e \sim 10^{20}\ m^{-3}$ and $\ln\Lambda = 17$) the mean free path is nearly 10 km. This is another reason for containing the plasma in a circular vessel.

At the densities and temperatures reached in fusion plasmas, significant kinetic pressure is obtained in the plasma core and large pressure (p) gradients produce strong forces on the plasma. The ∇p forces are balanced by $\mathbf{j} \times \mathbf{B}$ forces arising from the magnetic field interacting with toroidal and poloidal plasma current density ($\mathbf{j}$). This force balance is known as the magnetic equilibrium.

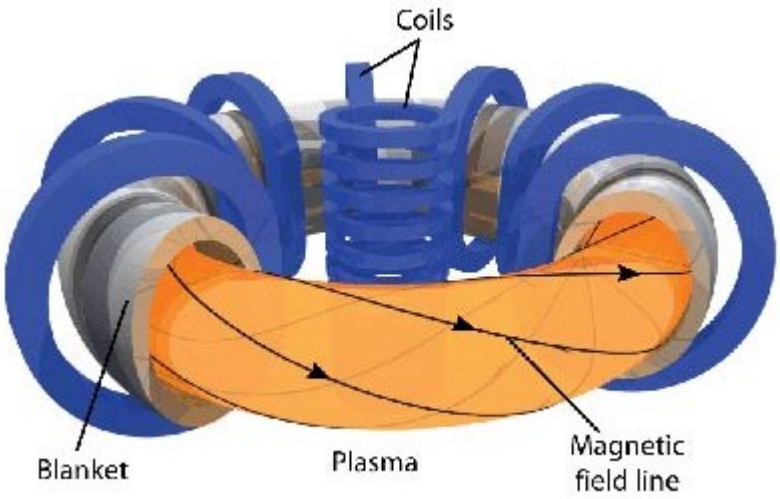


Figure 2.2: Schematic view of a tokamak. The plasma is confined by magnetic field lines running helically around the toroidal axis. Picture from [2].

The poloidal magnetic field can be generated by using the plasma as a secondary circuit in a transformer. In this setup the plasma acts as a single secondary loop generating the poloidal magnetic field. A large current is induced in the plasma itself, which is an excellent electric conductor. This plasma current produces heat, just as a wire warms up when an electric current flows through it. To reach ignition, a self sustained plasma by power release from its own fusion reactions, the fuel must be heated to around 100 million degrees. Maintaining the plasma at this temperature requires control of its density and reduction of the heat losses. As a result from any electron heating process, the resistance of the medium decreases with the temperature as $T_e^{-3/2}$, where T_e is the electron temperature. Consequently, Ohmic heating is a convenient method in the beginning of a discharge, but it becomes inefficient at higher temperatures and additional heating methods must be implemented.

The inductive voltage in the plasma is the time derivative of the total flux (ϕ_p) [11], i.e. the sum of the variation of stored magnetic energy and the Ohmic power. Thus, the inductive voltage is:

$$V_{ind} = -\frac{d}{dt}\left(\phi_p\right) = V_{loop} + \frac{1}{I_p}\frac{d}{dt}\left(E_{magn}\right), \tag{2.5}$$

where $E_{magn} = \mu_0 R l_i I_p^2/4$ is the internal magnetic energy, μ_0 is the vacuum permeability, I_p is the plasma current, R is the major radius and l_i is the internal inductance. $V_{loop} = P_{ohm}/I_p$ is the resistive part of the voltage. In operation with constant plasma current, so called current flattop, the second term in Eq. 2.5 vanishes. In tokamak experiments diagnostics usually provide measurements of the inductive voltage at the plasma edge [12]. For analysis of current drive and runaway electron experiments it is usually the Ohmic part of the inductive voltage, i.e.. the first term in 2.5 that is of interest. Therefore estimations of the second term must be subtracted in such analysis. Another difficulty in the data analysis is that the inductive loop voltage is measured outside the wall, such that the voltage can at its best be measured at the plasma surface. In some conditions, like in current flattop one can assume that the loop voltage profile is flat.

2.1.1 Particle trapping

The magnetic moment is defined as the product of the current associated with the gyro-motion of a charged particle and its surrounding area:

$$\mu = \pi r_g^2 I = \pi r_g^2 \frac{q^2 B}{2\pi m} = \frac{m v_\perp^2}{2B}. \tag{2.6}$$

The magnetic moment of a gyrating particle is a constant of motion or a so called adiabatic invariant, a property of a physical system that stays constant when changes occur slowly. The invariance of μ is important in the magnetic mirror effect, which occurs when the guiding center of a particle approaches regions with stronger magnetic field. The magnetic mirror force acts parallel to the magnetic field lines, opposite to ∇B:

$$\mathbf{F} = -\mu \nabla \mathbf{B}, \tag{2.7}$$

so that the parallel acceleration is

$$\dot{v}_\parallel = -\frac{\mu}{m} \nabla_\parallel B. \tag{2.8}$$

Conservation of energy

$$E = \frac{1}{2}\left(m v_\perp^2 + m v_\parallel^2\right) = \mu B + \frac{1}{2} m v_\parallel^2, \tag{2.9}$$

implies that

$$v_\parallel = \pm\sqrt{2\left(E - \mu B\right)}. \tag{2.10}$$

The particle is passing the high field regions if $v_\parallel > 0$, i.e. if

$$E = \frac{1}{2} m v_{\parallel,0}^2 + \mu B_{min} > \mu B_{max}, \tag{2.11}$$

where $v_{\parallel,0}$ is the velocity parallel to the magnetic field lines on the minimum magnetic field coordinate on a given magnetic flux surface. From this expression, the criterion for passing particles is obtained

$$\frac{v_{\parallel,0}}{v_{\perp,0}} > \sqrt{\frac{B_{max}}{B_{min}} - 1}. \tag{2.12}$$

If $E < \mu B_{max}$, the particle is trapped in the magnetic well, reflected at the point where its parallel velocity equals zero.

2.2 Runaway electrons

The collisional friction force acting on an electron in a plasma increases linearly at small velocity, like in a conventional fluid or gas, but reaches a global maximum value of $F(v) = m v \nu_{ee}(v)$ at the thermal velocity $v = v_{th}$. The collision frequency for suprathermal electrons decreases with the velocity as

$$\nu_{ee} = \frac{e^4 n_e \ln\Lambda}{4\pi\epsilon_0^2 m_e^2 v^3}. \tag{2.13}$$

Thus, in an electric field electrons with velocity above the critical value will be accelerated continuously, in other words they run away. Ions are also accelerated but experience a higher friction force. Also other plasma species, like positrons, may run away [13, 14].

Runaway electrons are often formed during disruptions. A disruption is a fast, unstable event that leads to a sudden loss of plasma confinement. In typical tokamak plasmas macroscopic instabilities are often present. In disruptions, the plasma can not recover from such instabilities.

A typical chain of events in a plasma disruption is illustrated in Fig. 2.3 that shows data from the DIII-D tokamak. When a stability limit of the plasma is reached, it may shift position and come into contact with plasma facing components, which can lead to an influx of particles, especially impurities, from the wall. The radiation due to the impurities and the heat conduction leads to a loss of thermal energy; this phase is referred to as the thermal quench (TQ). In this sudden relaxation of the equilibrium the plasma cools down quickly (on the order of ms), and this dramatic drop of temperature causes a huge increase of the plasma resistivity (ρ) since

$$\rho \sim T^{-3/2}. \tag{2.14}$$

The thermal plasma current is simply related to the electric field via Ohm's law: $j_{th} = E_{||}/\rho$. Hence, if $E_{||}$ were not to change as a result the change of resistivity the plasma current would decay very rapidly. However, the inductive property of the system prevents the current from changing significantly on such short time scales. Instead it induces a sharp increase of the parallel electric field so as to try to maintain the current. This can be seen more formally by combining Maxwell's equation into

$$\nabla^2 \mathbf{E} = \mu_0 \frac{\partial \mathbf{j}}{\partial t} = \mu_0 \frac{\partial}{\partial t} \left(\mathbf{E}/\rho + \mathbf{j_{re}} \right), \tag{2.15}$$

where, we have also introduced a current carried by non-thermal electrons, j_{re}, the runaway electron current. The boundary conditions are set by the tokamak structure, e.g. assuming a perfectly conducting inner wall, the parallel electric field must be zero at the wall.

From Eq. 2.15 we can see that a decline in thermal current as a result an increasing resistivity will result in an increase of the parallel electric field, which strives to maintain the current. Consequently, the actual current decay, or current quench (CQ), occurs on a time scale typically much longer than the thermal quench and a high electric field is therefore present during a significant period of time. The latter leads to generation of runaway electrons, as described in more detail below. On the longer time scale, the current carried by the runaway electrons will partly replace the current initially carried by the thermal electrons. After the CQ a plateau of runaway current may persist for long periods of time if the runaway electrons are well confined.

In fact, we can be more precise about the evolution of the parallel electric field as a result of the thermal quench. We start by assuming that the resistivity increases very rapidly (almost like a step function in time). According to Eq. 2.15 the parallel electric field must then react such that locally $E_{||} \approx \rho j_0$, where j_0 is the current density just before the start of the thermal quench (if this were not the case the left hand side of the above equation would have to exhibit a behaviour close to a delta function in time, which is clearly not possible). Thus, the parallel electric field must react such that it not only prevents the total plasma current to decay rapidly but also strive to maintain the local current density for a short period of time during the thermal quench. However, it should be noted that Eq. 2.15 has the structure of a diffusion equation and that on longer time scales, the electric field profile will diffuse and the simple relation above between the electric field and and the initial current density is no longer valid (the characteristic time scale for electric field diffusion is given by $\mu_0 \sigma a^2$, where a is the plasma minor radius; the characteristic time is of the order a few 10 ms for a JET plasma at 10 eV, a temperature typical of the post thermal quench phase). When simulating runaway generation during a disruption it is therefore generally necessary to calculate the evolution of the electron distribution function and the electric field self consistently.

The beam runaway electrons will eventually lose its stability or the runaways electrons will acquire energies high enough for them to deconfine (due to orbit width effects). The result is that they will strike the first wall of the tokamak vacuum vessel, and the associated highly localised energy deposition can cause significant damage [15].

The most hazardous runaway electrons are formed in tokamak disruptions. However, the formation of runaway electrons does not necessarily require the extreme conditions found in

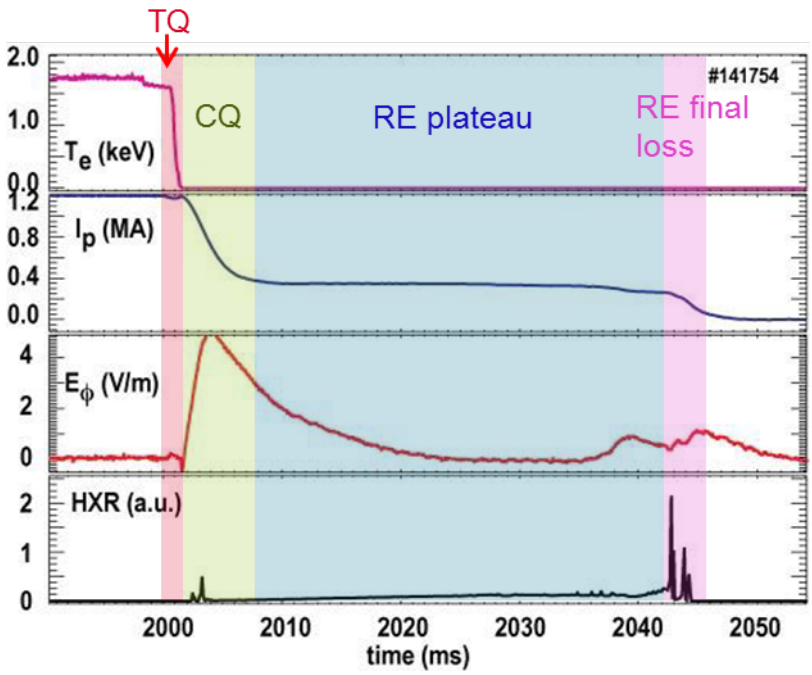


Figure 2.3: Chain of events in a typical disruption in the DIII-D tokamak [3].

disruptions. In low density plasmas, runaway electrons may also be generated during the current flattop in a quiescent plasma [16], free of equilibrium transients, or during current ramp up or ramp down. Runaway electrons have been detected in non-disruptive scenarios in several of the existing tokamaks [6].

Various methods to mitigate the formation of runaway electrons in tokamak plasmas are based on either increasing the plasma density, and thereby the collisionality, by so-called massive gas injection (MGI) [17], or on deconfining the runaway electrons before they can reach too high energy, by the means of resonant magnetic perturbations (RMP) [18]. Even though such mitigation methods have been demonstrated in present tokamak experiments, they might not provide a solution for runaways during disruptions in large tokamaks like ITER [19].

The generation of runaway electrons that were accelerated by the electric field are referred to as Dreicer generation. This mechanism may lead to an additional amplification of the runaway electron population when runaway electrons collide head on with bulk electron and transfer some momentum so that they get kicked out into the runaway region in momentum space. This multiplication of runaway electrons through knock on collisions is known as the avalanche mechanism and is predicted to scale experimentally with the plasma current [5]. Consequently runaway avalanches are expected to be of great concern for ITER.

2.2.1 Dreicer generation

The acceleration by a DC field of electrons that diffuse via small angle collisions beyond the critical momentum (p_c), defined as the minimum momentum for which collisions are too weak to prevent acceleration of the electrons by the electric field to even higher energies, is referred to as the Dreicer mechanism [20]. If the electric field exceeds the collisional friction force on an electron, it will be continuously accelerated. Owing to the Dreicer mechanism a tail of the Maxwellian electron distribution can run away above a critical velocity. The tail of the electron distribution is continuously recovered through collisional processes which leads to a continuous diffusion of electrons into the runaway region.

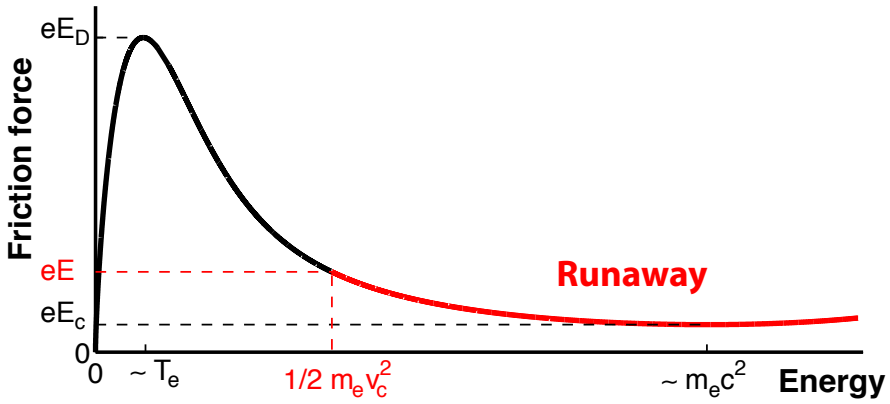


Figure 2.4: The friction force as a function of electron energy, with its maximum at thermal velocity. A suprathermal electron experiences less friction and in the presence of a local electric field, electrons may run away if the accelerating force from the electric field exceeds the friction force.

The electrons gyrate around the magnetic field lines, but are free to move along the magnetic field lines. In the toroidal direction, a retarding friction force is experienced by the electrons. The threshold for when electrons experience unbounded acceleration, if only accounting for collisional losses, can be derived analytically and is called the critical electric field limit, E_c. In the presence of a strong toroidal electric field (E) collisional drag may consequently be too weak to counteract the acceleration of electrons, which may result in continuously accelerated electrons.

The friction force is illustrated in Fig. 2.4. For slow electrons ($v < v_{th}$) the friction force increases with velocity, like in a conventional gas. For electrons moving faster than the thermal velocity, the friction force decreases due to less frequent collisions as the fast electrons spend less time in the vicinity of the particles they collide with

$$F(v) = mv\nu_{ee} \approx m_e v \frac{n_e e^4 \ln\Lambda}{4\pi\epsilon_0^2 m_e^2 v^3} \sim \frac{1}{v^2}. \tag{2.16}$$

The velocity of an electron cannot exceed the speed of light, but its momentum can increase continuously since the relativistic mass increases as γm_0, where m_0 is the electron rest mass and $\gamma = 1/\sqrt{1-(v/c)^2}$ is the Lorentz factor. As the electron approaches the speed of light, it will lose energy to synchrotron radiation, which adds a local minimum at the critical momentum p_c.

For an electron in an electric field the equation of motion becomes

$$m_e \frac{dv}{dt} = eE - m_e v\nu(v), \tag{2.17}$$

which implies acceleration if $E > m_e v\nu(v)/e$. Thus, if no other loss mechanisms than the collisional drag are present [21], runaway electrons may be generated if the electric field exceeds the critical field [20]

$$E_c = \frac{m_e v\nu}{e} = \frac{n_e e^3 \ln\Lambda}{4\pi\varepsilon_0^2 m_e c^2}, \tag{2.18}$$

where n_e is the electron density, c is the speed of light, e is the elementary charge, and $\ln\Lambda$ is the Coulomb logarithm. From Eq. 2.17 also the critical velocity can be derived

$$m_e \frac{dv}{dt} = eE\left(1 - \frac{v_e n_e e^4 \ln\Lambda}{4\pi\varepsilon_0^2 m_e c^2 v^3 eE}\right) = eE\left(1 - \frac{v_c^2}{v^2}\right). \tag{2.19}$$

The critical velocity, at which Eq. 2.19 is zero, becomes

$$v_c^2 = \frac{n_e e^3 \ln\Lambda}{4\pi\varepsilon_0^2 m_e E}. \tag{2.20}$$

At the Dreicer field limit $E_D (> E_c)$, all electrons will run away:

$$E_D = \frac{n_e e^3 \ln\Lambda}{4\pi\varepsilon_0^2 T_e} = E_c \frac{m_e c^2}{T_e}, \tag{2.21}$$

where $T_e = m_e v_{th}^2$ is the electron bulk temperature.

As the faster electrons run away they are replaced by electrons diffusing through the tail of the distribution function. This rate has been calculated in literature [21, 22]. The number of runaways generated per second through the Dreicer effect is defined as the flux of electrons across the runaway threshold. It is derived for a completely ionized plasma in Ref. [23], and is valid for $E/E_D \ll 1$:

$$\left(\frac{\partial n_r}{\partial t}\right)_D \sim \frac{2}{\sqrt{\pi}} n_e \nu(v_{th}) \left(\frac{E}{E_D}\right)^{1/2} \exp\left(-\frac{E_D}{4E} - \left(\frac{2E_D}{E}\right)^{1/2}\right). \tag{2.22}$$

The growth rate for a uniform plasma in a uniform electric field was calculated numerically by Kulsrud [4] by solving the Fokker-Planck equation. These results are often used for benchmarking.

2.2.2 Avalanche generation

It was first suggested by Sokolov [24] that the Dreicer effect alone can not be responsible for the generation of runaway electrons and that the high runaway generation could be explained by an additional amplifying mechanism. This secondary runaway generation is caused by close collisions between existing runaways and thermal electrons. Such collisions might be infrequent, but if they do occur there is a high chance that after the collision both electrons will have a velocity that is higher than the critical momentum. This amplification of the runaway electron population is called the avalanche mechanism. The avalanche effect results in an exponential growth of the runaway population. It grows linearly with the electric field strength, as opposed to the Dreicer effect that has an exponential dependence. A detailed description of the dynamics of runaway avalanches due to knock-on collisions is given in Chapter 4. It is difficult to find an exact solution for the avalanche growth rate. Exact analytical solutions were found in different limits in Ref. [5]. An exact solution is found for $E/E_c \gg 1$ and $Z = -1$, corresponding to no pitch-angle scattering:

$$\left(\frac{\partial n_r}{\partial t}\right)_A \sim \frac{n_r}{2\tau \ln\Lambda} \left(E/E_c - 1\right). \tag{2.23}$$

An expression of the avalanche growth rate was derived from a fit of the exact growth rate for different limits [5]:

$$\begin{aligned}\left(\frac{\partial n_r}{\partial t}\right)_A \quad \sim \quad & n_r \frac{E/E_c - 1}{\tau \ln\Lambda} \sqrt{\frac{\pi\varphi}{3(Z_{eff}+5)}} \times \\ & \left(1 - \frac{E_c}{E} + \frac{4\pi(Z_{eff}+1)^2}{3\varphi(Z_{eff}+5)(E^2/E_c^2 + 4/\varphi^2 - 1)}\right)^{-1/2},\end{aligned} \tag{2.24}$$

where $\varphi = 1 - 1.46\epsilon^{1/2} + 1.72\epsilon$ and $\epsilon = r/R$ is the inverse aspect ratio. This equation is valid for small ϵ. In a cylindrical plasma the growth rate is found from the above expression by $\varphi(\epsilon = 0) = 1$. For $Z = 1$ the growth rate becomes

$$\left(\frac{\partial n_r}{\partial t}\right)_A \sim \sqrt{\frac{\pi}{2}} \frac{n_r}{3\tau \ln \Lambda} \left(E/E_c - 1\right). \tag{2.25}$$

2.3 Tokamak geometry

Electrons may be located by their position in phase space, the combination of configuration and momentum space. Common phase space coordinates for runaway electron studies in tokamaks are introduced in this section.

2.3.1 Configuration space

Toroidally shaped plasmas can conveniently be described by the cylindrical base (R,Z, ϕ), see Fig. 2.1. The Z coordinate, defined on $-\infty < Z < \infty$ is taken along the toroidal axis, ϕ is in the toroidal direction, defined on $0 \leq \phi < 2\pi$ and R is in the radial direction so that $R = Z \times \phi$ defined on $0 \leq R < \infty$. The magnetic axis of the torus is at $R = R_p$.

Another convenient base for toroidal geometries are space-polar coordinates (ψ, θ, ϕ) where θ is the poloidal angle, see Fig. 2.1. Assuming a plasma equilibrium, the radial direction may be parametrised in closed flux-surfaces defined from the origin (R_p, Z_p), with $\psi = \int\int B_p dS = constant$, where B_p is the poloidal magnetic field and dS the surface element. $\psi(R, \theta)$ must be a monotonic function of R, which is ensured for nested flux-surfaces.

2.3.2 Momentum space

The position of an electron in phase space consists of the real space coordinate and the momentum space coordinate. Two curvilinear coordinate systems are considered. The first one is the spherical coordinate system (p, ξ, φ), where ξ is the cosine of the angle between the particle momentum p and the direction along the magnetic field line, known as the pitch angle, and φ is the gyro-angle. The coordinates are defined on

$$0 \leq p < \infty \tag{2.26}$$
$$-1 \leq \xi \leq 1 \tag{2.27}$$
$$0 \leq \varphi \leq 2\pi \quad . \tag{2.28}$$

The other coordinate system is the cylindrical coordinate system $(p_\parallel, p_\perp, \varphi)$ where $p_\parallel = \xi p$ and $p_\perp = \sqrt{1 - \xi^2} p$.

The motion of charged particles in a tokamak can be decomposed into a gyrating motion perpendicularly to the magnetic field lines of the frequency $|q|B/m$ and motion along the magnetic field lines, known as guiding center motion. If the gyrating motion is fast compared to other physical processes, this motion can be averaged over the leading order to study the guiding-center motion. This process is known as gyro-averaging and eliminates φ so that the momentum space coordinate base becomes

$$(p_\parallel, p_\perp, \varphi) \quad \rightarrow \quad (p_\parallel, p_\perp) \tag{2.29}$$
$$(p, \xi, \varphi) \quad \rightarrow \quad (p, \xi). \tag{2.30}$$

In the runaway electron calculations done in this thesis, such gyro-averaged momentum dynamics are applied.

Chapter 3

Kinetic description of a tokamak plasma

The basic difference between a gas and a plasma is that a plasma is composed of charged particles, which react to electromagnetic forces. The most complete description of a plasma with N particles would rely on the solution of the $3N$ equations of motion where the calculation of the force acting on each particle has to account for the influence of all the other particles in the system. Such calculations are not practical and moreover would generate a lot of unnecessary information about the microscopic behaviour of every particle in the system. Since we are interested in macroscopic quantities like density, temperature and currents, a statistical approach is taken. The electromagnetic fields that determine the forces on each particle are functions of the charge and current distributions in the plasma and hence of the distribution function itself. Therefore the solution of the kinetic equation is very complicated even in the collisionless limit.

The dominant effect of collisions in plasmas occurs through the cumulative effect of small angle collisions. In this section we introduce the equation that describes the effects of these collisions, known as the Fokker-Planck (FP) equation. We also introduce the LUKE code, a solver of the relativistic bounce averaged FP-equation, and present some of its applications.

3.1 The Fokker-Planck equation

The evolution of the electron distribution in a plasma is governed by the Fokker-Planck equation, a convection-diffusion equation in phase space. It describes the multiple scattering processes of the particles in the plasma. The dominant interactions are Coulomb collisions (see Sec. 3.1.1), which occur when two particles pass each other close enough to be within the so called Debye sphere, where the particle is electrostatically influenced by other charged particles. The radius of the Debye sphere is the scale over which charged particles screen out electric fields in plasmas and is known as the Debye length

$$\lambda_D = \sqrt{\frac{\epsilon_0 T_e}{e^2 n_e}} \tag{3.1}$$

$$= 2.35 \cdot 10^5 \left(\frac{T_e}{n_e}\right)^{1/2} m \ \ (T_e\ [keV]), \tag{3.2}$$

where ϵ_0 is the vacuum permittivity, e the electron charge, T_e the electron temperature and n_e the electron density. The Debye length is the characteristic length scale of the plasma and is important since collisions in a plasma typically are on the order of this length scale since the charge is shielded for impact parameters $b \gg \lambda_D$. In a typical tokamak plasma the Debye length is on the order of $10^{-4} - 10^{-3}$ m.

The characteristic collision time (τ) between electrons corresponds to the required time for cumulative small angle collisions to deflect the path of the electron by a significant angle (on

the order of $\pi/2$):

$$\tau = \frac{4\pi\epsilon_0^2 m_e^2 v^3}{q_e^4 n_e \ln\Lambda}, \tag{3.3}$$

where v is the velocity of the electron relative to the thermal background and $\ln\Lambda$ is the Coulomb logarithm which is the factor by which small-angle collisions are more effective than large-angle collisions.

Besides collisions, the formulation can describe wave-plasma interaction and the force on particles in an electric field. In plasma physics the Fokker-Planck equation is fundamental in heating, current drive, resonant wave-particle interaction and runaway electron dynamics.

The total number of particles in the volume around the point $\mathbf{z} = (\mathbf{x}, \mathbf{p})$ at the time t is given by:

$$\int f(\mathbf{x}, \mathbf{p}, t)\, \mathrm{d}^3\mathbf{p}\, \mathrm{d}^3\mathbf{x} = N(t). \tag{3.4}$$

The current density is given by

$$\mathbf{J}(\mathbf{x}, t) = q \iiint \mathbf{v} f(\mathbf{x}, \mathbf{p}, t)\, \mathrm{d}^3\mathbf{p}, \tag{3.5}$$

where $f(\mathbf{x}, \mathbf{p}, t)$ is the distribution function of particles with charge q, with $\mathbf{x}$ being the position in configuration space, $\mathbf{p}$ is the relativistic momentum and $\mathbf{v} = \mathbf{p}/(\gamma m_e)$ with $\gamma = \sqrt{1 + p/mc}$. The movement of the particle in the plasma can be expressed as $\dot{\mathbf{z}} = (\dot{\mathbf{x}}, \dot{\mathbf{p}})$. The distribution function must satisfy the continuity equation, expressing conservation of total number of particles:

$$\frac{\partial f}{\partial t} + \frac{\partial}{\partial \mathbf{z}}(\dot{\mathbf{z}} f) = 0, \tag{3.6}$$

which when the equations of motions are divergence free is known as the Vlasov equation:

$$\frac{\partial f}{\partial t} + \mathbf{v} \cdot \nabla f + \dot{\mathbf{p}} \cdot \frac{\partial f}{\partial \mathbf{p}} = 0. \tag{3.7}$$

The electric and magnetic fields in $\dot{\mathbf{p}} = q(\mathbf{E} + \mathbf{v} \times \mathbf{B})$ include the small-scale fluctuations responsible for interaction of individual particles. In this context small-scale means less than the Debye length (Eq. 3.1). The effects of these collisions can be included in a separate collision operator $C_{FP}(f, f_\alpha)$, where α denotes all plasma particle species, including the electrons themselves. The Fokker-Planck equation, which now includes only the macroscopic average electric ($\mathbf{E}$) and magnetic fields ($\mathbf{B}$), is the Vlasov equation with the effects of small scale fluctuations gathered in a collision term on the right hand side:

$$\frac{df}{dt} = \frac{\partial f}{\partial t} + \mathbf{v} \cdot \nabla f + \dot{\mathbf{p}} \cdot \frac{\partial f}{\partial \mathbf{p}} = C_{FP}(f, f_\alpha). \tag{3.8}$$

Here $\dot{\mathbf{p}} = q\,(\mathbf{E} + \mathbf{v} \times \mathbf{B})$ is the Lorentz force acting on the electrons from both constant equilibrium and oscillating radio frequency electromagnetic fields. In general Eqs. 3.7 and 3.8 are not easy to solve, essentially because the forces acting on the system can depend in complicated ways on the distribution function itself. Charged particles in motion constitute a current and therefore affect the electromagnetic fields. These equations are in general nonlinear integro-differential equations.

3.1.1 Coulomb collisions

In a plasma the dominant interactions between particles are Coulomb collisions, which occur when two particles pass each other so close enough for their own electric fields to interact. In such events the impact parameter b, is of the order of the Debye length. The probability for a head on collision is very small. Instead, the cumulative effect of several small angle deflections

give rise to a geometrically large effect. The Coulomb collisions are defined as the change in particle velocity after a certain amount of time during which the particle has experienced the cumulative effect of many Coulomb interactions with other charged particles.

The Coulomb force experienced by the charged particle causes it to deviate from its original path. The longer the particles are close to each other the longer the Coulomb force is active and the more the path of the particle is affected. Thus electrons that are very fast experience less effective collisions and the drag force associated with the collisions therefore decreases with increasing speed for sufficiently fast electrons.

When an electron passes a stationary ion with charge Ze at the distance b it will experience Coulomb force, directed along the line of sight between the particles:

$$F_{C\perp} = \frac{Ze^2}{4\pi\epsilon_0 b^2}, \tag{3.9}$$

during the duration b/v, where v the relative velocity. The change in perpendicular momentum is approximately given by

$$\Delta m_e v_\perp \approx \frac{Ze^2}{4\pi\epsilon_0 vb}. \tag{3.10}$$

As an electron passes through a field of ions with density n it will experience such Coulomb collisions with many ions.

The form of the collision operator $C_{FP}(f, f_\alpha)$ on the right hand side of Eq. 3.8 can be found by defining the rate of change of the electron distribution function owing to collisions during the time Δt:

$$C_{FP} = \frac{f(\mathbf{x}, \mathbf{p}, t + \Delta t) - f(\mathbf{x}, \mathbf{p}, t)}{\Delta t}. \tag{3.11}$$

The distribution function at the time $(t+\Delta t)$ is obtained from the integrated effect of scattering in $\Delta\mathbf{p}$:

$$f(\mathbf{x}, \mathbf{p}, t + \Delta t) = \int f(\mathbf{x}, \mathbf{p} - \mathbf{\Delta p}, t)\psi(\mathbf{p} - \Delta\mathbf{p}, \Delta\mathbf{p})\, d(\Delta\mathbf{p}), \tag{3.12}$$

where $\psi(\mathbf{p}, \Delta\mathbf{p})$ is the probability for an electron with momentum $\mathbf{p}$ to be scattered by $\Delta\mathbf{p}$ during the time Δt. The integrand in the above equation can be expanded in Taylor series in $\Delta\mathbf{p}$:

$$\begin{aligned} f(\mathbf{x}, \mathbf{p} - \mathbf{\Delta p}, t)\psi(\mathbf{p} - \Delta\mathbf{p}, \Delta\mathbf{p}) &= f(\mathbf{x}, \mathbf{p}, t)\psi(\mathbf{p}, \Delta\mathbf{p}) - \sum_\alpha \frac{\partial}{\partial p_\alpha}(f\psi)\Delta p_\alpha \\ &\quad + \frac{1}{2}\sum_{\alpha,\beta} \frac{\partial^2}{\partial p_\alpha \partial p_\beta}(f\psi)\Delta p_\alpha \Delta p_\beta. \end{aligned} \tag{3.13}$$

Given that $\int \psi(p, \Delta p)\, d(\Delta p) = 1$ and by substituting Eq. 3.13 into Eq. 3.12 we have:

$$f(\mathbf{x}, \mathbf{p}, t + \Delta t) - f(\mathbf{x}, \mathbf{p}, t) =$$

$$-\sum_\alpha \frac{\partial}{\partial p_\alpha}\left(f(\mathbf{x}, \mathbf{p}, t)\int \psi(\mathbf{p}, \Delta\mathbf{p})\Delta p_\alpha\, d(\Delta\mathbf{p})\right) \tag{3.14}$$

$$+\frac{1}{2}\sum_{\alpha,\beta} \frac{\partial^2}{\partial p_\alpha \partial p_\beta}\left(f(\mathbf{x}, \mathbf{p}, t)\int \psi(\mathbf{p}, \Delta\mathbf{p})\Delta p_\alpha \Delta p_\beta\, d(\Delta\mathbf{p})\right). \tag{3.15}$$

Inserting the above equation into Eq. 3.11 gives the Fokker-Planck operator:

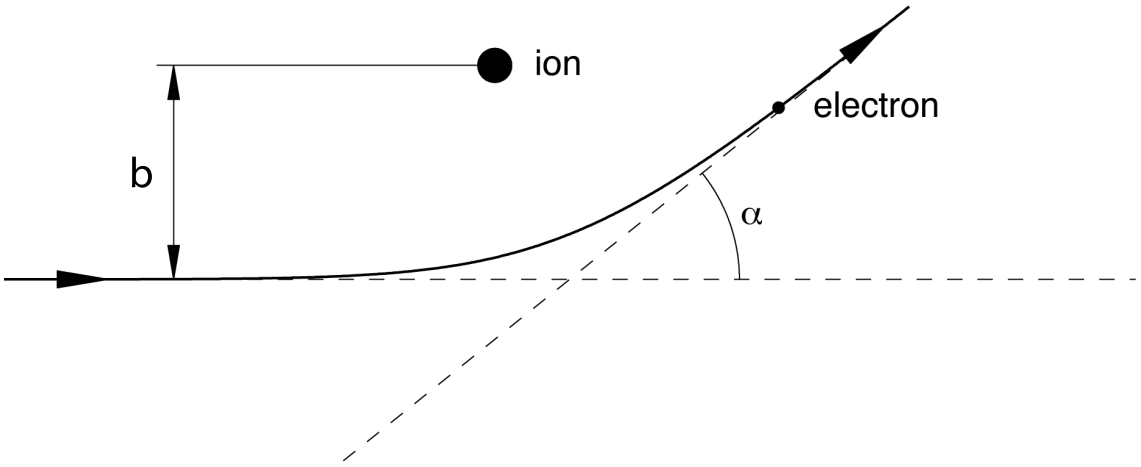


Figure 3.1: An electron scattering of an ion with the deflection angle α depending on the impact parameter b.

$$C_{FP} = -\sum_{\alpha} \frac{\partial}{\partial v_\alpha} \left(\langle \Delta p_\alpha \rangle f \right) + \frac{1}{2} \sum_{\alpha,\beta} \frac{\partial^2}{\partial p_\alpha \partial p_\beta} \left(\langle \Delta p_\alpha \Delta p_\beta \rangle f \right), \tag{3.16}$$

where

$$\langle \Delta p_\alpha \rangle = \int \psi \Delta p_\alpha \, d(\Delta p)/\Delta t, \tag{3.17}$$

and

$$\langle \Delta p_\alpha \Delta p_\beta \rangle = \int \psi \Delta p_\alpha \Delta p_\beta \, d(\Delta p)/\Delta t \tag{3.18}$$

give the average time rate of change of Δp_α and $\Delta p_\alpha \Delta p_\beta$. Equation 3.17 represents the friction and Eq. 3.18 the diffusion tensor. Thus, the first term in Eq. 3.16 describes the friction, or slowing down, and the second the energy diffusion.

The assumption of small deflection angle, is fulfilled for $\Lambda \equiv \lambda_D / b_{min} \gg 1$. The so called Coulomb logarithm becomes

$$\ln \Lambda = \frac{2\pi}{\sqrt{n}} \left(\frac{\epsilon_0 T_e}{e^2} \right)^{3/2}, \tag{3.19}$$

which in a tokamak plasma is around $10 - 20$. For a good approximation it is sufficient to account for only collisions which marginally change the momentum of the incident particles. The rarer head-on collisions, that represent a $1/\ln\Lambda$ correction, are not included in this small angle collision model and need to be treated separately, as will be done in Chapter 4.

3.2 The bounce-averaged Fokker-Planck equation

In order to simulate the distribution function of electrons in an axisymmetric tokamak we turn to the relevant gyro averaged Fokker-Planck equation and adopt a zero banana width approximation [25]:

$$\frac{\partial f}{\partial t} + \mathbf{v}_\parallel \cdot \nabla f - e\mathbf{E}_\parallel \cdot \nabla_{\mathbf{p}} f = C_{FP}(f), \tag{3.20}$$

where f is the distribution function on a given flux surface, which we will write as a function of invariants of the unperturbed motion of an electron in the equilibrium magnetic field:

$$f = f(p, \xi_0, \rho, \theta), \tag{3.21}$$

where p is the momentum $\xi_0 = p_{||0}/p$ is the pitch angle evaluated at the position of the minimum magnetic field along the flux surface, ρ is a flux surface label and θ is an angle determining the poloidal position along a flux surface (it can be a generalised angle, see below); $\mathbf{v}_{||}$ is the parallel guiding centre velocity; $C_{FP}(f)$ is a Fokker-Planck collision operator. Of course, with the distribution function expressed in these invariants of the unperturbed motion one can easily transform to local momentum space coordinates. In fact, only the local pitch angle, ξ, needs to be transformed. Conservation of the magnetic momentum yields:

$$\xi_0^2 = 1 - \frac{B_{min}}{B(\theta)}\left(1 - \xi^2\right) \tag{3.22}$$

Before we proceed further, it is useful to briefly consider the spatial coordinates. We use the commonly adopted representation of the magnetic field in an axi-symmetric torus [26]:

$$\mathbf{B} = I(\psi)\nabla\phi + \nabla\phi \times \nabla\psi, \tag{3.23}$$

where $I(\psi)$ is a flux function, ϕ is the toroidal angle and ψ is the poloidal flux. The poloidal coordinate θ is required to have a period of 2π and to vary only in the poloidal plane, i.e. $\nabla\theta \cdot \nabla\phi = 0$; no further restrictions are made (it could e.g. be the angle in a straight field line coordinate system). Below, however, we will specialise to straight θ angle, since it is used in the LUKE code (see Sec. 3.3).

Expressing the coordinates in terms of the flux surface label, $\rho = \rho(\psi)$, the coordinate system (ρ, θ, ϕ) has a Jacobian given by:

$$\sqrt{g} = \frac{\frac{\partial\psi}{\partial\rho}}{|\nabla\theta \cdot (\nabla\phi \times \nabla\psi)|} = \frac{\frac{\partial\psi}{\partial\rho}}{|\mathbf{B} \cdot \nabla\theta|} \tag{3.24}$$

At this stage we are making the assumptions that the analysed electrons are in the banana regime, which is well justified for runaway electrons. This means that an electron executes many nearly identical orbits before it is significantly perturbed by collisions and the electric field. Consequently, the collisional time scale τ_c is much longer than the bounce time τ_b, i.e. the time for a complete revolution of an orbit. One can utilise this separation of time scales by expanding the distribution function in a τ_b/τ_c series [27, 7]:

$$f = f_0 + \frac{\tau_b}{\tau_c} f_1 + \ldots, \tag{3.25}$$

where f_0 is the distribution function of the unperturbed orbit and f_1 represents a small perturbation. Inserting this expansion in the Fokker-Planck equation (3.20) and noting that $\mathbf{v}_{||} \sim 1/\tau_b$, one finds to lowest order in τ_b/τ_c:

$$\mathbf{v}_g \cdot \nabla f_0 = \mathbf{v}_g \cdot \nabla\theta \frac{\partial f_0}{\partial\theta} = 0 \tag{3.26}$$

Consequently, the zero order distribution function is independent of the poloidal position of a particle along its unperturbed orbit when expressed as a function of invariants of the unperturbed motion. The poloidal orbit of a particle in the zero banana width approximation is therefore determined by the two invariants of the unperturbed motion p and ξ_0, cf. e.g. [7]. Thus, we can write:

$$f_0 = f_0(p, \xi_0, \rho) \tag{3.27}$$

To the next order in τ_b/τ_c we obtain:

$$\frac{\partial f_0}{\partial t} + \mathbf{v}_\parallel \cdot \nabla\theta \frac{\partial f_1}{\partial \theta} - e\mathbf{E}_\parallel \cdot \nabla_{\mathbf{p}} f_0 = C_{FP}(f_0) \tag{3.28}$$

We now define the bounce average operator as the integral along the orbit:

$$\{\dots\} = \frac{1}{\tau_b}\int_{\theta_{min}}^{\theta_{max}} (\dots)\frac{d\theta}{\mathbf{v}_{||}\cdot\nabla\theta} = \frac{1}{\tau_b}\int_{\theta_{min}}^{\theta_{max}} (\dots)\frac{Bd\theta}{v_\parallel \mathbf{B}\cdot\nabla\theta} = \frac{1}{\tau_b}\int_{\theta_{min}}^{\theta_{max}} (\dots)\frac{Bds}{v_\parallel B_p}, \tag{3.29}$$

where the bounce time, τ_b, and the associated bounce frequency, ω_b, are given by:

$$\tau_b = \frac{2\pi}{\omega_b} = \int_{\theta_{min}}^{\theta_{max}} \frac{Bd\theta}{v_\parallel \mathbf{B}\cdot\nabla\theta} = \frac{2\pi}{\omega_b} = \int_{s_{min}}^{s_{max}} \frac{Bds}{v_\parallel B_p}, \tag{3.30}$$

where ds is a length element along a flux surface, given by the metric element $ds = \sqrt{g_{\theta\theta}}d\theta$ in the poloidal direction and the integral is over a closed orbit for a passing electron and between the turning points for a trapped electron (i.e. over half the orbit). In practice this means integrating from 0 to 2π for passing particles. For trapped particles the path along the inner and outer leg along the orbit are identical in the zero banana width approximation, it is therefore sufficient to carry out the integral between the lower, θ_{max}, and upper, θ_{min}, turning points. It should, however, be pointed that only factors that are even in θ will give a finite contribution to the bounce averaged operator for trapped particles. This is the case because the complete integration over booth the inner and outer leg will give zero for factors that are odd in θ.

We now specialise the angle coordinates to normal toroidal ones (θ, ϕ), in these coordinates the metric element above is simply given as, see Fig 3.2, $\sqrt{g_{\theta\theta}} = r/|\hat{r}\cdot\hat{\psi}|$, where $\hat{r}$ and $\hat{\psi}$ are unit vectors on the direction of r and $\nabla\psi$ respectively, and r is the radius from the magnetic axis to a point on the flux surface. The bounce average and the bounce time can be expressed as,

$$\{\dots\} = \frac{1}{\tau_b}\left[\frac{1}{2}\sum_\sigma\right]\int_{\theta_{min}}^{\theta_{max}} (...)\frac{B}{B_p v_\parallel}\frac{rd\theta}{|\hat{r}\cdot\hat{\psi}|} \tag{3.31}$$

and

$$\tau_b = \int_{\theta_{min}}^{\theta_{max}} \frac{B}{B_p v_\parallel}\frac{rd\theta}{|\hat{r}\cdot\hat{\psi}|} \tag{3.32}$$

where the sum over σ applies to trapped particles only (i.e. we have made it explicit that only factors that are odd functions of θ contributes to the bounce average).

Applying the bounce averaged operation to the first order equation above and recognising that f_1 must be periodic in θ yields:

$$\frac{\partial f_0}{\partial t} = \left\{e\mathbf{E}_\parallel \cdot \nabla_{\mathbf{p}} f_0\right\} + \{C_{FP}(f_0)\} \tag{3.33}$$

This is the 0^{th}-order bounce averaged Fokker-Planck equation solved by LUKE.

An important feature to point out in this context is the fact that the zero order distribution function is independent of the poloidal position when expressed as a function of the invariants of the unperturbed motion. This does not mean that the distribution function expressed in local momentum space coordinates at a poloidal point is independent of the position. Instead we have the implicit dependence to take into account, such that

$$f_0(p, \xi, \psi, \theta) = f_0\left(p, \xi_0(\theta), \psi\right) \tag{3.34}$$

Thus, for example an anisotropic distribution function will give rise poloidally varying density.

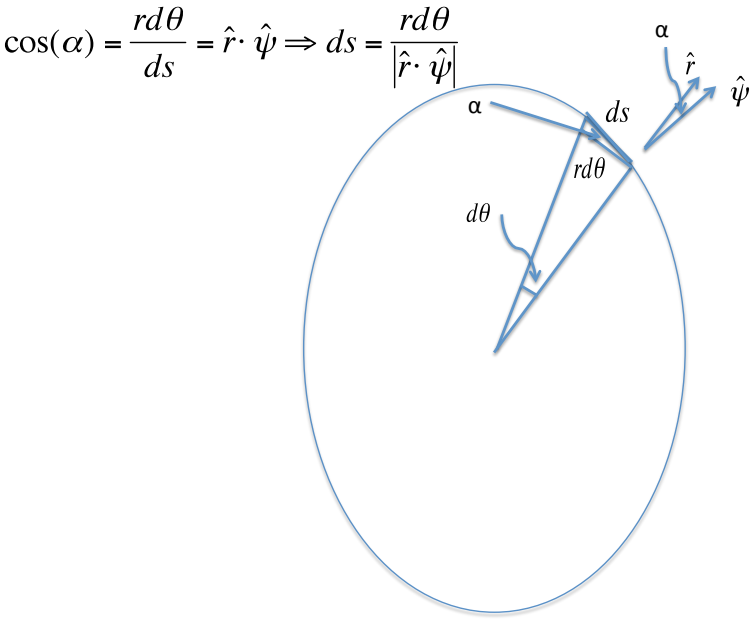


Figure 3.2: The angle coordinates used for the bounce averaged Fokker-Planck equation.

3.3 The LUKE code

The LUKE code (LU solver for Kinetic Equation) solves the kinetic equation for a hot magnetized plasma placed in an axisymmetric magnetic configuration with nested magnetic flux surfaces. It has previously been used for current drive and Dreicer runaway calculations, showing good agreement with theoretical results [4] including the effect of the effective charge (see Fig. 3.3). It uses the finite difference method to solve the bounce-averaged relativistic electron kinetic equation

$$\frac{df}{dt} = \frac{\partial f}{\partial t} + \mathbf{v}\cdot\nabla f + \dot{\mathbf{p}}\cdot\frac{\partial f}{\partial \mathbf{p}} = C_{FP}(f, f_\alpha) + S, \tag{3.35}$$

which is Eq. 3.5 with an added source term represents any sources or sinks of particles. The above equation is solved on a non-uniform or uniform radial, momentum and bounce-averaged pitch angle grid (ρ, p, ξ) in non-uniform magnetic equilibrium where $p = \gamma v/c$ is the normalized momentum and $\xi = p_\parallel/p$ is the cosine of the particle pitch angle which characterizes the particle orbit around a magnetic field line. In these coordinates, the kinetic equation can be expressed as:

$$\frac{\partial f}{\partial t} + \frac{eE_\parallel}{m_e c}\left(\xi\frac{\partial f}{\partial p} + \frac{1-\xi^2}{p}\frac{\partial f}{\partial \xi}\right) = C_{FP}(f, f_\alpha) + S, \tag{3.36}$$

where the second term represents the force from the electric field. The time evolution of the electron distribution function f is found by solving the above equation with a usually taken to be Maxwellian distribution as initial condition. Moments of the distribution functions are

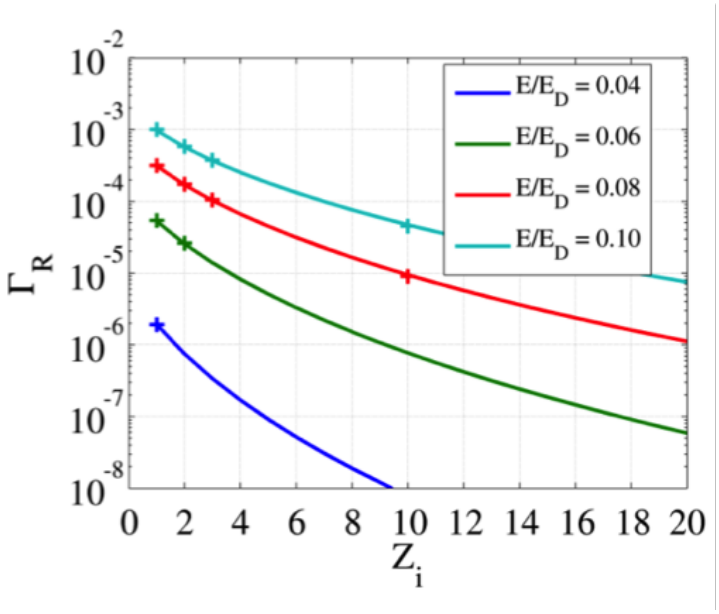


Figure 3.3: Dreicer growth rate calculated by LUKE shows excellent agreement with predictions by Kulsrud [4].

evaluated, such as the plasma current density (Eq. 3.5). A detailed user manual for the LUKE code is found in Ref. [7].

Calculations are valid in the region of the plasma where the weak collisional limit is satisfied, in other words where electrons can complete a full poloidal orbit before being scattered off by Coulomb interaction.

The model uses a relativistic collision operator for small angle collisions ($C_{FP}(f, f_\alpha)$ in Eq. 3.36) and a recently added description of the large angle (knock-on) collisions leading to the avalanche effect (S in Eq. 3.36), which enables a description of the full 2-D momentum dynamics of the runaway population. Knock-on electrons are principally scattered off with a perpendicular component of the momentum with respect to the local magnetic field direction. In a non-uniform magnetic field configuration highly magnetized electrons could be subject to magnetic trapping effects resulting in a runaway electron growth rate off the magnetic axis that differs from the estimates for a cylindric geometry. Such toroidicity effects are studied by implementing a 2-D kinetic description of the knock-on momentum dynamics, including the momentum dynamics both perpendicular and parallel to the magnetic field lines.

Disruptions are interesting but complex processes for studying the birth of runaway electrons, since they include magnetohydrodynamic (MHD) instabilities, anomalous transport and complex evolution of the magnetic field topology [28]. However, the generation of runaway electrons does not necessarily require the extreme conditions found in disruptions. In low density plasmas, the electric field can exceed the critical electric field also during the current flattop in a quiescent plasma, free of equilibrium transients, or during current ramp up or ramp down. An advantage of studying runaway formation in these so called non-disruptive scenarios is that the key parameters for the runaway electron mechanisms, mainly the electric field strength, electron density and temperature, can be better diagnosed than in disruptions. Runaway electrons have been detected in non-disruptive scenarios in several of the existing tokamaks [6]. Quiescent plasmas with nested magnetic flux surfaces are therefore more suitable for studying the formation of runaway electrons.

In this work the formation of runaway electrons generated from the combined effect of Dreicer and avalanche is studied with the LUKE code, a solver of the 3-D (one spatial and two

velocity dimensions) linearized bounce-averaged relativistic electron Fokker-Planck equation [7]. The motion of the electrons is gyro-averaged resulting in 2-D momentum dynamics, (p, ξ_0). Toroidal symmetry is assumed and the code is independent of the toroidal coordinate ϕ. The LUKE code handles arbitrary shapes of the flux surfaces, but in this work the magnetic flux surfaces are assumed to remain circular and concentric like in the Tore Supra tokamak except for the modelling of the COMPASS scenarios where elongated scenarios have been modelled (see Chap. 7). The flux surfaces are assumed to remain intact throughout the runaway formation process, an assumption that is too restrictive for the thermal quench in disruptive scenarios.

3.3.1 Normalization

In the LUKE code, the momentum grid is normalized to the local (or central) thermal momentum $p_{th} = m_e v_{th} = \sqrt{m_e T_e}$. LUKE uses normalized, dimensionless operators normalized to the reference density ($n_e^\dagger$), reference temperature $T_e^\dagger$ and the reference (thermal) collision frequency ($\nu_{coll}^\dagger$) [7]. The reference values are taken from the local flux surface or from values on the magnetic axis. The electron density is given by integrating the electron distribution function f over momentum space:

$$\int f(r,p) d^3p = n_e(r). \tag{3.37}$$

Normalized to a reference density $n_e^\dagger$, which gives $\bar{f} = f/n_e^\dagger$ and $\bar{n}_e = n(r)/n_e^\dagger$ it becomes

$$\int \bar{f}(r,p) d^3p = \bar{n}_e(r). \tag{3.38}$$

The time scales are normalized to the local collisional time scale. The normalized time step in the LUKE code is $dt_n = dt/\tau_{coll}^\dagger$, where $\tau_{coll}^\dagger$ is the thermal electron collision time.

3.3.2 Important time scales

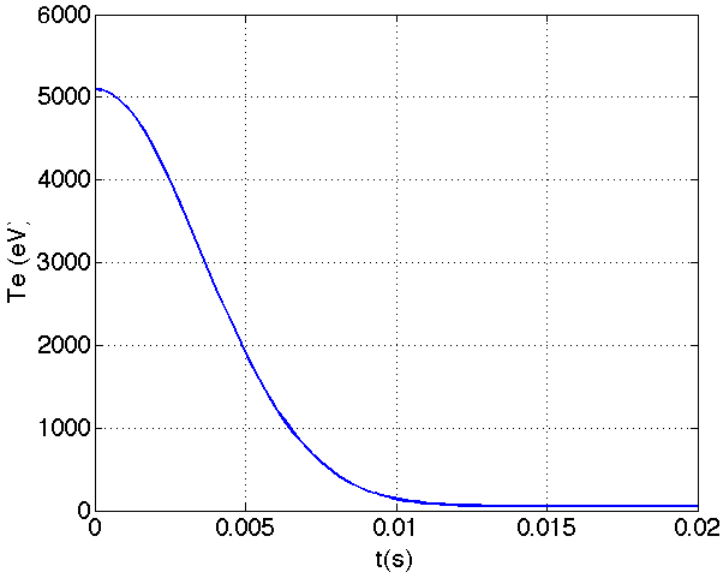
Estimates of the time scale of the thermal quench, defined as the time scale of the convective loss of the plasma along the field, is given in Ref. [28]

$$\tau_{TQ} = kaL^{2/3}B^{2/3}T_e^{-5/6} \ \ [\mathsf{ms}], \tag{3.39}$$

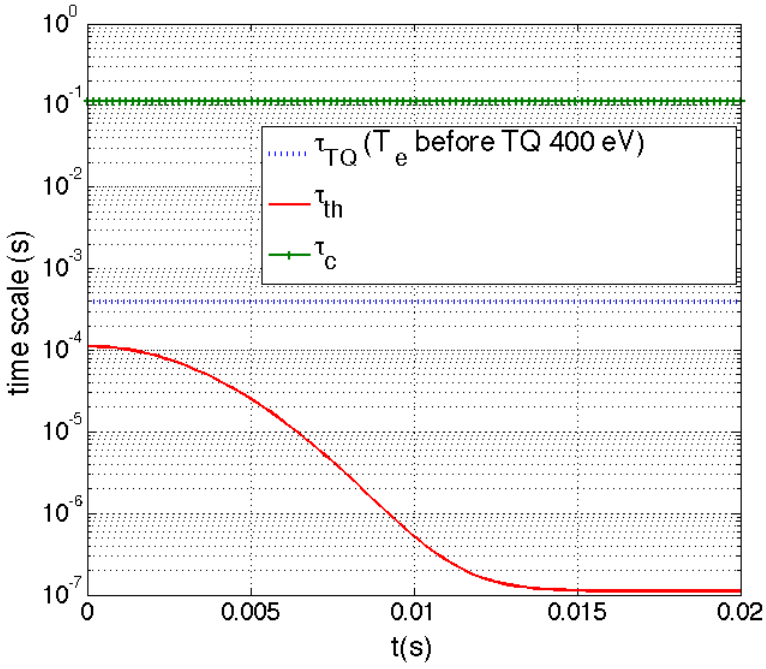
where $L = \pi q R$, B is the magnetic field strength, a is the minor radius, q is the safety factor, $k \approx 6$, R the major radius and T_e the temperature prior to the thermal quench near the plasma edge. Equation 3.39 predicts the time scale of the outflow of plasma from the core. The typical thermal quench time scale for a prescribed temperature evolution (Fig. 3.4a) and Tore Supra like parameters is compared with the collisional time scale (Eq. 3.3), where the velocity $v = v_{th}$ for thermal electrons and $v = c$ for relativistic electrons in Fig. 3.4b. The time scale of the thermal quench associated with transport of plasma because of stochastic and non-closed field lines is found to be comparable with the thermal collision time but shorter than the collisional time scale for relativistic electrons $\tau(c)$, making the possibility of self-consistent calculation of the electron distribution function with the LUKE code in a rapid cooling event highly questionable. As a consequence of the rapid loss of the plasma, a well confined seed of runaway electrons near the magnetic axis may be all that remains from the suprathermal electron population in the post thermal quench phase. After the thermal quench the runaway electrons are in many cases well confined for seconds, in the so called runaway electron current plateau [3]. The high confinement in this phase likely implies recovery of the nested magnetic flux surfaces and the runaway electrons in the current plateau could in principle be modelled with the LUKE code until their final deconfinement at the end of the current plateau. However, since the non-Maxwellian electron distribution function after the thermal quench is unknown, the initial conditions necessary for runaway calculations are undefined.

With the restrictions of disruption modelling in mind, the objective of this work is to study the formation of runaway electrons in non-disruptive scenarios owing to the combined effect of Dreicer and avalanche with a fast solver of the electron distribution function in order to make predictions for the birth of runaway electrons in tokamak experiments.

The difficult task of modelling the transient temperature and electric field found in disruptions, would require a proper description of the thermal quench with implemented radiative or convective loss mechanisms of the plasma energy including MHD instabilities. The coupling of the kinetic LUKE code with a fluid code such as JOREK [29], would be necessary for such a purpose, but is beyond the scope of this work. The kinetic modelling of the formation of runaway electrons is therefore done for non-disruptive scenarios as found in the current flattop with constant electric field and plasma temperature.



(a)



(b)

Figure 3.4: A prescribed central temperature evolution in a thermal quench (a). Comparison of typical time scale for thermal quench with the initial temperature near the edge $T_e = 400$ eV (Eq. 3.39) with thermal and relativistic collisional time scales (b).

Chapter 4

Dynamics of secondary generation of runaway electron

In the conditions associated with large tokamak disruptions the plasma consists mainly of two electron populations; bulk electrons at thermal energy and fast relativistic electrons that have been accelerated by a strong electric field. The LUKE code [7] calculates the generation of primary runaway electrons by solving the Fokker-Planck equation. The modeling of the primary runaway electron generation shows good agreement with theoretical results [4]. However, acceleration in electric field is not the only mechanism behind runaway electron generation. Through knock-on collisions between electrons from the two populations, bulk electrons can receive an energy kick from the fast electron and get knocked beyond the collisional momentum space, where it can be accelerated to relativistic energies by the electric field. If the primary electron remains above the critical momentum after the collision, a multiplication of the runaway electron has taken place. The electron that received an energy kick can then collide with a bulk electron and the process is repeated, setting off an avalanche of relativistic electrons. This is known as the avalanche mechanism or secondary generation of runaway electrons. Relativistic electron populations originating from runaway electron avalanches have been frequently observed in various plasmas, e.g. large tokamak disruptions [30] and electric discharges associated with thunderstorms [31].

The description of the generation of secondary runaway electrons, also known as knock-on collisions, which is expected to play a major roll in large tokamaks like ITER, is beyond the Fokker-Planck approximation, that only includes distant collisions with slight variation in momenta, in other words weak deflections. For secondary generation, when relativistic electrons kick bulk electrons into the runaway region through close collisions, with small impact parameters, the deflection is strong and a source term for the avalanche mechanism must be incorporated beyond the Fokker-Planck collision operator. In this chapter the electron dynamics of these close collisions is described. The scattering angle and an avalanche source term is derived. Since such knock-on electrons are principally scattered off with a large perpendicular component of the momentum with respect to the local magnetic field direction, these particles are highly magnetized. Consequently, the momentum dynamics require a full 2-D kinetic description, since the electrons are highly sensitive to the magnetic non-uniformity of a toroidal configuration. For this purpose, a bounce-averaged knock-on source term is implemented. Owing to the bounce-averaged formalism, the dimensionality of the problem is reduced from 4D to 3D as the knock-on source term is averaged over the poloidal motion of the electrons.

4.1 Elastic electron-electron collisions

The dynamics of a bulk electron exchanging energy with a relativistic electron by close collisions is illustrated in Fig. 4.1. The Lorentz factor is $\gamma = \frac{1}{\sqrt{1-(v/c)^2}} = \sqrt{1+p^2}$ and the momentum

$p = \gamma v/c$, where the momentum is normalized to $m_0 c$. The energy of a particle is $E = \gamma m_0 c^2 = m_0 c^2 + (\gamma - 1) m_0 c^2$, where the first term is the rest energy and the second term the kinetic energy.

The four-momentum, defined in Appendix A, is

$$\mathbf{P} = \frac{1}{m_0 c}(\frac{E}{c}, \gamma m_0 \mathbf{v}) = \gamma(1, \frac{\mathbf{v}}{c}) \Longleftrightarrow \mathbf{P}\cdot\mathbf{P} = \gamma^2(1 - \frac{v^2}{c^2}) = 1. \tag{4.1}$$

In the elastic collision between two electrons both energy and three-momentum is conserved:

$$\mathbf{P}_0 + \mathbf{P}_1 = \mathbf{P}_2 + \mathbf{P}_3 \iff \mathbf{P}_0 + \mathbf{P}_1 - \mathbf{P}_2 = \mathbf{P}_3. \tag{4.2}$$

By squaring both sides of the equation, and using the definition of four-momentum as in Appendix A we obtain:

$$1 + \mathbf{P}_0 \cdot \mathbf{P}_1 - \mathbf{P}_0 \cdot \mathbf{P}_2 - \mathbf{P}_1 \cdot \mathbf{P}_2 = 0, \tag{4.3}$$

where

$$\mathbf{P}_0\mathbf{P}_1 = \gamma_0\gamma_1 - \mathbf{p_0} \cdot \mathbf{p_1},\ \mathbf{P}_0\mathbf{P}_2 = \gamma_0\gamma_2 - \mathbf{p_0} \cdot \mathbf{p_2},\ \mathbf{P}_1\mathbf{P}_2 = \gamma_1\gamma_2 - \mathbf{p_1} \cdot \mathbf{p_2}. \tag{4.4}$$

In the system of two colliding electrons, we have the freedom of choosing the reference frame. A reference axis along the motion of one of the electrons is chosen (we will call this the longitudinal direction). We can then choose our reference frame so that the other electron (the bulk electron) has no velocity in the parallel direction. Even if the parallel momentum of the target electron ($p_{0\|}$) can be considered negligible compared to the parallel momentum of incoming electron $p_{1\|}$, the target electron could still have some perpendicular momentum, in which case $\gamma_0 > 1$. Thus $p_1 = p_{1\|}$ and $p_0 = p_{0\perp}$. The momentum conservation gives

$$1 + \gamma_0\gamma_1 - \gamma_0\gamma_2 + p_0 p_2 sin(\theta_2) - \gamma_1\gamma_2 + p_1 p_2 \cos(\theta_2) = 0. \tag{4.5}$$

The scattering angle $\xi^* = \cos(\theta_2(\gamma_0, \gamma_1, \gamma_2))$ becomes:

$$\begin{aligned} \xi^* &= \pm\sqrt{\frac{p_0^2 - \frac{(1+\gamma_0\gamma_1-\gamma_0\gamma_2-\gamma_1\gamma_2)^2}{p_2^2}}{p_0^2 + p_1^2} + \left(\frac{(1 + \gamma_0\gamma_1 - \gamma_0\gamma_2 - \gamma_1\gamma_2)p_1}{p_2(p_0^2 + p_1^2)}\right)^2} \\ &- \frac{(1 + \gamma_0\gamma_1 - \gamma_0\gamma_2 - \gamma_1\gamma_2)p_1}{p_2(p_0^2 + p_1^2)}, \end{aligned} \tag{4.6}$$

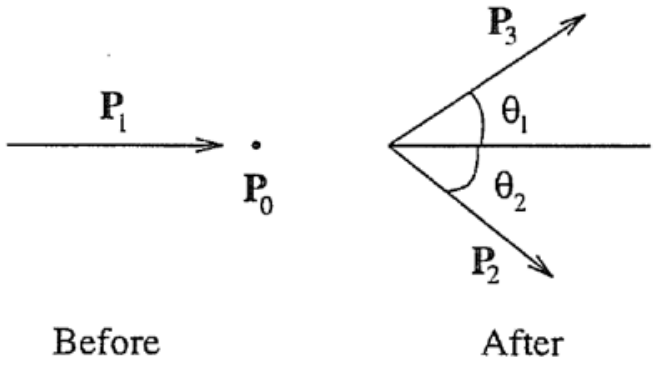
which can also be expressed as

$$\begin{aligned} \xi^* &= \pm\sqrt{\frac{p_0^2}{p_0^2 + p_1^2} + \frac{(1 + \gamma_0\gamma_1 - \gamma_0\gamma_2 - \gamma_1\gamma_2)^2}{p_2^2(p_0^2 + p_1^2)}\left(\frac{p_1^2}{p_0^2 + p_1^2} - 1\right)} \\ &- \frac{(1 + \gamma_0\gamma_1 - \gamma_0\gamma_2 - \gamma_1\gamma_2)p_1}{p_2(p_0^2 + p_1^2)}. \end{aligned} \tag{4.7}$$

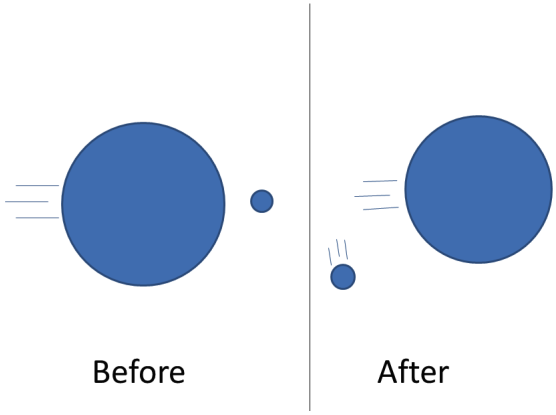
The full derivation is given in Appendix B. Note that in the limit $p_0 \to 0$ and $\gamma_0 \to 1$ the terms under the root sign are zero and only the last term remains and equals to Eq. 4.10. From this relation we can study the dependence of initial energies of the two electrons. The scattering angle θ_2 is found to be slightly sensitive to γ_0 and γ_1. See Fig. 4.2. For γ_1 $(10 - 100)$ the angle is affected, see Fig. 4.3. The thermal electrons of a 5 keV plasma are at $\gamma_0 \approx 1.01$. It is clear that the initially slow electron will have significant transverse momentum after the collision.

If the target electron is assumed to be at rest, so that $p_0 = 0$ and $\gamma_0 = 1$:

$$\mathbf{P}_0\mathbf{P}_1 = \gamma_1,\ \mathbf{P}_0\mathbf{P}_2 = \gamma_2,\ \mathbf{P}_1\mathbf{P}_2 = \gamma_1\gamma_2 - p_1 p_2 \cos(\theta_2). \tag{4.8}$$



(a)



(b)

Figure 4.1: Illustration of close collisions between a relativistic electron and an electron at rest (a). Since the electron mass is proportional to the Lorentz factor γ the relativistic mass of the relativistic electron is much larger than the mass of the electron at rest (b).

The momentum conservation becomes:

$$1 + \gamma_1 - \gamma_2 - \gamma_1\gamma_2 + p_1 p_2 \cos(\theta_2) = 0, \tag{4.9}$$

so that the cosine pitch angle becomes

$$\xi^* = \cos(\theta_2) = \frac{-(1+\gamma_1)(1-\gamma_2)}{p_1 p_2} = \frac{-(1+\gamma_1)(1-\gamma_2)}{\sqrt{(\gamma_1^2-1)(\gamma_2^2-1)}} = \frac{\sqrt{\gamma_1+1}\sqrt{\gamma_2-1}}{\sqrt{\gamma_1-1}\sqrt{\gamma_2+1}}. \tag{4.10}$$

By substituting $\xi^* = p_{2||}/p_2$ and $\gamma_2^2 = 1 + p_{2||}^2 + p_{2\perp}^2$ we observe that the solutions lie on ellipses in momentum space $(p_{||}, p_\perp)$, of which the semi axes are defined by γ_1:

$$\left(\frac{p_{2||}}{\sqrt{\gamma_1^2-1}} - \frac{1}{2}\right)^2 + \frac{p_{2\perp}^2}{2(\gamma_1-1)} = \frac{1}{4}. \tag{4.11}$$

See Appendix C for the full derivation of Eq. 4.11. In addition, γ_2 will determine the point on the ellipse that fulfills Eq. 4.11. For very energetic primary runaways $\gamma_1 \to \infty$ and we get

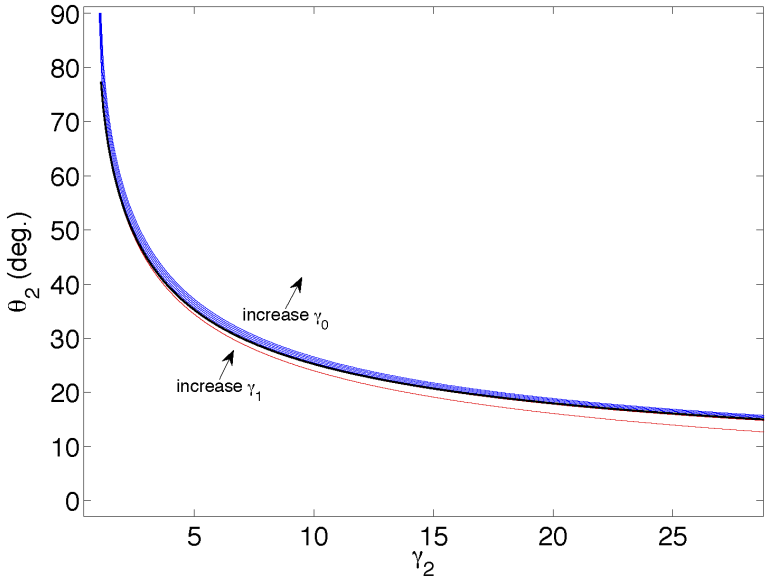


Figure 4.2: The dependence of the scattering angle of initial energies of the target electrons (γ_2). Black line is $\gamma_0 = 1, \gamma_1 = 10^5$. For blue lines $\gamma_0 = [1 : 0.01 : 1.1]$ and $\gamma_1 = 10^5$. Red line is $\gamma_1 = 100$ and $\gamma_0 = 1$.

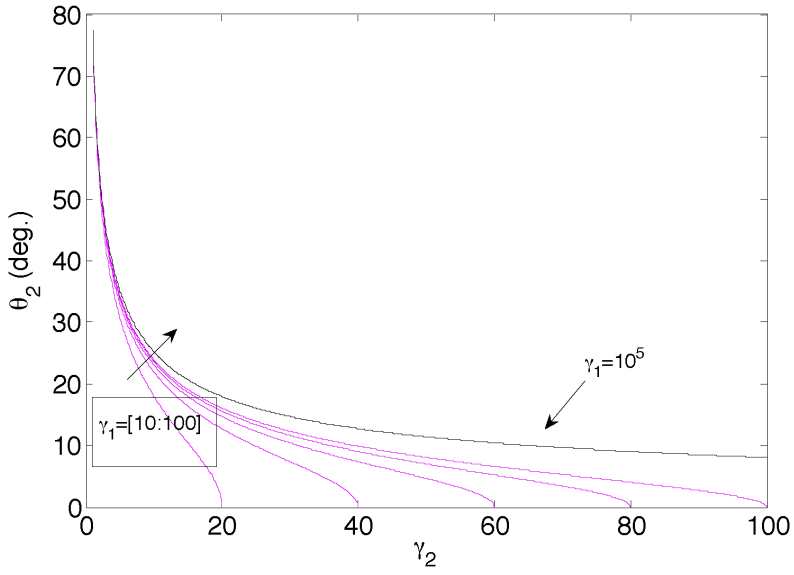


Figure 4.3: The scattering angle θ_2 at various initial energies of the primary electron (γ_1) as a function of the energy of the initially slow electron (γ_2). Here $\gamma_1 = 10 : 20 : 100$ and $\gamma_0 = 1$.

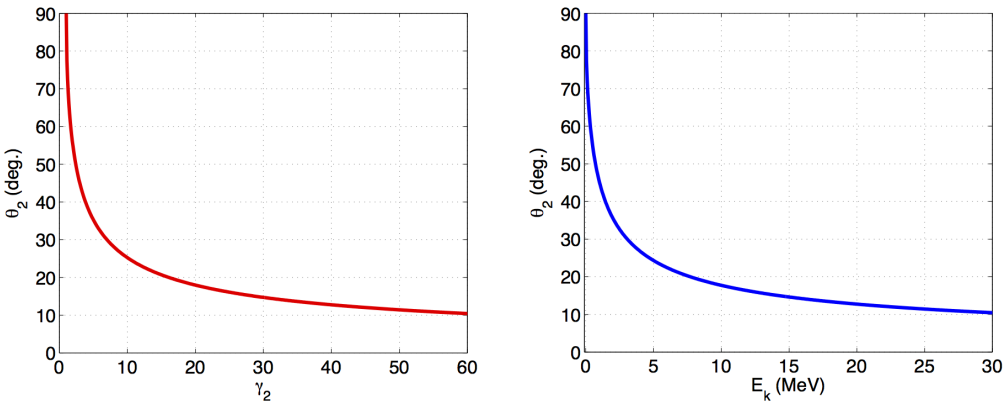


Figure 4.4: Scattering angle of as a function of the Lorentz factor (γ_2) and kinetic energy ($E_k = (\gamma_2 - 1)m_0c^2$) of the secondary electron.

$$\xi^* = \sqrt{\frac{\gamma_2 - 1}{\gamma_2 + 1}}. \tag{4.12}$$

The scattering angle $\theta_2 = \arccos(\xi^*)$ as a function of γ_2 and kinetic energy E_k is shown in Fig. 4.4. Again, we note that unless the energy of the secondary electron is rather large after the collision, its momentum will be mainly perpendicular to the magnetic field lines.

4.2 The knock-on source term

The relativistic differential cross section of electron electron elastic scattering in the laboratory frame of reference was derived by Møller [32]. This cross section has been used to describe electron electron knock on collisions in tokamak plasmas [5, 33] where electrons are knocked out from the bulk distribution through large angle scattering. The avalanche process is described with a knock-on source term, proportional to the Møller cross section. In previous runaway avalanche calculations, the bulk electrons are assumed to be at rest in the laboratory frame ($\gamma_0 = 1$, where γ_0 is the Lorentz factor of the bulk electrons) [5, 33]. In Ref. [5] the cross section is used with the seed runaways of infinite energy and thus they experience no momentum loss in the knock-on collision. On the other hand, in Ref. [33] the energy of the seed electron is finite. In both cases, the target electron, which is part of the bulk is assumed to be at rest before the collision.

The knock-on source term $\mathbf{S}$ determines to where in momentum space the secondary electron is scattered, after it has experienced a collision with a primary relativistic electron. This operator is to be incorporated in the LUKE code. It has the following form [5]:

$$\mathbf{S} = n_e n_r c \frac{d\sigma}{d\Omega}. \tag{4.13}$$

Here $d\sigma/d\Omega$ is the relativistic electron electron cross section given by quantum electrodynamic calculations by Møller (see Appendix D for a full derivation) [32]:

$$d\sigma = 2\pi r_e^2 \sum(\gamma_1, \gamma_2) d\gamma_2 = 2\pi r_e^2 \sum(\gamma_1, \gamma_2) \frac{d\gamma_2}{dp_2} dp_2 = 2\pi r_e^2 \sum(\gamma_1, \gamma_2) \frac{p_2}{\gamma_2} dp_2, \tag{4.14}$$

where $d\gamma/dp = p/\gamma$. The volume element is $d\Omega = 2\pi p_2^2 dp_2 d\xi_2$ and r_e is the classical electron radius:

$$r_e = \frac{1}{4\pi\epsilon_0}\frac{e^2}{m_e c^2}. \tag{4.15}$$

Thus,

$$\frac{d\sigma}{d\Omega} = r_e^2 \frac{\sum(\gamma_1,\gamma_2)}{p_2\gamma_2}\delta(\xi - \xi^*(p_2)), \tag{4.16}$$

where

$$\begin{aligned}\sum(\gamma_1,\gamma_2) &= \frac{\gamma_1^2}{(\gamma_1^2-1)(\gamma_2-1)^2(\gamma_1-\gamma_2)^2} \\ &\times\Big\{(\gamma_1-1)^2 - \frac{(\gamma_2-1)(\gamma_1-\gamma_2)}{\gamma_1^2}\cdot\Big[2\gamma_1^2+2\gamma_1-1-(\gamma_2-1)(\gamma_1-\gamma_2)\Big]\Big\}.\end{aligned} \tag{4.17}$$

The delta function in Eq. 4.16 corresponds to the angular relation imposed by energy and momentum conservation (Eq. 4.10). The expression in Eq. 4.17 can be simplified, in the limit for very energetic primary runaway electron ($\gamma_1 \to \infty$):

- $$\frac{\gamma_1^2}{(\gamma_1^2-1)(\gamma_2-1)^2(\gamma_1-\gamma_2)^2}(\gamma_1-1)^2 \sim \frac{\gamma_1^4}{\gamma_1^4(\gamma_2-1)^2} \to \frac{1}{(\gamma_2-1)^2},$$
- $$\begin{aligned}&\tfrac{\gamma_1^2}{(\gamma_1^2-1)(\gamma_2-1)^2(\gamma_1-\gamma_2)^2}\tfrac{(\gamma_2-1)(\gamma_1-\gamma_2)}{\gamma_1^2}\cdot\Big[2\gamma_1^2+2\gamma_1-1-(\gamma_2-1)(\gamma_1-\gamma_2)\Big] \\ &\sim \tfrac{\gamma_1^2}{\gamma_1^4(\gamma_2-1)}\tfrac{\gamma_1}{\gamma_1^2}\cdot 2\gamma_1^2 \sim \tfrac{2\gamma_1^5}{\gamma_1^6(\gamma_2-1)} \to 0.\end{aligned}$$

In this limit the expression simplifies to $\sum_{\gamma_1\to\infty}(\gamma_1,\gamma_2) \approx \frac{1}{(\gamma_2-1)^2}$ and the differential cross section becomes

$$\frac{d\sigma}{d\Omega} = r_e^2 \frac{1}{p\gamma(\gamma-1)^2}\delta(\xi - \xi^*(p)), \tag{4.18}$$

where p is the momentum of the target particle after the collision. Here we have dropped the index on γ_2 and p_2 since the expression is now independent of γ_1 and p_1. Equation 4.18 can also be expressed as:

$$\frac{d\sigma}{d\Omega} = r_e^2\frac{1}{p}\frac{d}{d\gamma}\frac{1}{(1-\gamma)}\delta(\xi-\xi^*(p)) = r_e^2\frac{1}{p^2}\frac{d}{dp}\Big(\frac{1}{1-\sqrt{1+p^2}}\Big)\delta(\xi-\xi^*(p)). \tag{4.19}$$

The knock-on source term is

$$\mathbf{S}(p,\psi,\xi,\theta) = n_e n_r c\frac{d\sigma}{d\Omega} = n_e n_R c r_e^2 \frac{1}{p\gamma(\gamma-1)^2}\delta(\xi-\xi^*(p)). \tag{4.20}$$

Using the definitions $n_e = \bar{n}_e n_e^\dagger$, $n_r = \bar{n}_r n_e^\dagger$, where $n_e^\dagger$ is a reference density, $p = \bar{p}\beta_{th}$ and $\beta_{th} = v_{th}/c$ we obtain

$$\mathbf{S}(p,\psi,\xi,\theta) = \bar{n}_e\bar{n}_r\frac{c r_e^2 n_e^{\dagger 2}}{\beta_{th}^\dagger}\frac{1}{\bar{p}\gamma(\gamma-1)^2}\delta(\xi-\xi^*(\bar{p})). \tag{4.21}$$

The collision frequency in the bulk is

$$\nu_{coll}^\dagger = \frac{n_e^\dagger q^4 \ln\Lambda^\dagger}{4\pi\epsilon_0^2 m_e^2 c^3 \beta_{th}^{\dagger 3}}, \tag{4.22}$$

so that

$$r_e = \frac{1}{4\pi\epsilon_0}\frac{e^2}{m_e c^2} \;\longrightarrow\; cr_e^2 = \frac{\nu_{coll}^{\dagger}\beta_{th}^{\dagger 3}}{4\pi n_e^{\dagger}\ln\Lambda^{\dagger}}. \tag{4.23}$$

Thus, $\mathbf{S}$ can be written as:

$$\mathbf{S}(p,\psi,\xi,\theta) = \frac{1}{4\pi}\frac{\nu_{coll}^{\dagger}\beta_{th}^{\dagger 2}n_e^{\dagger}}{\ln\Lambda^{\dagger}}\bar{n}_e\bar{n}_r\frac{1}{\bar{p}\gamma(\gamma-1)^2}\delta(\xi-\xi^*(\bar{p})). \tag{4.24}$$

The knock-on source term in the equation $\frac{\partial f}{\partial t} = S$ has the unit $\left[m^{-3}s^{-1}\right]$. The normalized expression is:

$$\frac{\partial \bar{f} n_e^{\dagger}}{\partial t_n \tau_{coll}^{\dagger}} = \mathbf{S} \;\leftrightarrow\; \frac{\partial \bar{f}}{\partial t_n} = \frac{\mathbf{S}\tau_{coll}}{n_e^{\dagger}} = \bar{\mathbf{S}} = \frac{\mathbf{S}}{\mathbf{S}^{\dagger}}, \tag{4.25}$$

where $\mathbf{S}^{\dagger} = n_e^{\dagger}\nu_{coll}^{\dagger}$. The normalized knock-on source term is

$$\bar{\mathbf{S}} = \frac{\frac{1}{4\pi}\frac{\nu_{coll}^{\dagger}\beta_{th}^{\dagger 2}n_e^{\dagger}}{\ln\Lambda^{\dagger}}\bar{n}_e\bar{n}_r\frac{1}{\bar{p}\gamma(\gamma-1)^2}\delta(\xi-\xi^*(\bar{p}))}{n_e^{\dagger}\nu_{coll}^{\dagger}}, \tag{4.26}$$

which simplifies to:

$$\bar{\mathbf{S}} = \frac{1}{4\pi}\frac{\beta_{th}^{\dagger 2}}{\ln\Lambda^{\dagger}}\bar{n}_e\bar{n}_r\frac{1}{\bar{p}\gamma(\gamma-1)^2}\delta(\xi-\xi^*(\bar{p})). \tag{4.27}$$

This is the expression implemented for LUKE calculations. It can also be written

$$\bar{\mathbf{S}} = \frac{1}{4\pi}\frac{1}{\ln\Lambda^{\dagger}}\bar{n}_e\bar{n}_r\frac{1}{\bar{p}^2}\frac{d}{d\bar{p}}\left(\frac{1}{1-\sqrt{1+\beta_{th}^2\bar{p}^2}}\right)\delta(\xi-\xi^*(\bar{p})), \tag{4.28}$$

where

$$\xi^*(\bar{p}) = \frac{\sigma p\beta_{th}^{\dagger}}{\sqrt{1+\beta_{th}^{\dagger 2}p^2}} = \sigma\sqrt{\frac{\gamma-1}{\gamma+1}}, \tag{4.29}$$

and $\sigma = sign(v_{||})$ indicates the direction of acceleration for the runaway electrons parallel to the magnetic field. The momentum $\bar{p}$ is normalized to $p_{th} = mv_{th}$.

4.2.1 Runaways with moderate energy

In the knock-on source term derived in Ref. [33], the avalanche is initiated by a runaway electron distribution function, rather than a monokinetic beam of runaway electrons at the speed of light. The distribution function gives the number of particles per unit volume in phase space so that

$$n_r(t,\psi) = \int f\,dV = 2\pi\int_{-1}^{+1}\delta(\xi_1-1)d\xi_1\int_0^{p_{max}} f_r(t,\psi,p_1)p_1^2dp_1 \tag{4.30}$$

$$= 2\pi\int_0^{p_{max}} f_r(t,\psi,p_1)p_1^2dp_1, \tag{4.31}$$

with $\xi_1 = 1$, i.e. no pitch angle on the incoming electrons, as a first approximation. n_r is the number of runaway electrons per unit volume. Using the above expression for the density in Eq. 4.20 and $v_1 = p_1/\gamma_1$ gives:

$$\mathbf{S}(p,\psi,\xi,\theta) = 2\pi n_e c r_e^2 \int_{-1}^{+1} \delta(\xi_1 - 1) d\xi_1 \times \int_0^{p_{max}} \frac{\sum(\gamma_1,\gamma_2)}{p_2\gamma_2} \delta(\xi_2 - \xi^*(p_1,p_2)) f_r(t,\psi,p_1) \frac{p_1^3}{\gamma_1} dp_1. \tag{4.32}$$

Using the general relation for Dirac's delta function $\delta(g(x)) = \sum_k \delta(x - x_k)/|g'(x_k)|$ where x_k are the zeros of the function $g(x)$ and $g'(x) = \frac{dg}{dx}$, we get

$$\delta(\xi_2 - \xi^*(p_1,p_2)) = \sum_k \delta(p_1 - p_k)/|\xi^{*'}(p_k)|, \tag{4.33}$$

where using relation 4.10 gives

$$|\xi^{*'}(p_k)| = |\frac{d\xi^*}{dp_1}| = \frac{\xi^*}{p_1\gamma_1}. \tag{4.34}$$

Thus

$$\mathbf{S}(p,\psi,\xi,\theta) = 2\pi n_e c r_e^2 \left[\frac{\sum(\gamma_1,\gamma_2)}{p_2\gamma_2} f_r(t,\psi,p_1) \frac{p_1^4}{\xi^*} \right]_{\xi_2 = \xi^*(p_1,p_2)}, \tag{4.35}$$

which agrees with the operator in Eq. (9) from Ref. [33]:

$$\mathbf{S} = n c r_e^2 \overline{f(p_1,t)} p_1^2 S_0(\gamma,\gamma_1), \tag{4.36}$$

with

$$S_0(\gamma_1,\gamma_2) = \frac{\sum(\gamma_1,\gamma_2)}{p_2\gamma_2\xi^*}, \tag{4.37}$$

and $\overline{f(p_1,t)} = \int_0^1 d\xi_1 2\pi p_1^2 f(p_1,t)$ for positive p_1, while for negative p_1 the limits of the integral are -1 and 0. Since

$$c r_e^2 = \frac{\nu_{coll}^\dagger \beta_{th}^3}{4\pi \ln\Lambda^\dagger}, \tag{4.38}$$

the avalanche source term in normalized units becomes:

$$\begin{aligned} \bar{\mathbf{S}}(p,\psi,\xi,\theta) &= 2\pi n_e \frac{\nu_{coll}^\dagger \beta_{th}^3}{4\pi \ln\Lambda^\dagger} \left[\frac{\sum(\gamma_1,\gamma_2)}{p_2\gamma_2} f_r(t,\psi,p_1) \frac{p_1^4}{\xi^*} \right]_{\xi_2 = \xi^*(p_1,p_2)} / (n_e^\dagger \nu_{coll}^\dagger) \\ &= \bar{n}_e \frac{\beta_{th}^{\dagger 2}}{2\ln\Lambda^\dagger} \left[\frac{\sum(\gamma_1,\gamma_2)}{\bar{p}_2\gamma_2} f_r(t,\psi,\bar{p}_1) \frac{(\gamma_1^2-1)^2}{\xi^*} \right]_{\xi_2 = \xi^*(\bar{p}_1,\bar{p}_2)}, \end{aligned} \tag{4.39}$$

where p_1 satisfies $\beta_{th}^{\dagger 2} \bar{p}_1 \bar{p}_2 \xi_2 = (\gamma_2 - 1)(\gamma_1 + 1)$. Note that p_1 is an implicit function of ξ_2^* and p_2 by the relation

$$p_1 = \frac{2 p_2 \xi_2^*}{\xi_2^{*2}(\gamma_2 + 1) + 1 - \gamma_2}, \tag{4.40}$$

derived from Eq. 4.10.

As observed in Ref. [33], the dependence of γ_1 in S_0 is weak (see Figure 4.5). As a consequence $\mathbf{S}$ and the avalanche growth rate, also has a weak γ_1 dependence. If the initial momentum γ_0 is varied so that $\gamma_0 > 1$, ($\gamma_0 = 1 : 0.001 : 1.01$), where 1.01 corresponds to $T_e = 5$ keV, we note that γ_0 affects the source function mainly at low γ_2, see Fig. 4.6.

Integrating the knock-on source term over momentum space gives the runaway rate:

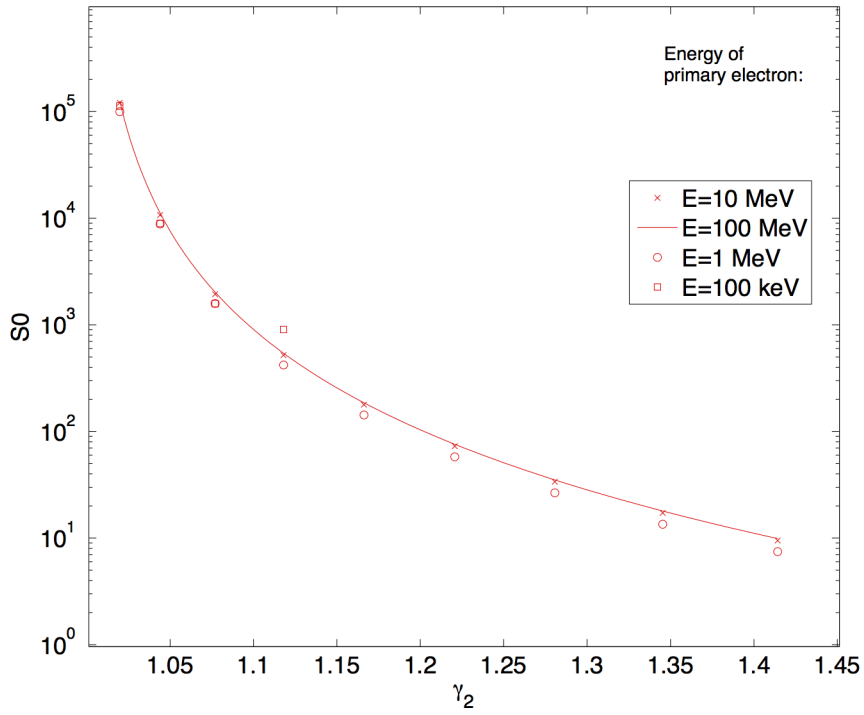


Figure 4.5: The source function S_0 of Eq. 4.37 as a function of the secondary electron energy after the collision (γ_2) for various primary kinetic energies (γ_1).

$$\frac{dn_r}{dt} = \int d^3p\, \mathbf{S} = 2\pi \int_0^\infty dp\, p^2 \int_{-1}^{1} d\xi\, \mathbf{S}. \tag{4.41}$$

The source term in Eq. 4.36 should be more accurate than Eq. 4.24, since it is weighted over the distribution function of the runaway electrons where the Rosenbluth operator only takes the seed density (n_r) (with velocity $v_{seed} = c$) into account. A divergence appears when $\mathbf{S}$ is integrated over ξ at $\xi = 1$, that is for $\gamma_1 = \gamma_2$ (at all p). This comes from the $1/(\gamma_1 - \gamma_2)^2$ factor in the differential cross section (Eq. D.19). The problem appears when $\gamma_1 = \gamma_2$, i.e. when the seed electron gives all its momentum to the target electron (exchange of the particles). This is allowed by momentum conservation. The singularity problem is instead avoided by noting that it is sufficient to integrate up to $\xi = 1/2$, since we can assume that the knocked electron maximally receives half of the incident energy of the primary runaway electron [34]. In other words, the two electrons are interchangeable and one of them will always have energy below $1/2 \cdot \gamma_1$ after the interaction.

4.2.1.1 Legendre polynomial expansion

In the description of knock on collisions from a source of electrons with intermediate energy, the full distribution in velocity and pitch-angle space of the primary electrons (f_0) must be taken into account. This calculation holds only in the limit where $p_2 \ll p_1$, so that the initial electron distribution function is very weakly modified by the knock-on process. Otherwise, a two-particle distribution function with appropriate averaging must be considered which is a more difficult problem.

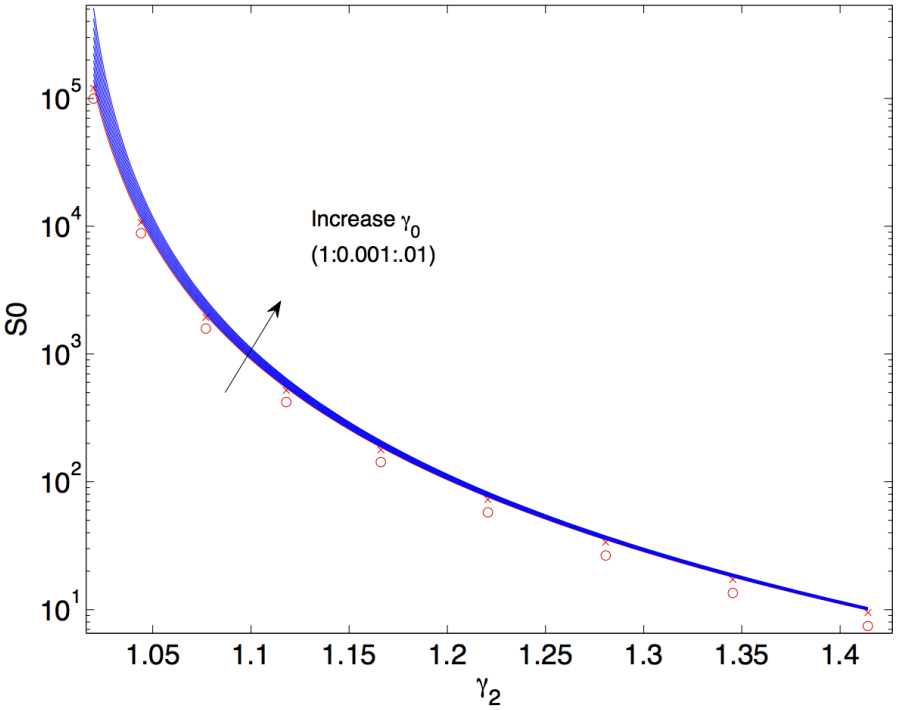


Figure 4.6: Including $\gamma_0 > 1$ (blue) for primary kinetic energy $E_1 = 100$ MeV. Including some (perpendicular) momentum of the target particle affects the magnitude of S_0 (Eq. 4.37) for low γ_2.

The addition of a 3D description of the dynamics of the primary electrons implies high computational effort. However, the required number of integrations may be reduced by taking advantage of the azimuthal symmetry of the distribution function around the magnetic field line direction using projection on Legendre polynomials. Legendre polynomial expansion is applied to the pitch angle of the primary electron distribution function as well as to the angle around the coordinate along the magnetic field line due to azimuthal symmetry. With this formulation, the momentum of the knocked out electron is determined for any direction of observation with the same numerical accuracy. The projection of the distribution function and the differential cross-sections over the Legendre polynomial basis is equivalent to determining their value for all azimuthal directions.

For a function $h(x)$ we define the series:

$$h(x) = \sum_{m=0}^{\infty} \left(m + \frac{1}{2} \right) h^{(m)} P_m(x), \tag{4.42}$$

where P_m is the m^{th} degree of Legendre polynomial and

$$h^{(m)} = \int_{-1}^{+1} h(x) P_m(x)\, dx. \tag{4.43}$$

The source term for the knock on process is:

$$S(t,\theta,\psi,p_2,\xi_2) = cn_e(t,\psi)\int_0^{p_{max}} \frac{p_1}{\gamma_1}p_1^2 dp_1 \times \int_0^{2\pi} d\varphi_1 \int_0^1 d\xi_1 \frac{d\sigma}{d^3p_2}(p_1,p_2,\xi^*) f_0(t,\theta,\psi,p_1,\xi_1). \quad (4.44)$$

From Fig. 4.7 the azimuthal angle φ_1 is related to $\xi_1 = \hat{p}_1 \cdot \hat{b}$ and $\xi_2 = \hat{p}_2 \cdot \hat{b}$ by the relation:

$$\hat{p}_1 \cdot \hat{p}_2 = \xi = \xi_1\xi_2 + \sqrt{1-\xi_1^2}\sqrt{1-\xi_2^2}\cos\varphi_1. \quad (4.45)$$

Assuming an azimuthal symmetry of the distribution function around the magnetic field line one gets $f_0(t,\psi,\theta,p_1,\xi_1,\varphi_1) = f_0(t,\psi,\theta,p_1,\xi_1)$ and the same for the probability of scattering for the secondary electrons around the primary electron velocity direction, it is possible to simplify the source term in Eq. (4.44) by using Legendre polynomials and perform the integral $\int_0^{2\pi} d\varphi_1$ analytically and $\int_0^1 d\xi_1$ by replacing it with a sum over Legendre polynomials. The differential cross section becomes

$$\frac{d\sigma^{(m)}}{d^3p_2}(p_1,p_2) = \int_{-1}^{1} \frac{d\sigma}{d\Omega_2}(p_1,p_2,\xi) P_m(\xi) d\xi \quad (4.46)$$

$$= r_e^2 \frac{\sum(\gamma_1,\gamma_2)}{p_2\gamma_2} \int_{-1}^{1} \delta\left(\xi - \xi^*(p_1,p_2)\right) P_m(\xi) d\xi \quad (4.47)$$

$$= r_e^2 \frac{\sum(\gamma_1,\gamma_2)}{p_2\gamma_2} P_m(\xi^*(p_1,p_2)). \quad (4.48)$$

In the above expression

$$\xi^* = \sqrt{\left(\frac{\gamma_1+1}{\gamma_1-1}\right)\left(\frac{\gamma_2-1}{\gamma_2+1}\right)}, \quad (4.49)$$

is the cosine pitch angle between the incoming electron and the scattered electron. The distribution of source electrons is $f_0^{(m')}(t,\theta,\psi,p_1) = \int_{-1}^{1} f_0(t,\theta,\psi,p_1,\xi_1) P_{m'}(\xi_1) d\xi_1$. Thus the source term in Eq. (4.44) becomes:

$$S(t,\theta,\psi,p_2,\xi_2) = cn_e \int_0^{p_{max}} \frac{p_1}{\gamma_1}p_1^2 dp_1 \int_0^{2\pi} d\varphi_1 \int_0^1 d\xi_1 \times \sum_{m=0}^{\infty}\sum_{m'=0}^{\infty} (m+\frac{1}{2})(m'+\frac{1}{2}) \frac{d\sigma^{(m)}}{d^3p_2} P_m(\xi) f_0^{(m')}(t,\theta,\psi,p_1) P_{m'}(\xi_1) \quad (4.50)$$

$$= cn_e \int_0^{p_{max}} \frac{p_1}{\gamma_1}p_1^2 dp_1 \sum_{m=0}^{\infty}\sum_{m'=0}^{\infty} (m+\frac{1}{2})(m'+\frac{1}{2}) \frac{d\sigma^{(m)}}{d^3p_2} f_0^{(m')}(t,\theta,\psi,p_1) \times \int_0^{2\pi} d\varphi_1 \int_0^1 d\xi_1 P_m(\xi) P_{m'}(\xi_1).$$

According to the spherical harmonic addition theorem

$$P_m(\xi) = P_m(\xi_1)P_m(\xi_2) + 2\sum_{n=1}^{m} \frac{(m-n)!}{(m+n)!} P_m^n(\xi_1) P_m^n(\xi_2) \cos(n\varphi_1), \quad (4.51)$$

where P_m^n is the associated Legendre polynomial. When integrating Eq. (4.51) over φ_1 only the first term will contribute, since the second term is proportional to $\int_0^{2\pi} \cos(n\varphi_1)d\varphi_1 = 0$. Thus

$$\begin{aligned} S(t,\theta,\psi,p_2,\xi_2) &= cn_e \int_0^{p_{max}} \frac{p_1}{\gamma_1} p_1^2 dp_1 \sum_{m=0}^{\infty}\sum_{m'=0}^{\infty} (m+\frac{1}{2})(m'+\frac{1}{2}) \frac{d\sigma^{(m)}}{d^3p_2} f_0^{(m')}(t,\theta,\psi,p_1) \times \\ &\int_0^{2\pi} d\varphi_1 \int_0^1 d\xi_1 P_m(\xi_1) P_m(\xi_2) P_{m'}(\xi_1). \end{aligned} \tag{4.52}$$

Performing the integrations in ξ_1 and φ_1 and using the orthogonality relation:

$$\int_{-1}^{1} P_m(\xi_1) P_{m'}(\xi_1) dx = \frac{\delta_{mm'}}{m+1/2}, \tag{4.53}$$

where $\delta_{mm'}$ is the Kronecker delta, the source term becomes:

$$\begin{aligned} S(t,\theta,\psi,p_2,\xi_2) &= 2\pi c n_e \int_0^{p_{max}} \frac{p_1}{\gamma_1} p_1^2 dp_1 \sum_{m=0}^{\infty} (m+\frac{1}{2}) \frac{d\sigma^{(m)}}{d^3p_2} f_0^{(m)}(t,\theta,\psi,p_1) P_m(\xi_2) \\ &= 2\pi c r_e^2 n_e \sum_{m=0}^{\infty} (m+\frac{1}{2}) P_m(\xi_2) \left[\int_0^{p_{max}} \frac{p_1^3}{\gamma_1} dp_1 \frac{\sum(\gamma_1,\gamma_2)}{p_2\gamma_2} P_m(\xi^*(p_1,p_2)) f_0^{(m)}(t,\theta,\psi,p_1) \right] \\ &= 2\pi c r_e^2 n_e \sum_{m=0}^{\infty} (m+\frac{1}{2}) P_m(\xi_2) \left[\int_0^{p_{max}} \frac{p_1^3}{\gamma_1} dp_1 \frac{\sum(\gamma_1,\gamma_2)}{p_2\gamma_2} P_m(\xi^*(p_1,p_2)) \int_{-1}^{1} f_0(t,\theta,\psi,p_1,\xi_1) P_{m'}(\xi_1) d\xi_1 \right] \end{aligned} \tag{4.54}$$

As a verification we consider the case of a monokinetic beam of primary electrons, such that $f_0^{(m)}(t,\theta,\psi,p_1,\xi_1) \simeq f_0(t,\psi,p_1) = f_0(t,\psi,p_1)\delta(\xi_1 - 1)$. Then, using the orthogonality relation (Eq. 4.53) so that $\sum_{m=0}^{\infty}(m+\frac{1}{2})P_m(\xi_2)P_m(\xi^*) = \delta(\xi_2 - \xi^*(p_1,p_2))$ the expression reduces to:

$$S(t,\theta,\psi,p_2,\xi_2) = 2\pi c r_e^2 n_e \int_0^{p_{max}} \frac{p_1^3}{\gamma_1} \frac{\sum(\gamma_1,\gamma_2)}{p_2\gamma_2} f_0(t,\psi,p_1)\delta(\xi_2 - \xi^*) dp_1. \tag{4.55}$$

which agrees with the expression previously derived for the source function from a high velocity monokinetic beam of runaway electrons in Eq. 4.32.

For implementation in LUKE, the operator must be projected on to the poloidal coordinate for the minimum magnetic field so that $\xi(\theta) \to \xi(\theta = \theta_0) = \xi_0$. Except for in the distribution function, there is a poloidal dependence in the $P_m(\xi)$. Thus, according to the definition of bounce average, the bounce averaged knock-on source term becomes:

$$\{S\}(\psi,p,\xi_0) = \frac{1}{\lambda\tilde{q}}\left[\frac{1}{2}\sum_\sigma\right]_T \int_{\theta_{min}}^{\theta_{max}} \frac{d\theta}{2\pi}\frac{1}{|\hat{\psi}\cdot\hat{r}|}\frac{r}{R_p}\frac{B}{B_P}\frac{\xi_0}{\xi}\times \tag{4.56}$$

$$2\pi c r_e^2 n_e \sum_{m=0}^{\infty}(m+\frac{1}{2})P_m(\xi)\int_0^{p_{max}} \frac{p_1^3}{\gamma_1}dp_1\frac{\sum(\gamma_1,\gamma_2)}{p_2\gamma_2}P_m(\xi^*(p_1,p_2))f_0^{(m)}(t,\theta,\psi,p_1)$$

$$= \frac{1}{\lambda\tilde{q}}\left[\frac{1}{2}\sum_\sigma\right]_T \int_{\xi(\theta_{min})}^{\xi(\theta_{max})} \frac{d\xi}{2\pi}\frac{2\xi}{-\Psi'(1-\xi_0^2)}\frac{1}{|\hat{\psi}\cdot\hat{r}|}\frac{r}{R_p}\frac{B}{B_P}\frac{\xi_0}{\xi}\times \tag{4.57}$$

$$2\pi c r_e^2 n_e \sum_{m=0}^{\infty}(m+\frac{1}{2})P_m(\xi)\int_0^{p_{max}} \frac{p_1^3}{\gamma_1}dp_1\frac{\sum(\gamma_1,\gamma_2)}{p_2\gamma_2}P_m(\xi^*(p_1,p_2))f_0^{(m)}(t,\theta,\psi,p_1) \quad =$$

$$\frac{1}{\lambda\tilde{q}}\sum_k \frac{1}{2\pi}\frac{2\xi_0}{-\Psi'(\psi,\theta_k^*)(1-\xi_0^2)}\frac{1}{|\hat{\psi}\cdot\hat{r}|_{\theta_k^*}}\frac{r_{\theta_k^*}}{R_p}\frac{B_{\theta_k^*}}{B_{P,\theta_k^*}}\times \tag{4.58}$$

$$2\pi c r_e^2 n_e \sum_{m=0}^{\infty}(m+\frac{1}{2})P_m(\xi_{\theta_k^*})\int_0^{p_{max}} \frac{p_1^3}{\gamma_1}dp_1\frac{\sum(\gamma_1,\gamma_2)}{p_2\gamma_2}P_m(\xi^*(p_1,p_2))f_0^{(m)}(t,\theta_k^*,\psi,p_1)$$

$$= \frac{1}{\lambda\tilde{q}\pi}\sum_k \frac{1}{|\hat{\psi}\cdot\hat{r}|_{\theta_k^*}}\frac{r_{\theta_k^*}}{R_p}\frac{B_0}{B_{P,\theta_k^*}}\frac{\xi_0(1-\xi^{*2})}{-\Psi'(\psi,\theta_k^*)(1-\xi_0^2)^2}\times \tag{4.59}$$

$$2\pi c r_e^2 n_e \sum_{m=0}^{\infty}(m+\frac{1}{2})P_m(\xi_{\theta_k^*})\int_0^{p_{max}} \frac{p_1^3}{\gamma_1}dp_1\frac{\sum(\gamma_1,\gamma_2)}{p_2\gamma_2}P_m(\xi^*(p_1,p_2))f_0^{(m)}(t,\theta_k^*,\psi,p_1).$$

We use the relation

$$1-\xi^{*2} = 1-\frac{\gamma-1}{\gamma+1} = \frac{\gamma+1-\gamma+1}{\gamma+1} = \frac{2}{\gamma+1}: \tag{4.60}$$

$$\{S\}(\psi,p,\xi_0) = \frac{1}{\lambda\tilde{q}\pi}\sum_k \frac{1}{|\hat{\psi}\cdot\hat{r}|_{\theta_k^*}}\frac{r_{\theta_k^*}}{R_p}\frac{B_0}{B_{P,\theta_k^*}}\frac{2}{(\gamma+1)}\frac{\xi_0}{-\Psi'(\psi,\theta_k^*)(1-\xi_0^2)^2}\times \tag{4.61}$$

$$2\pi c r_e^2 n_e \sum_{m=0}^{\infty}(m+\frac{1}{2})P_m(\xi^*)\int_0^{p_{max}} \frac{p_1^3}{\gamma_1}dp_1\frac{\sum(\gamma_1,\gamma_2)}{p_2\gamma_2}P_m(\xi^*(p_1,p_2))f_0^{(m)}(t,\theta_k^*,\psi,p_1).$$

The electron distribution function, evaluated at the poloidal angle $\theta = 0$ where the magnetic field is minimum (on the outer equatorial plane) is determined by numerically solving the bounce-averaged Fokker–Planck equation in the zero banana width approximation. The distribution function $f_0(t,\psi,\theta,p_1,\xi) \to f_0(t,\psi,p_1,\xi_0)$ is obtained using the relation

$$\xi d\xi = \Psi(\psi,\theta)\xi_0 d\xi_0. \tag{4.62}$$

We obtain

$$f_0(\xi_0) = \sum_{m=0}^{\infty}\left(m+\frac{1}{2}\right)f_0^{(m)}P_m(\xi_0), \tag{4.63}$$

where P_m is the m^{th} degree of Legendre polynomial.

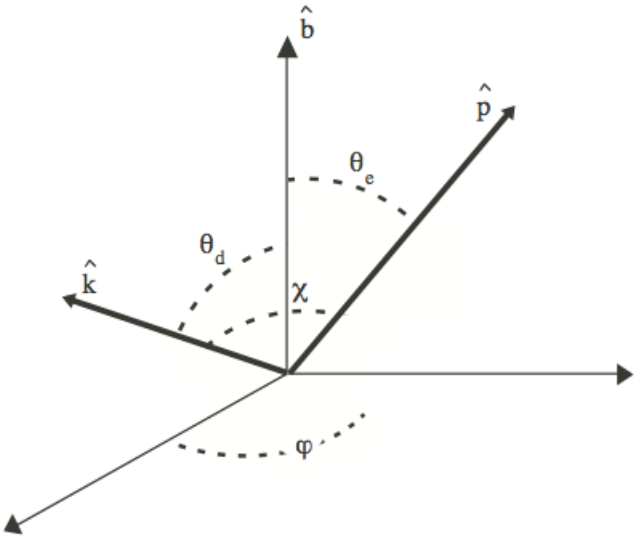


Figure 4.7: Directions of incident electron and knocked out electron with respect to the local magnetic field direction.

$$f_0^{(m)} = \int_{-1}^{+1} f_0(t,\psi,\theta,\xi,p_1)P_m(\xi)\,d\xi = \tag{4.64}$$

$$\Psi(\psi,\theta)\int_{-1}^{+1} f_0(t,\psi,p_1,\xi_0)\frac{\xi_0}{\xi}H(|\xi_0|-\sqrt{1-\frac{1}{\Psi(\psi,\theta)}})P_m(\xi)\,d\xi_0 \tag{4.65}$$

$$S(t,\theta,\psi,p_2,\xi_2) = cn_e\int_0^{p_{max}}\frac{p_1}{\gamma_1}p_1^2dp_1\sum_{m=0}^{\infty}\sum_{m'=0}^{\infty}(m+\frac{1}{2})(m'+\frac{1}{2})\frac{d\sigma^{(m)}}{d^3p_2}f_0^{(m')}(t,\theta,\psi,p_1) \tag{4.66}$$

$$\int_0^{2\pi}d\varphi_1\int_0^1\Psi(\psi,\theta)\frac{\xi_0}{\xi}d\xi_0P_m(\xi_1)P_m(\xi_2)P_{m'}(\xi_1). \tag{4.67}$$

The implementation of the source term describing knock-on collisions initiated by runaway electrons with intermediate energies (Eq. 4.66) would be the next step in improving the description of runaway avalanches in the LUKE code.

4.2.2 Bounce average of the knock-on source term

Since knock-on accelerated electrons emerge with high perpendicular momentum [5], it is necessary to properly account for the guiding-center dynamics in non-uniform magnetic field geometry and treat the full 2-D momentum electron dynamics. In a non-uniform magnetic field, the magnetic moment is an adiabatic invariant such that the guiding center parallel velocity varies along the electron trajectory. The avalanche source term presented in Eq. 4.28 is 4-dimensional (p,ψ,ξ,θ). By averaging over the poloidal motion, a procedure known as bounce average, the dimension is reduced to 3D (p,ψ,ξ_0). The pitch angle coordinate ξ in Eq. 4.28 can be expressed as a function of (ξ_0,ψ,θ) where ξ_0 is the pitch angle measured at the poloidal position θ_0 of the minimum magnetic field $B_0(\psi)$ on a magnetic flux surface. When the collisional time is longer than the bounce period [7], the rapid poloidal motion ensures that the electron distribution

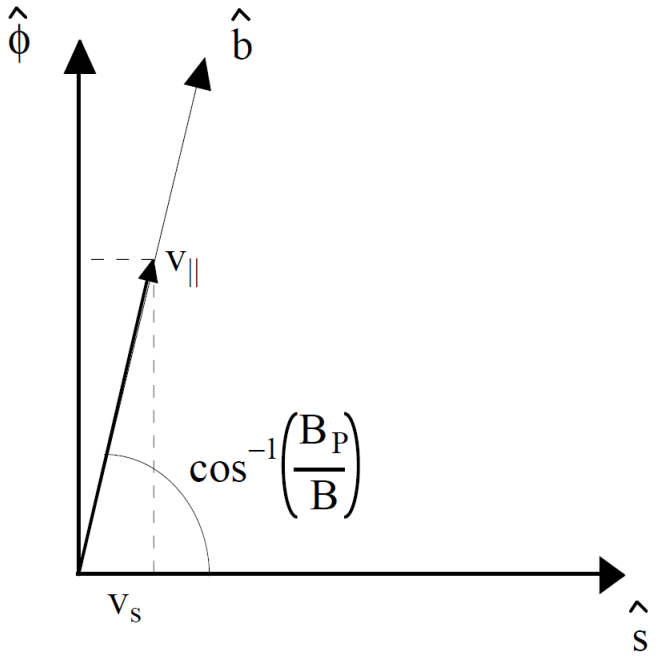


Figure 4.8: Geometry in the toroidal plane. The guiding center velocity v_s goes along the poloidal field lines. $\hat{\phi}$ is the toroidal direction and $\hat{s}$ the poloidal direction.

$f(\psi, p, \xi_0)$ is independent of the poloidal angle θ. The poloidal angle dependence can thus be averaged out of the kinetic equation by bounce-averaging. The relation for bounce average of an operator $\mathbf{A}$ is [7]:

$$\{\mathbf{A}\} = \frac{1}{\tau_b}\left[\frac{1}{2}\sum_{\sigma}\right]_T \int_{s_{min}}^{s_{max}} \frac{ds\mathbf{A}}{|v_s|}, \tag{4.68}$$

where the sum over σ applies to trapped particles only. $v_s = ds/dt$ is the guiding center velocity along the poloidal field lines defined in Fig. 4.8, where $\hat{\phi}$ is in the toroidal direction and $\hat{s}$ in the poloidal. $v_{||}$ is the velocity parallel to the magnetic field lines so that

$$\frac{v_s}{v_{||}} = \frac{B_p}{B} \implies \frac{1}{v_s} = \frac{1}{v_{||}}\frac{B}{B_p} = \frac{1}{v\xi}\frac{B}{B_p}. \tag{4.69}$$

Since $v_{||}/v \simeq p_{||}/p = \xi$ in the weak relativistic limit, where ξ is the cosine of the pitch angle defined in Eq. 4.10 and $|v_{||}| = v\xi|\xi_0|/\xi_0$. The bounce time, i.e. the time it takes for a passing particle to complete a full orbit in the poloidal plane, or for a trapped particle to complete half a bounce period is defined as:

$$\tau_b = \int_{s_{min}}^{s_{max}} \frac{ds}{|v_s|} = \int_{s_{min}}^{s_{max}} \frac{ds}{|v_{||}|}\frac{B}{B_P}, \tag{4.70}$$

where the limits s_{min} and s_{max} are the turning points for trapped electrons. The arc length $ds = \sqrt{g_{\theta\theta}}d\theta$, where $g_{\theta\theta} = r^2/|\hat{\psi}\cdot\hat{r}|^2$ is the metric element in the flux coordinate system (ψ, θ, ϕ), see [7]. The coordinate r is defined from the origin, or magnetic axis (R_p, Z_p), so that $r = \sqrt{(R-R_p)^2 + (Z-Z_p)^2}$. We have $ds = d\theta\, r/|\hat{\psi}\cdot\hat{r}|$ and the bounce time becomes:

$$\tau_b = \frac{2\pi}{v|\xi_0|}\int_{\theta_{min}}^{\theta_{max}} \frac{d\theta}{2\pi}\frac{r}{|\hat{\psi}\cdot\hat{r}|}\frac{\xi_0}{\xi}\frac{B}{B_P}. \tag{4.71}$$

The bounce time can be normalized as

$$\tau_b(\psi,\xi_0) = \frac{2\pi R_p}{v|\xi_0|}\tilde{q}(\psi)\lambda(\psi,\xi_0), \tag{4.72}$$

where

$$\lambda\left(\psi,\xi_0\right) = \frac{1}{\widetilde{q}(\psi)}\int_{\theta_{\min}}^{\theta_{\max}} \frac{d\theta}{2\pi}\frac{1}{|\hat{\psi}\cdot\hat{r}|}\frac{r}{R_p}\frac{\xi_0}{\xi}\frac{B}{B_P}, \tag{4.73}$$

$$\tilde{q}(\psi) \equiv \int_0^{2\pi} \frac{d\theta}{2\pi}\frac{1}{|\hat{\psi}\cdot\hat{r}|}\frac{r}{R_p}\frac{B}{B_p}, \tag{4.74}$$

where R_p is the tokamak major radius. Using the normalized bounce time, the expression for bounce average of an operator $\mathbf{A}$ becomes:

$$\{\mathbf{A}\}(\psi,p,\xi_0) = \frac{1}{\lambda\widetilde{q}}\left[\frac{1}{2}\sum_{\sigma}\right]_T\int_{\theta_{min}}^{\theta_{max}} \frac{d\theta}{2\pi}\frac{1}{|\hat{\psi}\cdot\hat{r}|}\frac{r}{R_p}\frac{B}{B_P}\frac{\xi_0}{\xi}\mathbf{A}(\psi,p,\xi). \tag{4.75}$$

The bounce average of the knock-on source term is:

$$\{\bar{\mathbf{S}}\} = \frac{1}{\lambda\widetilde{q}}\left[\frac{1}{2}\sum_{\sigma}\right]_T\int^{\theta_{max}}_{\theta_{min}} \frac{d\theta}{2\pi}\frac{1}{|\hat{\psi}\cdot\hat{r}|}\frac{r}{R_p}\frac{B}{B_p}\frac{\xi_0}{\xi}\bar{\mathbf{S}}(\psi,p,\xi). \tag{4.76}$$

'T' is for trapped particle and B_p is the poloidal component of the magnetic filed. We write the knock-on source term as $\bar{\mathbf{S}}(p,\psi,\xi,\theta) = \bar{\mathbf{S}}^*\delta(\xi-\xi^*(\bar{p}))$ where

$$\bar{\mathbf{S}}^* = \frac{1}{4\pi}\frac{\beta_{th}^{\dagger 2}}{\ln\Lambda^\dagger}\bar{n}_e\bar{n}_R\frac{1}{\bar{p}\gamma(\gamma-1)^2}. \tag{4.77}$$

Since $\bar{\mathbf{S}}^*$ is independent of θ, $\{\bar{\mathbf{S}}\} = \bar{\mathbf{S}}^*\{\delta\left(\xi-\xi^*(\bar{p})\right)\}$:

$$\{\bar{\mathbf{S}}\} = \bar{\mathbf{S}}^*\frac{1}{\lambda\widetilde{q}}\left[\frac{1}{2}\sum_{\sigma}\right]_T\int^{\theta_{max}}_{\theta_{min}} \frac{d\theta}{2\pi}\frac{1}{|\hat{\psi}\cdot\hat{r}|}\frac{r}{R_p}\frac{B}{B_p}\frac{\xi_0}{\xi}\delta\left(\xi-\xi^*(\bar{p})\right). \tag{4.78}$$

where ξ is a function of θ according to the relation given in Appendix E:

$$\xi = \sigma\sqrt{1-\Psi(\psi,\theta)(1-\xi_0^2)}. \tag{4.79}$$

Here $\Psi(\psi,\theta) = B(\psi,\theta)/B_0(\psi)$ and $\sigma = sign(v_{||}) = sign(\xi_0)$ indicates the direction of acceleration of the runaway electrons. Using the general relation for Dirac's delta function $\delta(g(x)) = \sum_k \delta(x-x_k)/|g'(x_k)|$ where x_k are the zeros of the function $g(x)$ and $g'(x) = dg/dx$ provided that g is a continuously differentiable function with g' non-zero.

$$\delta(\xi-\xi^*) = \sum_k \frac{2\delta(\theta-\theta_k^*)|\xi^*|}{|\Psi'(\psi,\theta_k^*)|(1-\xi_0^2)}, \tag{4.80}$$

where θ_k^* is the poloidal angle where the secondary electron emerges and satisfies

$$\sigma\sqrt{1-\Psi(\psi,\theta_k^*)(1-\xi_0^2)} - \xi^* = 0, \tag{4.81}$$

or

$$\Psi(\psi,\theta_k^*) = \frac{B_{\theta_k^*}}{B_0} = \frac{1-\xi^{*2}}{1-\xi_0^2} = \frac{2}{(1-\xi_0^2)(\gamma+1)}, \tag{4.82}$$

which is the equation we use to evaluate θ_k. We obtain

$$\{\delta(\xi-\xi^*)\} = \frac{1}{\lambda\widetilde{q}}\left[\frac{1}{2}\sum_{\sigma}\right]_T \int_{\theta_{min}}^{\theta_{max}} \frac{d\theta}{2\pi}\frac{1}{|\hat{\psi}\cdot\hat{r}|}\frac{r}{R_p}\frac{B}{B_p}\frac{\xi_0}{\xi}\sum_k \frac{2|\xi^*|}{|\Psi'(\psi,\theta_k^*)|(1-\xi_0^2)}\delta(\theta-\theta_k^*), \quad (4.83)$$

and since the integrand is an even function of ξ the expression simplifies to

$$\{\delta(\xi-\xi^*)\} = \frac{1}{\lambda\widetilde{q}}\int_{\theta_{min}}^{\theta_{max}} \frac{d\theta}{2\pi}\frac{1}{|\hat{\psi}\cdot\hat{r}|}\frac{r}{R_p}\frac{B}{B_p}\frac{\xi_0}{\xi}\sum_k \frac{2|\xi^*|}{|\Psi'(\psi,\theta_k^*)|(1-\xi_0^2)}\delta(\theta-\theta_k^*). \quad (4.84)$$

Consequently

$$\{\delta(\xi-\xi^*)\} = \frac{1}{\lambda\widetilde{q}}\frac{1}{2\pi}\sum_k \frac{1}{|\hat{\psi}\cdot\hat{r}|_{\theta_k^*}}\frac{r_{\theta_k^*}}{R_p}\frac{B_{\theta_k^*}}{B_{p,\theta_k^*}}\frac{\xi_0}{\xi_{\theta_k^*}}\frac{2|\xi^*|}{|\Psi'(\psi,\theta_k^*)|(1-\xi_0^2)}, \quad (4.85)$$

or, since $B_{\theta_k^*} = \frac{1-\xi^{*2}}{1-\xi_0^2}B_0$ (see Eq. E.10) and $\xi_{\theta_k^*} = \xi^*$

$$\{\delta(\xi-\xi^*)\} = \frac{1}{\lambda\widetilde{q}}\frac{1}{\pi}\sum_k \frac{1}{|\hat{\psi}\cdot\hat{r}|_{\theta_k^*}}\frac{r_{\theta_k^*}}{R_p}\frac{B_0}{B_{p,\theta_k^*}}|\xi_0|\frac{(1-\xi^{*2})}{|\Psi'(\psi,\theta_k^*)|(1-\xi_0^2)^2}, \quad (4.86)$$

and thus the normalized, bounce averaged knock-on source term is

$$\{\bar{\mathbf{S}}\} = \bar{\mathbf{S}}^*\frac{1}{\lambda\widetilde{q}}\frac{1}{\pi}\sum_k \frac{1}{|\hat{\psi}\cdot\hat{r}|_{\theta_k^*}}\frac{r_{\theta_k^*}}{R_p}\frac{B_0}{B_{p,\theta_k^*}}\frac{|\xi_0|(1-\xi^{*2})}{|\Psi'(\psi,\theta_k^*)|(1-\xi_0^2)^2}. \quad (4.87)$$

Using the relation in Eq. 4.60

$$\{\bar{\mathbf{S}}\} = \frac{1}{4\pi}\frac{\beta_{th}^{\dagger 2}}{\ln\Lambda^\dagger}\bar{n}_e\bar{n}_R\frac{1}{\bar{p}\gamma(\gamma-1)^2}\frac{1}{\lambda\widetilde{q}}\frac{2}{\pi}\sum_k \frac{1}{|\hat{\psi}\cdot\hat{r}|_{\theta_k^*}}\frac{r_{\theta_k^*}}{R_p}\frac{B_0}{B_{p,\theta_k^*}}\frac{1}{(\gamma+1)}\frac{|\xi_0|}{|\Psi'(\psi,\theta_k^*)|(1-\xi_0^2)^2}$$

$$= \frac{1}{2\pi^2}\frac{\beta_{th}^{\dagger 2}}{\ln\Lambda^\dagger R_p}\bar{n}_e\bar{n}_R\frac{1}{\bar{p}\gamma(\gamma-1)^2(\gamma+1)}\frac{B_0}{\lambda\widetilde{q}}\frac{|\xi_0|}{(1-\xi_0^2)^2}\sum_k\Big[\frac{1}{|\hat{\psi}\cdot\hat{r}|_{\theta_k^*}}\frac{r_{\theta_k^*}}{B_{p,\theta_k^*}}\frac{1}{|\Psi'(\psi,\theta_k^*)|}\Big], \quad (4.88)$$

which can, by the relation $p^2 = (\gamma^2-1) = (\gamma-1)(\gamma+1)$ and $p = \bar{p}\beta_{th}$, be written as:

$$\{\bar{\mathbf{S}}(p,\psi,\xi_0)\} = \frac{1}{2\pi^2}\frac{1}{\ln\Lambda^\dagger R_p}\bar{n}_e\bar{n}_R\frac{1}{\bar{p}^3\gamma(\gamma-1)}\frac{B_0}{\lambda\widetilde{q}}\frac{|\xi_0|}{(1-\xi_0^2)^2}\sum_k\Big[\frac{1}{|\hat{\psi}\cdot\hat{r}|}\frac{r}{B_p}\frac{1}{|\Psi'|}\Big]_{\theta_k^*}. \quad (4.89)$$

To evaluate the summation term in Eq. 4.89 we use the following relations in the coordinate system (R, Z, ϕ):

$$\mathbf{r} = (R-R_p)\hat{R} + (Z-Z_p)\hat{Z}. \quad (4.90)$$

This is illustrated in Fig. 4.9. Thus,

$$r(\psi,\theta) = \sqrt{(R(\psi,\theta)-R_p)^2 + (Z(\psi,\theta)-Z_p)^2}, \quad (4.91)$$

$$\hat{r} = (\hat{r}\cdot\hat{R})\hat{R} + (\hat{r}\cdot\hat{Z})\hat{Z} = \left(\frac{R-R_p}{r}\right)\hat{R} + \left(\frac{Z-Z_p}{r}\right)\hat{Z}, \quad (4.92)$$

where Z_p is $Z(0,\theta)$. Also, from [7]

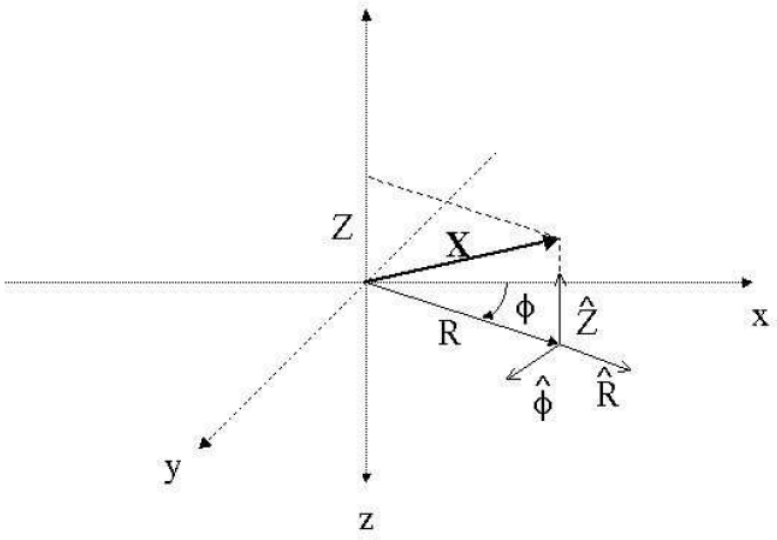


Figure 4.9: Coordinate system (R, Z, ϕ).

$$\hat{\psi} = \frac{\nabla\psi}{|\nabla\psi|}, \tag{4.93}$$

$$|\hat{\psi}\cdot\hat{r}| = \frac{(\nabla\psi\cdot\hat{R})(R-R_p)+(\nabla\cdot\hat{Z})(Z-Z_p)}{r|\nabla\psi|}, \tag{4.94}$$

where

$$\nabla\psi\cdot\hat{R} = -RB_Z,\ \nabla\psi\cdot\hat{Z} = RB_R,\ B_p = \frac{|\nabla\psi|}{R}. \tag{4.95}$$

Using these relations in Eq. 4.89 gives

$$\{\bar{\mathbf{S}}(p,\psi,\xi_0)\} = \frac{1}{2\pi^2}\frac{1}{\ln\Lambda^\dagger R_p}\bar{n}_e\bar{n}_R\times$$

$$\frac{1}{\bar{p}^3\gamma(\gamma-1)}\frac{B_0}{\lambda\widetilde{q}}\frac{|\xi_0|}{(1-\xi_0^2)^2}\sum_k\Big[\frac{(R-R_p)^2+(Z-Z_p)^2}{|-B_Z(R-R_P)+B_R(Z-Z_p)|}\frac{1}{|\Psi'|}\Big]_{\theta_k^*}. \tag{4.96}$$

This is the knock-on source term to be discretized and implemented in the LUKE code. The source term is factorized as

$$\{\bar{\mathbf{S}}\} = \bar{\mathbf{S}}^*\cdot BF, \tag{4.97}$$

where the bounce factor BF equals 1 for cylindric geometry and $BF = C\cdot\alpha$ in the more general case:

$$C = \frac{2}{\pi}\frac{|\xi_0|}{(1-\xi_0^2)^2}\frac{1}{(\gamma+1)}\frac{1}{\lambda\widetilde{q}}, \tag{4.98}$$

$$\alpha = \sum_k\frac{1}{|\hat{\psi}\cdot\hat{r}|_{\theta_k^*}}\frac{r_{\theta_k^*}}{R_p}\frac{B_0}{B_{p,\theta_k^*}}\frac{1}{|\Psi'(\psi,\theta_k^*)|}. \tag{4.99}$$

4.2.3 Discretization of the source term

The electron distribution function f solved in LUKE is calculated on a half grid on points $(i+1/2, j+1/2, l+1/2)$ in phase space (p, ξ_0, ψ). The variables in the source term are therefore also calculated on the half grid:

- $\bar{p}$ and γ on the i+1/2 grid
- ξ_0 on j+1/2
- $\tilde{q}$ on l+1/2
- λ on (j+1/2,l+1/2)

The analytic expression of the knock-on source term is implemented on discrete form on the same grid. To determine $\theta_k(i+1/2, j+1/2, l+1/2)$ we use the relation (Eq. 4.82) :

$$\Psi(\psi, \theta_k^*) = \frac{B_{\theta_k^*}}{B_0} = \frac{1-\xi^{*2}}{1-\xi_0^2} = \frac{2}{(1-\xi_0^2)(\gamma+1)}. \tag{4.100}$$

$\Psi_{i+1/2,j+1/2}$ is evaluated on each flux surface (l+1/2). The term to calculate in θ_k is:

$$\sum_k \Big[\frac{1}{|\hat{\psi}\cdot\hat{r}|}\frac{r}{B_p}\frac{1}{|\Psi'|}\Big]_{\theta_k^*}, \tag{4.101}$$

which as in Eq. 4.96 can be expressed as:

$$\sum_k \Big[\frac{(R-R_p)^2+(Z-Z_p)^2}{|-B_Z(R-R_P)+B_R(Z-Z_p)|}\frac{1}{|\Psi'|}\Big]_{\theta_k^*}. \tag{4.102}$$

This term has a poloidal and flux surface dependence (θ and ψ). The term $\theta_k(i+1/2, j+1/2, l+1/2)$ on discrete form is evaluated from:

$$\Psi(\theta^*_{k,i+1/2,j+1/2,l+1/2}) = \frac{2}{(1-\xi^2_{0,j+1/2})(\gamma_{i+1/2}+1)}. \tag{4.103}$$

And the discretization of the source term is:

$$\{\bar{\mathbf{S}}\}_{i+1/2,j+1/2,l+1/2} = \frac{1}{2\pi^2}\frac{1}{\ln\Lambda^\dagger R_p}\bar{n}_{e,l+1/2}\bar{n}_{R,l+1/2}\times \tag{4.104}$$

$$\frac{1}{\bar{p}^3_{i+1/2}\gamma_{i+1/2}(\gamma_{i+1/2}-1)}\frac{B_0}{\lambda_{j+1/2,l+1/2}\widetilde{q}_{l+1/2}}\frac{|\xi_{0,j+1/2}|}{(1-\xi^2_{0,j+1/2})^2}\sum_k\Big[\frac{1}{|\hat{\psi}\cdot\hat{r}|}\frac{r}{B_p}\frac{1}{|\Psi'|}\Big]_{\theta^*_{k,i+1/2,j+1/2,l+1/2}},$$

where the bounce coefficients are:

$$\lambda(\psi,\xi_0) = \frac{1}{\tilde{q}}\int_{\theta_{min}}^{\theta_{max}}\frac{d\theta}{2\pi}\frac{B}{R_p}\frac{[(R-R_p)^2+(Z-Z_p)^2]}{|B_R(Z-Z_p)-B_Z(R-R_p)|}\frac{\xi_0}{\xi}, \tag{4.105}$$

$$\tilde{q}(\psi) = \int_0^{2\pi}\frac{d\theta}{2\pi}\frac{B}{R_p}\frac{[(R-R_p)^2+(Z-Z_p)^2]}{|B_R(Z-Z_p)-B_Z(R-R_p)|}. \tag{4.106}$$

4.2.4 Analytic solution in circular concentric configuration

For the case of a circular, concentric configuration, the bounce-factor from Eq. 4.97 can be evaluated analytically. From Eq. 4.98 and 4.99 we have:

$$C = \frac{2}{\pi}\frac{|\xi_0|}{(1-\xi_0^2)^2}\frac{1}{(\gamma+1)}\frac{1}{\lambda\widetilde{q}}, \tag{4.107}$$

$$\alpha = \sum_k \frac{1}{|\hat{\psi}\cdot\hat{r}|_{\theta_k^*}}\frac{r_{\theta_k^*}}{R_p}\frac{B_0}{B_{p,\theta_k^*}}\frac{1}{|\Psi'(\psi,\theta_k^*)|}. \tag{4.108}$$

In a circular, concentric configuration $|\hat{\psi}\cdot\hat{r}| = 1$. The magnetic field can be expressed as:

$$B = B_0\frac{R_0}{R} = B_0\frac{R_p+r}{R_p+r\cos(\theta)} = B_0\frac{1+\epsilon}{1+\epsilon\cos(\theta)}, \tag{4.109}$$

where $R = R_p + rcos(\theta)$ and $R_0 = R_p + r$. Thus,

$$\Psi^* = \frac{B^*}{B_0} = \frac{1+\epsilon}{1+\epsilon\cos(\theta^*)}, \tag{4.110}$$

with the inverse aspect ratio $\epsilon = r/R_p$. From Eq. 4.82:

$$B^* = B_0\frac{2}{(1-\xi_0^2)(\gamma+1)}. \tag{4.111}$$

Using the above equation and Eq. 4.109 yields an analytic expression for $\cos(\theta^*)$:

$$\frac{2}{(1-\xi_0^2)(\gamma+1)} = \frac{1+\epsilon}{1+\epsilon\cos(\theta^*)} \Rightarrow \tag{4.112}$$

$$\cos(\theta^*) = \frac{1}{\epsilon}\left(\frac{(1+\epsilon)(1-\xi_0^2)(\gamma+1)}{2} - 1\right). \tag{4.113}$$

Also $|\Psi'(\psi,\theta_k^*)|$ can be evaluated for the circular case using Eq. 4.110:

$$\frac{d\Psi}{d\theta} = \frac{d}{d\theta}\left(\frac{1+\epsilon}{1+\epsilon\cos(\theta)}\right) = \epsilon\sin(\theta)\frac{(1+\epsilon)}{(1+\epsilon\cos(\theta))^2}, \tag{4.114}$$

$$|\Psi'(\psi,\theta_k^*)| = |\epsilon\sin(\theta^*)\frac{(1+\epsilon)}{(1+\epsilon\cos(\theta^*))^2}|. \tag{4.115}$$

Regarding the poloidal magnetic field (B_p) in 4.108, it can be evaluated through the relation

$$B_p(r,\theta) = B_{\theta,cyl}\frac{R_p}{R} = \frac{B_{\theta,cyl}}{1+\epsilon\cos(\theta)}, \tag{4.116}$$

$$B_p(r,\theta) = \frac{|\nabla\psi(r)|}{R} = \frac{|\nabla\psi(r)|}{R_p(1+\epsilon\cos(\theta))}. \tag{4.117}$$

Ampere's law gives the integrated magnetic field around a closed loop to the electric current passing through the loop:

$$\int_0^{2\pi} B_{\theta,cyl}(r)\cdot r\,d\theta = \int\int_S J\cdot dS = \mu_0 I(r), \tag{4.118}$$

$$B_{\theta,cyl} = \frac{\mu_0 I(r)}{2\pi r}, \tag{4.119}$$

where $B_{\theta,cyl}$ is the mean poloidal magnetic field at the radial position r (independent of θ). Finally, the poloidal magnetic field in a circular concentric configuration is:

$$B_p(r,\theta) = \frac{|\nabla\psi\,(r)\,|}{R} = \frac{\mu_0 I\,(r)}{2\pi r(1+\epsilon\cos\,(\theta))}. \tag{4.120}$$

The integral of the poloidal magnetic field around closed curve is proportional to the total current (I) passing through a surface S (enclosed by the curve).

$$B_p\,(r) = \frac{\mu_0 I\,(r)}{2\pi r}. \tag{4.121}$$

Inserting these results into Eq. 4.108 gives

$$\alpha = \sum_k \epsilon \frac{B_0}{\mu_0 I(r)} 2\pi r\,(1+\epsilon\cos\,(\theta))\,\frac{|\,(1+\epsilon\cos\,(\theta_k^*))^2\,|}{|\epsilon\sin\,(\theta_k^*)\,(1+\epsilon)\,|}, \tag{4.122}$$

when approaching the cylindrical case, i.e. $\epsilon \to 0$ $\alpha \to \sum_k \frac{B_0}{\mu_0 I(r)} 2\pi r \frac{1}{|\sin(\theta^*)|}$.

4.2.5 Integrability of the avalanche source term

The bounce averaged knock-on source term in Eq. 4.96 diverges for the poloidal points corresponding to the borders of the domain of the knock-on source term, where $B = B_0$ (at $\theta = 0$ and 2π) and $B = B_{max}$ at $\theta = \pm\pi$. In ξ-space the singularities are found at:

$$\xi_{0,min} = \sqrt{1 - 2/(\gamma+1)}, \tag{4.123}$$

$$\xi_{0,max} = \sqrt{1 - 2\frac{B_0}{B_{max}}\frac{1}{(\gamma+1)}}. \tag{4.124}$$

The singularity comes from the factor $\frac{1}{|\Psi'(\psi,\theta_k^*)|}$ in Eq. 4.108 where none of the other factors can compensate when $|\Psi'(\psi,\theta_k^*)| \to 0$ and $\frac{1}{|\Psi'(\psi,\theta_k^*)|} \to \infty$. For circular, concentric configuration, according to Eq. 4.115:

$$|\Psi'(\psi,\theta_k^*)| = |\epsilon\sin\,(\theta^*)\,\frac{(1+\epsilon)}{(1+\epsilon\cos\,(\theta^*))^2}|, \tag{4.125}$$

$$\Psi'(\psi,\theta_k^*) \approx \epsilon\sin\,(\theta^*)\,(1+\epsilon)\,(1-2\epsilon\cos\,(\theta^*)) \approx \epsilon\sin\,(\theta^*)\,, \tag{4.126}$$

$$\frac{1}{\Psi'(\psi,\theta_k^*)} \approx \frac{1}{\epsilon\sin\,(\theta^*)}. \tag{4.127}$$

We want to ensure the integrability of S over ξ_0 in a circular, concentric geometry. From Eq. 4.112 an expression for ξ_0 is obtained:

$$\xi_0^2 = 1 - K\frac{(1+\epsilon\cos\,(\theta^*))}{(1+\epsilon)} = \frac{1+\epsilon-K\,(1+\epsilon\cos\,(\theta^*))}{(1+\epsilon)} = \frac{1-K+\epsilon\,(1-K\cos\,(\theta^*))}{(1+\epsilon)}, \tag{4.128}$$

where $K = \frac{2}{\gamma+1} < 1$ is a constant for a given γ. For a small ϵ the above expression can be expanded as:

$$\xi_0^2 = \frac{1-K+\epsilon\,(1-K\cos\,(\theta^*))}{(1+\epsilon)} \approx (1-K+\epsilon\,(1-K\cos\,(\theta^*)))\cdot(1-\epsilon)\,, \tag{4.129}$$

and in the first order of ϵ,

$$\xi_0 \approx \sqrt{1-K}\left(\sqrt{1+\frac{\epsilon\left(1-K\cos\left(\theta^*\right)\right)}{1-K}}\right) \approx \sqrt{1-K}\left(1+\frac{\epsilon}{2}\frac{\left(1-K\cos\left(\theta^*\right)\right)}{1-K}\right). \tag{4.130}$$

4.2.5.1 At $\theta = 0$ and 2π

By Eq. 4.130, at $\theta = 0$

$$\xi_{0,lim} = \sqrt{1-K}\left(1+\frac{\epsilon}{2}\right). \tag{4.131}$$

$\xi_0 - \xi_{0,lim} = \sqrt{1-K}\left(\frac{\epsilon}{2}\frac{(1-K\cos(\theta^*))}{1-K} - \frac{\epsilon}{2}\right) \approx \sqrt{1-K}\frac{\epsilon}{2}\left(\frac{1-K\left(1-\frac{\theta^{*2}}{2}\right)}{1-K} - 1\right) = \frac{\epsilon}{4}\left(\frac{K\theta^{*2}}{\sqrt{1-K}}\right)$.
Thus,

$$\theta^* = \pm\sqrt{\xi_0 - \xi_{0,lim}}\cdot const., \tag{4.132}$$

where $const. = \sqrt{\frac{4\sqrt{1-K}}{\epsilon K}}$. Finally,

$$\frac{1}{\Psi'(\psi,\theta_k^*)} \sim \frac{1}{\theta} \sim \frac{1}{\sqrt{\xi_0 - \xi_{0,lim}}}, \tag{4.133}$$

which is integrable over ξ_0 for $\xi_0 \to \xi_{0,lim}$ and therefore the knock-on source term S is integrable (for $p > 0$).

4.2.5.2 At $\theta = \pm\pi$

At around $\Psi^* = \Psi_{max}$ at $\theta = \pm\pi$ Eq. 4.130 gives:

$$\xi_{0,lim} = \sqrt{1-K}\left(1+\frac{\epsilon(1+K)}{2(1-K)}\right), \tag{4.134}$$

and

$$\xi_0 \approx \sqrt{1-K}\left(1+\frac{\epsilon}{2}\frac{\left(1+K\left(1-\left(\pi-\theta^*\right)^2/2\right)\right)}{1-K}\right), \tag{4.135}$$

where the expansion $-\cos\left(\theta^*\right) = \cos\left(\pi-\theta^*\right) \approx 1 - \frac{\left(\pi-\theta^*\right)^2}{2}$ is used. Then

$$\xi_{0,lim} - \xi_0 = \sqrt{1-K}\frac{\epsilon}{2}\left(\frac{(1+K)}{(1-K)} - \frac{\left(1+K\left(1-\left(\pi-\theta^*\right)^2/2\right)\right)}{1-K}\right) = \tag{4.136}$$

$$\sqrt{1-K}\frac{\epsilon K}{4}\frac{\left(\pi-\theta^*\right)^2}{1-K} = \frac{\epsilon K}{4}\frac{\left(\pi-\theta^*\right)^2}{\sqrt{1-K}}. \tag{4.137}$$

Thus,

$$\pi - \theta^* = \pm\sqrt{\xi_0 - \xi_{0,lim}}\cdot const., \tag{4.138}$$

where $const. = \sqrt{\frac{4\sqrt{1-K}}{\epsilon K}}$. Finally,

$$\frac{1}{\Psi'(\psi,\theta_k^*)} \sim \frac{1}{\pi-\theta} \sim \frac{1}{\sqrt{\xi_0 - \xi_{0,lim}}}, \tag{4.139}$$

which is integrable over ξ_0 for $\xi_0 \to \xi_{0,lim}$ and therefore the knock-on source term S is integrable (for $p > 0$).

Chapter 5

The avalanche mechanism in the LUKE code

In this chapter, the implementation of the avalanche mechanism in the LUKE code is described. Calculations of the runaway electron formation from the combined effect of the Dreicer and the avalanche mechanism are carried out. It is found that in certain conditions the runaway electron population is initially built up by Dreicer acceleration, which lead to the set off of an avalanche of runaway electrons. The importance of the avalanche mechanism is investigated by a parametric study in bulk electron temperature and parallel electric field space. Dependencies of key parameters such as electric field strength, electron temperature, and density are investigated. The kinetic modelling of the formation of runaway electrons is restricted to non-disruptive scenarios as found in the current flattop with non-transient electric field and plasma temperature. In these calculations runaway electrons are confined to the flux-surface where they are generated, such that the growth rate derived herein should be considered as upper estimates. The predictions are related to experimental data in discharges where runaway electrons are detected in non-disruptive scenarios for several tokamaks [6]. In addition, non-disruptive Tore Supra discharges in near critical electric field are analyzed.

5.1 Implementation of knock-on collisions in the LUKE code

Runaway electrons are commonly generated in the center of a tokamak, which corresponds to the cylindrical limit. In this section the effect of the avalanche physics implemented in the LUKE code is validated against analytic result [5] in cylindric geometry. To include the effect of runaway avalanche in LUKE, the avalanche source term presented in Chapter 4 for the cylindrical geometry [5] is implemented:

$$\mathbf{S}(p,\psi,\xi,\theta) = n_e n_r c \frac{d\sigma}{d\Omega} = n_r \frac{1}{4\pi\tau \ln\Lambda} \frac{1}{p^2} \frac{d}{dp}\left(\frac{1}{1-\sqrt{1+p^2}}\right)\delta(\xi-\xi^*(p)). \tag{5.1}$$

This source term differs from [5] with a factor of 2π due to a different normalization of the distribution function. An analytic expression of the avalanche growth rate is obtained by integrating the avalanche operator over the runaway region $p > p_c$ in momentum space. This approach may overestimate the true avalanche rate, since it neglects the fact that some time must elapse between an electron entering the runaway region and the electron gaining sufficient energy to cause secondary generation.

An analytic estimate of the avalanche growth rate is obtained by integrating the knock-on source term in Eq. 4.28 over the runaway region $p > p_c$ in momentum space, as done in Ref. [5]

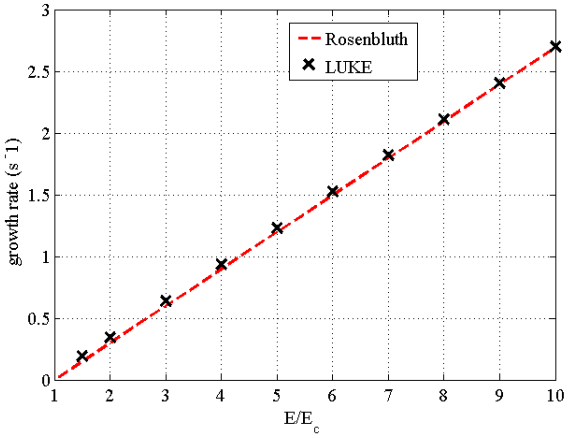


Figure 5.1: The knock-on process in LUKE (crosses) benchmarked against analytic growth rate in Ref. [5] (dashed line), when using the same momentum space thresholds.

$$\frac{1}{n_r}\frac{\partial n_r}{\partial t} = \frac{1}{n_r}\int_{p_c}^{\infty} \mathbf{S}\, d^3p = \frac{1}{n_r} 2\pi \int_{p_c}^{\infty}\int_{-1}^{1} \mathbf{S}\, p^2 dp\, d\xi = \frac{1}{2\tau \ln\Lambda}\left[\frac{1}{1-\sqrt{1+p^2}}\right]_{p_c}^{\infty}. \tag{5.2}$$

If $E/E_c \gg 1$ and p_c is small:

$$\frac{1}{n_r}\frac{\partial n_r}{\partial t} = \frac{1}{2\tau \ln\Lambda}\left(\frac{1}{\sqrt{1+p_c^2}-1}\right) \approx \frac{1}{2\tau \ln\Lambda}\left(\frac{1}{1+\frac{1}{2}p_c^2-1}\right). \tag{5.3}$$

For $p_c^2 = 2E_c/E/(1+\xi)$, $p_c^2(0) = 2E_c/E$ the growth rate for $E > E_c$ becomes:

$$\frac{1}{n_r}\frac{\partial n_r}{\partial t} = \frac{1}{2\tau \ln\Lambda}\left(E/E_c - 1\right). \tag{5.4}$$

The term -1 has been added in the numerator to ensure that no runaway generation occurs for $E/E_c < 1$.

The Rosenbluth model (4.28) for the runaway electron generation through knock-on collisions is implemented in the code LUKE and benchmarked against the growth rate in Eq. 5.4 in the case of cylindrical geometry in Fig. 5.1, by using the same momentum thresholds as in Ref [5].

In the LUKE code electrons with a momentum larger than $p_{re} \equiv \max[p_c; p(E_k = 1\,\mathrm{MeV})]$ are accounted for in the population n_r of primary runaway electrons for the knock-on collision process. The numerical momentum grid boundary p_{max} must be chosen to be larger than or equal to p_{re}, and electrons leaving the domain through the boundary remain accounted for in n_r. To be valid, the Rosenbluth approximation requires that: (a) primary runaway electrons in the knock-on collision process have a velocity near the speed of light, and (b) primary electrons have a momentum much larger than target electrons. The condition (a) is ensured by the 1 MeV minimum condition in p_{re}, which corresponds to $v/c \geq 0.94$, whereas the condition (b) is guaranteed by restricting the model to plasmas with $T_e \ll 1$ MeV. The growth rate is evaluated by LUKE as the flux of electrons through p_{re} when an electron gains enough energy to diffuse through the momentum space boundary. The Rosenbluth approximation is further justified by the weak dependence of the knock-on source term upon the incident electron energy in the energy range $1 - 100$ MeV (Fig. 4.5) [33].

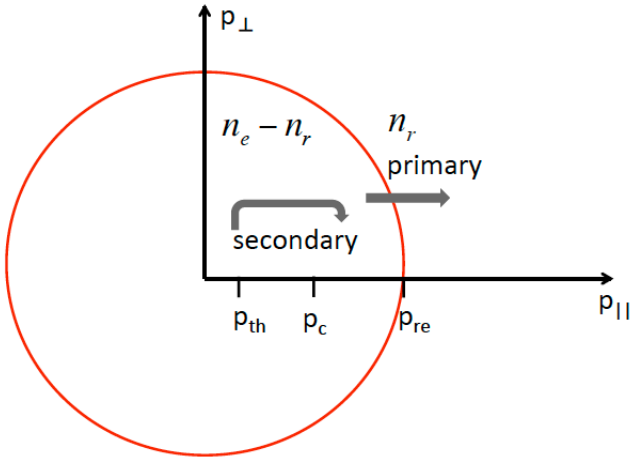


Figure 5.2: The LUKE momentum space is divided into two separate populations: the bulk electrons with momentum $p < p_{re}$ and the runaway electrons $p > p_{re}$. The knock-on collisions between the populations n_r and n_e can lead to secondary runaway electrons. Electrons that escape the domain $p < p_{re}$ either by electrons diffusing through p_{re} or by getting contribute to the runaway electron population n_r.

The bulk electron density is defined as the integral of the bulk electron distribution in momentum space:

$$\int_0^{p_{re}} f(r,p)d^3p = n_e(r). \tag{5.5}$$

The bulk and the runaway region, corresponding to $p < p_{re}$ and $p > p_{re}$ respectively, are shown in Fig. 5.2. The runaway electron population is the integral over both Dreicer and knock-on runaway fluxes

$$n_r(t) = \int_0^t \left(\gamma_D + \int_{p_{re}}^{p_{max}} S\, d^3p \right) dt, \tag{5.6}$$

where $\gamma_D = \iint \mathbf{S_p}(\psi, p, \xi) \cdot d\mathbf{S}$ is the integral of the particle flux through the surface $p = p_{re}$. In order to ensure conservation of number of particles in LUKE, a sink term is implemented to compensate for the knock-on source term

$$\mathbf{S} = \mathbf{S}_+ - < \mathbf{S}_+ > \frac{f_M}{< f_M >}, \tag{5.7}$$

where f_M is the bulk distribution, assumed to be Maxwellian and $< ... >= \int_0^{p_{max}} ... d^3p$. The source and sink terms ensure that the number of electrons $n_e + n_r = n_{tot}$ is conserved.

5.1.1 Runaway electron growth rate

The runaway electron dynamics implemented in LUKE captures the combined effect of Dreicer and knock-on processes. We investigate the evolution of the runaway electron population under the influence of a constant electric field. Figure 5.3 shows the evolution of the runaway electron population with and without the avalanche effect in a constant electric field. At first, there are very few runaway electrons, the avalanche contribution becomes significant when a runaway electron distribution has been built up by Dreicer effect. Then, an exponential growth of the runaway electron population is observed - describing the avalanche effect. The growth rate

consists of contributions from the two mechanisms Dreicer (D) and avalanche (A). Both mechanisms are proportional to the bulk density $n_e = n_{tot} - n_r$ such that the runaway production rate can be expressed on the generic form

$$\frac{\partial n_r}{\partial t} = n_e(\gamma_D + \gamma_A) \;\rightarrow\; \frac{1}{(n_{tot} - n_r)}\frac{\partial n_r}{\partial t} = \gamma_D + \gamma_A. \tag{5.8}$$

The avalanche growth rate is proportional to the runaway electron density (n_r). To quantify the avalanche growth rate, we express the avalanche term as:

$$\gamma_A = n_r \bar{\gamma}_A, \tag{5.9}$$

where $\bar{\gamma}_A$ is an avalanche multiplication factor. The growth rate of runaway electrons can be expressed as. Thus Eq. 5.8 becomes

$$\frac{1}{(1 - n_r)}\frac{\partial n_r}{\partial t} = \gamma_D + n_r \bar{\gamma}_A. \tag{5.10}$$

It is important to note that the Dreicer growth rate is not directly comparable to the avalanche factor $\bar{\gamma}_A$ which is not a growth rate (it is normalized to the runaway electron population), but a factor depending on the electric field and trapping due to toroidal geometry. Thus, the avalanche multiplication factor is a measurement of the intrinsic possibility of a runaway avalanche, for a given magnetic equilibrium and parallel electric field. The actual runaway production due to avalanche is a product of the avalanche multiplication factor ($\bar{\gamma}_A$) and the runaway electron density (n_r), $\gamma_A = n_r \bar{\gamma}_A$. The total growth rate is thus dependent on the momentaneous runaway electron population, and is therefore time dependent. For example, $\bar{\gamma}_A$ can be non-zero, even though the runaway electrons born due to avalanche is negligible, until a seed of primary runaway electrons is established . Also, even with a significant existing runaway electron population, when the knock on electrons get trapped to a large extent, the avalanche production can be small.

Equation 5.10 is an affine function of $n_r(t)$, where the constant term is the Dreicer growth rate and the avalanche multiplication factor is given by the slope. In Fig. 5.4 the growth rate given by Eq. 5.10 is illustrated for $E/E_c = 40$ and 60 and $T_e = 0.5$ keV. The growth rates from the LUKE calculations are evaluated numerically, the Dreicer as a constant value (γ_D) and the avalanche multiplication factor ($\bar{\gamma}_A$) from the slope of the curve. The Dreicer growth rate calculated by LUKE agrees well with predictions from Kulsrud [4] where the Fokker-Planck equation is solved numerically.

Since the secondary source term will enhance the fast electron density above $p_{\min}$, for a given electric field, the effect of strong Coulomb collisions will greatly increase the loss of runaway electrons. All the history of the fast tail build-up plays a crucial role on the dynamics at time t, and consequently, only a time evolution is meaningful for studying this problem which has basically no stationary regime. A stationary regime may only be found if $E_{\|}$ evolves so that the plasma current is kept time-independent.

The runaway growth rate and runaway fraction for $E/E_c = [2 : 8]$ is shown in Fig. 5.5a and 5.5b. The slope of the curve gives the avalanche factor ($\bar{\gamma}_A$), demonstrated in Fig. 5.6.

5.1.2 Treatment of suprathermal electrons

For the sake of simplicity, the Rosenbluth model in Ref. [5] considers only secondary electrons born with a momentum larger than p_c. However, electrons accelerated via a knock-on collision to intermediate momentum $p_{th} < p < p_c$ could contribute to the runaway growth rate indirectly by populating the suprathermal region and thereby modifying the Dreicer flux. With the LUKE code, it is possible to go beyond this estimate, for a more realistic description of the runaway electron distribution function by also including the secondary electrons with momentum in the

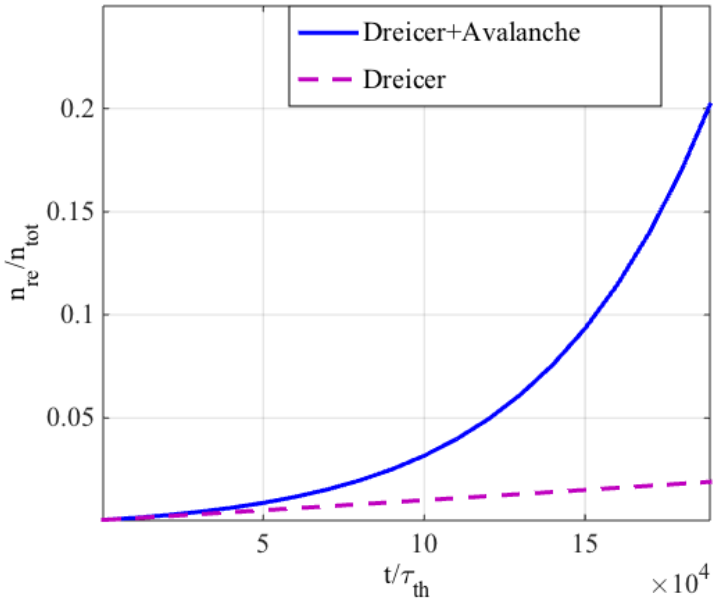


Figure 5.3: The fraction of runaway electrons ($E/E_c = 30$ and $T_e = 0.5$ keV) as a function of time normalized to thermal collision time, with and without the avalanche effect due to the knock-on collisions. .

collisional momentum region $p < p_c$. Numerically, three thresholds must be defined when implementing the Rosenbluth model (4.28): the minimum and maximum values for the secondary electron momentum, and the minimum value p_{re} above which runaway electrons are counted as primary electrons in the knock-on process. In order to determine these parameters, the lower threshold above which knock-on collisions are included is varied and the results are shown in Fig. 5.7 for electric field $E/E_c = 2$ and $E/E_c = 5$ ($T_e = 5$ keV). We can see that the indirect contribution of knock-on collisions to suprathermal energies $p_{th} < p < p_c$ is negligible, such that it is appropriate to set the lower threshold for secondary electron momentum at p_c. A scan in electric field strength for $p_{min} = p_{th}$ and p_c presented in Fig. 5.8 leads to the same conclusion. However, it must be pointed out that these calculations are done for constant electric field and the knock-on born electrons near the runaway region could be crucial in a transient electric field where the boundary between the runaway momentum region and the collisional region varies in time.

The avalanche theory by Rosenbluth accounts for runaway electrons born due to knock-on collisions in momentum space in the interval $[p_c, \infty]$. For the secondary runaway electrons due to knock-on collisions in LUKE, a finite upper limit p_{max} must be chosen above which the contribution to the runaway electron population is neglected (see Fig. 5.2). Energy conservation imposes that the higher threshold for secondary electron momentum is lower than p_{re}. The knock-on production decreases with momentum, with the knock-on source term (Eq. 4.28) $\mathbf{S} \to 0$ for $p \to \infty$. In LUKE p_{max} has to be defined at large enough momentum to account for the dominant part of the knock-on collision contribution. The avalanche multiplication factor ($\bar{\gamma}_A$) as a function of a lower cutoff (p_{min}) for the population of secondary electrons has been computed in order to quantify at what value the avalanche production becomes negligible. It is found that most contribution to the avalanche factor comes from the knock-on electrons born near the critical momentum p_c. We see in Fig. 5.7 that setting $p_{re} = 4p_c$ is sufficient to account for more than 80% of knock-on collisions.

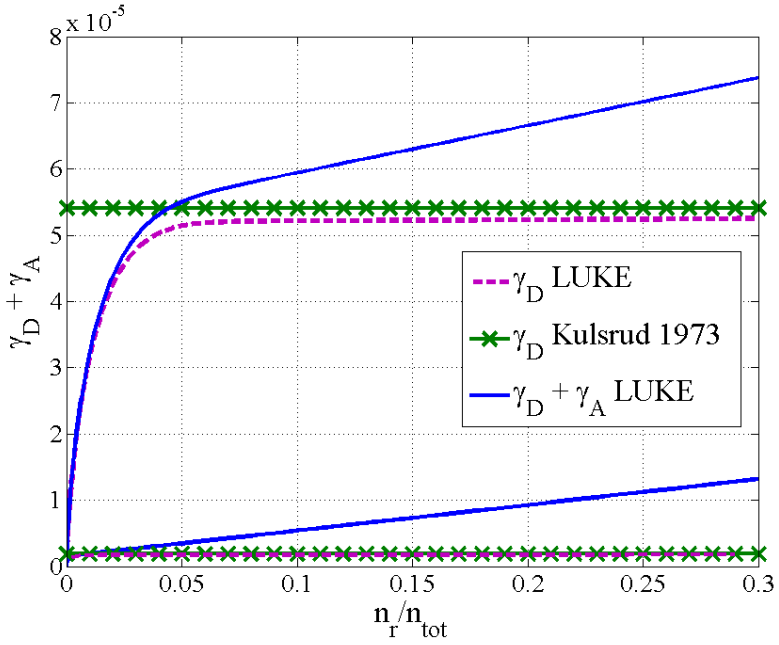
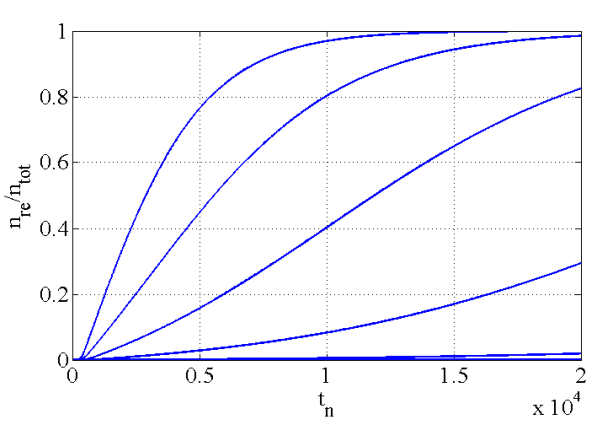
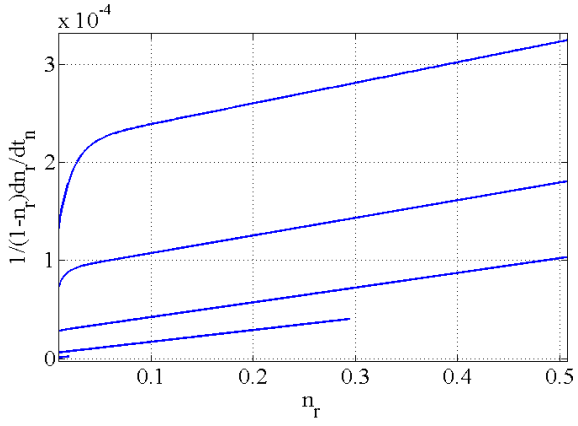


Figure 5.4: The growth rate in constant electric field and $T_e = 0.5$ keV for $E/E_c = 40$ (the curves with lower growth rate) and $E/E_c = 60$ (curves with higher growth rate) as a function of the runaway electron density, with and without the avalanche effect. The Dreicer contribution is in good agreement with Kulsrud's theory [4]. The growth rates are normalized to the thermal collision frequency ($\nu_{th} = 1/\tau(v_{th})$).



(a) .



(b)

Figure 5.5: Runaway electron fraction (a) and growth rate (b) calculated with LUKE, including runaway avalanches, for electric field strength $E/E_c = [2:8]$ and $\beta = 0.01$.

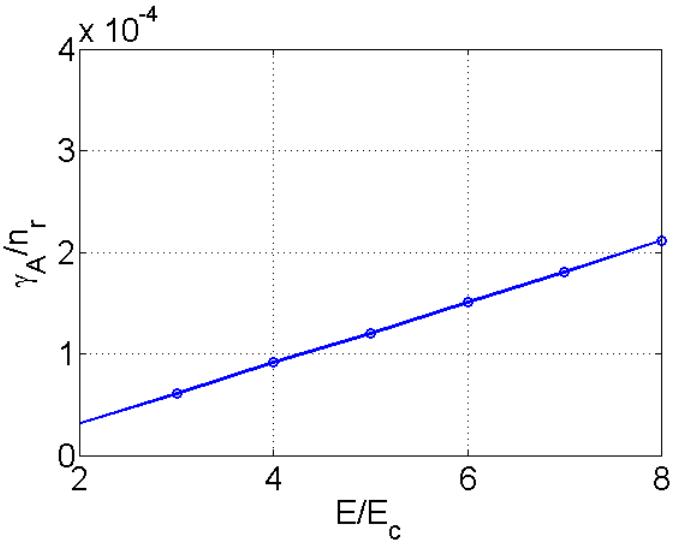


Figure 5.6: The avalanche multiplication factor ($\bar{\gamma}_A$) vs electric field strength.

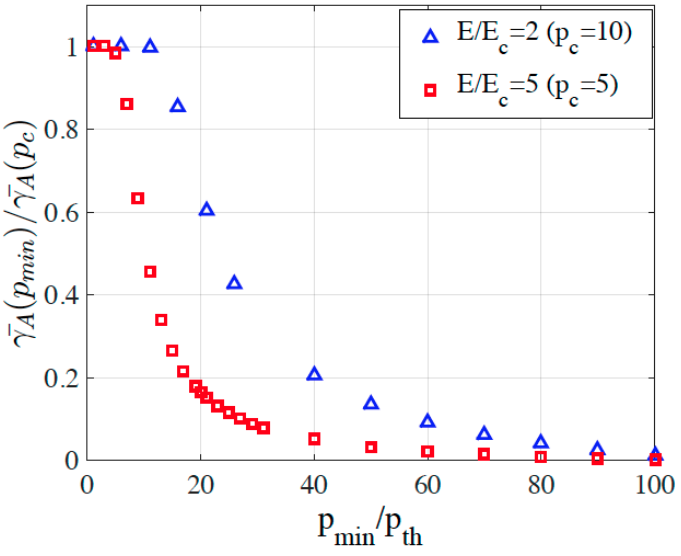


Figure 5.7: Avalanche multiplication factor as a function of the lower momentum cut off p_{min}/p_{th} for $T_e = 5$ keV, normalized to the avalanche factor at $p_{min} = p_c$.

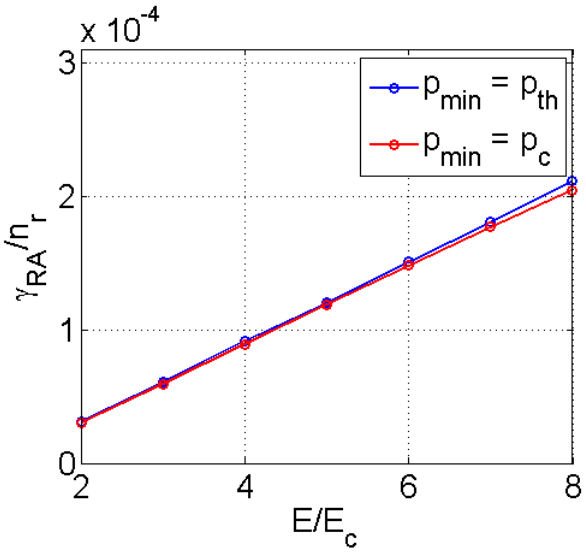


Figure 5.8: The avalanche growth rate, including ($p_{min} = p_{th}$) or excluding ($p_{min} = p_c$) the suprathermal knock on electrons.

5.2 The relative importance of runaway avalanches

The results presented in Sec. 5.1.1 (see Fig. 5.3) have shown that the runaway electron distribution can be significantly modified by including the effect of knock-on collisions. In order to understand the mechanisms that govern the runaway electron generation processes a parametric study is performed with the aim to investigate which runaway formation process; Dreicer or avalanche, that dominates in non-disruptive tokamak experiments.

The relative importance of the avalanche mechanism to the Dreicer mechanism can be estimated by comparing the analytic avalanche growth rate in Eq. 5.4 and the Dreicer generation from Eq. 2.22. The ratio of the two growth rates is

$$\left(\frac{\partial n_r}{\partial t}\right)_A \Big/ \left(\frac{\partial n_r}{\partial t}\right)_D = \frac{\gamma_A}{\gamma_D} \sim$$
$$\sim \frac{\sqrt{\pi}}{4}\frac{n_r}{n_e}\frac{1}{\ln\Lambda}\left(\frac{v_{th}}{c}\right)^3\left(\frac{E}{E_c}-1\right)\left(\frac{E}{E_D}\right)^{-1/2}\exp\left(\frac{E_D}{4E_D}+\sqrt{\frac{2E_D}{E}}\right). \qquad (5.11)$$

By letting a small fraction of the electrons run away in LUKE, the relative importance of the avalanche effect as a function of plasma temperature and electric field strength can be evaluated numerically from the fraction of the runaway electrons that originate from Dreicer and knock-on collisions. In Fig. 5.9 the fraction of runaway electrons born from knock-on collisions is shown, when 1% of the initial electron population has run away in a cylindrical magnetic configuration with constant electric field, density and temperature. The fraction of runaway electrons has to be small enough for the equilibrium parameters to remain constant and to consider the current as driven by two separate populations; the bulk and the runaway tail. The relative importance of secondary runaway electrons grows at lower temperature and electric field, as the slower primary generation in high collisionality (low temperature) allows for runaway avalanches to take off. The duration of the electric field required to reach the runaway fraction varies strongly in the parameter space presented in Fig. 5.9. The time required for 1% of the electrons to run away is illustrated for various electron temperatures ($T_e = 0.05$, 0.5, 2 and 5 keV) in Fig. 5.10. The formation of runaway electrons slows down as the collisionality increases at lower bulk

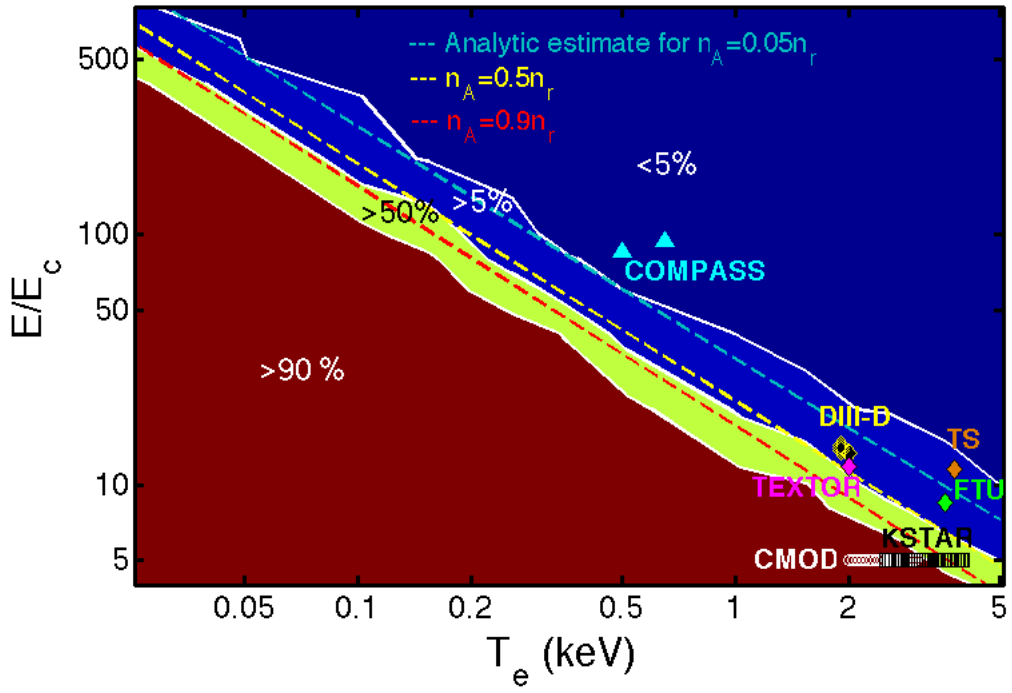


Figure 5.9: The fraction of runaway electrons originating from knock-on collisions (n_A/n_r) as modelled in LUKE. The analytic estimate of when 5% (cyan line), 50% (yellow line) and 90% (red line) of the runaway electrons come from avalanche is obtained from Eq. 5.11. The parametric study is related to non-disruptive scenarios where runaway electrons were generated in several tokamaks. All data points are taken from Ref. [6] except for the Tore Supra (TS) point (discharge #40719) and COMPASS points (discharge #8555 and #8630).

temperature. The sensitivity of runaway electron formation on the electron temperature has been shown in Ref. [35].

The numerical results are compared with the analytic estimate from Eq. 5.11 with $n_r/n_e = 0.01$. The condition for the dominance of the avalanche effect $\gamma_A/\gamma_D > 1$ is plotted in Fig. 5.9 along with the boundaries for which $n_A/n_r = 5\%$ and 90%.

In order to relate the study to experimental tokamak scenarios, it must be noted that the simulations are performed for constant electric field and temperature. Consequently, the study is restricted to non-disruptive scenarios with well-diagnosed and quiescent conditions from several tokamaks, where runaway electrons have been observed in the current flattop with the relevant plasma parameters maintained essentially constant. Results from scenarios with reproducible measurements of electron density, loop voltage and plasma temperature at the runaway electron onset from DIII-D, FTU, TEXTOR, Alcator C-Mod and KSTAR were recently published in Ref. [6]. From this study the threshold electric field normalized to the critical field is found to be significantly higher than predicted by collisional theory where the birth of runaway electrons is expected at $E/E_c > 1$, provided that no additional runaway electron loss mechanisms are present [4]. However, the condition for runaway onset in collisional theory does not take the time required to generate runaway electrons into account. Estimations from LUKE calculations in Fig. 5.10 shows that this time scale can be unrealistically large as compared to the tokamak discharge duration. The time to generate a small fraction of runaway electrons from a Maxwellian distribution is finite for $E/E_c > 1$ but as $E/E_c \to 1$, the required

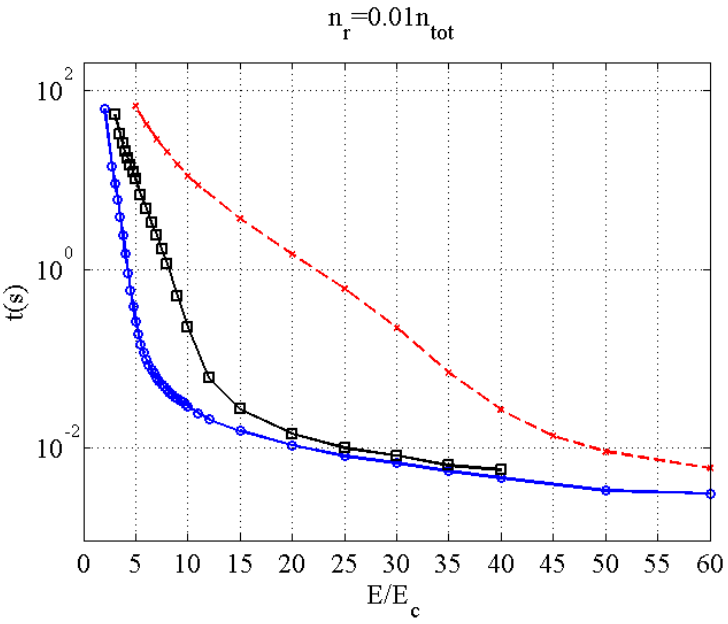
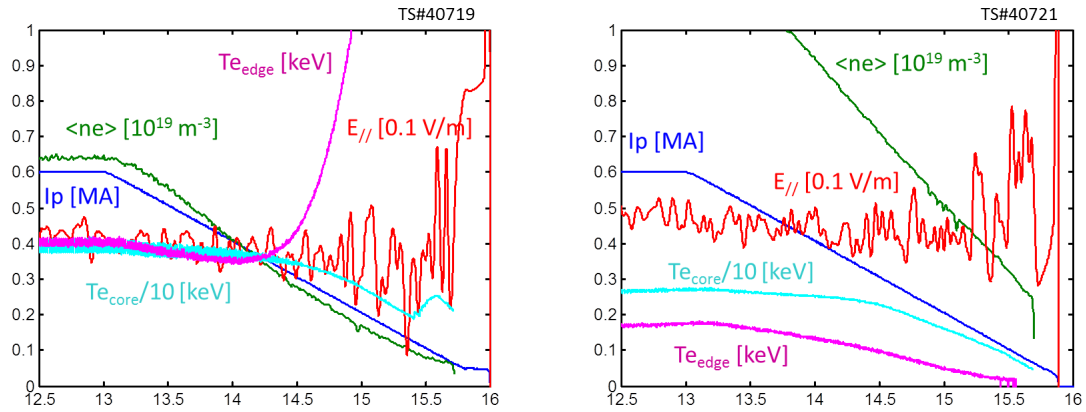


Figure 5.10: The time required for 1% of the initially Maxwellian electrons to run away, for the electron temperature $T_e = 0.5$ keV (dashed line), 2 keV (solid line and squares) and 5 keV (solid line and circles) .

time to generate runaway electrons $t \to \infty$. However, it is not the only explanation since the study in Ref. [6] found that the E/E_c threshold for suppression is also well above unity.

Runaway electrons have been generated in the Tore Supra (TS) tokamak in low density discharges ($n_e < 10^{19}\ m^{-3}$). The TS pulses #40719 and #40721 are performed after a boronization and suprathermal electrons are observed in the former discharge but not in the latter. Both are Ohmic discharges at $I_p = 0.6$ MA in the current flattop. Possible signature of suprathermal electrons are observed in #40719 by the ECE edge chords at current ramp-down, when the density is low ($< n_e >= 0.4 \cdot 10^{19}\ m^{-3}$), see Fig. 5.11a. The uniform E-field, estimated as the time derivative of the resistive flux [11], is $E_\parallel = 0.038 \pm 0.003$ V/m and the core temperature is 3.8 keV. The determination of the magnetic flux at the plasma boundary is described in Ref. [36]. No suprathermal electrons are detected by electron cyclotron emission (ECE) in the following pulse #40721 at a higher electron density, see Fig. 5.11b. Similar result is found from HXR measurements from the vertical camera detecting emission of $20 - 200$ keV (Fig. 5.15). A peak of photo-neutrons is observed at the plasma termination for the lower density shot (#40719) but not for the higher density shot (#40721), see Fig. 5.12. From the combined observations on ECE, HXR and photo-neutron measurements, the presence of relativistic electrons during the ramp-down of #40719 is identified. During the current flattop of #40719, the electron density is $< n_e >= 0.64 \cdot 10^{19}\ m^{-3}$, corresponding to $E/E_c \approx 8$, but there is no clear signature of runaway electrons until $E/E_c \approx 11$. The suprathermal generation in #40719 is added to the $(E/E_c, T_e)$ scan (see Fig. 5.9) and falls in the region where Dreicer generation is dominant. In the higher density pulse (#40721) $E/E_c \approx 4$ during the current flattop and no suprathermal electrons are detected. These results are in line with those of Ref. [6] where $E/E_c \sim 3 - 12$ is required to generate a detectable population of runaway electrons in the various tokamaks. The runaway formation in these discharges is investigated through LUKE calculations in Chapter 7.

Relating the data from the experiments in Ref. [6] and the TS discharge #40719 to the parameter scan done in LUKE (Fig. 5.9) reveals that the scenarios fall in or close to the



(a) (b)

Figure 5.11: Signature of suprathermal electrons on the edge ECE chord at around $t = 14.5$ s are seen in the Tore Supra discharge #40719 (a). When the density is higher (#40721) (b), there is no sign of supra thermal electrons.

region where the avalanche mechanism becomes significant for the runaway electron growth rate (Fig. 5.9). Data from two COMPASS discharges where runaway electrons are observed (#8555 and #8630) fall in the region where the Dreicer effect is dominant [37]. Runaway electrons are commonly produced in the current ramp-up phase of the COMPASS tokamak, as a consequence of relatively high E/E_c ratio $(20 - 200)$. The circular 130 kA discharge #8555 is part of the line averaged electron density $< n_e >$ scan from $1 - 4 \cdot 10^{19}\ m^{-3}$, where $< n_e >$ for this particular shot is $2 \cdot 10^{19}\ m^{-3}$ during the flattop. The raise of runaway activity is observed with HXR NaI(Tl) scintillator and photoneutron detector as the $< n_e >$ decreased from discharge to discharge, while Parail-Pogutse instability appeared for all discharges with $\bar{n}_e$ lower than in the discharge #8555. The D-shaped 160 kA discharge #8630 was done for the purpose of the sawteeth-runaway correlation studies with the electron density $< n_e >= 9 \cdot 10^{19}$ m^{-3}. Even though the discharge had relatively high $< n_e >$, the runaway activity correlated with the sawteeth instability is visible in HXR and photoneutron signals. Data from these two COMPASS discharges #8555 and #8630 are plotted on Fig. 5.9, where E/E_c at runaway electron onset in the ramp-up phase are 85 and 94, respectively. The electron density at the time of the runaway detection is $1.1 \cdot 10^{19}$ and $0.80 \cdot 10^{19}\ m^{-3}$. In COMPASS, interferometry is used for the line averaged electron density measurements, while Thomson scattering is used for electron temperature T_e and electron density n_e profile measurements.

These observations suggest that knock-on collisions may be play an important role in the formation of runaway electron generation in tokamak plasmas, even in non-disruptive scenarios.

We also relate the simulations to data from a typical DIII-D disruption [3] in Fig. 5.16. The line averaged electron density originates from a mid plane horizontal interferometer and the electron temperature is from 3^{rd} harmonic ECE up to the current quench (CQ), then assuming $T_e \sim 5$ eV during the CQ (from spectroscopy and L/R time) and then assuming $T_e \sim 2$ eV during the RE plateau (from spectroscopy). Since the electric field is measured outside the vacuum vessel, a central electric field is estimated with the 1D modelling tool GO [38], where density and temperature data is used to model the electric field evolution. These results indicate that in scenarios with large temperature drops, avalanche generation may be a crucial ingredient in modelling of tokamak plasma disruptions.

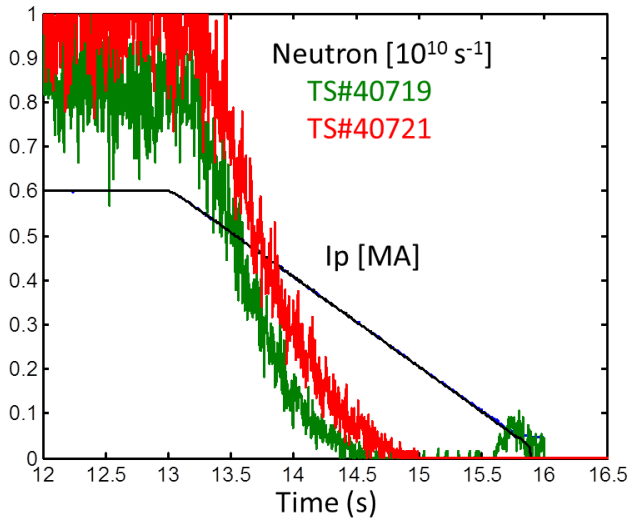
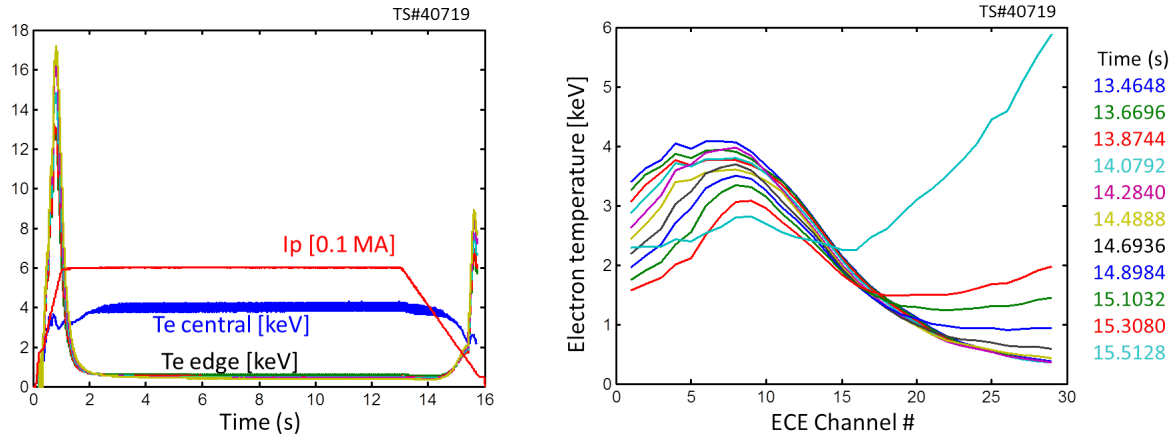
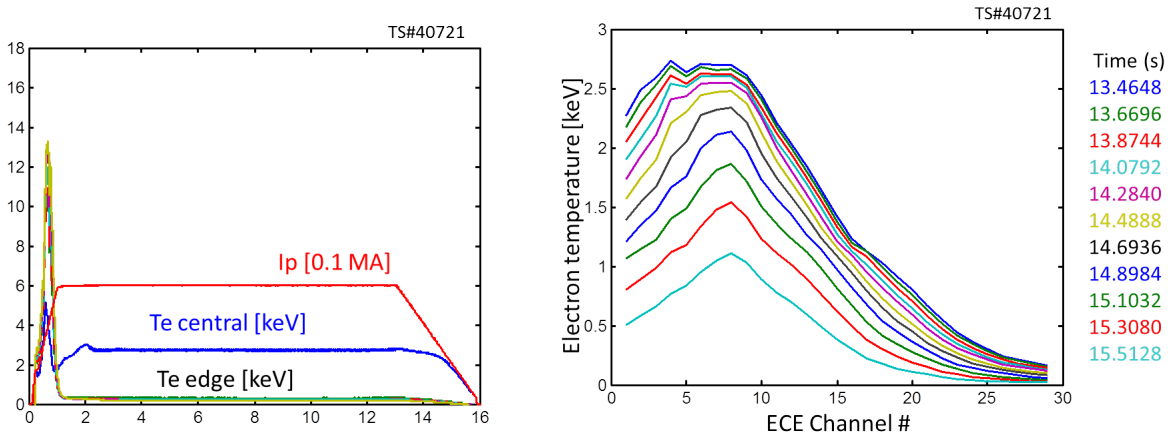


Figure 5.12: Photo-neutron signal in at the end of the current flattop and in the ramp down for the two Tore Supra pulses. A peak of neutrons is observed at the plasma termination for the low density shot (#40719) but none for the higher density shot (#40721).



(a) (b)

Figure 5.13: Electron cyclotron emission in the Tore Supra discharge #40719.



(a) (b)

Figure 5.14: Electron cyclotron emission in the Tore Supra discharge #40721.

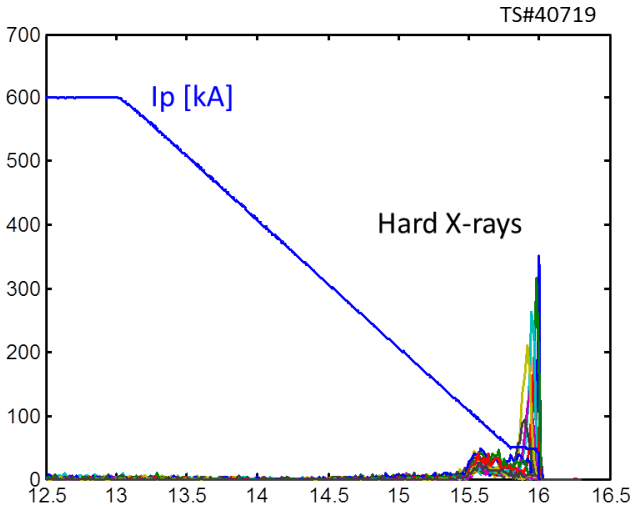


Figure 5.15: HXR data from the vertical camera (channels 1-21) in the energy range $E_{HXR} = 20 - 200$ keV. The HXR emission produced in the current ramp down in #40719 is a signature of suprathermal electrons, whereas in the higher density discharge #40721 no HXR emission is detected.

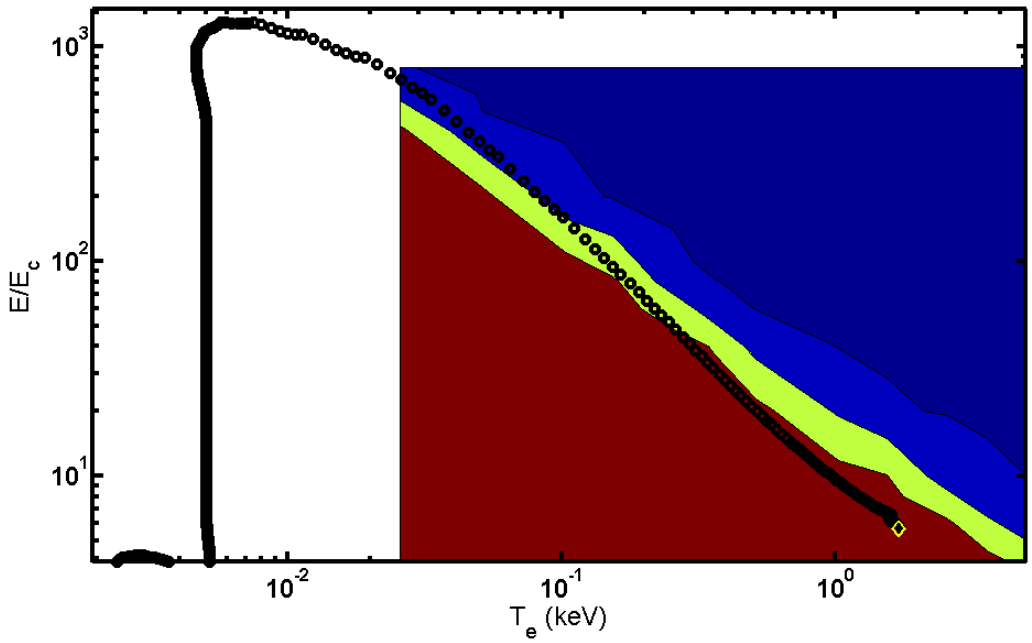


Figure 5.16: Relation to E-field evolution in a DIII-D disruption (black circles), the pre-disruptive phase illustrated with a yellow diamond, plotted on to the LUKE parameter scan.

Chapter 6

Toroidal effects on runaway dynamics

In this chapter the effect of magnetic trapping on runaway electron formation processes through the Dreicer and the avalanche mechanism is investigated. The numerical result of the avalanche reduction off the magnetic axis obtained through LUKE calculations are compared with analytic predictions. The fate of the trapped electrons is investigated by calculating the effect of Ware pinch, where the trapped-electron runaways are transported inwards to less restrictive trapping regions, where they may detrap and run away [39]. The knock-on collisions leading to runaway avalanches are implemented through the bounce-averaged knock-on operator (Eq. 4.96).

6.1 Toroidal effects on runaway electron growth rate

The reduction of the Dreicer runaway rate away from the magnetic axis has been identified in previous work [40], as well as with the code LUKE [7]. At least three effects contribute to reduce the growth rate: the overall effect of the electric field on trapped electrons cancels out over one bounce period; the acceleration of passing electrons is also reduced as their pitch angle increases towards the high field side; the existence of a magnetic trapping cone creates larger pitch-angle gradients in the circulating region, thereby increasing the effect of pitch-angle scattering.

As discussed in Sec. 4.1, secondary electrons emerging from the knock-on collisions are typically highly magnetized. Since the trapping effect increases off the magnetic axis in a non-uniform magnetic field configuration, the further away from the magnetic axis the electrons appear, the more they tend to be born trapped.

To quantify the tendency of magnetic trapping, the evolution of the runaway population is calculated in a scenario with circular plasma cross section and magnetic non-uniformity, with inverse aspect ratio ranging from $\epsilon = 0$ to $\epsilon = a/R = 1$. The inverse aspect ratio of the Tore Supra tokamak is $\epsilon \approx 0.3$. The calculations in Fig. 6.1 show that the runaway electron population grows significantly slower off the magnetic axis than in the center.

In order to study the trapping effects on the runaway population, the Dreicer growth rate γ_D and the avalanche multiplication factor $\bar{\gamma}_A$ are calculated with the code LUKE and quantified separately. The Dreicer growth rate is found to be strongly affected by the non-uniformity of the magnetic field, as shown in Fig. 6.2. A fit of the numerical results gives an analytic expression of the Dreicer growth rate $\gamma_D/\gamma_{D,cyl} = 1 - \sqrt{2\epsilon/(1+\epsilon)}$. The results indicate that for $\epsilon > 0.5$ runaway generation from Dreicer acceleration vanishes.

Also for the avalanche effect, a reduction of $\bar{\gamma}_A$ away from the magnetic axis is observed in Fig. 6.3, with an avalanche multiplication factor that decreases with the inverse aspect ratio. In order to derive an analytic estimate for the avalanche growth rate including the effect of magnetic trapping owing to a non-uniform magnetic configuration, it is assumed that all electrons with momentum $p > p_c$ will contribute to the runaway population (as in Ref. [5]), except the secondary electrons that appear in the trapped momentum region $p < p_T$. The

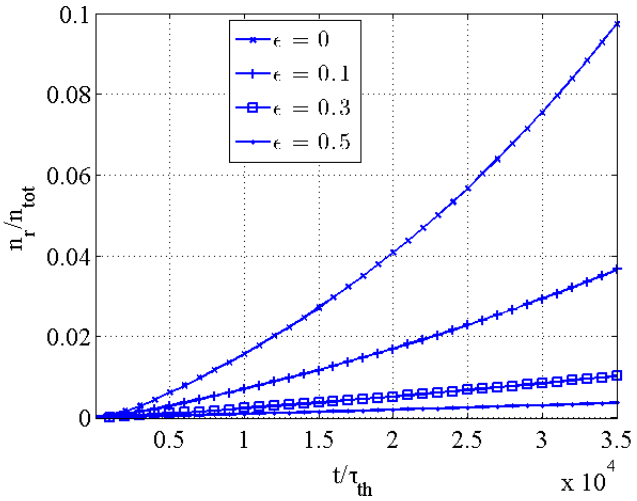


Figure 6.1: The evolution of the runaway electron population, including the avalanche effect owing to knock-on collisions, depends strongly on the radial position in a non-uniform magnetic field configuration, where $\epsilon = r/R$ is the inverse aspect ratio coordinate. $E/E_c = 40$, $T_e = 0.5$ keV and the time t is normalized to the thermal collision time τ_{th}.

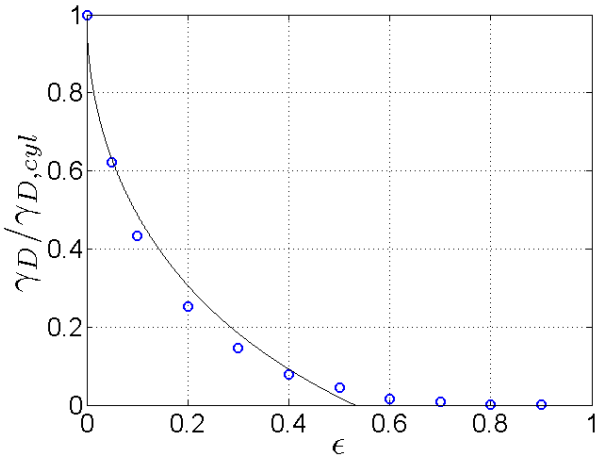


Figure 6.2: Radial dependence of Dreicer growth rate, normalized to the growth rate for cylindrical case, i.e. $\epsilon = 0$, compared to a fit $(1 - 1.2\sqrt{2\epsilon/(1+\epsilon)})$ [7].

magnetic trapping criterion on the momentum p_T of secondary electrons born via knock on collisions is

$$\frac{B(\theta)}{B_{max}} > \frac{2}{\sqrt{1+p_T^2}+1}, \tag{6.1}$$

where $B_{max}/B(\theta) = (1+\epsilon\cos\theta)/(1-\epsilon)$ in a circular concentric magnetic configuration. Electrons are assumed to run away if their momentum exceeds both the critical momentum and the trapping condition in Eq. 6.1. The lower integration limit p_{min} for the analytic estimate of the avalanche growth rate is thus given by $\max(p_c, p_T)$. An analytic expression for the inverse aspect ratio dependent avalanche growth rate is obtained by integrating the source term from over momentum space from p_{min} to $p_{max} = \infty$, which results in a locally modified, inverse aspect ratio dependent avalanche growth rate

$$\frac{dn_r}{dt_n}(\theta,\epsilon) = \frac{1}{2}\frac{1}{\ln\Lambda^\dagger}\bar{n}_e\bar{n}_r\frac{1}{\sqrt{1+p_{min}^2}-1} \tag{6.2}$$

$$= \frac{1}{2}\frac{1}{\ln\Lambda^\dagger}\bar{n}_e\bar{n}_r\,\mathsf{min}\left(\frac{E}{E_c}, \frac{(1-\epsilon)^2}{2\epsilon(1+cos\theta)}\right). \tag{6.3}$$

The radial dependence is derived by finding a local expression in the poloidal angle θ for a circular concentric configuration and averaging over the flux surface to find a global flux surface dependent growth rate. The general relation for flux surface average of a volumic quantity is:

$$< \Phi >_V (\psi) = \frac{\int\int_{dV}\Phi(\psi,\theta)dV}{\int\int_{dV}dV}, \tag{6.4}$$

where

$$\int\int_{dV(\psi)} dV = \int\int_{dV(\psi)} \frac{Rr}{|\nabla\psi||\hat{\psi}\cdot\hat{r}|}d\psi d\theta d\phi = d\psi\int_0^{2\pi}d\theta\int_0^{2\pi}d\phi\frac{Rr}{|\nabla\psi||\hat{\psi}\cdot\hat{r}|}. \tag{6.5}$$

Under the assumption of axisymmetry, it is shown in [7] that the flux surface average of an operator Φ becomes:

$$< \Phi >_V (\psi) = \frac{1}{\hat{q}(\psi)}\int_0^{2\pi}\frac{d\theta}{2\pi}\frac{1}{|\hat{\psi}\cdot\hat{r}|}\frac{r}{R_p}\frac{B_0(\psi)}{B_P}\Phi(\psi,\theta), \tag{6.6}$$

where $\hat{q}$ is the pseudo safety factor

$$\hat{q} = \int_0^{2\pi}\frac{d\theta}{2\pi}\frac{1}{|\hat{\psi}\cdot\hat{r}|}\frac{r}{R_p}\frac{B_0}{B_P}. \tag{6.7}$$

It is assumed that all electrons with momentum $p > p_c$ will run away, except the electrons that appear in the trapped region $p < p_T$ obtained from the usual condition on magnetically trapped electrons $\xi_0(\psi) \leq \xi_{0T} = \sqrt{1-1/\Psi_{max}}$, where $\xi_{0T}(\psi)$ is the pitch angle, defined at the minimum $B_0(\psi)$ on a given flux surface, such that the parallel velocity of the particle vanishes at the maximum $B_{max}(\psi)$. The momentum of an electron has to exceed both the critical momentum and the trapping condition to contribute to the runaway population. Thus the lower integration limit p_{min} is given by $\max(p_c, p_T)$. The flux surface averaged growth rate becomes:

$$
\begin{aligned}
< \quad & \frac{dn_r}{dt_n} >_V (\psi) = \\
= \quad & \frac{1}{\hat{q}(\psi)} \int_0^{2\pi} \frac{d\theta}{2\pi} \frac{1}{|\hat{\psi}\cdot\hat{r}|} \frac{r}{R_p} \frac{B_0(\psi)}{B_P} \int_{p_{min}}^{p_{max}} 2\pi p^2 dp \int_{-1}^{+1} \bar{S}(\psi, p, \xi, \theta) d\xi \\
& = \frac{1}{\hat{q}(\psi)} \int_0^{2\pi} \frac{d\theta}{2\pi} \frac{1}{|\hat{\psi}\cdot\hat{r}|} \frac{r}{R_p} \frac{B_0(\psi)}{B_P} \int_{p_{min}}^{p_{max}} 2\pi p^2 \bar{S}^* dp \int_{-1}^{+1} \delta(\xi - \xi^*(\theta, p)) d\xi, \qquad (6.8)
\end{aligned}
$$

where $\bar{S}^*$ is the momentum dependent part of the knock-on operator

$$
\bar{S}^*(p) = \frac{1}{4\pi} \frac{\beta_{th}^{\dagger 2}}{\ln \Lambda^\dagger} \bar{n}_e \bar{n}_r \frac{1}{\bar{p}\gamma(\gamma-1)^2} = \frac{1}{4\pi} \frac{1}{\ln \Lambda^\dagger} \bar{n}_e \bar{n}_r \frac{1}{\bar{p}^2} \frac{d}{d\bar{p}} \left(\frac{1}{1 - \sqrt{1 + \beta_{th}^2 \bar{p}^2}}\right). \qquad (6.9)
$$

The trapping condition is given by $\xi = 0$ by the following relation

$$
\xi_0 = \pm\sqrt{1 - \frac{(1-\xi^2)}{\Psi(\psi, \theta)}},\ \xi_{0T} = \pm\sqrt{1 - \frac{1}{\Psi_{max}}}. \qquad (6.10)
$$

The integration over ξ gives:

$$
\int_{-1}^{+1} \delta(\xi - \xi^*(\theta, p)) d\xi = \begin{cases} 0, & |\xi_0| < \sqrt{1 - 1/\Psi_{max}} \\ 1, & \xi_0 \geq \sqrt{1 - 1/\Psi_{max}} \end{cases}. \qquad (6.11)
$$

This condition can be accounted for with the Heaviside step function $H\left(|\xi_0| - \sqrt{1 - 1/\Psi_{max}}\right)$. We perform a variable transform $\xi \to \xi_0$

$$
\delta(\xi - \xi^*(\theta, p)) = \frac{\delta(\xi_0 - \xi_0^*)}{|d\xi/d\xi_0|} = \frac{\delta(\xi_0 - \xi_0^*)\xi}{\xi_0 \Psi}, \qquad (6.12)
$$

which leads to

$$
\int_{-1}^{+1} \delta(\xi - \xi^*(\theta, p)) d\xi = \int_{-1}^{+1} \delta(\xi_0 - \xi_0^*) d\xi_0. \qquad (6.13)
$$

The growth rate becomes:

$$
\begin{aligned}
< \quad & \frac{dn_r}{dt_n} >_V (\psi) = \frac{1}{\hat{q}(\psi)} \int_0^{2\pi} \frac{d\theta}{2\pi} \frac{1}{|\hat{\psi}\cdot\hat{r}|} \frac{r}{R_p} \frac{B_0(\psi)}{B_P} \times \qquad (6.14) \\
& \int_{p_{min}}^{p_{max}} 2\pi p^2 \bar{S}^* dp \int_{-1}^{+1} \delta(\xi_0 - \xi_0^*)\, H\left(|\xi_0| - \sqrt{1 - 1/\Psi_{max}}\right) d\xi_0.
\end{aligned}
$$

To express the argument of the Heaviside function in p, we have

$$
\Psi^* = \frac{(1 - \xi^{*2})}{(1 - \xi_0^2)} = \frac{2}{(\gamma + 1)(1 - \xi_0^2)}. \qquad (6.15)
$$

Thus,

$$
\gamma(\xi_{0T}) = \frac{2}{(1 - \xi_{0T}^2)\Psi^*} - 1. \qquad (6.16)
$$

Using the trapping condition in Eq. (6.10)

$$\gamma_T = 2\frac{\Psi_{max}}{\Psi^*} - 1 = 2\frac{B_{max}}{B^*} - 1,\ p_T = \sqrt{\left(2\frac{B_{max}}{B^*} - 1\right)^2 - 1}, \tag{6.17}$$

where $B^* = B(\theta^*)$. In a circular concentric magnetic configuration

$$B_{max}/B(\theta) = B_{max}/B(\theta) = B_{max}(1+\epsilon\cos(\theta))/(B_0(1+\epsilon)) = (1+\epsilon\cos(\theta))/(1-\epsilon). \tag{6.18}$$

If the acceleration of the electrons is only limited by the trapping condition, the local growth rate in the angle θ is

$$\begin{aligned} \tfrac{dn_r}{dt_n}(\theta,\psi) &= \tfrac{1}{2}\tfrac{1}{\ln\Lambda^\dagger}\bar{n}_e\bar{n}_r\tfrac{1}{\sqrt{1+p_T^2}-1} \\ &= \tfrac{1}{2}\tfrac{1}{\ln\Lambda^\dagger}\bar{n}_e\bar{n}_r\tfrac{1}{2(B_{max}/B(\theta)-1)} \\ &= \tfrac{1}{2}\tfrac{1}{\ln\Lambda^\dagger}\bar{n}_e\bar{n}_r\tfrac{(1-\epsilon)}{2\epsilon(1+\cos(\theta))}. \end{aligned} \tag{6.19}$$

The avalanche growth rate is obtained by integrating the source function over momentum space from $p_{min} = \max(p_c(E/E_c), p_T(\theta))$ where

$$p_T^2 = 4\epsilon(1+cos\theta)/(1-\epsilon), \tag{6.20}$$

$$p_c^2 = 2E_c/E. \tag{6.21}$$

The growth rate becomes

$$\frac{dn_r}{dt_n}(\theta,\psi) = \frac{1}{2}\frac{1}{\ln\Lambda^\dagger}\bar{n}_e\bar{n}_r\frac{1}{\sqrt{1+p_{min}^2}-1} = \frac{1}{2}\frac{1}{\ln\Lambda^\dagger}\bar{n}_e\bar{n}_r\mathsf{min}\left(\bar{E}, \frac{(1-\epsilon)}{2\epsilon(1+cos\theta)}\right), \tag{6.22}$$

where $\bar{E} = E/E_c$. For $\bar{E}$ finite we have $p_c > 0$. Thus as the growth rate is averaged over the poloidal angle $p_{min} \to p_c$ as $\theta \to \pi$. The poloidal angle where $p_c = p_T$ we name θ_{bound} and it constitutes the boundary between the region where the avalanche rate is limited either by the drag force or by the magnetic trapping effect. The angle is obtained from the condition $p_c = p_T$:

$$1 + cos\theta_{bound} = (1-\epsilon)/(2\epsilon\bar{E}),\ \theta_{bound} = \pm\arccos((1-\epsilon)/(2\epsilon\bar{E}) - 1). \tag{6.23}$$

If $\epsilon\bar{E}/(1-\epsilon) < 1/4$, p_c constitutes the lower integration limit and if $\epsilon\bar{E}/(1-\epsilon) > 1/4$, $p_{min} = p_T(\theta)$. Averaged over the flux surface according to volumic flux surface average the growth rate is:

$$
\begin{aligned}
& < \frac{dn_r}{dt_n} >_V (\psi) \\
= \; & \frac{1}{\hat{q}}\Big(\frac{1}{2\pi}\int_0^{\theta_{bound}} \frac{1}{|\hat{\psi}\cdot\hat{r}|}\frac{r}{R_p}\frac{B_0(\psi)}{B_P}\frac{dn_r}{dt_n}(p_T(\theta))d\theta + \\
& + \frac{1}{2\pi}\int_{\theta_{bound}}^{\pi} \frac{1}{|\hat{\psi}\cdot\hat{r}|}\frac{r}{R_p}\frac{B_0(\psi)}{B_P}\frac{dn_r}{dt_n}(p_c)d\theta + \\
+ \; & \frac{1}{2\pi}\int_{\pi}^{-\theta_{bound}} \frac{1}{|\hat{\psi}\cdot\hat{r}|}\frac{r}{R_p}\frac{B_0(\psi)}{B_P}\frac{dn_r}{dt_n}(p_c)d\theta \\
& + \frac{1}{2\pi}\int_{-\theta_{bound}}^{2\pi} \frac{1}{|\hat{\psi}\cdot\hat{r}|}\frac{r}{R_p}\frac{B_0(\psi)}{B_P}\frac{dn_r}{dt_n}(p_T(\theta))d\theta\Big) \\
& = \frac{1}{\hat{q}}\left(\frac{1}{\pi}\int_0^{\theta_{bound}} \epsilon\frac{B_0(\psi)}{B_P}\frac{dn_r}{dt_n}(p_T(\theta))d\theta + \frac{1}{\pi}\int_{\theta_{bound}}^{\pi} \epsilon\frac{B_0(\psi)}{B_P}\frac{dn_r}{dt_n}(p_c)d\theta\right) \qquad (6.24) \\
& = \frac{1+\epsilon}{\epsilon}\frac{B_p}{B}\left(\frac{1}{\pi}\int_0^{\theta_{bound}} \epsilon\frac{B_0(\psi)}{B_P}\frac{dn_r}{dt_n}(p_T(\theta))d\theta + \frac{1}{\pi}\int_{\theta_{bound}}^{\pi} \epsilon\frac{B_0(\psi)}{B_P}\frac{dn_r}{dt_n}(p_c)d\theta\right) \\
& = \left(\frac{1+\epsilon}{\epsilon}\frac{B_p}{B}\frac{1}{\pi}\int_0^{\theta_{bound}} \epsilon\frac{B_0(\psi)}{B_P}\frac{dn_r}{dt_n}(p_T(\theta))d\theta + (1+\epsilon)\frac{1}{\pi}\int_{\theta_{bound}}^{\pi} \frac{B_o}{B}\frac{dn_r}{dt_n}(p_c)d\theta\right) \\
& = \frac{1}{2}\frac{1}{\ln\Lambda^\dagger}\bar{n}_e\bar{n}_r\left((1+\epsilon)\frac{B_p}{B}\frac{1}{\pi}\int_0^{\theta_{bound}} \frac{B_0(\psi)}{B_P}\frac{(1-\epsilon)}{2\epsilon(1+cos\theta)}d\theta + (1+\epsilon)\bar{E}\frac{1}{\pi}\int_{\theta_{bound}}^{\pi} \frac{(1+\epsilon\cos(\theta))}{1+\epsilon}d\theta\right).
\end{aligned}
$$

In the above calculation we used that for circular concentric flux surfaces $|\hat{\psi}\cdot\hat{r}|$=1, $\epsilon = r/R_p$ and

$$
\begin{aligned}
\hat{q} \; &= \; \int_0^{2\pi}\frac{d\theta}{2\pi}\frac{r}{R_p}\frac{B_0}{B_p} = \int_0^{2\pi}\frac{d\theta}{2\pi}\epsilon\frac{B_0}{B_p} = \int_0^{2\pi}\frac{d\theta}{2\pi}\epsilon\frac{B_0}{B}\frac{B}{B_p} \qquad (6.25) \\
&= \int_0^{2\pi}\frac{d\theta}{2\pi}\epsilon\frac{(1+\epsilon\cos(\theta))}{(1+\epsilon)}\frac{B}{B_p} = \frac{\epsilon}{(1+\epsilon)}\frac{B}{B_p}.
\end{aligned}
$$

Note that B/B_p is independent of θ. The first term within brackets in Eq. (6.24) is evaluated as follows:

$$
\begin{aligned}
&(1+\epsilon)\frac{B_p}{B}\frac{1}{\pi}\int_0^{\theta_{bound}}\frac{B_0(\psi)}{B_P}\frac{(1-\epsilon)}{2\epsilon(1+cos\theta)}d\theta \\
&= (1+\epsilon)\frac{B_p}{B}\frac{1}{\pi}\int_0^{\theta_{bound}}\frac{B_0(\psi)}{B_P}\frac{B}{B}\frac{(1-\epsilon)}{2\epsilon(1+cos\theta)}d\theta \\
&= (1+\epsilon)\frac{1}{\pi}\int_0^{\theta_{bound}}\frac{B_0(\psi)}{B}\frac{(1-\epsilon)}{2\epsilon(1+cos\theta)}d\theta \\
&= (1+\epsilon)\frac{1}{\pi}\int_0^{\theta_{bound}}\frac{(1+\epsilon\cos(\theta))}{(1+\epsilon)}\frac{(1-\epsilon)}{2\epsilon(1+cos\theta)}d\theta \\
&= (1-\epsilon)\frac{1}{\pi}\int_0^{\theta_{bound}}\frac{(1+\epsilon\cos(\theta))}{2\epsilon(1+cos\theta)}d\theta \\
&= (1-\epsilon)\frac{1}{\pi}\int_0^{\theta_{bound}}\frac{1}{2\epsilon}\left(\frac{1}{2\cos^2(\theta/2)}+\frac{\epsilon\cos(\theta)+\epsilon-\epsilon}{(1+\cos(\theta))}\right)d\theta \\
&= (1-\epsilon)\frac{1}{\pi}\int_0^{\theta_{bound}}\frac{1}{2\epsilon}\left(\frac{1}{2\cos^2(\theta/2)}+\epsilon-\frac{\epsilon}{2\cos^2(\theta/2)}\right)d\theta \\
&= \frac{1}{\pi}\frac{(1-\epsilon)}{2\epsilon}\left[\tan(\theta/2)+\epsilon\theta-\epsilon\tan(\theta/2)\right]_0^{\theta_{bound}} \\
&= \frac{1}{\pi}\frac{(1-\epsilon)}{2\epsilon}\left((1-\epsilon)\tan(\theta_{bound}/2)+\epsilon\theta_{bound}\right).
\end{aligned}
\tag{6.26}
$$

The flux surface averaged growth rate in Eq. (6.24) becomes:

$$
\begin{aligned}
&< \frac{dn_r}{dt_n}(\theta,\psi) >_V = \frac{1}{2\ln\Lambda^\dagger}\bar{n}_e\bar{n}_r\bar{E}\times \\
&\left(\frac{1}{\pi}\frac{1}{\hat{q}(\psi)}\int_0^{\theta_{bound}}\frac{1}{|\hat{\psi}\cdot\hat{r}|}\frac{r}{R_p}\frac{B_0(\psi)}{B_P}\frac{1}{\bar{E}}\frac{1}{2\left(B_{max}/B(\theta)-1\right)}d\theta+\frac{1}{\pi}\times(\pi-\theta_{bound}-\epsilon\sin(\theta_{bound}))\right)
\end{aligned}
$$

$$
= \frac{1}{2\ln\Lambda^\dagger}\bar{n}_e\bar{n}_r\bar{E}\left(\frac{1}{\pi}(1-\epsilon)\frac{1}{\bar{E}}\frac{1}{2\epsilon}\left((1-\epsilon)\tan(\theta_{bound}/2)+\epsilon\theta_{bound}\right)+\left(1-\frac{\theta_{bound}}{\pi}-\frac{\epsilon}{\pi}\sin(\theta_{bound})\right)\right)
$$

$$
= \frac{1}{2\ln\Lambda^\dagger}\bar{n}_e\bar{n}_r\bar{E}\left(1-\frac{\theta_{bound}}{\pi}-\frac{\epsilon}{\pi}\sin(\theta_{bound})+(1-\epsilon)\frac{1}{2\bar{E}\epsilon\pi}\left((1-\epsilon)\tan(\theta_{bound}/2)+\epsilon\theta_{bound}\right)\right). \tag{6.27}
$$

Where

$$
\tan(\theta_{bound}/2) = \frac{\sin(\theta_{bound})}{1+cos(\theta_{bound})} = \frac{\sqrt{(1-\epsilon)/(\epsilon\bar{E})-(1-\epsilon)^2/(2\epsilon\bar{E})^2}}{(1-\epsilon)/(2\epsilon\bar{E})} = \frac{\sqrt{4\epsilon\bar{E}-(1-\epsilon)}}{\sqrt{1-\epsilon}}, \tag{6.28}
$$

and

$$
\frac{\epsilon}{\pi}\sin(\theta_{bound}) = \frac{\epsilon}{\pi}\sqrt{(1-\epsilon)/(\epsilon\bar{E})-(1-\epsilon)^2/(2\epsilon\bar{E})^2} = \frac{1}{\pi}\sqrt{\frac{\epsilon(1-\epsilon)}{\bar{E}}}\sqrt{1-\frac{(1-\epsilon)}{4\epsilon\bar{E}}}. \tag{6.29}
$$

For $\epsilon E/E_c \gg 1$, $\theta_b \to \pi$, the growth rate is reduced by a factor $(1-\epsilon)^2/\left(\pi\sqrt{\epsilon E/E_c}\right)$. The inverse aspect ratio dependence of the estimated avalanche growth rate obtained from Eq.

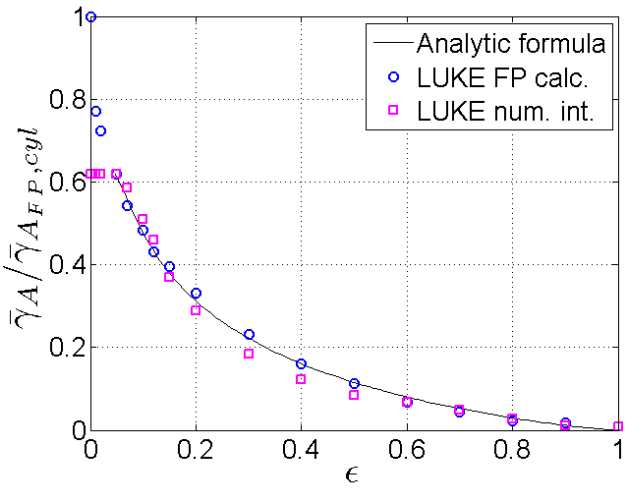


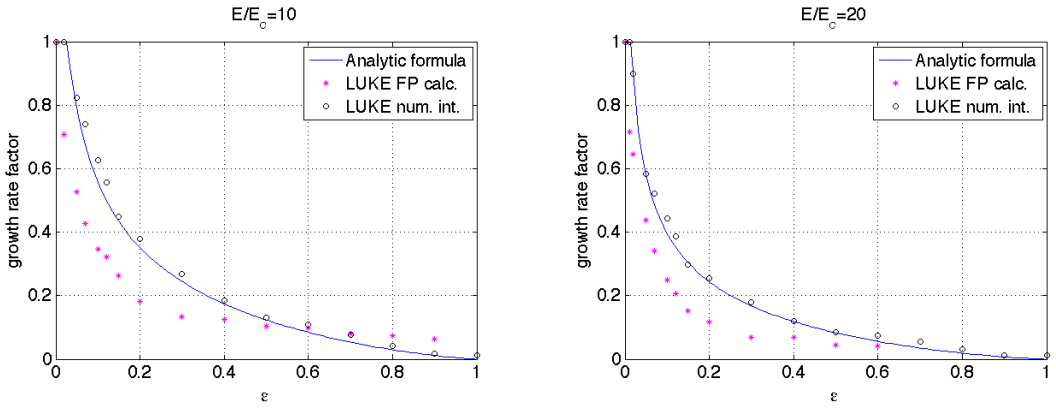
Figure 6.3: Radial dependence of the avalanche multiplication factor from bounce-averaged LUKE calculations (circles), normalized to to the avalanche multiplication factor for the cylindrical case $\epsilon = 0$. The numerical integration over the knock-on source term in Eq. 4.28 with the toroidal dependence in the momentum integration boundary is plotted in squares. The solid line shows the analytic estimate of the growth rate off the magnetic axis from Eq. 6.27.

6.3 is compared to numerical results. In addition, a numerical integration of the source term is also performed, with the same criterion on the lower integration boundary in momentum space p_{min} as the analytic estimate in Eq. 6.22. The analytic result is also compared to avalanche growth rate from Fokker-Planck calculations with the LUKE code. In that case, the trapping conditions are the same as in the analytic result, except for that the critical momentum is pitch angle dependent $p_c^2 = E_c/(E\xi)$. The LUKE calculated avalanche multiplication factor and the analytic estimate show good agreement (Fig. 6.3).

The growth rate obtained from bounce-averaged calculations suggests that the formation of runaway electrons is slower the further away from the magnetic axis they appear. In other words, the time scale of the local growth rate could be longer than suggested by collisional theory [4, 5]. Potential loss mechanisms, such as transport of fast electrons due to magnetic field perturbations [41] could therefore act more efficiently on the runaway electrons formed off the magnetic axis than the ones formed on axis which could lead to well confined runaway electrons at the center of the plasma.

The inverse aspect ratio dependence of the growth rate derived in the previous section (see Eq. 6.27) is compared to numerical results. Numerical integration of the source term is performed, with the same criterion on the lower integration boundary in momentum space (p_{min}) as in the analytic formula. The upper integration boundary (p_{max}) is set to at least four times the critical momentum. At momentum higher than that, the growth rate has shown to be negligible. The analytic result is also compared to an avalanche growth rate obtained from Fokker-Planck calculations with the LUKE code. In that case, the trapping conditions is the same as in the analytic result, but the critical momentum is dependent on the pitch angle. Since $p_c^2 = 2E_c/(E(1+\xi))$ the analytic approximation of $\xi = 0$ made in Eq. 6.27 is an upper estimate for p_c. Thus, the growth rate calculated by LUKE can be expected to be smaller or equal to the analytic estimate.

Figure 6.3 shows the reduction factor of the growth rate for $E/E_c = 5$, i.e. relative to the growth rate in a cylindric plasma ($\varepsilon = 0$). The numerical integration of the source term shows good agreement with the analytic result (Eq. 6.27). Close to the center, at low inverse aspect



(a) (b)

Figure 6.4: Growth rate factor as a function of the inverse aspect ratio (ε) for $E/E_c = 10$ (a) and $E/E_c = 20$ (b).

ratio, there is no effect of the trapping, due to the fact that the critical momentum is higher than the trapped momentum over the whole flux surface. This effect becomes smaller with increasing E/E_c (Figure 6.4a and 6.4b), since the critical momentum decreases and becomes smaller compared to the trapping condition p_T and thus less influential. However, for the Fokker-Planck calculations the trapping influences the growth rate away from the magnetic axis. This can be explained by the fact that p_c, a function of ξ, is less restrictive than $p_c(\varepsilon = 0)$. Another possible explanation is pitch angle collisions that couple the dynamics between the trapped and the passing region.

In the Fokker Planck calculations the pitch angle dependence of the critical momentum has been taken into account. It is also important to note that the analytic and numerical integration case was performed for effective charge $Z = -1$ but the Fokker Planck calculation for $Z = 1$.

6.1.1 Verification of the bounce averaged knock-on operator

A flux surface averaged quantity can be obtained directly from the definition of the flux surface average of a volumic quantity as shown in the previous section. The same result can be derived from a relation including the bounce averaged quantity. Thus, the bounce averaged knock on operator can be verified by calculating the flux surface averaged growth rate from knock on collisions through two ways, that should give the same result:

1. Through the general relation of flux surface average of the growth rate from the knock on operator $\mathbf{S}(\psi, p, \xi, \theta)$, see Eq. (6.27).

2. From the bounce averaged operator $\{\bar{\mathbf{S}}\}(\psi, p, \xi_0)$, derived in the following subsection.

Growth rate from the bounce averaged knock on operator

The bounce averaged knock on operator is:

$$\{\bar{\mathbf{S}}\}(\psi, p, \xi_0) = \bar{\mathbf{S}}^* \frac{1}{\lambda \widetilde{q}} \left[\frac{1}{2}\sum_{\sigma}\right]_T \int_{\theta_{min}}^{\theta_{max}} \frac{d\theta}{2\pi} \frac{1}{|\hat{\psi}\cdot\hat{r}|} \frac{r}{R_p} \frac{B}{B_p} \frac{\xi_0}{\xi} \delta\left(\xi - \xi^*(\bar{p})\right) \tag{6.30}$$

$$= \frac{1}{2\pi^2} \frac{1}{\ln\Lambda^\dagger R_p} \bar{n}_e \bar{n}_R \frac{1}{\bar{p}^3 \gamma(\gamma-1)} \frac{B_0}{\lambda \widetilde{q}} \frac{|\xi_0|}{(1-\xi_0^2)^2} \sum_k \left[\frac{1}{|\hat{\psi}\cdot\hat{r}|} \frac{r}{B_p} \frac{1}{|\Psi'(\theta_k^*)|}\right]_{\theta_k^*}. \tag{6.31}$$

It is shown in [7] that a flux surfaced averaged quantity can be retrieved from the bounce averaged quantity through the relation:

$$< \frac{dn_r}{dt_n} >_V (\psi) = \frac{\tilde{q}}{\hat{q}} \int_{p>p_c} 2\pi p^2 \int_{\xi_0} \lambda \{\bar{\mathbf{S}}\} H \left(|\xi_0| - \sqrt{1 - 1/\Psi_{max}} \right) d\xi_0 dp \tag{6.32}$$

$$= \frac{\tilde{q}}{\hat{q}} \int_0^\infty 2\pi p^2 H(p > p_c) \int_{\xi_0} \lambda \{\bar{\mathbf{S}}\} H \left(|\xi_0| - \sqrt{1 - 1/\Psi_{max}} \right) d\xi_0 dp \tag{6.33}$$

$$= \frac{\tilde{q}}{\hat{q}} \int_{p>p_c} 2\pi p^2 \int_{|\xi_0|>\xi_{0T}} \lambda \frac{1}{2\pi^2} \frac{1}{\ln \Lambda^\dagger R_p} \bar{n}_e \bar{n}_R \frac{1}{\bar{p}^3 \gamma(\gamma-1)} \frac{B_0}{\lambda \tilde{q}} \times \tag{6.34}$$

$$\frac{|\xi_0|}{(1-\xi_0^2)^2} \sum_k \Big[\frac{1}{|\hat{\psi} \cdot \hat{r}|} \frac{r}{B_p} \frac{1}{|\Psi'(\theta_k^*)|} \Big]_{\theta_k^*} d\xi_0 dp. \tag{6.35}$$

This includes a change of variables from $(\xi, \theta)\ \epsilon\ [-1,1], [-\pi, \pi]$ to $(\xi_0, \theta)\ \epsilon\ [-1,1], [\theta_{min}, \theta_{max}]$. The cancellation of λ and $\tilde{q}$ leads to:

$$< \frac{dn_r}{dt_n} >_V (\psi) = \frac{1}{\hat{q}} \int_{p>p_c} p^2 \int_{|\xi_0|>\xi_{0T}} \frac{1}{\pi} \frac{1}{\ln \Lambda^\dagger R_p} \bar{n}_e \bar{n}_R \frac{1}{\bar{p}^3 \gamma(\gamma-1)} B_0 \times \tag{6.36}$$

$$\frac{|\xi_0|}{(1-\xi_0^2)^2} \sum_k \Big[\frac{1}{|\hat{\psi} \cdot \hat{r}|} \frac{r}{B_p} \frac{1}{|\Psi'(\theta_k^*)|} \Big]_{\theta_k^*} d\xi_0 dp. \tag{6.37}$$

At a given ξ_0, $\Psi = B(\theta)/B_0$ is bijective and there is one solution on each θ interval $[-\pi, 0]$ and $[0, \pi]$, thus one $\theta^*(\xi_0)$ on each interval. From Eq. 6.15

$$\frac{\partial \Psi^*}{\partial \xi_0} = \frac{4\xi_0}{(1-\xi_0^2)^2(\gamma+1)}, \tag{6.38}$$

$$\frac{|\xi_0|}{(1-\xi_0^2)^2} = \frac{1}{4} |\frac{\partial \Psi^*}{\partial \xi_0}| (\gamma+1). \tag{6.39}$$

The condition of the trapped electron contribution to the growth rate can be transformed from ξ_{0T} to a condition on p_T. We get:

$$< \frac{dn_r}{dt_n} >_V (\psi) = \frac{1}{\hat{q}} \int_{p>p_c, p_T(\theta)} p^2 \int_{\xi_0} \frac{1}{4\pi} \frac{1}{\ln \Lambda^\dagger R_p} \bar{n}_e \bar{n}_R \frac{(\gamma+1)}{\bar{p}^3 \gamma(\gamma-1)} B_0 \times \tag{6.40}$$

$$|\frac{\partial \Psi^*}{\partial \xi_0}| \sum_k \Big[\frac{1}{|\hat{\psi} \cdot \hat{r}|} \frac{r}{B_p} \frac{1}{|\Psi'(\theta_k^*)|} \Big]_{\theta_k^*} \left[\frac{1}{2} \sum \right]_T d\xi_0 dp. \tag{6.41}$$

We can rewrite the factor as

$$\frac{(\gamma+1)}{\bar{p}^3 \gamma(\gamma-1)} = \frac{(\gamma+1)}{\bar{p}(\gamma^2-1)\gamma(\gamma-1)} = \frac{1}{\bar{p}\gamma(\gamma-1)^2} \tag{6.42}$$

$$= \frac{1}{\bar{p}^2} \frac{d}{dp} \left(\frac{1}{1 - \sqrt{1+\bar{p}^2}} \right) \tag{6.43}$$

The integration domain in ξ_0 is limited by $\Psi(\theta) = 1$, when $\xi_0 \to \xi^*$ at $\theta = -\pi$ $(k=1)$ and $\Psi(\theta) = \Psi_{max}$, when $\xi_0 \to \sqrt{1 - (1-\xi^{*2})/\Psi_{max}}$ at $\theta = \pi$ $(k=2)$.

$$
\begin{aligned}
< \frac{dn_r}{dt_n} >_V (\psi) &= \frac{1}{\hat{q}} \frac{1}{4\pi} \frac{1}{\ln \Lambda^\dagger R_p} \bar{n}_e \bar{n}_R B_0 \int_{p>max(p_c,p_T(\theta))} p^2 \int_{\xi_0} \frac{1}{\bar{p}^2} \frac{d}{dp} \left(\frac{1}{1-\sqrt{1+\bar{p}^2}} \right) |\frac{\partial \Psi^*}{\partial \xi_0}| \times \\
&\sum_k \Big[\frac{1}{|\hat{\psi} \cdot \hat{r}|} \frac{r}{B_p} \frac{1}{|\Psi'(\theta_k^*)|} \Big]_{\theta_k^*} d\xi_0 dp \qquad (6.44) \\
&= \frac{1}{\hat{q}} \frac{1}{4\pi} \frac{1}{\ln \Lambda^\dagger R_p} \bar{n}_e \bar{n}_R B_0 \int_{p>max(p_c,p_T(\theta))} \frac{d}{dp} \left(\frac{1}{1-\sqrt{1+\bar{p}^2}} \right) \times \\
&\left(\int_{\xi_0} \left(\Big[\frac{1}{|\hat{\psi} \cdot \hat{r}|} \frac{r}{B_p} \left(-\frac{\partial \theta^*}{\partial \Psi^*} \right) |\frac{\partial \Psi^*}{\partial \xi_0}| \Big]_{k=1} + \Big[\frac{1}{|\hat{\psi} \cdot \hat{r}|} \frac{r}{B_p} \left(\frac{\partial \theta^*}{\partial \Psi^*} \right) |\frac{\partial \Psi^*}{\partial \xi_0}| \Big]_{k=2} \right) d\xi_0 \right) dp.
\end{aligned}
$$

Through a variable change $\xi_0 \rightarrow \theta_k^*$ we obtain:

$$
\begin{aligned}
< \frac{dn_r}{dt_n} >_V (\psi) &= \frac{1}{\hat{q}} \frac{1}{4\pi} \frac{1}{\ln \Lambda^\dagger R_p} \bar{n}_e \bar{n}_R B_0 \times \qquad (6.45) \\
&(\int_0^{-\pi} - \Big[\frac{1}{|\hat{\psi} \cdot \hat{r}|} \frac{r}{B_p} \Big]_{k=1} \int_{p>max(p_c,p_T(\theta))} \frac{d}{dp} \left(\frac{1}{1-\sqrt{1+\bar{p}^2}} \right) d\theta^* + \\
&+ \int_0^{\pi} \Big[\frac{1}{|\hat{\psi} \cdot \hat{r}|} \frac{r}{B_p} \frac{\partial \theta^*}{\partial \Psi^*} \Big]_{k=2} \int_{p>max(p_c,p_T(\theta))} \frac{d}{dp} \left(\frac{1}{1-\sqrt{1+\bar{p}^2}} \right) d\theta^* dp) \\
&= \frac{1}{\hat{q}} \frac{1}{4\pi} \frac{1}{\ln \Lambda^\dagger R_p} \bar{n}_e \bar{n}_R B_0 \times \\
&(\int_{-\pi}^{0} \Big[\frac{1}{|\hat{\psi} \cdot \hat{r}|} \frac{r}{B_p} \Big]_{k=1} \int_{p>max(p_c,p_T(\theta))} \frac{d}{dp} \left(\frac{1}{1-\sqrt{1+\bar{p}^2}} \right) d\theta^* + \\
&+ \int_0^{\pi} \Big[\frac{1}{|\hat{\psi} \cdot \hat{r}|} \frac{r}{B_p} \frac{\partial \theta^*}{\partial \Psi^*} \Big]_{k=2} \int_{p>max(p_c,p_T(\theta))} \frac{d}{dp} \left(\frac{1}{1-\sqrt{1+\bar{p}^2}} \right) d\theta^* dp) \\
&= \frac{1}{\hat{q}} \frac{1}{2} \frac{1}{\ln \Lambda^\dagger} \bar{n}_e \bar{n}_R \left(\int_{-\pi}^{\pi} \Big[\frac{1}{2\pi} \frac{1}{|\hat{\psi} \cdot \hat{r}|} \frac{B_0 r}{B_p R_p} \Big] \int_{p>max(p_c,p_T(\theta))} \frac{d}{dp} \left(\frac{1}{1-\sqrt{1+\bar{p}^2}} \right) dp\, d\theta^* \right).
\end{aligned}
$$

For circular concentric flux surfaces $|\hat{\psi} \cdot \hat{r}|$=1. The integral in momentum space goes from p_{min} = $\max(p_c(E/E_c), p_T(\theta))$ where

$$
\begin{aligned}
p_T^2 &= 4\epsilon(1+cos\theta)/(1-\epsilon), \qquad (6.46) \\
p_c^2 &= 2E_c/E. \qquad (6.47)
\end{aligned}
$$

Thus the growth rate becomes:

$$
\begin{aligned}
< \frac{dn_r}{dt_n} >_V (\psi) &= \frac{1}{\hat{q}} \frac{1}{2} \frac{1}{\ln \Lambda^\dagger} \bar{n}_e \bar{n}_R \times \\
&(2 \int_0^{\theta_{bound}} \frac{1}{2\pi} \epsilon \frac{B_0}{B_p} \int_{p>p_T(\theta)} \frac{d}{dp} \left(\frac{1}{1-\sqrt{1+\bar{p}^2}} \right) dp\, d\theta^* \qquad (6.48) \\
&+ 2 \int_{\theta_{bound}}^{\pi} \frac{1}{2\pi} \epsilon \frac{B_0}{B_p} \int_{p>p_c} \frac{d}{dp} \left(\frac{1}{1-\sqrt{1+\bar{p}^2}} \right) dp\, d\theta^*).
\end{aligned}
$$

We have recovered the same expression as in Eq. 6.24, that is the flux surface averaged growth rate directly from the definition of flux surface average. This cross check verifies the implemented bounce averaged operator in LUKE.

6.2 The fate of the trapped electrons

Following the results of the previous section, we found that in a non-uniform magnetic configuration, a fraction of the electron population that would have directly contributed to the runaway population in a cylindrical plasma, is momentaneously reduced due to magnetic trapping. In this section, the fate of these trapped-electron runaways is investigated. In a tokamak, trapped electrons subject to a strong electric field cannot run away immediately, because their parallel velocity does not increase over a bounce period. However, they do pinch towards the tokamak center. As they pinch towards the center, the trapping cone becomes more narrow, so eventually they can be detrapped and run away. When they run away, trapped electrons will have very a different signature from circulating electrons subject to the Dreicer mechanism.

Let us describe more precisely the expected signature of the trapped runaways. As opposed to circulating electrons, trapped electrons cannot run away immediately, because their parallel velocity cannot increase. However, to conserve canonical angular momentum, they do pinch towards the tokamak center. As they pinch towards the center, the trapping effect becomes weaker, so eventually they do run away. We call this the trapped-electron runaway effect, by which we refer to electrons that were initially trapped, before running away. However, when they do run away, trapped electrons will have very different signatures from the circulating electrons that run away in several ways.

First, the initially-trapped runaway electrons can only run away in the center of the tokamak, near the magnetic axis. Second, since they were initially trapped, they must initially have had a relatively high perpendicular velocity (say measured at the maximum over the trapped-electron orbit of the parallel velocity), at least on the order of the maximum parallel velocity. Now, during the process of detrapping, when the electron drifts toward the magnetic axis, neither this maximum parallel velocity nor this perpendicular velocity can change by much. Since the parallel velocity must be on the order of the runaway speed to eventually run away when detrapping occurs, then so must the perpendicular velocity. More specifically, the trapped-electron runaways will have a distinct pitch angle depending on the radial location where they appear.

This suggests that, as opposed to initially-circulating runaway electrons, the initially-trapped runaway electrons will have two very different characteristics: one, they will be even more tightly focused near the magnetic axis of the tokamak than the circulating runaways; and, two, they will have very high perpendicular velocities, on the order of the critical velocity. In this section we aim to quantify these two signatures of the trapped-electron runaways. Moreover, we calculate also the birth-delay time of these runaways, since, upon application of a DC electric field, these electrons first need to undergo detrapping, before the run away can progress.

How important are the trapped-electron runaways? For an initially Maxwellian distribution function, there will be very few trapped-electron runaways compared to the usual runaways. This is because both types of runaway electrons are drawn just from the far tail of the electron parallel velocity distribution function, but the trapped-electron runaways are further drawn only from the far tail electron perpendicular velocity distribution function. However, the relative number of trapped-electron runaways might increase importantly for two reasons: one, the usual runaway electrons may not be well-confined, whereas, the trapped-electron runaways, since born near the magnetic axis, are very well confined; and, two, knock-on collisions with runaway electrons produce a non-thermal spectrum of secondary runaway electrons, of which a significant number may be trapped-electron runaways due to their high perpendicular velocities [42]. This might produce a runaway avalanche effect, not dependent on the confinement

of circulating runaway electrons, in which confined trapped runaways produce more trapped runaway electrons.

6.2.1 Radial detrapping condition

First, we derive the detrapping condition due to the inward drift of energetic trapped electrons, in the absence of collisions. These electrons would run away on the basis of having large enough parallel velocity, except that a large perpendicular velocity initially prevents that through the magnetic trapping.

Let the electric field in the toroidal direction (ϕ) be given by:

$$E_\phi = -\frac{\partial A_\phi}{\partial t}. \tag{6.49}$$

where $\mathbf{A}$ is the magnetic vector potential. The toroidal canonical momentum is a constant of motion because of axisymmetry. It is given by:

$$P_\phi = R(\gamma m_0 v_\phi + q_e A_\phi), \tag{6.50}$$

where R is the distance from the rotational axis to the magnetic axis. The toroidal velocity is related to the velocity component parallel to the magnetic field by:

$$v_\phi = \frac{B_\phi}{B} v_\parallel. \tag{6.51}$$

Thus Eq. (6.50) becomes:

$$P_\phi = R(\gamma m_0 \frac{B_\phi}{B} v_\parallel + q_e A_\phi). \tag{6.52}$$

Since P_ϕ is a constant of the motion, we have

$$\frac{d}{dt}\left(P_\phi\right) = 0. \tag{6.53}$$

Consider the canonical toroidal momentum of a trapped particle at the turning point of the banana orbit at minor radius and time (r, t), where $v_\parallel = 0$. The next turning point will be at $(r + \delta r,\, t + \delta t)$. At these points we have:

$$P_\phi = R q_e A_\phi. \tag{6.54}$$

From Eqs. (6.53) and (6.54) we obtain:

$$\delta r \frac{\partial (R A_\phi)}{\partial r} + \delta t R \frac{\partial (A_\phi)}{\partial t} = 0. \tag{6.55}$$

In the first term, assuming axisymmetry, we find the poloidal magnetic field

$$B_\theta = -\frac{1}{R}\frac{\partial}{\partial r}\left(R A_\phi\right), \tag{6.56}$$

which inserted in Eq. (6.55) gives a drift speed towards the magnetic axis:

$$-\delta r R B_\theta - \delta t R E_\phi = 0 \;\rightarrow\; \frac{\delta r}{\delta t} = -\frac{E_\phi}{B_\theta}. \tag{6.57}$$

This drift is known as the Ware pinch [43] and acts on all trapped particles. For a trapped electron with kinetic momentum $(p_\parallel, p_\perp)$ we will investigate the detrapping due to this drift. The trapping condition is given by

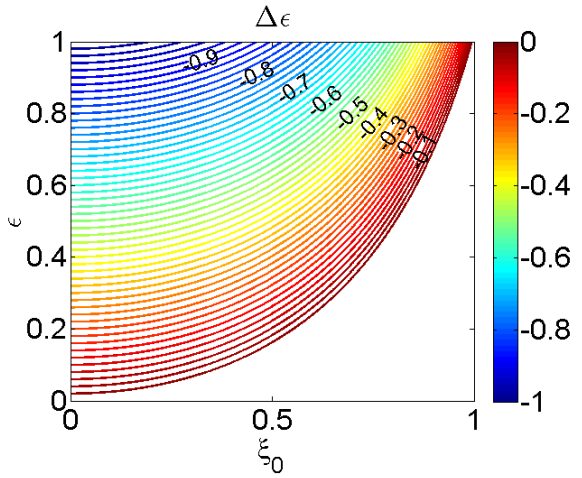


Figure 6.5: The inward radial displacement ($\Delta\epsilon$) required for trapped electron initially at radial position ϵ and pitch angle ξ_0 to become circulating.

$$|\xi_0| < \xi_{0T}(\psi) = \sqrt{1 - \frac{(1 - \frac{r}{R})}{1 + \frac{r}{R}}}, \tag{6.58}$$

where ξ_{0T} is the pitch angle, defined at the minimum $B_0(\psi)$ on a given flux-surface, such that the parallel velocity of the particle vanishes at the maximum $B_{max}(\psi)$. R is the major radius and r the radial coordinate. As the electron drifts radially inwards from r to $r - \delta r$ during the time δt the local trapping condition experienced by the electron will change.

Consider now a magnetically trapped electron at inverse aspect ratio coordinate $\epsilon = r/R$ with momentum $p = \sqrt{p_\parallel^2 + p_\perp^2}$. On a given poloidal coordinate, at for example the minimum magnetic field, the particle has parallel and perpendicular momentum $p_{\parallel 0}$ and $p_{\perp 0}$ so that its pitch angle on the minimum magnetic field is $\xi_0 = p_{\parallel 0}/p$. At the turning point in the banana orbit the momentum is $p_\parallel = 0$ and $p_\perp = p$.

As the trapped electrons undergo inward pinch, the trapping condition changes, i.e.

$$\xi_{0T} - \xi_0 = \Delta\xi_0 \to 0. \tag{6.59}$$

Hence, an electron with a given ξ_0 will remain trapped until it reaches the radial position $\epsilon^{'} = r/R$ where $\xi_0 = \xi_{0T}(\epsilon^{'})$. At this radial position, its parallel momentum component is sufficient for the electron to become passing. The position where the trapped electrons transition from trapped to passing is:

$$\xi_0 \to \xi_{0T} = \sqrt{1 - \frac{1 - \epsilon^{'}}{1 + \epsilon^{'}}} \;\to\; \epsilon^{'} = \frac{\xi_0^2}{2 - \xi_0^2}. \tag{6.60}$$

Hence, the inward radial displacement required for detrapping is

$$\Delta\epsilon = \epsilon - \epsilon' = \epsilon - \frac{\xi_0^2}{2 - \xi_0^2}. \tag{6.61}$$

Figure 6.5 shows the required displacement $\Delta\epsilon$ and Fig. 6.6 the radial position ($\epsilon' = r/R$) where the electrons can detrap and run away. ϵ and ξ_0 are its initial radial position and cosine pitch angle.

Thus, there results a distribution of runaway electrons with a distinct radially-dependent, pitch-angle profile, as calculated from Eq. (6.60), and as presented in Fig. 6.6.

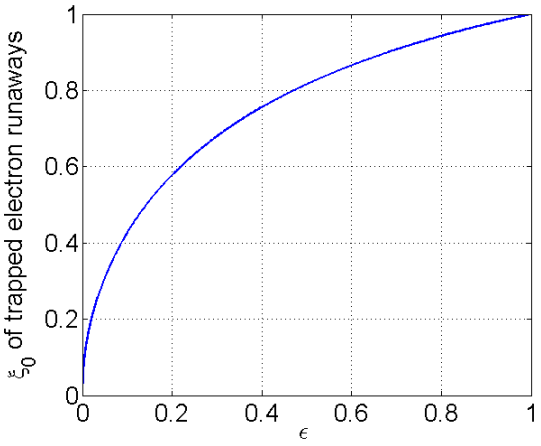


Figure 6.6: The trapped-electron runaways will appear with a distinct pitch angle (ξ_0) in the radial extent.

6.2.2 Runaway time

Suppose an electron is just reaching the point of being detrapped. Its parallel velocity is $v_{\|0} \leq \sqrt{\frac{2\epsilon}{1-\epsilon}} v_{\perp 0}$ until the electron reaches the critical radius ($\epsilon^{'}$) that satisfies

$$v_{\|0} = \sqrt{\frac{2\epsilon^{'}}{1-\epsilon^{'}}} v_{\perp 0}, \tag{6.62}$$

where $\epsilon^{'} = \frac{\xi_0^2}{2-\xi_0^2}$ is given by Eq. (6.60). As opposed to usual runaway electrons, with $v_\perp \sim v_{th}$ and $v_{||} > v_c$, where v_c is the critical velocity, the trapped-electron runaways will have higher perpendicular velocity

$$v_{\perp 0} \geq \sqrt{\frac{1-\epsilon^{'}}{2\epsilon^{'}}} v_c = \sqrt{\frac{1-\xi_0^2}{\xi_0^2}} v_c. \tag{6.63}$$

The unique pitch angle of the trapped runaway electrons $\xi_0(\epsilon)$, defined in Eq. (6.60), shows that the trapped-electron runaways will appear with high perpendicular momentum. From this criterion we will now predict the velocity distribution of the trapped-electron runaways. If the passing electron has high enough velocity, it runs away on detrapping. The pitch angle dependent critical momentum for $E/E_c \gg 1$ is estimated as [5, 40]:

$$p_c^2 \approx \frac{2}{1+\xi_0} \frac{E_c}{E}, \tag{6.64}$$

where p_c is normalized to $m_0 c$ and E_c is the critical electric field, the minimum electric field that runaway electrons may be generated if no other loss mechanisms than the collisional drag are present. The minimum perpendicular velocity of the trapped-electron runaways is presented in Fig. 6.7, normalised to $v_c(\xi_0 = 1)$.

The time it takes for the initially trapped electron to approach $\Delta\xi_0 \to 0$ is given by Eq. (6.57):

$$dt_W = -\frac{B_\theta}{E_\phi} R \Delta\epsilon = -\frac{B_\theta}{E_\phi} R \left(\epsilon - \frac{\xi_0^2}{2-\xi_0^2} \right). \tag{6.65}$$

For an equilibrium with $B_\theta = 0.05\,\mathrm{T}$ and $E_\phi = 0.8\,\mathrm{V/m}$. The time required for a trapped electron to become passing is shown in Fig. 6.8.

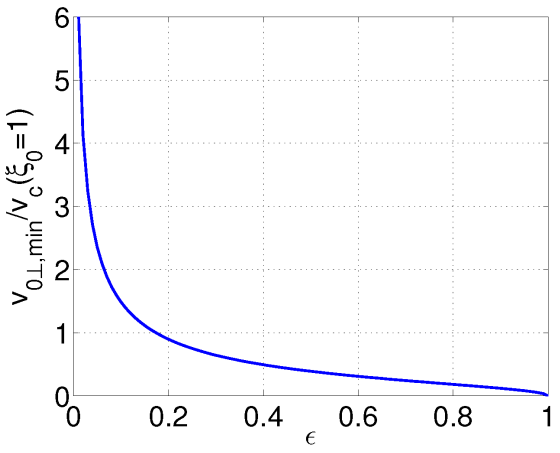


Figure 6.7: The radial distribution of the minimum perpendicular velocity of the trapped-electron runaways, normalised to the critical velocity for $\xi_0 = 1$.

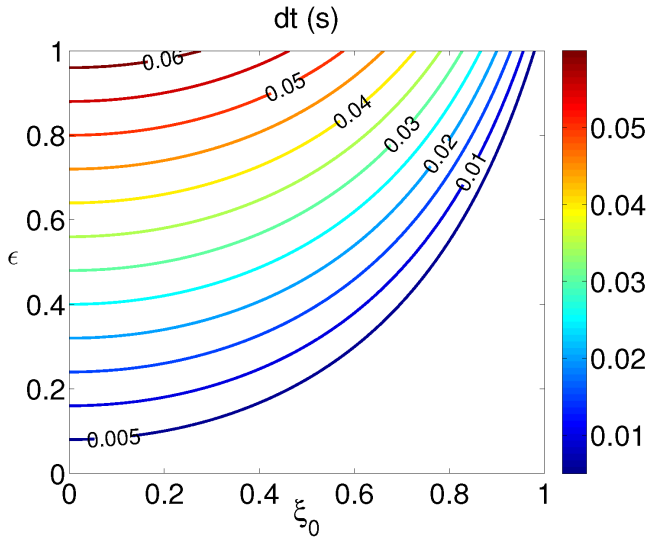


Figure 6.8: Time (s) for trapped electrons at (ξ_0, ϵ) to reach the radial position where they become passing electrons, for $B_\theta = 0.05\,\mathrm{T}$, $E_\phi = 0.8\,\mathrm{V/m}$ and $R = 1\,\mathrm{m}$.

In a disruption in an ITER-like scenario the toroidal electric field can be much stronger; around 38 V/m has been predicted [15]. In that case, the Ware pinch detrapping time scale would be much shorter; see Fig. 6.9.

Note that the calculations regarding both the detrapping time and the detrapping radius are not particularly sensitive to the current profile, or what is called also the q-profile, at least in the limit that the excursion from the flux surface is small compared to the radius of the flux surface. To see this, note that if a trapped electron lies close to a flux surface, it will see a magnetic mirror ratio of the field at the inboard side to the field at the low-field side. Since this effect is independent of the poloidal magnetic field, the detrapping condition, expressed by Eq. 6.60, is likewise dependent only on the radial coordinate and not on the poloidal field profile. Corrections due to the Shafranov shift of the flux surfaces, the banana orbit widths, the other deviations from the magnetic surfaces, can then be addressed as corrections to the main effect

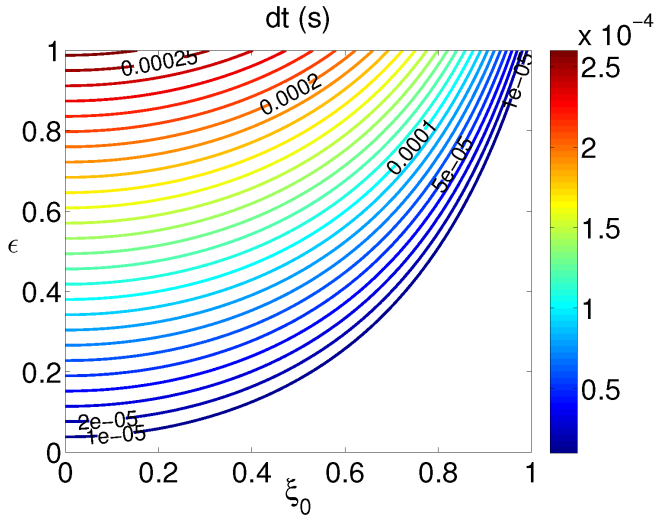


Figure 6.9: Time (s) for trapped electrons at (ξ_0, ϵ) to reach the radial position where they become passing electrons, for $B_\theta = 0.01$ T, $E_\phi = 38$ V/m and $R = 1$ m.

described.

Although poloidal magnetic field B_θ has little effect on the detrapping condition, it does have a strong effect on the detrapping time. This time is in fact proportional to B_θ. For simplicity, we took the E_ϕ/B_θ velocity to be constant. In fact, as the electron pinches inward, the poloidal field decreases, thereby speeding the drift. Thus, a more precise formulation of Eq. 6.65 would involve an integral over dr, where E_ϕ/B_θ is treated as dependent on r. However, the detrapping time will be dominated by the slow speeds, so that, for example, the vanishing of the poloidal field at the plasma center will not deeply affect the characteristic detrapping time. In any event, very near the magnetic axis, the approximations used here break down, particularly those concerning the deviation from the flux surface compared to the radius of the flux surface.

6.2.3 Collisional effects

These calculations describe an electron born trapped but energetic enough to be collisionless, so that it will spend some time being trapped and then run away closer to the magnetic axis. However, in fact, the electron also experiences slowing down from collisions, so it might not be energetic enough once it becomes detrapped. The collision free approximation would be valid when the pinch time is small compared to the slowing down time of runaway electrons. However, if the time scale of the pinch is longer, the electron may slow down such that it may not have the energy required to run away when it finally detraps. If the pinch time is on the order of the slowing down time, the initial momentum has to be larger than the critical momentum. If the effective charge Z_{eff} is small, we might imagine that slowing down affects $p_\parallel$ and $p_\perp$ equally, so the detrapping condition does not change.

The change in momentum due to collisions during the time the electron is trapped (Δt) is Δp_{fr}. Thus the initial momentum required for an electron to run away has to be larger than the usual critical momentum p_c (Eq. 6.64). Hence, the effective critical momentum required for a trapped electron to eventually run away can be formulated as

$$p_{c,eff} = p_c + \Delta p_{fr}(dt_W), \tag{6.66}$$

where dt_W is the time it takes for the electron to detrap; initially trapped electrons run away if $p > p_{c,eff}$. The collisionless predictions of the trapped-electron runaway effect is valid under the assumption that the time for pitch angle scattering is not smaller than the time it takes to detrap due to the Ware pinch. This gives a condition on the Ware pinch time. The relativistic collision time

$$\tau_c = \frac{4\pi\epsilon_0^2 m_0^2 c^3 (p/m_0 c)^3}{\gamma q^4 n_e \ln\Lambda}, \tag{6.67}$$

must be larger scale than the time for detrapping (Eq. 6.65). Comparing the Ware pinch time with the collision time gives:

$$dt_W = -\Delta\epsilon \frac{B_\theta R}{E_\phi} < \frac{4\pi\epsilon_0^2 m_0^2 c^3 (p/m_0 c)^3}{\gamma q^4 n_e \ln\Lambda}. \tag{6.68}$$

For a maximum inward displacement, $\Delta\epsilon = -1$, the above condition tells us that collisional effect can only be neglected when:

$$\frac{(p/m_0 c)^3}{\gamma} = \gamma^2 (v/c)^3 > \frac{B_\theta n_e R}{E_\phi} \frac{q^4 \ln\Lambda}{4\pi\epsilon_0^2 m_0^2 c^3}. \tag{6.69}$$

The above expression tells us that for high enough energy ($\gamma m_0 c^2$), compared to the right hand side, where the parameters are B_θ, E_ϕ, n_e and R, the collision free approach can be taken. If the condition in Eq. 6.69 is not fulfilled, collisions should be included in the calculations.

For ITER-like parameters and an assumed current profile the solution to the energy is shown in Fig. 6.10. The density is $n_e = 10^{20}\,\mathrm{m}^{-3}$ and the electric field strength is assumed to be constant; $E_\phi = 10\,\mathrm{V/m}$, $38\,\mathrm{V/m}$ and $100\,\mathrm{V/m}$. The magnetic field is calculated from a current density profile with a total plasma current of $I_p = 15\,\mathrm{MA}$. The assumed current profile has small current density near the edge, so that the maximum of the poloidal magnetic field is not at the edge. This explains the maximum in the energy condition. The radial dependence of the density and the electric field strength are not taken into account.

The minimum energy required for the collision time to be longer than the Ware pinch time is on the order of MeV for ITER-like parameters during a disruption (see Eq. 6.76). Considering that runaway electrons have many tens of MeV, it can be expected that runaway electrons produced from knock-on collisions should well be in this range where collisions can be neglected. Of course, there can trapped-electron runaways with energy less than that, but then account must be taken of collisions. That regime is left for a future study.

Also, the time of radial drift due to the Ware pinch must be compared to the time needed for the electron to be deflected so that it is no longer on a trapped orbit. In the limit $\epsilon \ll 1$, the change of the pitch angle necessary to make trapped particles become detrapped can be approximated as

$$\Delta\xi_0 \sim \xi_{0T} \simeq \sqrt{\frac{2\epsilon}{(1+\epsilon)}} \sim \sqrt{\epsilon}. \tag{6.70}$$

The small angle collisions a random-walk change in the pitch angle ξ_0, the effective collision frequency for detrapping is approximately

$$\nu_{c,eff} \sim \frac{\nu_c}{\Delta\xi_0^2} \sim \frac{\nu_c}{\epsilon}. \tag{6.71}$$

Thus the average time for detrapping due to pitch angle scattering goes like:

$$\tau_{eff} \sim \tau_c \epsilon. \tag{6.72}$$

If the condition $dt_W < \tau_{eff}$ applies, the Ware pinch may be dominant over pitch angle scattering

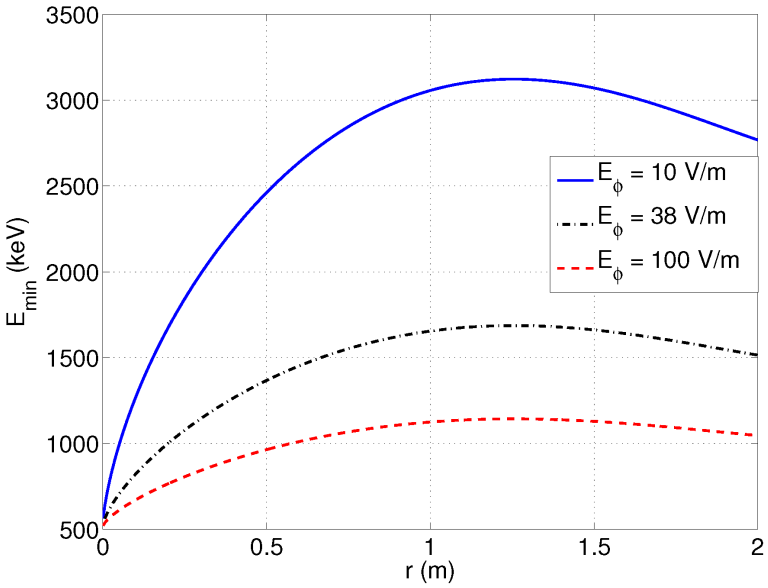


Figure 6.10: The minimum energy needed for the Ware pinch to be faster than the collision time, for the parameters $E_\phi = 10\,\mathrm{V/m}$, $38\,\mathrm{V/m}$ and $100\,\mathrm{V/m}$, $n_e = 10^{20}\,\mathrm{m}^{-3}$ and $R = 6.2\,\mathrm{m}$. The poloidal magnetic field is calculated from a current density profile with a total plasma current of $I_p = 15\,\mathrm{MA}$.

$$-\Delta\epsilon R\frac{B_\theta}{E_\phi} < \frac{4\pi\epsilon_0^2 m_0^2 c^3 (p/m_0 c)^3}{\gamma q^4 n_e \ln\Lambda}\epsilon. \tag{6.73}$$

For $-\Delta\epsilon \approx \epsilon$ we get:

$$\frac{B_\theta}{E_\phi}R < \frac{4\pi\epsilon_0^2 m_0^2 c^3 (p/m_0 c)^3}{\gamma q^4 n_e \ln\Lambda}, \tag{6.74}$$

and the same requirement on the energy of the electrons as in Eq. (6.69). In order to get a more comprehensible condition, we consider the condition for $\gamma \gg 1$ and obtain for $E = \gamma m_0 c^2$:

$$E > \sqrt{\frac{B_\theta n_e R}{E_\phi}\frac{q^4 \ln\Lambda c}{4\pi\epsilon_0^2}}, \tag{6.75}$$

which gives

$$E \gtrsim 2.8\sqrt{\frac{B_\theta n_e R}{E_\phi}} \qquad [\mathrm{MeV}], \tag{6.76}$$

where n_e given in $10^{20}\,\mathrm{m}^{-3}$, B_θ in T, E_ϕ in V/m and R in m.

Just like the collisional slowing down, the synchrotron reaction force [44] limits the energy of the particle. This additional drag scales with the particle momentum as [45]:

$$F_{rad,\,p} = -\frac{\gamma p(1-\xi^2)}{\tau_r}, \tag{6.77}$$

where τ_r is the radiation damping scale:

$$\tau_r = \frac{6\pi\varepsilon_0\gamma(m_0c)^3}{q^4B^2} \approx 5.2\frac{\gamma}{Z^4B^2}. \tag{6.78}$$

In addition the synchrotron reaction force limits the pitch angle

$$F_{rad,\,\xi} = -\frac{p\xi\sqrt{1-\xi^2}}{\gamma\tau_r}. \tag{6.79}$$

This force could affect the trapped-electron runaways in the Ware pinch process, as electrons would detrap faster, i.e. at a larger radius than predicted in Sec. 6.2.1, if $p_\perp/p_\parallel$ decreases. The limitations of the collisionless theory was discussed and a regime was identified where the Ware pinch detraps trapped runaway electrons fast enough for the collisions to be negligible ($dt_W \ll \tau_c$). A similar condition can be set for the radiation loss time $dt_W \ll \tau_r$. By comparing the time scale of collisional damping with the one of the radiation damping:

$$\frac{\tau_c}{\tau_r} = \frac{2\epsilon_0}{3m_en_e\ln\Lambda}\gamma\Big(\frac{v}{c}\Big)^3Z^4B^2 \approx 0.04\frac{\gamma}{n_{e,19}}\Big(\frac{v}{c}\Big)^3Z^4B^2, \tag{6.80}$$

for $\ln\Lambda = 16$ where $n_{e,19}$ is the electron density in the unit $10^{19}\,\mathrm{m}^{-3}$. For relevant plasma parameters and electrons for this problem and $v/c < 1$, the condition $\tau_c \ll \tau_r$ is fulfilled unless γ gets very large. From the minimum energy defined in Fig. 6.10, where the Lorentz factor γ is in the range of $1-6$, for higher γ the time scale of the synchrotron reaction force may be short enough to change the pitch before the detrapping radius is reached, if the product B^2Z^4/n_e becomes large. To properly account for the combined effect of synchrotron reaction and collisional drag on the trapped-electron runaway distribution during the Ware pinch would require further investigation by numerical studies.

6.2.4 Trapped-Electron Runaway Growth Rate

The runaway electron growth rate can be expressed as a sum of the Dreicer generated runaway electrons (first term) and the runaway electrons generated through the knock-on process (second term):

$$\frac{dn_{RE}}{dt} = \left[\frac{dn_{RE}}{dt}\right]_D + \frac{n_{RE}}{\tau_{RE}}. \tag{6.81}$$

If we include toroidicity in the equation we get a loss term, $T(\epsilon)$, from the electrons that are born into the trapped region and can not instantly run away [42]. However, owing to the Ware pinch, there is a correction to the growth rate loss. The growth rate including these corrections can be expressed as:

$$\frac{dn_{RE}}{dt} = \left(\left[\frac{dn_{RE}}{dt}\right]_D + \frac{n_{RE}}{\tau_{RE}}\right)\left[1 - T(\epsilon)(1 - W(\epsilon,t))\right], \tag{6.82}$$

where $T(\epsilon)$ is the growth rate loss from the trapped electrons. The Ware pinch ($W(\epsilon,t)$) is the correction to the reduction of magnetic trapping effect in Eq. (6.60). The time dependent Ware pinch term is obtained by integrating the distribution function of trapped electrons $f_T(\epsilon)$ from the boundary between passing and trapping condition $\epsilon = \xi_0^2/(2-\xi_0^2)$ to the minimum radius at which the Ware pinch can release a trapped electron $\epsilon_W(t) = \epsilon + \frac{E_\phi t}{B_\theta R}$.

$$W(\epsilon,t) = \int_\epsilon^{\epsilon_W(t)} f_T\; d\epsilon. \tag{6.83}$$

The trapped-electron distribution function can be estimated as $f_T(\epsilon) \approx const.\sqrt{\epsilon}$ [42]. In that case the Ware pinch correction becomes:

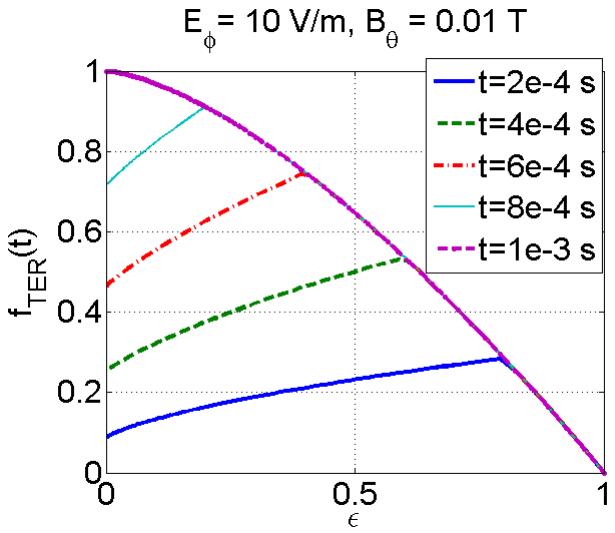


Figure 6.11: The radial distribution function of the trapped-electron runaways, given the initial trapped electron distribution function $f_T \approx \sqrt{\epsilon}$ for the parameters $E_\phi = 10\,\mathrm{V/m}$, $B_\theta = 0.01\,\mathrm{T}$ and $R = 1\,\mathrm{m}$.

$$W(\epsilon, t) = const. \int_{\epsilon}^{\epsilon_W(t)} \sqrt{\epsilon}\, d\epsilon = const. \Big((\epsilon_W - \mathcal{H}(\epsilon_W - 1)(\epsilon_W - 1))^{3/2} - \epsilon^{3/2} \Big), \tag{6.84}$$

where $\mathcal{H}$ is the Heaviside step function due to the fact that $\epsilon \leq 1$. In Fig. 6.11 the time dependent distribution function of the trapped-electron runaways ($f_{TER}(\epsilon, t)$) is plotted for $B_\theta = 0.01\,\mathrm{T}$, $E_\phi = 10\,\mathrm{V/m}$ and $R = 1\,\mathrm{m}$. It shows the expected trapped-electron runaway distribution in the radial extent, if we assume that collisional effects are negligible.

The appearance of the trapped-electron runaways in the radial extent can be found by studying the time dependent release of trapped-electrons owing to the Ware pinch. The avalanche growth rate decays off the magnetic axis and can be estimated as the integral of the knock-on source term ($\mathbf{S}$) [5] with the lower integration limit as the maximum of the critical momentum and the momentum that coincides with the trapped/passing boundary [42]:

$$\frac{1}{n_r}\frac{\partial n_r}{\partial t} = \frac{1}{n_r} 2\pi \int_{p_c}^{\infty} \int_{\xi_T}^{1} \mathbf{S}\, p^2 dp\, d\xi. \tag{6.85}$$

To estimate the appearance of the trapped-electron runaways, the contribution to the avalanche will instead originate from the source term between the minimum pitch angle at which electrons may be pinched ($\xi_{0W}(\epsilon, t)$) to the position of detrapping $\xi_{0T}(\epsilon)$. From the bounce-averaged knock-on operator implemented in the 3-D Fokker-Planck solver LUKE [46] a radial distribution of trapped-electron runaways is obtained. The time dependent contribution to the runaway population from the Ware pinch is obtained by integrating the source term of trapped knock-on electrons from the trapped/circulating boundary $\epsilon = \xi_0^2/(2 - \xi_0^2)$ to the minimum radius at which the Ware pinch can release a trapped electron $\epsilon_W(t) = \epsilon + \frac{E_\phi t}{B_\theta R}$. This results in a radial distribution of used to be trapped electrons born in knock-on collisions, shown in Fig. 6.12. The distribution function is normalized to the central value of the time where the distribution function saturates, i.e. when all remaining trapped electrons are too collisional to run away. This calculation shows that the trapped-electron runaways will appear near the center and may contribute to the avalanche growth rate.

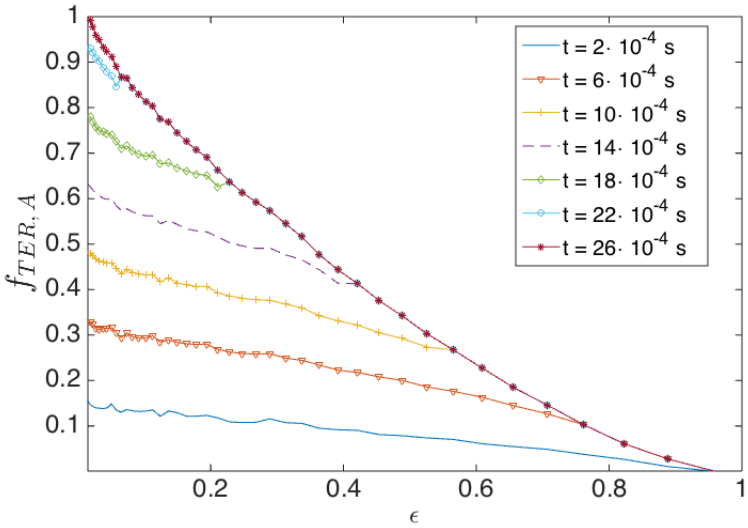


Figure 6.12: The radial distribution function of the trapped-electron avalanche, with $E_\phi = 10\,\mathrm{V/m}$ and $B_\theta = 0.01\,\mathrm{T}$, calculated from the bounce-averaged knock-on operator implemented in the LUKE code.

6.2.5 Discussion

The effect that we described in this section is how initially trapped electrons become runaway electrons. They eventually run away because they do have high parallel velocity, comparable to the critical runaway velocity. But they are trapped in the first place because also their perpendicular velocity is comparable to the critical runaway velocity. Hence, they drift towards the axis, where they become detrapped with perpendicular velocity comparable to the critical runaway velocity. That will distinguish the trapped runaways from the passing runaways, which have average perpendicular energies.

In this picture, there are several signatures to the trapped-electron runaways: First, and most significantly, there is the high perpendicular velocity, which will produce more intense synchrotron radiation. Second, they will be concentrated in the plasma center, with the highest perpendicular velocities and therefore the most intense (per electron) emission, found closest to the axis (where the trapping is weakest). Third, in a disruption, there will be a turn-on time for the electrons to reach the radial detrapping position and only then to begin to run away. All these signatures should be most prominent during a disruption, where the electric field is large, and might be used to inform on plasma conditions. These signatures, as diagnosed through the synchrotron radiation, should be distinct from the synchrotron radiation of normal runaways [47, 48]. For very long times, however, the synchrotron radiation may eventually deplete the perpendicular energy, making the signatures less distinctive.

Apart from the synchrotron radiation signature, the large perpendicular energies of the trapped-electron runaways suggest that they may be easier to control magnetically. Runaway electrons can be lost through interactions with ripple fields [49, 50], coherent wave instabilities such as Alfvénic instabilities [51], or magnetic perturbations [52]. In all of these cases, the strength of the interaction will be larger for larger perpendicular velocities.

Recently, there has been interest in the creation of runaway positrons in tokamaks, and the information that might be obtained from them upon annihilation [13, 14, 53]. When large tokamaks disrupt, large electron-positron pair production is expected to occur. The positron runaways behave just like runaway electrons, only they run away in the opposite direction. Just like there are circulating positron runaways, there will be trapped positron runaways.

These trapped positron runaways will pinch towards the tokamak magnetic axis just like the trapped-electron runaways. Except they will travel in the opposite toroidal direction, which will affect the Doppler shift of the synchrotron radiation, the trapped positron runaways will have a completely analogous signature to the trapped-electron runaways. Moreover, since the positrons would only be produced in large numbers through the avalanche effect involving very high energy runaways, there will be relatively more of the trapped positron runaways (compared to the usual positron runaways) than there would be trapped-electron runaways (compared to the usual runaway electrons). This effect would be enhanced to the extent that the most energetic runaways – and those most capable of the pair production – would be found near the low field side of the tokamak [54], where the trapping effect is also most significant.

Note that the trapped-electron runaway effect that we discuss is for runaway electrons that run away eventually in the direction in which they support the plasma current. The same is true for the runaway positrons. When the tokamak current is maintained by a DC electric field, it is after all the thermal electrons that carry the toroidal current, and the runaway electrons carry current in the same direction, only they are accelerated to far higher energies. This would also be true during start-up of the tokamak [55], if the start-up relies on an inductive current. In such a case, there is also danger from runaway electrons, since the plasma may not be dense enough to hold back the runaways. Moreover, in the case of radio frequency (RF) assisted start-up of the current, like through electron cyclotron heating, there might be more electrons produced at higher energies, which could then run away in the direction in which the runaways support the current.

Whether or not the runaways are in a direction to support the plasma current is an important distinction that comes into play in non-inductive start-up of the tokamak current. In the case of non-inductive current drive, for example by RF waves [56], there is the opportunity to start up the tokamak or to recharge the transformer [57]. In such a case, the loop voltage is driven negative; in other words, as the RF current in increased, a loop voltage is induced which opposes the RF-driven current. This DC electric field also produces runaway electrons, only now they are so-called *backwards runaways*, which are runaway electrons that carry current counter to the toroidal current [58]. However, in the case of very sudden ramp-up with RF waves, when the RF current is overdriven, in other words, when the RF-driven current is made much larger than the inductive current, then the opposing loop voltage can be much larger than the normal loop voltage in a tokamak [59, 60, 61]. There is then the concern that there could be damage caused by the runaways that might be produced by the unusually strong electric field induced to counteract the current. Note, however, that in such a case, any runaways produced will be traveling in the direction unsupportive of the tokamak current, as opposed to the usual case of in support of the tokamak current. In this case, in conserving toroidal angular momentum, the DC electric field causes trapped-electrons to move away from the magnetic axis rather than toward it. This has a profound consequence, because the trapped electrons, in moving outward, encounter a more stringent trapping condition. Hence, in the case of RF ramp-up, while circulating backwards runaways are produced, no production whatsoever can be expected of backwards trapped-electron runaways (or, for the same reason, backwards trapped-positron runaways). Thus, in vigorous RF ramp-up regimes, while the circulating backwards runaways might be of some concern, at least the trapped-electron runaways do not add to that concern.

A recurring question is to what extent RF current drive generates runaway electrons. This question should also be posed for the trapped-electron runaways. In the case of RF current drive, if the current drive effect relies on RF wave interactions with suprathermal electrons, there is risk of producing runaway electrons. It is particularly the case for lower hybrid current drive [62], where a suprathermal electron tail is formed at high parallel velocities that could supply more runaway electrons than could a Maxwellian distribution. It is also the case for electron cyclotron current drive [63], where heating in perpendicular velocity makes electrons collide less frequently and become more likely to run away. In these cases, the RF heating of passing electrons enhances the runaway current through the usual runaway effect. However,

there is also a trapped particle runaway effect when the RF current drive affects trapped electrons. Consider first waves that provide parallel momentum to energetic trapped electrons, such as low parallel-phase-velocity waves [64]. Since the particles remain trapped, there is an RF-pinch effect similar to the Ware pinch effect [65]. If the wave momentum is in the direction supportive of the total current, then as with the Ware pinch effect, the pinch will be inwards. Moreover, like with the Ware pinch, the trapped electrons experience less stringent trapping conditions when they pinch, so they can eventually run away like a trapped runaway. One important difference is that, as opposed to the Ware pinch effect where the electric field pinches the electron, without increasing its energy, in the case of the RF pinch effect, the RF waves pinch the electron, while increasing its energy. As a result the trapped runaways become detrapped sooner, and so run away at larger radii. It must be pointed out that the RF pinch may only occur if the wave-particle resonance is present continuously through the pinching process, i.e. if the spatial distribution of the waves has sufficient radial extent. In any event, in inputting parallel momentum with waves that would be supportive of the toroidal current, whereas targeting electrons with higher parallel velocity can increase the number of runaway electrons, targeting electrons with low parallel velocity can increase the number of trapped runaways.

In contrast, in the case of perpendicular heating rather than parallel heating of trapped electrons, such as by electron cyclotron waves, there is no pinch effect bringing electrons to less stringent trapping conditions. In fact, the perpendicular heating causes the electrons to be more deeply trapped. Hence, there is no trapped-particle runaway effect for heating by electron cyclotron waves.

Chapter 7

Modelling of runaway electrons in tokamak plasmas

As described in Sec. 3.3 the properties of the LUKE code restricts the modelling to non-disruptive tokamak plasmas with non-ergodic magnetic flux surfaces. However, recent equilibria reconstructions show that in the central region of the plasma the flux surfaces are nested during the runaway electron plateau [66]. This phase of the disruption might be possible to model with LUKE, given an estimate of the seed of runaway electrons formed during the thermal quench. Those studies are left for future work.

Flattop scenarios with rather constant plasma parameters, like in current flattop usually with low density are suitable for studying the formation of runaway electrons with the LUKE code. Data from such scenarios are available from several machines. Current ramp-up and ramp-down can also be modelled given the existence of reliable temperature and density measurements. In this chapter modelling with the code LUKE for non-disruptive tokamak scenarios is presented. Global plasma parameters such as parallel electric field and plasma equilibrium are calculated with the fast integrated modelling code METIS [67] for the Tore Supra and COMPASS tokamaks. Several suitable discharges have ben modelled. Results are validated against experimental observations. For Tore Supra scenarios the modelling is compared to tomographic HXR emission from the fast electron population through HXR signal reconstruction accounting for geometry and detector specifications [68]. This allows for comparison of both profile and amplitude of the fast electron Bremsstrahlung.

One of the difficulties in predicting the formation lies in the appearance of sawtooth instabilities in the #40719 Tore Supra discharge, as a consequence of the low density. For this purpose, equilibria with high enough time resolution to capture the sawtooth oscillations, based on ECE temperature measurements, are calculated with the CRONOS code [67, 69] and the electron distribution function through a few sawteeth periods can be calculated with LUKE.

The modelling presented in this chapter is a first step in validating the LUKE code against experimental observations in order to use the code for predictions for future scenarios. The equilibria and kinetic profiles prescribed by METIS are based on experimental data from various diagnostics, but does not take the presence of runaway electrons into account in the equilibrium and kinetic profile reconstruction. The use of METIS modelling without coupling with the LUKE code for self-consistent calculation of electric field and runaway electron current is valid as long as the runaway electron population is only a perturbation to the Ohmic current, i.e. small enough to influence the electric field negligibly. Future work includes a self-consistent equilibrium reconstruction where the influence of the runaway current on the electric field profile is accounted for. That would result in a valid description of runaway formation in scenarios with rather high runaway current. It is assumed that the flux surfaces remain intact throughout the simulation period. The reason is that the runaway electrons formed on a certain flux surface coordinate are assumed to remain there during the remaining part of the discharge. Modelling

of disruptive scenarios is outside the validity range of the tools in their present form, as loss mechanisms and MHD stabilities are not described in the codes. The coupling of the kinetic LUKE code with a fluid code such as JOREK [29], would be necessary for such a purpose, but is beyond the scope of this work.

7.1 Modelling of non-disruptive scenarios with LUKE/METIS

The global discharge evolution, MHD equilibrium and kinetic profiles for each plasma scenario are obtained from the fast integrated tokamak simulator METIS (Minute Embedded Tokamak Integrated Simulator). METIS provides interpretative simulations of Tore Supra discharges yielding particle and impurity densities, ion and electron temperature profiles, bootstrap current and plasma momentum. It also calculates the electric field radial profile parallel to the magnetic field lines $E_{\|}(r)$, used for simulation of inductive discharges [67]. The METIS code computes the time evolution of the global plasma quantities for given waveforms of the control parameters. It solves the current diffusion equation assuming an approximate equilibrium evolution.

The temperature and density profiles are fitted from experimental data from the Tore Supra database. Equilibrium files are prescribed by the METIS code, using experimental temperature and density data as input, weighted with Bayesian analysis [70]. The advantage of the Bayesian analysis is increased reliability of the reconstruction of the plasma profiles from experimental data. METIS provides magnetic field, parallel electric field, temperature and density profiles as well as effective charge estimates. Input files are prepared along the discharge time evolution, the frequency depending on how steady the plasma parameters are. For example in the current flattop, the results are not very sensitive to the time step, but in ramp-up and ramp-down higher time resolution is needed.

Based on the METIS input, the LUKE code calculates the effect of the runaway mechanisms on the electron distribution function. The time evolution of the distribution function is considered and the external runaway electron population at the end of one time slice is given as input in the following time step:

$$n_{re,init,t} = n_{re,end,t-1}, \tag{7.1}$$

which is equivalent to assuming that the runaway electrons remain confined throughout the entire discharge at the flux surface coordinate where they were formed. Experiments show that runaway electrons are usually ejected from the plasma along the discharge [71, 72, 6, 37], but the processes of runaway confinement and loss mechanisms are complex and not included in our model. In other words, runaway electrons that are generated are assumed to remain at the same radial position throughout the rest of the discharge.

The momentum grid of the LUKE code is normalized to the local thermal momentum, as a consequence the grid needs to be normalized to the temperature changes and input from previous time steps are interpolated onto the new momentum grid. In the first time step the initial distribution function is taken to be Maxwellian (f_M). Given the initial distribution function the LUKE code calculates the effect on the distribution function during the time dt_n. The internal runaway electron population is transferred between time steps by interpolating the electron distribution function onto the new momentum grid. The calculated non-Maxwellian distribution function is used as initial distribution function in the consecutive time step, with local temperature and density ($n_b = n_e - n_{re}$) updated through addition/subtraction of a Maxwellian function and by renormalization onto the momentum grid, normalized to the new thermal momentum. Thus, the evolution of the distribution function becomes

$$f_{init,t} = f_{end,t-1} + (n_{b,t} - n_{b,t-1}) f_M(n_{e,t}, T_{e,t}), \quad (7.2)$$
$$f_{init,0} = f_M(n_{e0}, T_{e0}). \quad (7.3)$$

The '*init*' index denotes that the value or function is used in the initial part of the time slice. Given this criteria, the time slice has to be small enough for the equilibrium to remain rather constant within the time slice.

A term for anomalous fast electron radial transport in the kinetic equation is implemented in the LUKE code and can be introduced in the calculations as a free parameter [73]. The transport model is based on transport model by Rechester and Rosenbluth [74]. It has the usual form of

$$D_r = D_{r0} \left(v_\parallel / \hat{v}_{th} \right) H \left(v_\parallel - 3.5 \hat{v}_{th} \right), \quad (7.4)$$

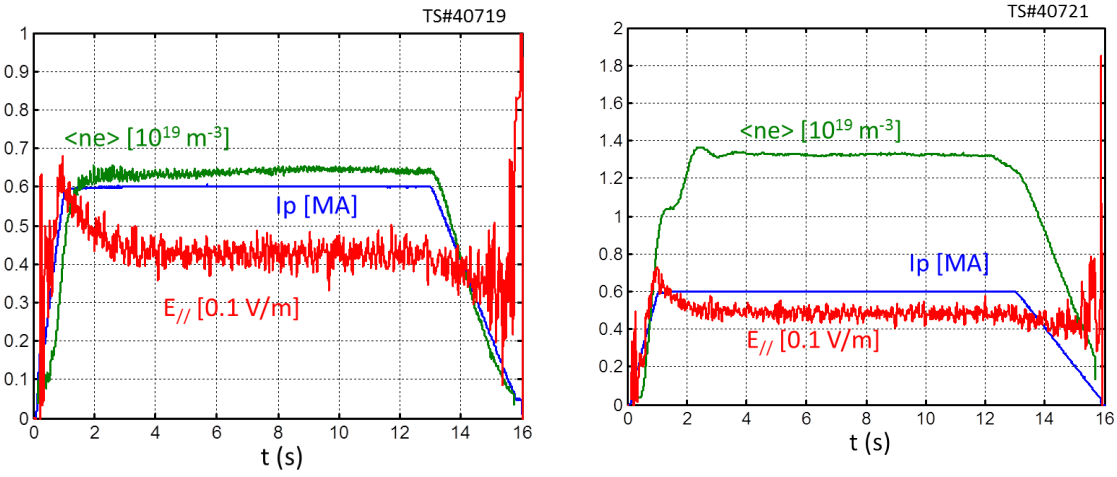
where D_{r0} is a radial transport coefficient and $\hat{v}_{th}$ is the thermal velocity taken at the center of the plasma. The $v_\parallel$ offset for the transport is a free parameter but in our simulations it is set to $3.5\hat{v}_{th}$, thereby affecting only suprathermal electrons. Fast electron radial transport has previously been used in lower hybrid current drive (LHCD) to smooth out local peaks in the power absorption. For example, in Ref. [75], it is found that adding a small radial transport ($D_{r0} = 0.1\ m^2/s$) in calculations of LHCD in Tore Supra leads to optimal agreement between reconstructed fast electron Bremsstrahlung emission and experimental measurements from hard X-ray tomography.

7.2 Tore Supra

Runaway electrons have been detected in the Tore Supra tokamak in low density discharges ($\bar{n}_e < 10^{19}\ m^{-3}$) in the current ramp down by electron cyclotron emission (ECE), hard X-ray (HXR) and photoneutron measurements. Such observations are seen in discharge #40719, where the electron density in the current flattop is $\bar{n}_e = 0.64 \cdot 10^{19} m^{-3}$, corresponding to $E/E_c \approx 8$ and $E/E_D \approx 0.06$. However, in a similar discharge (#40721) with higher density, no runaway electrons are observed even though the electric field exceeds the threshold field ($E/E_c \approx 4$ and $E/E_D \approx 0.02$). The signatures of runaway electrons were presented in Sec. 5.2. The evolution of the two discharges are presented in Fig. 7.1.

There is an experimental level on the diagnostics below which no detection can be done. Therefore, absence of runaway signatures does not guarantee that no runaway electrons or suprathermal electrons are formed, it could simply be a consequence of that the population is too small to be detected by the diagnostics. With METIS/LUKE simulations we can investigate whether any suprathermal electrons are formed also in the two pulses without runaway signature (#40721 and #39173), where $E > E_c$. The central temperature in #40719 and #40721 are different, but off the magnetic axis they are very similar. Most of the contribution to the resistivity comes from off axis, which explains why the loop voltages do not differ too much to drive the same current, see Fig. 7.2.

In order to understand the different outcome of the two non-disruptive TS scenarios, the formation of runaway electrons from the combined effect of Dreicer and avalanche is studied with the LUKE code. There are no direct measurements of the effective charge but in #40719 there is no gas puffing so the plasma is assumed to consist of deuterium. In #40721 helium is injected so the Z_{eff} is expected to be slightly higher.



(a) (b)

Figure 7.1: Measured line averaged electron density, plasma current and parallel electric field strength in discharge #40719 (a) and #40721 (b).

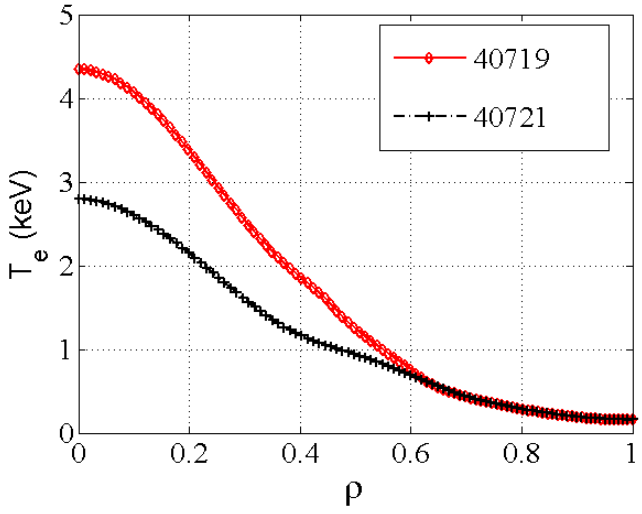


Figure 7.2: Temperature profiles for two Tore Supra discharges (#40719 and #40721) during the current flattop.

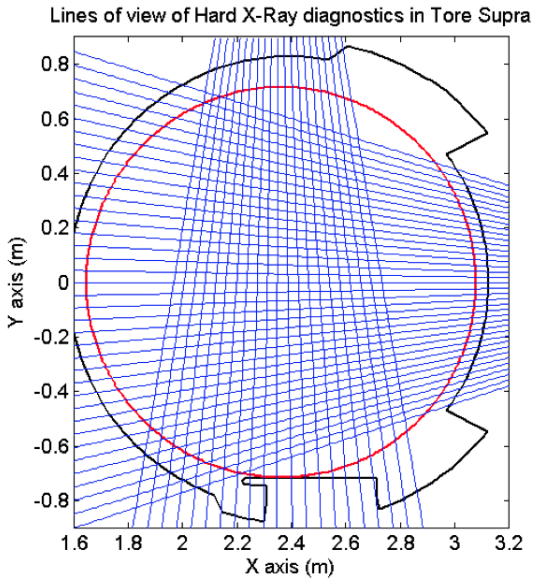


Figure 7.3: Schematic view of the hard X-ray tomographic system in Tore Supra. Blue lines show the lines of sight of the detectors, also called chords.

7.2.1 FEB reconstruction (R5X2)

Diagnostic for the fast electron physics in the Tore Supra tokamak is provided by fast electron Bremsstrahlung (FEB) emission measured by the HXR cameras. The HXR signal detected from vertical (chords $1-21$) and horizontal lines of sights (chords $22-59$) consisting of cadmium telluride (CdTe) detectors and provide information on the suprathermal electron population. Each detector measures the signal in a poloidal section of the plasma, integrated along the line of observation, see Fig. 7.3. Given the detector response function, a count rate signal is retrieved for each chord. The two cameras view the same circular and concentric plasma, which ideally would give similar count rate amplitude and profile from the two cameras. The vertical camera views the limiter, which may add background radiation under certain circumstances.

A synthetic diagnostic of the bremsstrahlung emission from suprathermal electrons by the code R5X2 allows for a direct comparison of simulations with experimental FEB emission. A unique reconstruction of the electron distribution from the measured FEB emission is not possible due to the mixing between angular, radial and momentum dependence of the fast electron tail [68]. The ill-conditioned character of this problem makes R5X2 an important synthetic tool, yielding a line integrated emission from the electron distribution based on the specifications of the HXR tomographic detection system [76].

The code R5X2 reconstructs the local emissivity of non-thermal bremsstrahlung from fast electrons in an arbitrary axisymmetric magnetic configuration using Legendre polynomial decomposition. Bremsstrahlung emission in the HXR photon energy lies in the energy range $30-200$ keV. In R5X2 the bremsstrahlung emission is reconstructed as a function of chord number, yielding an output which is directly comparable to the experimental HXR data.

7.2.2 Discharge #40719

An additional signature of the runaway electron population is the remaining current (~ 50 kA) at $15.7-16$ seconds, at the termination of the plasma as seen in Fig. 5.13a. This remaining current plateau could originate from a beam of well confined runaway electrons. Such a current is not observed in the higher density discharge (#40721).

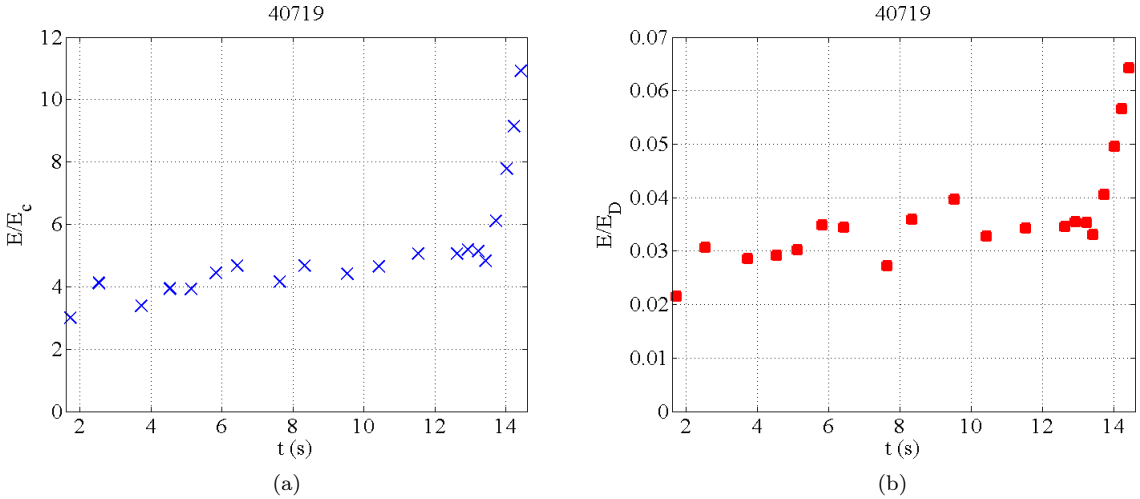
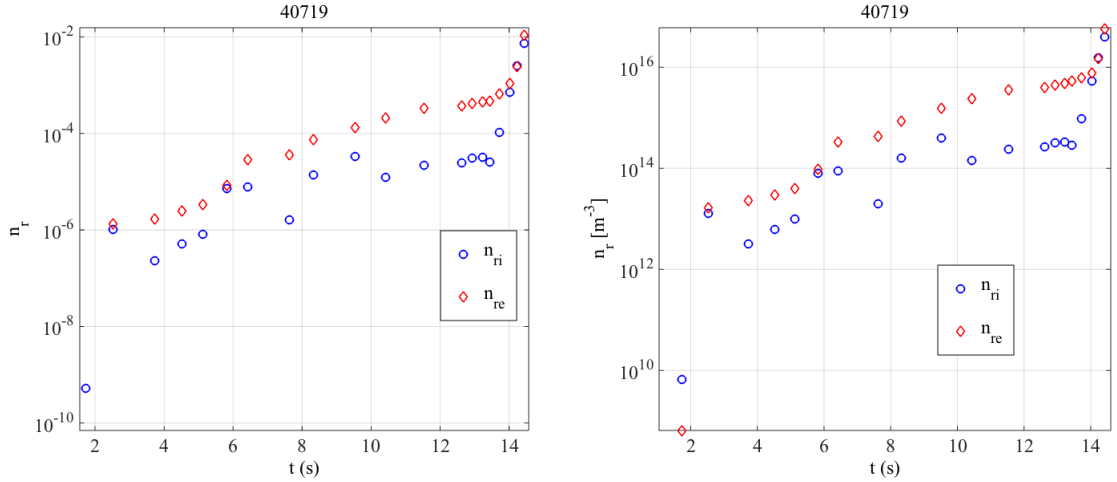


Figure 7.4: Central electric field evolution calculated with the METIS code, normalized to E_c (a) and E_D (b) in discharge #40719.

The central electric field evolution as calculated by METIS normalized to E_c and E_D are shown in Fig. 7.4. For #40719 the METIS/LUKE simulations show that runaway electrons are progressively formed during the current flattop (Fig. 7.5), concentrated near the magnetic axis. Even though the density is lower off-axis and the E-field profile is rather flat, E/E_D decreases with the radius due to the temperature profile. This would explain the slower Dreicer generation off the magnetic axis. Also, the increase of magnetic trapping effects off-axis contributes to a reduced runaway rate, as shown in Chap. 6. The simulations predict a fast build up of suprathermal electrons, see Fig. 7.6a.

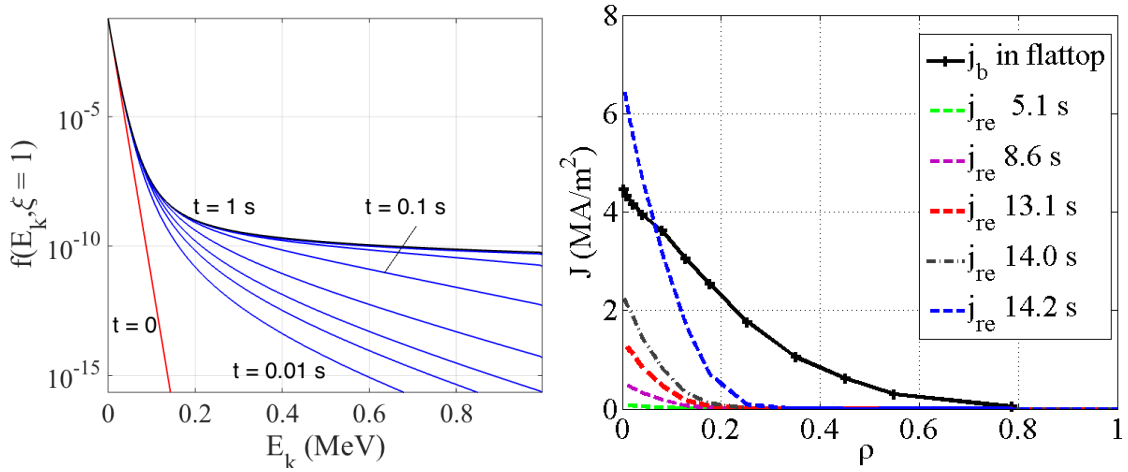
Figure 7.6b shows the calculated current density profile as carried by external runaway electrons (with kinetic energy ($E_k > 1$ MeV), when assuming that they move at the speed of light, compared to the current density profile of the bulk. The calculated Ohmic plasma current in the flattop at 13 s is 0.54 MA, compared to the experimental plasma current of 0.55 MA. To match the plasma currents, the effective charge had to be reduced from the one used in METIS ($Z_{eff} = 3.9$) to $Z_{eff} = 2.6$.

At the end of the current flattop the METIS/LUKE predicted current carried by external runaway electrons ($E_k > 1$ MeV) is 33 kA, which is consistent with the level of remaining current ($I_p = 50\,\mathrm{kA}$) likely carried by a well confined beam of runaway electrons, as observed in the termination of the plasma (Fig. 5.15). It is possible that runaway electrons are lost during the current (and density) ramp-down, but 50 kA may be considered as a lower estimate of the runaway electron current at the end of the current flattop. The HXR reconstruction with R5X2 in the energy range $50 - 110\,\mathrm{keV}$ is compared with the experimental count rate profile in Fig. 7.7. LUKE simulations predict a runaway electron population concentrated near the magnetic axis. The shape and amplitude of reconstructed FEB emission shows reasonable agreement with measurements.



(a) (b)

Figure 7.5: Internal (n_{ri}) and external (n_{ri}) runaway electron population, normalized to bulk density (a) and unnormalized (b).



(a) Electron distribution function at $\xi = 1$ in current flattop during 1 s.

(b) Current density of bulk (black) and current density carried by runaway electrons ($E_k > 1\,\mathrm{MeV}$).

Figure 7.6: Modelling results from TS discharge #40719.

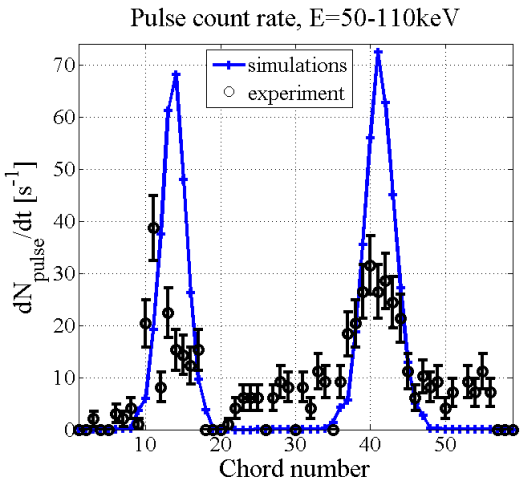


Figure 7.7: Reconstructed FEB profile in discharge #40719, compared to measured FEB emission from HXR cameras.

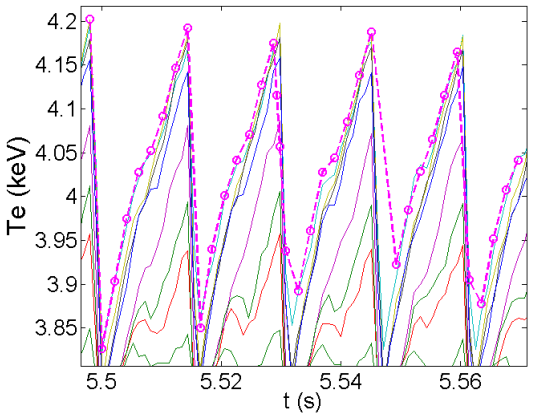


Figure 7.8: Sawteeth in discharge #40719 seen on ECE measurements. The dashed/circled line shows the temperature data points used for CRONOS simulations.

Data analysis of sawtooth activity

In #40719 there is a signature of sawteeth, likely due to the low density. The thermal collision time at the electron temperature minima is 85% of the collision time at the maxima. The generation of suprathermal electrons during sawtooth crashes in the TCV tokamak were investigated in Ref. [77].

The sawteeth oscillations are not accounted for in the METIS simulations, but with the CRONOS code the oscillating electron temperature can be included; at least for a part of the discharge (see Fig. 7.8). In order to investigate the effect of oscillating temperature and electric field strength, LUKE simulations are performed with core plasma modelled by CRONOS. Given an initial seed, from METIS/LUKE simulations for the same discharge, at the starting time of the CRONOS/LUKE simulations the effect of the oscillating temperature and electric field strength is investigated. The simulations show no direct correlation between the sawteeth crashes and runaway electron formation. The influence of the sawteeth on suprathermal electrons and runaway electrons requires further studies.

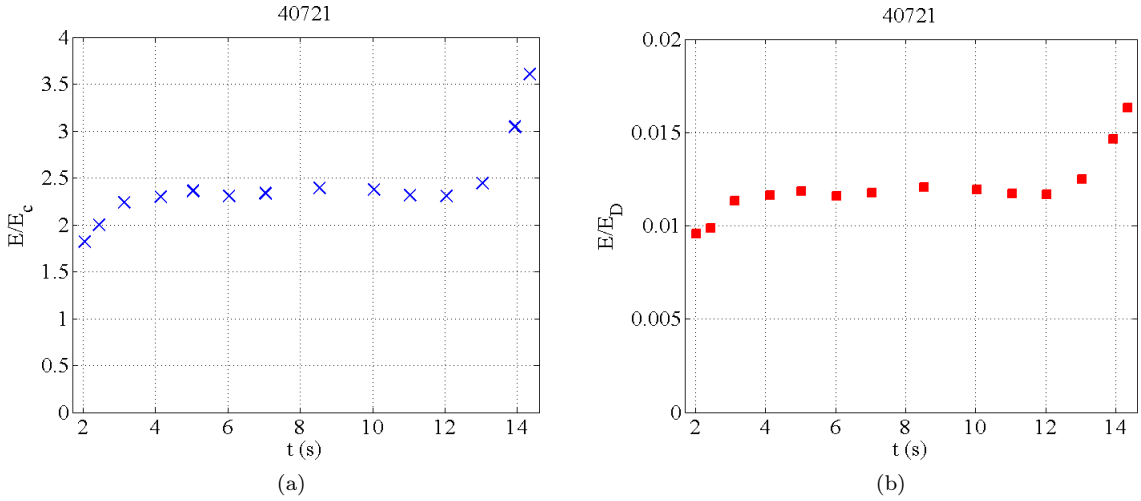


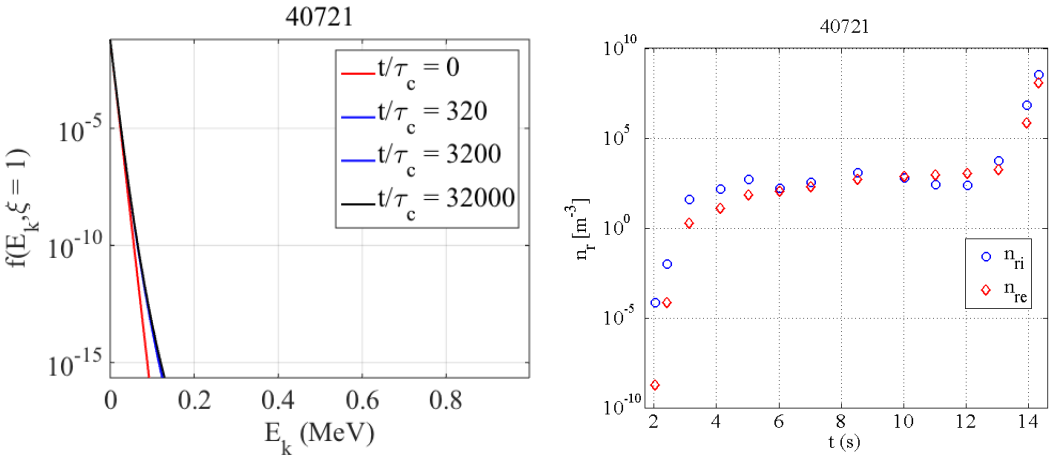
Figure 7.9: Central electric field evolution calculated with the METIS code, normalized to E_c (a) and E_D (b) in discharge #40721.

7.2.3 Discharge #40721

Helium is injected in this discharge, which is taken into account in the METIS simulations where including helium in the impurities induces a small change in the ion temperature. The on-axis electric field strength as calculated by METIS, normalized to E_c and E_D are presented in Fig. 7.9.

With METIS/LUKE simulations we can investigate whether suprathermal electrons are formed also in the discharge without experimental runaway signature (#40721), where $E > E_c$. The METIS/LUKE simulations show that only a small population of suprathermal electrons is formed during this pulse (see Fig. 7.10a and 7.10b). The simulation of #40721 confirms the experimental observations; the runaway production is negligible as the simulations show that the population of suprathermal electrons is formed during this pulse is negligible. In addition, the reconstructed FEB signal is close to zero, as seen on the experimental measurements (Fig. 7.11). The external runaway electron population, i.e. electrons with kinetic energy $E_k > 1$ MeV, is so small that it would only carry a current of around 5 mA at the end of the 10 seconds long current flattop.

The study predicts that, for an initial Maxwellian distribution function, 10 seconds of $E/E_c \approx 2.5$ is not sufficient for a significant runaway electron population to form in a 3 keV plasma. This result is consistent with the parametric study of runaway formation performed in Sec. 5.2 (Fig. 5.10), where it is found that 10 seconds of local electric field strength $E/E_c \approx 2.5$ is not sufficient for a significant runaway electron population to form in a 3 keV plasma. Furthermore, these results support the experimental observations of Ref. [6] where at least $E/E_c \sim 3 - 12$ is required to generate a detectable population of runaway electrons in various tokamaks.



(a) Electron distribution function at $\xi = 1$ in current flattop during 1 s.

(b) Internal (n_{ri}) and external (n_{ri}) runaway electron population.

Figure 7.10: Modelling results from TS discharge #40721.

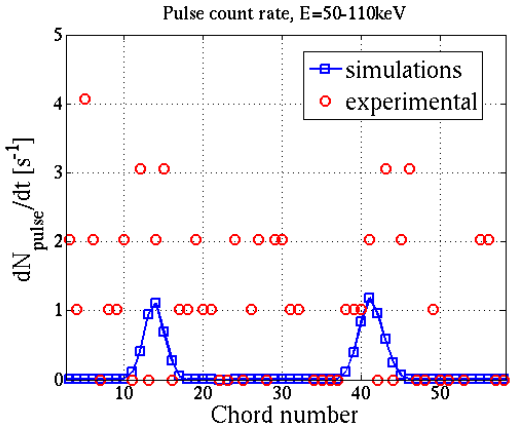
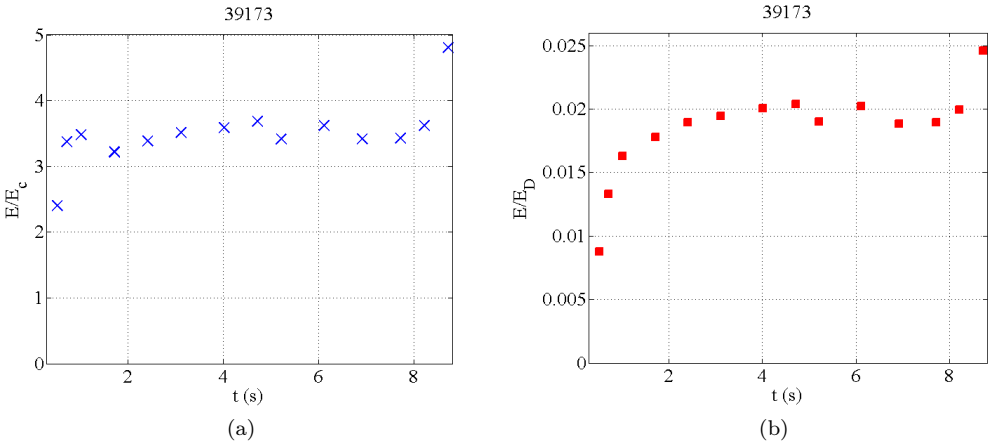


Figure 7.11: No HXR emission is predicted by LUKE, in agreement with experimental measurements.

7.2.4 Discharge #39173

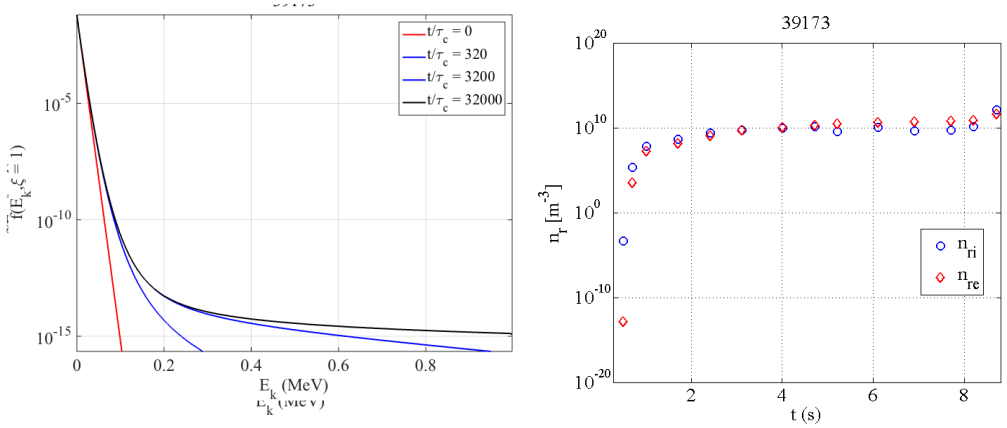
A discharge with density between those of #40719 and #40721 has also been modelled. The plasma current is 0.6 MA and line averaged electron density is $0.92 \cdot 10^{19}\ m^{-3}$. No sawteeth oscillations are observed. As expected E/E_c and E/E_D are of intermediate values to the two other Tore Supra discharges, the central values as predicted by METIS are seen in Fig. 7.12. No signatures of runaway electrons are seen on the HXR or ECE signals.

The METIS/LUKE simulations show a build up of a suprathermal population as seen on the distribution function (Fig. 7.13a), but the external runaway electron population remains very low throughout the discharge (Fig. 7.13b). Likely this low level of runaway electrons is beyond the detection limits of the diagnostics.



(a) (b)

Figure 7.12: Central electric field evolution as calculated by the METIS code, normalized to E_c (a) and E_D (b) in discharge #39173.



(a) Electron distribution function at $\xi = 1$ in current flattop during 1 s.

(b) Internal (n_{ri}) and external (n_{ri}) runaway electron population.

Figure 7.13: Modelling results from TS discharge #39173.

7.3 COMPASS

The COMPASS tokamak [78, 79] at the Institute of Plasma Physics (IPP) in Prague, Czech Republic is used extensively for runaway electron and disruption experiments [37]. It is a medium size tokamak with major radius of 0.56 m and minor radius of 0.20 m. The plasma can be circular or D-shaped with elongation up to 1.8. The plasma current I_p reaches up to 400 kA.

The discharges with runaway electrons in the current flattop in the COMPASS tokamak are rather different from the Tore Supra discharges. With a typical pulse length of 0.4 s, the discharge duration is much shorter than in Tore Supra, but the electric field relative to the critical field is much higher. The principle diagnostics for detection of runaway losses are NaI(Tl) scintillator detector for HXR emission and a photoneutron detector, positioned about 5 m from the vessel. The photoneutron detectors are more commonly referred to as lead shielded HXR detector as they are covered with 10 cm of lead. Thus, they detect HXR from electrons with around 1 MeV and above [80]. In the campaign of 2015, a Cherenkov detector was installed.

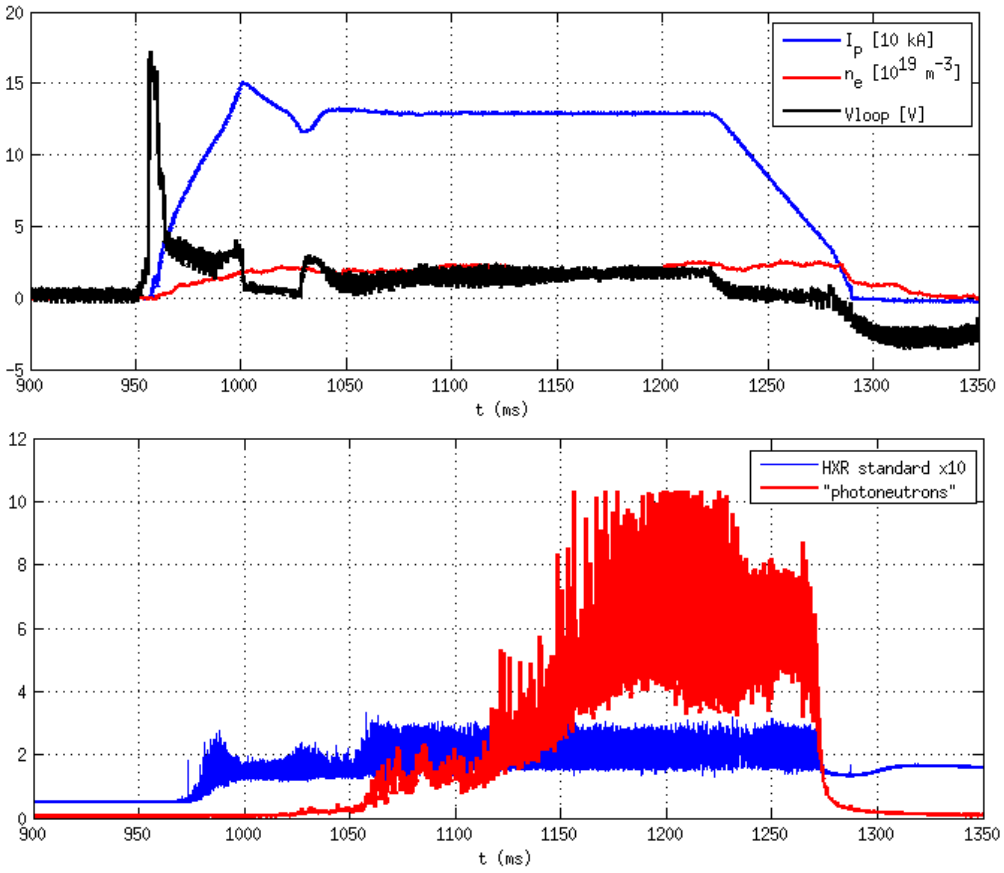


Figure 7.14: Experimental data from COMPASS shot #8555 shows clear signatures of runaway electron losses.

It is placed near the scrape-off layer and is the first diagnostics to detect the runaway electrons. It should be pointed out that the HXR and Cherenkov detectors show the signal of runaway losses, when runaway electrons are ejected from the plasma and strike surrounding structures (the wall for HXR and the detector itself for Cherenkov).

7.3.1 Discharge #8555

The circular 130 kA discharge #8555 (Fig. 7.14) is part of a set of discharges with line averaged electron density $\bar{n}_e$ scan from $1 - 4 \cdot 10^{19}\ m^{-3}$, where $\bar{n}_e$ for this particular shot is $2 \cdot 10^{19}\ m^{-3}$ during the flattop. The raise of runaway losses is observed with HXR NaI(Tl) scintillator and photoneutron detector as the $\bar{n}_e$ decreased from discharge to discharge, while Parail-Pogutse instability appeared for all discharges with $\bar{n}_e$ lower than in the discharge #8555. In COMPASS, interferometry is used for the line averaged electron density measurements, while Thomson scattering is used for electron temperature and electron density profile measurements.

The plasma shape is reconstructed by the equilibrium fitting code EFIT [81, 82], and based on that METIS calculates the equilibrium with this given shape, I_p, $\bar{n}_e$ and Z_{eff}. The on-axis electric field strength calculated by METIS, normalized to E_c and E_D are shown in Fig. 7.15. The METIS/LUKE simulations predict a significant runaway electron population in the flattop (Fig. 7.16 and 7.17). Signature of runaway electrons is found on the HXR detectors in the ramp-up as well as in the current flattop. In the absence of tomographic HXR detection, it is not possible to validate the simulated radial profile of the runaway electrons, but as for the Tore

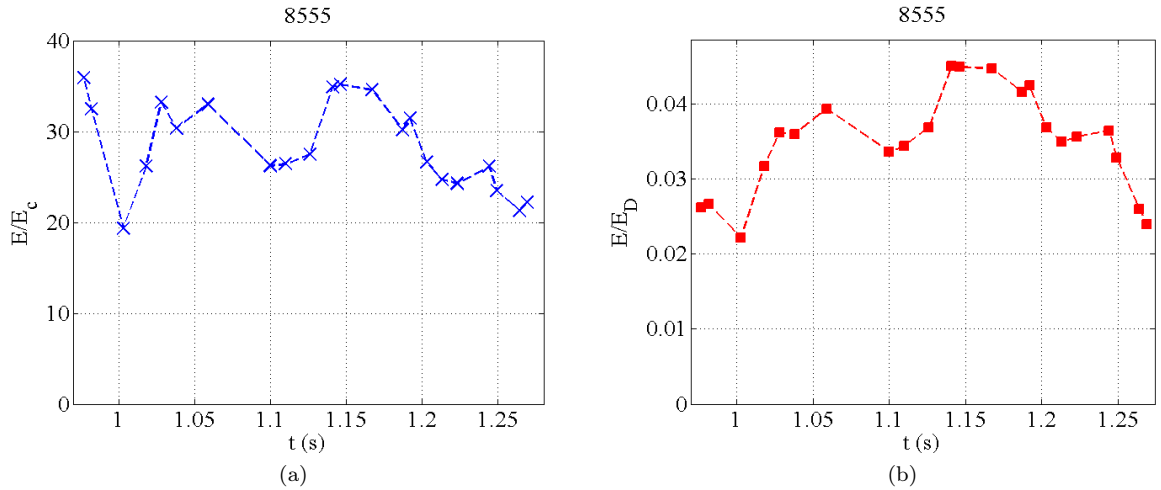


Figure 7.15: Central electric field evolution as predicted by the METIS code, normalized to E_c (a) and E_D (b) in discharge #8555.

Supra scenarios they are found to be centrally concentrated. The calculated current carried by runaway electrons is estimated from the current of the external runaway electrons with velocity near the speed of light which results in a too high I_p. The LUKE simulation overestimates the runaway electron population, as in the end of the discharge, the accumulated runaway electron population would carry a current of 1 MA, i.e. about eight times the flattop plasma current level. Clearly this result is unrealistic. These simulations assume that the runaway electrons are completely confined at the position of formation throughout the entire discharge. Drift losses occur, as seen on the elevated HXR signal in Fig. 7.14. The lack of losses in the model could explain the elevated runaway electron population.

Adding fast electron radial transport in the simulations reduce the runaway current. It is found that with a fast electron radial transport of $D_{r0} = 0.8\ m^2/s$, the current carried by runaway electrons drops to 70 kA, see Fig. 7.18. The transport is added to the suprathermal electrons in the LUKE domain. In other words, the electrons that have already diffused through the upper limit of the momentum grid are not affected by transport in our model. However, increasing the grid from 1 MeV up to 10 MeV, has a negligible effect on the results. This indicates that the runaway electrons are lost owing to transport before they can accelerate to higher energies.

With the large runaway electron population detected in this discharge, there is possibly a need for self-consistent calculations between the current carried by runaway electrons and the toroidal electric field. Such calculations could lead to a smaller and more realistic runaway electron population.

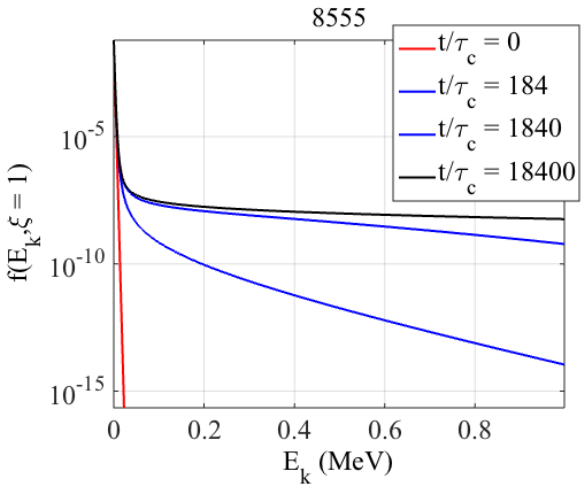
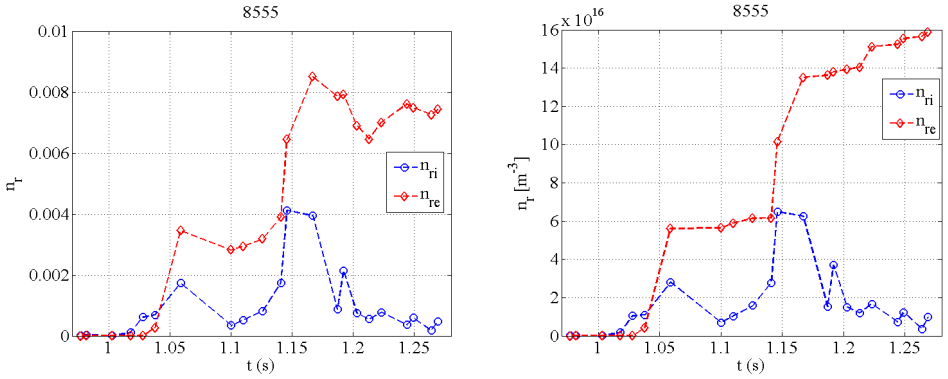
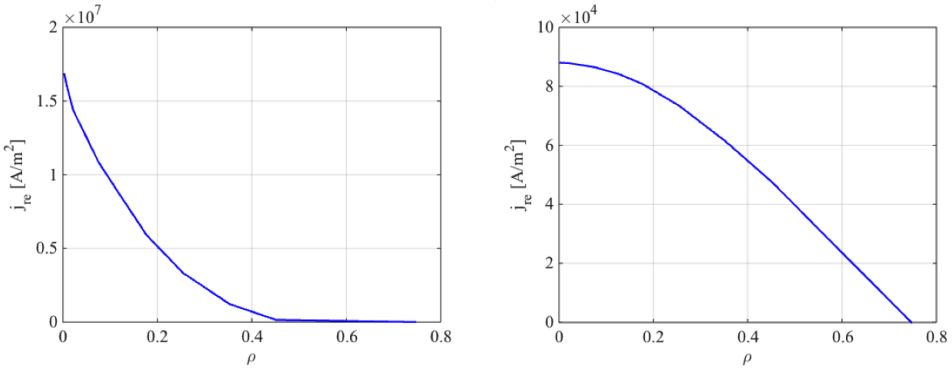


Figure 7.16: Runaway electron formation (a) and electron distribution function at $\xi = 1$ (b) in COMPASS discharge #8555 in current flattop during 0.1 s.



(a) (b)

Figure 7.17: LUKE predicts a significant runaway electron population through discharge #8555.



(a) (b)

Figure 7.18: Current profile carried by external runaway electrons without radial transport (a) and with radial transport ($D_{r0} = 0.8\ m^2/s$) (b) for discharge #8555.

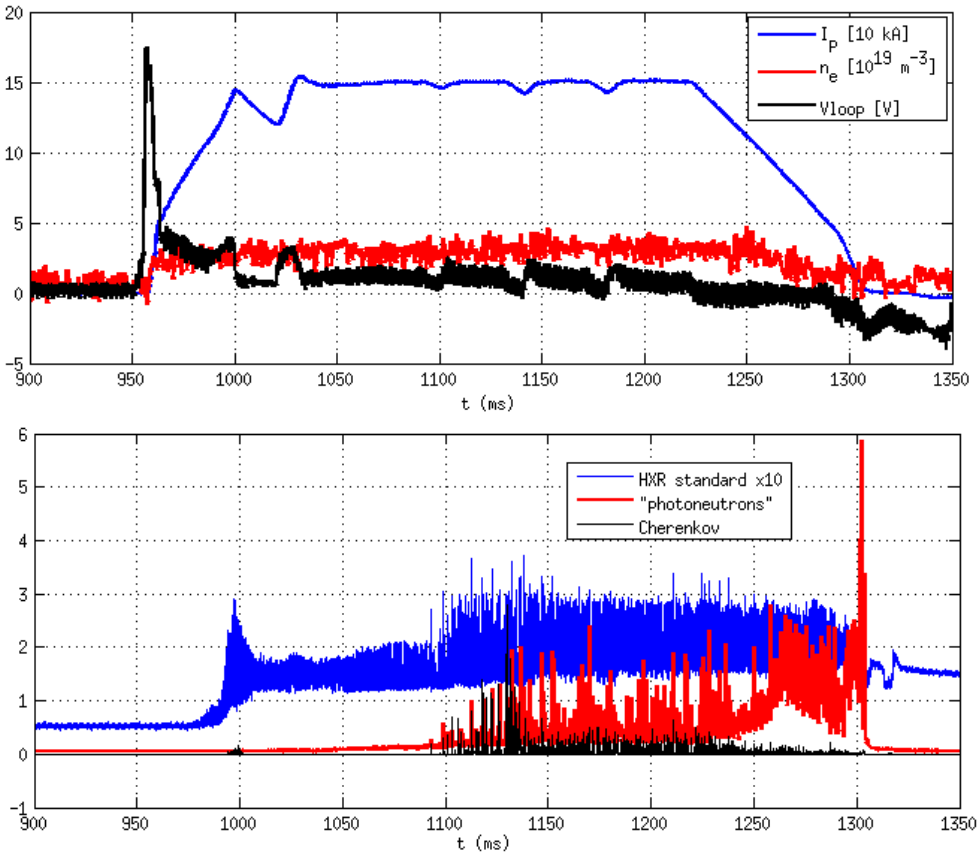


Figure 7.19: Experimental data from COMPASS shot #10007.

7.3.2 Discharge #10007

In this discharge, performed during the COMPASS runaway electron campaign in the spring 2015, the plasma current during flattop is 154 kA and the line averaged density $2.97 \cdot 10^{19}\ m^{-3}$ (Fig. 7.19). The plasma is elongated ($\kappa = b/a = 1.4$, where a is the plasma minor radius and b is the height of the plasma measured from the equatorial plane). During the current flattop the loop voltage is dropped three times.

Comparing #10005 ($\kappa = 1.2$) and #10006 ($\kappa = 1.1$) it is found that in the higher elongation discharge, a stronger MHD activity is observed. The activity decreases during the current drops while runaway electron losses on the shielded HXR are enhanced. This could indicate that runaway electrons are confined inside magnetic islands and released in the current drops when the islands disappear. In other words, changing the MHD activity affects runaway electrons. On the other hand, if there is less MHD activity (#10006), the voltage drops did not affect the runaway loss signal. This could mean that the runaway electrons remain well-confined. Understanding the mechanisms between runaway electrons and plasma elongation would require further studies.

For the LUKE simulations, the internal runaway electron population is very reactive to the change of loop voltage as seen in Fig. 7.20. The loop voltage drops and flattening in the evolution of the external runaway populations are also found to be correlated.

As for the other discharges, LUKE predicts a runaway electron population concentrated near the magnetic axis (Fig. 7.21). In this case, the runaway signals are lower than for the #8555 discharge. The LUKE calculated current is on a more reasonable order as the current

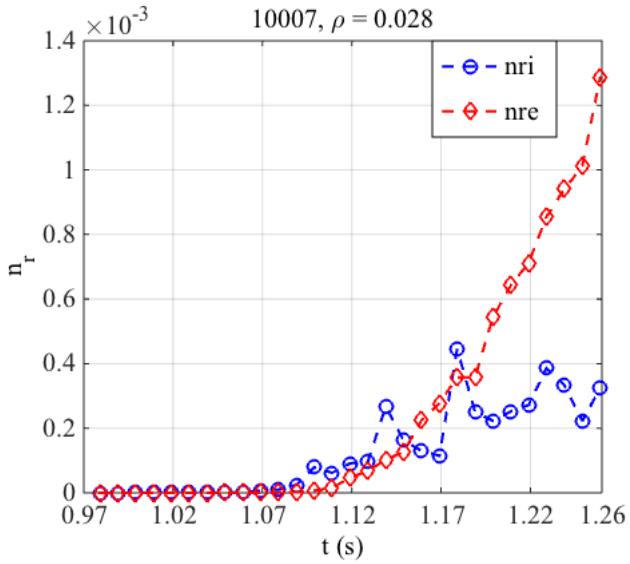
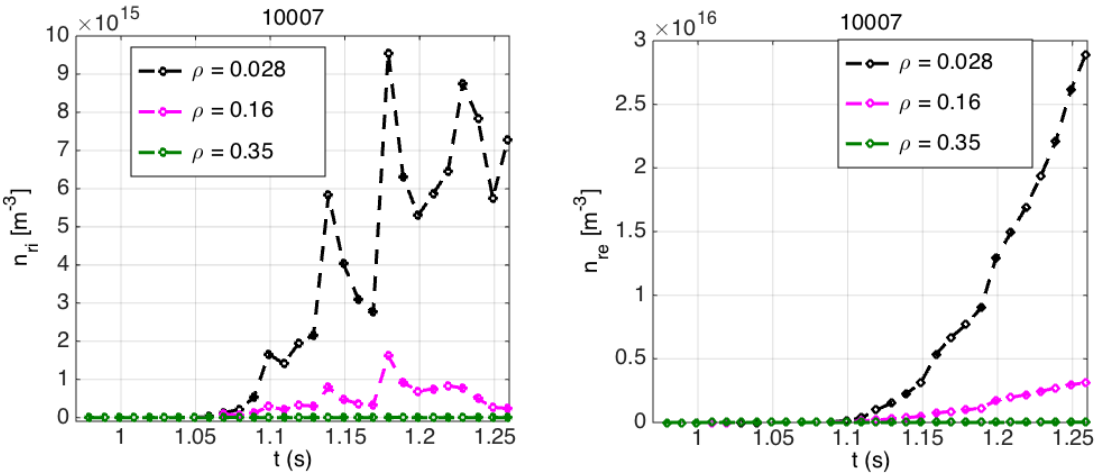


Figure 7.20: Evolution of external and internal runaway electron population, normalized to reference density.



(a) (b)

Figure 7.21: Simulation results at three radial positions; $\rho = 0.028, 0.16, 0.35$.

carried by runaway electrons reaches around 70 kA at the most (Fig. 7.22) compared to the total plasma current (154 kA).

7.3.3 Plasma elongation scan

The COMPASS discharge #10007 is part of a plasma elongation scan, in the range $\kappa = 1.0-1.4$. The ramp-up phases of plasma current are equivalent and the discharge specific shaping are applied in the beginning of the current flattop. The measured runaway losses (Fig. 7.23) indicate that the runaway electrons are somehow better confined in elongated plasmas. In the lower elongation plasmas we see runaway electrons escaping during the entire discharge while in elongated plasmas they are ejected at ramp-down (#10008).

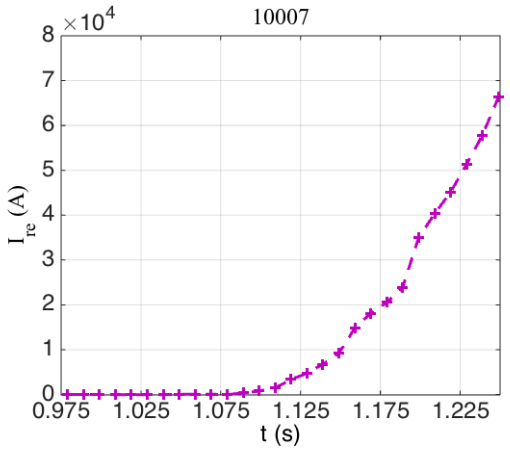


Figure 7.22: Evolution of current carried by runaway electrons with $E_k > 1$ MeV.

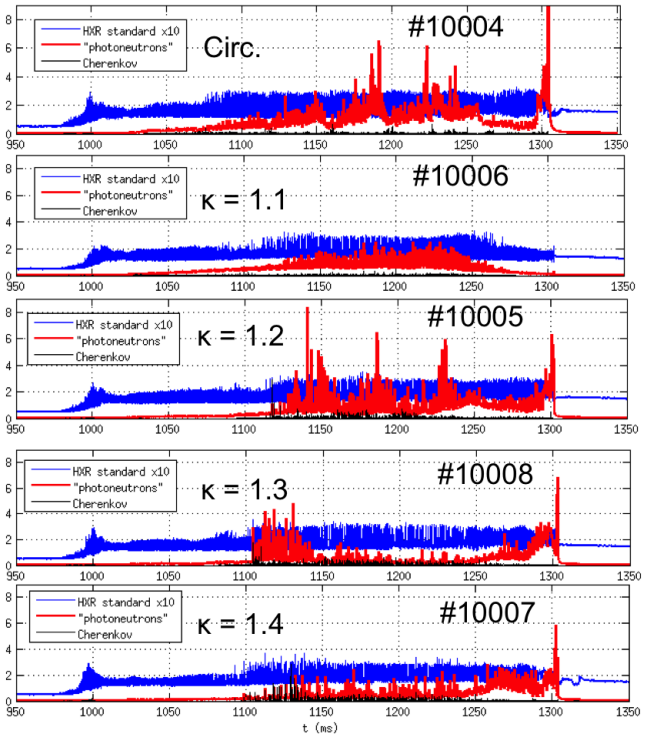


Figure 7.23: Runaway losses for discharges with different elongation during the current flattop.

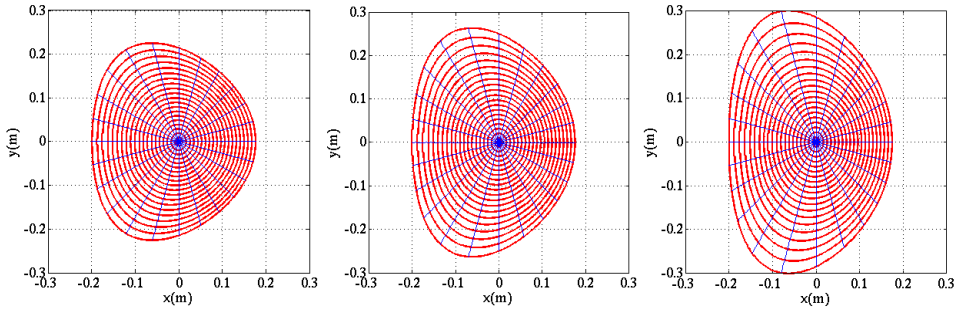


Figure 7.24: Magnetic geometry calculated by METIS for κ=1.2,1.4 and 1.6.

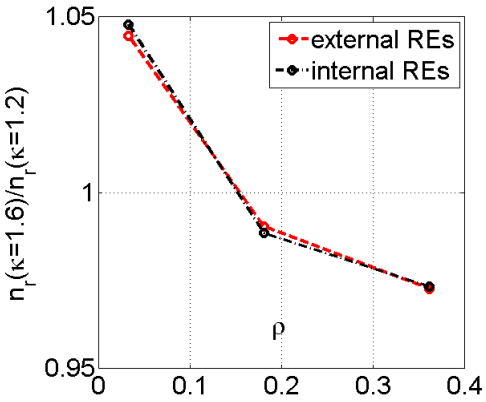


Figure 7.25: There is slightly more runaway electrons generated centrally for the higher elongation case but less off-axis than for the less elongated magnetic geometry.

MHD instabilities (i.e. magnetic islands) associated with the elongation could explain the different confinement of the runaway electrons. In order to investigate whether also the runaway formation processes depend on elongation, LUKE simulations are performed for various elongations based on the COMPASS scenarios. Different elongation also lead to slightly different density, temperature and electric field profiles. Therefore, in order to study the effect of elongation identical profiles are assumed and only the magnetic geometry is different (Fig. 7.24).

It is found that the predicted runaway formation does not differ much between the different elongations. At the end of the discharge there is very marginal difference, only a few percent, in the runaway electron population between $\kappa = 1.6$ and $\kappa = 1.2$. Higher elongation implies more runaway electrons near the center but less runaway electrons away from the center, as shown in Fig. 7.25.

The conclusion is that the magnetic geometry itself does not influence the runaway formation processes significantly. Likely the dependencies of elongation in plasma parameters (density, temperature and electric field profile) are important for the runaway formation processes.

7.4 Summary of modelling of non-disruptive scenarios

The Fokker-Planck solver LUKE is used to model runaway electron formation through Dreicer and avalanche mechanisms in non-disruptive Tore Supra scenarios in near-critical E-field with the background plasma simulated with the METIS code. Three non-disruptive Tore Supra scenarios with $E > E_c$ are studied. Simulations reveal progressive build-up of a suprathermal electron population during the flattop in the discharge where runaway electrons are detected (#40719) with $E/E_c \approx 8$, but not in the higher density discharge (#40721) where $E/E_c \approx 4$. A discharge with intermediate density and E/E_c (#39173) is studied. No clear signature of runaway electrons is observed and the LUKE simulations predict only a small suprathermal population, that is likely too small to be detected by the HXR cameras. These results agree with experimental observations from various other tokamaks [6] where it is found that at least $E/E_c \approx 3 - 12$ is required for a detectable runaway electron population to form. The order of magnitude of the current carried by runaway correspond well to experimental indications. The profile of the reconstructed FEB emission from suprathermal electrons is in reasonable agreement with measurements and shows concentration of runaway electrons in the center of the plasma.

A common point for all these non-disruptive discharges is that runaway electrons are mainly formed near the magnetic axis. Even though the density is lower off-axis, so is the temperature which makes E/E_D decreases with the radius. This would explain the slower Dreicer generation. Also, as discussed in Chapter 6, magnetic trapping effects increase off-axis, adding further to the slower Dreicer generation rate.

LUKE/METIS modelling is also performed for non-disruptive COMPASS discharges. These results are more difficult to validate due to the absence of tomographic HXR diagnostics. Several non-disruptive scenarios have been modelled. One of them (#8555) results in unrealistically high runaway fraction when no runaway loss mechanisms are taken into account. In such scenarios, where the runaway current is more than just a perturbation of the Ohmic current, the toroidal electric field should be calculated self-consistently with the runaway electron population. Such a self-consistent coupling between METIS and LUKE will be the next step in this work. When adding radial transport of fast electrons in the model, the predicted current carried by runaway electrons decreases rapidly. A reasonable level of current is found for a transport coefficient of $D_{r0} = 0.8\ m^2/s$. However, in runaway scenarios with less runaway electron population (#10007), the order of magnitude of the current that would be carried by energetic runaway electrons is on a reasonable order of magnitude even without any effect of radial transport.

Chapter 8

Conclusion

In this work formation of runaway electrons is studied through modelling of the electron distribution function under the combined influence of Dreicer and avalanche mechanisms. Runaway avalanches are described with a knock-on source term from the work of Rosenbluth and Putvinski [5], implemented as a bounce-averaged particle conserving source/sink term within the kinetic equation in the 3-D Fokker-Planck solver LUKE. Dependencies of key parameters such as electric field strength, electron temperature and density are investigated. It is found that under certain conditions the knock-on collisions leading to runaway electron avalanches amplify the conventional Dreicer generation in such a way that avalanches born runaway electrons dominate over Dreicer generated runaway electrons at low electron temperatures and low E/E_c, i.e. near critical field scenarios. In these scenarios a valid description of runaway electron formation processes therefore require inclusion of knock-on processes.

Since knock-on accelerated electrons emerge with high perpendicular momentum, the full 2-D guiding-center momentum dynamics is taken into account in the model, numerically manageable through a bounce-averaged description. Given the inhomogeneity of the magnetic field in toroidal plasmas, electrons that would contribute to the runaway population if the plasma was cylindrical may be trapped poloidally. The magnetic mirror effect is investigated, revealing strong reduction of both Dreicer and avalanche mechanisms off the magnetic axis. An analytical approximation for avalanche growth rate accounting for magnetic trapping is derived. A good agreement is found with numerical simulations performed with the LUKE code, which shows that a significant proportion of secondary electrons are knocked into the trapped region off the magnetic axis and therefore do not contribute directly to the runaway population. As a consequence the time scale of runaway electron formation is longer at the plasma edge than at the center. It means that potential loss mechanisms such as radial electron transport could compete with the acceleration of runaway electrons at the edge as there is more time for loss mechanisms to act on these runaway electrons.

The fate of the trapped electrons is also investigated analytically and the trapped-electron runaway effect is identified as detrapping of trapped energetic electrons as they Ware pinch towards the magnetic axis and less strict trapping conditions. Key parameters that distinguish these runaway electrons are calculated, namely the large perpendicular energy, the dependency of the perpendicular energy on radius, and the turn-on time for the appearance of the runaway electrons. We identified when these effects might be expected (in the case of positrons) and when they would be absent (in the case of RF ramp-up). Possible observables would be based on signals sensitive to perpendicular energy, such as synchrotron radiation. Similarly, the degree of manipulation by waves or magnetic perturbations is also sensitive to perpendicular energy.

The kinetic modelling of the formation of runaway electrons with the model is restricted to non-disruptive scenarios as may be found in the current flattop with non-transient electric field and plasma temperature. In the LUKE code, the magnetic flux surfaces are assumed to remain intact and concentric throughout the runaway electron formation process. The difficult task

of modelling the transient temperature and electric field typically found in disruptions would require a proper description of the thermal quench with implemented radiative or convective loss mechanisms of the plasma energy including MHD instabilities. The coupling of the kinetic LUKE code with a fluid code such as JOREK [29] would be useful for such a purpose, but is beyond the scope of this work. At the present the model, in which the flux surfaces are assumed to remain intact during the runaway electron formation process, can be considered to give an upper estimate of the runaway formation, since possible additional losses from magnetic field stochastization that may reduce the confinement of the electrons are not accounted for.

Moreover, quantifying the relative importance of avalanche generation as a function of plasma temperature and electric field strength, the simulations reveal that runaway electrons originating from knock-on collisions completely dominate over the Dreicer effect at low temperature and electric field strength and likely play a significant role in runaway generation processes in several tokamaks in non-disruptive scenarios that are presented in Ref. [6]. The onset of runaway electrons found in these experiments are related to LUKE simulations of corresponding electric field and temperature in order to gauge the importance of the avalanche effect, revealing that avalanches from knock-on collisions play a significant role even in non-disruptive scenarios.

The compilation of runaway electrons detected in non-disruptive scenarios from Ref. [6] in five different tokamaks (DIII-D, FTU, TEXTOR, Alcator C-Mod and KSTAR) is related to LUKE simulations of corresponding electric field and temperature in order to investigate the importance of the avalanche effect. In addition a low density scenario from the Tore Supra tokamak, where suprathermal electrons are detected across several diagnostics when $E/E_c = 11$ shows agreement with this study that suggests that $E/E_c = 3 - 12$ is required for a detectable runaway electron population to form.

The LUKE calculations predict runaway electron generation also in a near critical field, in agreement with collisional theory if no other runaway electron loss mechanisms than collisional damping are present. However, the time to generate runaway electrons is found to be significantly large compared to the duration of the phase in which $E/E_c > 1$ in near critical field experiments. In addition, the required time for runaway electron formation is very sensitive to the bulk electron temperature. The lack of runaway electron signatures near the critical electric field could therefore be explained by the long time scale required for their formation given a Maxwellian initial distribution function. To further understand the discrepancy between observations and theory, the existence of additional loss mechanisms that dominate during the current flattop must be addressed. One possible candidate is transport of fast electrons due to magnetic field perturbations [41]. Once such additional runaway electron loss mechanisms have been identified, the LUKE code may form an excellent test bed for quantifying such effects, which will be the objective of future work.

Finally, the modelling is applied to real tokamak scenarios. With equilibria obtained from METIS simulations, interpretative modelling is performed for non-disruptive scenarios where runaway electrons are detected in the current flattop in discharges from the Tore Supra and COMPASS tokamak. Simulations show progressive build-up of a suprathermal population during the flattop in the discharge where runaway electrons are detected (#40719), but not in the higher density discharge (#40721) where $E/E_c \approx 4$. Also a discharge with intermediate density and E/E_c (#39173) is studied. No clear signature of runaway electrons is observed and the LUKE simulations predict only a small suprathermal population, that is likely too small to be detected by the HXR cameras. These results agree with experimental observations from various other tokamaks [6] where at least $E/E_c \approx 3 - 12$ is required for a detectable runaway population to form. The order of magnitude of the current carried by runaway electrons correspond well to experimental indications. The reconstructed FEB emission profile from suprathermal electrons shows concentration of runaway electrons in the center of the plasma. It is in good agreement with experimental measurements.

LUKE/METIS modelling is also performed for non-disruptive COMPASS discharges. These results are more difficult to validate due to the absence of tomographic HXR diagnostics. Several

non-disruptive scenarios have been modelled. In one of them (#8555) the current carried by runaway electrons quickly dominates the Ohmic current, resulting in unrealistically high runaway fraction when no runaway loss mechanisms are taken into account. In such scenarios, where the runaway current is more than just a perturbation of the Ohmic current, the toroidal electric field should be calculated self-consistently with the runaway population. Such a self-consistent coupling between METIS and LUKE will be the next step in this work. When adding radial transport of fast electrons in the model, the predicted current carried by runaway electrons decreases rapidly. A reasonable level of current is found for a transport coefficient of $D_{r0} = 0.8\ m^2/s$. However, in runaway scenarios with less runaway population (#10007), the order of magnitude of the current that would be carried by energetic runaway electrons is on a reasonable order of magnitude even without the effect of radial transport.

A common point for all the non-disruptive discharges is that runaway electrons are found to form near the magnetic axis. The density is lower off-axis, which for a flat electric field profile makes E/E_c increase away from the magnetic axis. Since also the temperature is centrally peaked in the scenarios we model, E/E_D decreases with the radius. The temperature dependence would explain the slower formation of runaway electrons from the Dreicer mechanism. Also, as discussed in Chapter 6, magnetic trapping effects increase off-axis, adding further to the slower Dreicer generation rate and concentration of runaway electrons near the magnetic axis.

The LUKE/METIS simulations allow for investigation of the effect of plasma shaping effects on the runaway electron formation. In the spring of 2015 several similar discharges but with different elongation during the current flattop were carried out in the experimental campaign of the COMPASS tokamak. It appears as the runaway electrons are better confined in elongated plasmas. In the lower elongation plasmas runaway electrons losses occur during the entire discharge while in elongated plasmas they are ejected first in the current ramp-down. Only a marginal difference in the runaway electron formation processes is found for the different elongation scenarios in LUKE, given plasmas with identical density, temperature and electric field profiles and only different magnetic geometry. Likely consequences of the shaping on other plasma profiles or MHD instabilities such as magnetic islands play an important role for the formation or/and the confinement of the suprathermal electrons.

Bibliography

[1] T. Fülöp, G. Papp, and I. Pusztai. Fusion energy lecture notes. January 2012.

[2] *Fusion For Energy*. `http://fusionforenergy.europa.eu/understandingfusion/`.

[3] E.M. Hollmann, P.B. Parks, D.A. Humphreys, N.H. Brooks, N. Commaux, N. Eidietis, T.E. Evans, R. Isler, A.N. James, T.C. Jernigan, J. Munoz, E.J. Strait, C. Tsui, J. Wesley, and J.H. Yu. Effect of applied toroidal electric field on the growth/decay of plateau-phase runaway electron currents in DIII-D. *Nucl. Fusion*, 51:103026, 2011.

[4] R.M. Kulsrud, Y.-C. Sun, N.K. Winsor, and H.A. Fallon. Runaway electrons in a plasma. *Phys. Rev. Lett.*, 31(11):690–693, 1973.

[5] M.N. Rosenbluth and S.V. Putvinski. Theory for avalanche of runaway electrons in tokamaks. *Nucl. Fusion*, 37(10):1355–1362, 1997.

[6] R. S. Granetz, B. Esposito, J. H. Kim, R. Koslowski, M. Lehnen, J. R. Martin-Solis, C. Paz-Soldan, T. Rhee, J. C. Wesley, and L. Zeng. An ITPA joint experiment to study runaway electron generation and suppression. *Phys. of Plasmas*, page 072506, 2014.

[7] J. Decker and Y. Peysson. DKE: A fast numerical solver for the 3D drift kinetic equation. report EUR-CEA-FC-1736, Euratom-CEA, 2004.

[8] J.P. Freidberg. *Plasma Physics and Fusion Energy*. Cambridge University Press, 2007.

[9] JET Team. Fusion energy production from a deuterium-tritium plasma in the JET tokamak. *Nucl. Fusion*, 32(2), 1992.

[10] *ITER organization*. `https://www.iter.org`.

[11] S. Ejima, R.W. Callis, J.L. Luxon, R.D. Stambaugh, T.S. Taylor, and J.C. Wesley. Volt-second analysis and consumption in Doublet III plasmas. *Nucl. Fusion*, 22:1313, 1982.

[12] W.A. Houlberg. Volt-second consumption in tokamaks with sawtooth activity. *Nucl. Fusion*, 27(6), 1989.

[13] P. Helander and D.J. Ward. Positron creation and annihilation in tokamak plasmas with runaway electrons. *Phys. Rev. Lett.*, 90(13), 2003.

[14] T. Fülöp and G. Papp. Runaway positrons in fusion plasmas. *Phys. Rev. Lett.*, 108:225003, 2012.

[15] T. C. Hender, J.C Wesley, J. Bialek, A. Bondeson, A.H. Boozer, R.J. Buttery, A. Garofalo, T.P Goodman, R.S. Granetz, Y. Gribov, O. Gruber, M. Gryaznevich, G. Giruzzi, S. Günter, N. Hayashi, P. Helander, C.C. Hegna, D.F. Howell, D.A. Humphreys, G.T.A. Huysmans, A.W. Hyatt, A. Isayama, S.C. Jardin, Y. Kawano, A. Kellman, C. Kessel, H.R. Koslowski, R.J. La Haye, E. Lazzaro, Y.Q. Liu, V. Lukash, J. Manickam, S. Medvedev,

V. Mertens, S.V. Mirnov, Y. Nakamura, G. Navratil, M. Okabayashi, T. Ozeki, R. Paccagnella, G. Pautasso, F. Porcelli, V.D. Pustovitov, V. Riccardo, M. Sato, O. Sauter, M.J. Schaffer, M. Shimada, P. Sonato, E.J. Strait, M. Sugihara, M. Takechi, A.D. Turnbull, E. Westerhof, D.G. Whyte, R. Yoshino, H. Zohm, the ITPA MHD, Disruption, and Magnetic Control Topical Group. MHD stability, operational limits and disruptions. *Nucl. Fusion*, 47:S128–S202, 2007.

[16] R. Jaspers, K.H. Finken, G. Mank, F. Hoenen, J.A. Boedo, N.J.L. Cardozo, and F.C. Schuller. Experimental investigation of runaway electron generation in TEXTOR. *Nucl. Fusion*, 33(12):1775, 1993.

[17] M. Lehnen, A. Alonso, G. Arnoux, N. Baumgarten, S.A. Bozhenkov, S. Brezinsek, M. Brix, T. Eich, S.N. Gerasimov, A. Huber, S. Jachmich, U. Kruezi, P.D. Morgan, V.V. Plyusnin, C. Reux, V. Riccardo, G. Sergienko, M.F. Stamp, and JET EFDA contributors. Disruption mitigation by massive gas injection in JET. *Nucl. Fusion*, 51(12):123010, 2011.

[18] M. Lehnen, S.S. Abdullaev, G. Arnoux, S.A. Bozhenkov, M.W. Jakubowski, R. Jaspers, V.V. Plyusnin, V. Riccardo, and U. Samm. Runaway generation during disruptions in JET and TEXTOR. *Journal of Nucl. Materials*, 390-391, 2009.

[19] E. M. Hollmann, P. B. Aleynikov, T. Fülöp, D. A. Humphreys, V. A. Izzo, M. Lehnen, V. E. Lukash, G. Papp, G. Pautasso, F. Saint-Laurent, and J. A. Snipes. Status of research toward the ITER disruption mitigation system. *Phys. of Plasmas*, 22:021802, 2015.

[20] H. Dreicer. Electron and ion runaway in a fully ionized gas. I. *Phys. Rev.*, 115(2):238–249, 1959.

[21] J. W. Connor and R. J. Hastie. Relativistic limitations on runaway electrons. *Nucl. Fusion*, 15:415–424, 1975.

[22] M.D. Kruskal and I.B. Bernstein. On the theory of runaway electrons. Report MATT-Q-20, PPPL, Princeton University, 1962.

[23] A.V. Gurevich. On the theory of runaway electrons. *Sov. Phys. JETP*, 12(5):904–911, 1961.

[24] Yu A Sokolov. Multiplication of accelerated electrons in a tokamak. *JETP journal*, 29(218), 1979.

[25] J.A. Rome and Y.K.M. Peng. The topology of tokamak orbits. *Nuclear Fusion*, 19(9), 1979.

[26] W.D. D' haeseleer, W. N. G. Hitchon, J. D. Callen, and J. L. Shohet. *Flux Coordinates and Magnetic Field Structure - A Guide to a Fundamental Tool of the Plasma Theory.* Springer Series in Computational Physics. Springer-Verlag, 1991.

[27] P. helander and D. J. Sigmar. *Collisional Transport in Magnetized Plasmas.* Cambridge University Press, 2002.

[28] A.V. Nedospasov. Thermal quench in tokamaks. *Nucl. Fusion*, 48:032002, 2008.

[29] G.T.A. Huysmans and O. Czarny. MHD stability in X-point geometry: simulation of ELMs. *Nucl. Fusion*, 47:659–666, 2007.

[30] J.A. Wesson, R.D. Gill, M. Hugon, F.C. Schüller, J.A. Snipes, D.J. Ward, D.V. Bartlett, D.J. Campbell, P.A. Duperrex, A.W. Edwards, R.S. Granetz, N.A.O. Gottardi, T.C. Hender, E. Lazzaro, P.J. Lomas, and N. Lopes C. Disruptions in JET. *Nucl. Fusion*, 29:641–666, 1989.

[31] M. Tavani, M. Marisaldi, C. Labanti, F. Fuschino, A. Argan, A. Trois, P. Giommi, S. Colafrancesco, C. Pittori, F. Palma, M. Trifoglio, F. Gianotti, A. Bulgarelli, and V. Vittorini. Terrestrial gamma-ray flashes as powerful particle accelerators. *Phys. Rev. Lett.*, 106:018501, 2011.

[32] C. Møller. *Annalen der Physik (Leipzig)*, 14:531–585, 1932.

[33] S. C. Chiu, M.N. Rosenbluth, R.W. Harvey, and V.S. Chan. Fokker-Planck simulations of knock-on electron runaway avalanche and bursts in tokamaks. *Nucl. Fusion*, 38(11):1711–1721, 1998.

[34] R. W. Harvey, V. S. Chan, S. C. Chiu, T. E. Evans, M. N. Rosenbluth, and D. G. Whyte. Runaway electron production in DIII-D killer pellet experiments, calculated with the CQL3D-KPRAD model. *Phys. of Plasmas*, 7(11):4590–4599, 2000.

[35] A. Stahl, E. Hirvijoki, J. Decker, O. Embreus, and T. Fülöp. Effective critical electric field for runaway-electron generation. *Phys. Rev. Letters*, (114):115002, 2015.

[36] T. Wijnands and G. Martin. An advanced plasma control system for Tore Supra. *Fusion Technology*, 32:471–486, 1997.

[37] M. Vlainic, J. Mlynar, J. Cavalier, V. Weinzettl, R. Paprok, M. Imrisek, O. Ficker, J.-M. Noterdaeme, and the COMPASS Team. Post-disruptive runaway electron beam in COMPASS tokamak. *Journal of Plasma Physics*, 2015. Accepted For Publication.

[38] H. Smith, P. Helander, L.-G. Eriksson, D. Anderson, M. Lisak, and F. Andersson. Runaway electrons and the evolution of the plasma current in tokamak disruptions. *Phys. of Plasmas*, 13, 2006.

[39] E. Nilsson, J. Decker, N. J. Fisch, and Y. Peysson. Trapped-electron runaway effect. *Journal of Plasma Physics*, 81, 2015.

[40] L. G. Eriksson and P. Helander. Simulation of runaway electrons during tokamak disruptions. *Comp. Phys. Comm.*, 154:175–196, 2003.

[41] L. Zeng, H. R. Koslowski, Y. Liang, A. Lvovskiy, M. Lehnen, D. Nicolaiand J. Pearson, M. Rack, H. Jaegers, K. H. Finken, K. Wongrachand Y. Xu, and the TEXTOR team. Experimental observation of a magnetic-turbulence threshold for runaway-electron generation in the TEXTOR tokamak. *Phys. Rev. Letters*, 110:235003, 2013.

[42] E. Nilsson, J. Decker, Y. Peysson, R.S Granetz, F. Saint-Laurent, and M. Vlainic. Kinetic modelling of runaway electron avalanches in tokamak plasmas. *Plasma Phys. and Controlled Fusion*, 57(9):095006, 2015.

[43] A. A. Ware. Pinch effect for trapped particles in a tokamak. *Phys. Rev. Lett.*, 25(1), 1970.

[44] W. Pauli. *Theory of Relativity.* Dover Books on Physics. Dover Publications, 1958.

[45] P. Helander, L.G. Eriksson, and F. Andersson. Runaway acceleration during magnetic reconnection in tokamaks. *Plasma Phys. Control. Fusion*, 44B:247–262, 2002.

[46] J. Decker, A.K. Ram, A. Bers, Y. Peysson, C.N. Lashmore-Davies, R.A. Cairns, G. Taylor, and P. Efthimion. Current drive by electron Bernstein waves in spherical tokamaks. In *31st EPS Conference on Plasma Phys., London, 28 June - 2 July 2004*, volume 28G, page 2.166. Europhysics Conference Abstracts, 2004.

[47] A. Stahl, M. Landreman, G. Papp, E. Hollmann, and T. Fülöp. Synchrotron radiation from a runaway electron distribution in tokamaks. *Phys. of Plasmas*, 2013.

[48] M. Landreman, A. Stahl, and T. Fülöp. Numerical calculation of the runaway electron distribution function and associated synchrotron emission. *Computer Physics Communications*, 185(3):847 – 855, 2014.

[49] L. Laurent and J. M. Rax. Stochastic instability of runaway electrons in tokamaks. *Europhysics Lett.*, 11, 1990.

[50] J.M. Rax, N.J. Fisch, and L. Laurent. Fast particle resonances in tokamaks. *Plasma Phys. Control. Fusion*, 35(B):129–140, 1993.

[51] T. Fülöp and S. Newton. Alfvénic instabilities driven by runaways in fusion plasmas. *Phys. of Plasmas*, 21(8):080702, 2014.

[52] G. Papp, M. Drevlak, T. Fülöp, P. Helander, and G.I. Pokol. Runaway electron losses caused by resonant magnetic perturbations in ITER. *Plasma Phys. Control. Fusion*, 53(9):095004, 2011.

[53] J. Liu, H. Qin, N.J. Fisch, Q. Teng, and X. Wang. What is the fate of runaway positrons in tokamaks? *Phys. of Plasmas*, 21:064503, 2014.

[54] X. Guan, H. Qin, and N.J. Fisch. Phase-space dynamics of runaway electrons in tokamaks. *Phys. of Plasmas*, 17:092502, 2010.

[55] D. Mueller. The physics of tokamak start-up. *Phys. of Plasmas*, 20(5):058101, 2013.

[56] N.J. Fisch. Theory of current drive in plasmas. *Rev. Mod. Phys.*, 59(1):175–234, 1987.

[57] N.J. Fisch. Transformer recharging with alpha channeling in tokamaks. *Journal of Plasma Physics*, 76(3-4), 2010.

[58] C F. F. Karney and N. J. Fisch. Current in wave-driven plasmas. *Phys. Fluids*, 29(1):180–192, 1986.

[59] C. F. F. Karney, N. J. Fisch, and F. C. Jobes. Comparison of the theory and the practice of lower-hybrid current drive. *Phys. Rev. A*, 32(4):2554–2556, 1985.

[60] L. Miaohui, D. Bojiang, L. Wenke, K. Erhua, S. Jiafang, L. Fukun, W. Mao, and X. Handong. Investigation of lhcd efficiency and transformer recharging in the EAST tokamak. *Plasma Science and Technology*, 14(3), 2012.

[61] B. Ding, E. H. Kong, M. H. Li, L. Zhang, W. Wei, M. Wang, H. D. Xu, G. S. Xu, X. F. Han, L. M. Zhao, H. C. Hu, Y. Yang, L. Liu, A. Ekedahl, Y. Peysson, J. Decker, V. Basiuk, P. Huynh, J. F. Artaud, F. Imbeaux, J. F. Shan, F. K. Liu, Y. P. Zhao, X. Z. Gong, L. Q. Hu, X. Gao, H. Y. Guo, B. N. Wan, and J. G. Li. Investigations of lhw-plasma coupling and current drive in h-mode experiments in east. In *24th IAEA Fusion Energy Conference, San Diego, USA 8-13 October 2012*, pages EX/P6–21, 2012.

[62] N.J. Fisch. Confining a tokamak plasma with RF-driven currents. *Phys. Rev. Lett.*, 41(13):873–876, 1978.

[63] N.J. Fisch and A.H. Boozer. Creating an asymmetric plasma resistivity with waves. *Phys. Rev. Lett.*, 45(9):720–722, 1980.

[64] D. J. H Wort. The peristaltic tokamak. *Plasma Physics*, 13(3), 1971.

[65] N.J. Fisch and C. F. F. Karney. Current generation with low-frequency waves. *Phys. of Fluids*, 21(1):27–39, 1981.

[66] G. Pautasso, P.J. McCarthy, C. Fuchs, R. Dux, S. Potzel, G. Papp, M. Sertoli, G. Tardini, K. Lackner, A. Scarabosio, A. Mlynek, L. Giannone, the ASDEX Upgrade team, and the EUROfusion MST team. Generation and suppression of runaway electrons in ASDEX upgrade disruptions. In *42nd EPS Conference on Plasma Physics*, number P1.134, 2015.

[67] J. F. Artaud, V. Basiuk, F. Imbeaux, M. Schneider, J. Garcia, G. Giruzzi, P. Huynh, T. Aniel, F. Albajar, J. M. Ane, A. Bécoulet, C. Bourdelle, A. Casati, L. Colas, J. Decker, R. Dumont, L.G. Eriksson, X. Garbet, R. Guirlet, P. Hertout, G. T. Hoang, W. Houlberg, G. Huysmans, E. Joffrin, S.H. Kim, F. Köchl, J. Lister, X. Litaudon, P. Maget, R. Masset, B. Pégourié, Y. Peysson, P. Thomas, E. Tsitrone, and F. Turco. The CRONOS suite of codes for integrated tokamak modelling. *Nucl. Fusion*, 50(4):043001, 2010.

[68] Y. Peysson and J. Decker. Fast electron bremsstrahlung in axisymmetric magnetic configuration. *Phys. of Plasmas*, 15(9):092509, 2008.

[69] P. Maget, J.F. Artaud, L.G. Eriksson, G. Huysmans, A. Lazaros, P. Moreau, M. Ottaviani, J.L. Segui, and W. Zwingmann. MHD activity triggered by monster sawtooth crashes on Tore Supra. *Plasma Phys. Control. Fusion*, 47(2):357, 2003.

[70] M. Irishkin. *Comparaison automatisée de reconstructions Bayésiennes de profils expérimentaux avec des modèles physiques.* PhD thesis, Aix Marseille Université, 2014.

[71] C. Reux, V. Plyusnin, B. Alper, D. Alves, B. Bazylev, E. Belonohy, S. Brezinsek, J. Decker, S. Devaux, P. de Vries, A. Fil, S. Gerasimov, I. Lupelli, S. Jachmich, E.M. Khilkevitch, V. Kiptily, R. Koslowski, U. Kruezi, M. Lehnen, A. Manzanares, J. Mlynár, E. Nardon, E. Nilsson, V. Riccardo, F. Saint-Laurent, A.E. Shevelev, and C. Sozzi. Runaway beam studies during disruptions at JET-ILW. *Journal of Nucl. Materials*, 463:143–149, 2014.

[72] F. Saint-Laurent, G. Martin, T. Alarcon, A. Le Luyer, P. B. Parks, P. Pastor, S. Putvinski, C. Reux, J. Bucalossi, S. Bremond, and Ph. Moreau. Overview of runaway electron control and mitigation experiments on Tore Supra and lessons learned in view of ITER. *Fusion Science and Technology*, 64(4):711–718, 2013.

[73] Y. Peysson. Transport of fast electrons during lhcd in ts, jet and asdex. *Plasma Phys. Control. Fusion*, 35(12B):B253–B262, 1993.

[74] A. B. Rechester and M. N. Rosenbluth. Electron heat transport in a tokamak with destroyed magnetic surfaces. *Phys. Rev. Lett.*, 40(1), 1978.

[75] E. Nilsson, J. Decker, Y. Peysson, J.-F. Artaud, A. Ekedahl, J. Hillairet, T. Aniel, V. Basiuk, M. Goniche, F. Imbeaux, D. Mazon, and P. Sharma. Comparative modelling of lower hybrid current drive with two launcher designs in the Tore Supra tokamak. *Nucl. Fusion*, 53:083018, 2013.

[76] Y. Peysson and F. Imbeaux. Tomography of the fast electron bremsstrahlung emission during lower hybrid current drive on Tore Supra. *Rev. Sci. Instr.*, 70(10):3987–4007, 1999.

[77] I. Klimanov, T.P. Goodman A. Fasoli, and the TCV team. Generation of suprathermal electrons during sawtooth crashes in a tokamak plasma. *Plasma. Phys. Control. Fusion*, 49(3):L1–L6, 2007.

[78] R. Pánek, O. Bilyková, V. Fuchs, M. Hron, P. Chráska, P. Pavlo, J. Stöckel, J. Urban, V. Weinzettl, J. Zajac, and F. Žáček. Reinstallation of the COMPASS-D tokamak in IPP ASCR. *Czechoslovak Journal of Physics*, 56(2), 2006.

[79] R. Pánek, J. Adámek, M. Aftanas, P. Bílková, P. Böhm, P. Cahyna, J. Cavalier, R. Dejarnac, M. Dimitrova, O. Grover, P. Háček, J. Havlíček, A. Havránek, J. Horáček, M. Hron, M. Imríšek, F. Janky, M. Komm, K. Kovařík, J. Krbec, L. Kripner, T. Markovič, K. Mitošinková, J. Mlynář, D. Naydenkova, M. Peterka, J. Seidl, , J. Stöckel, E. Štefániková, M. Tomeš, J. Urban, P. Vondráček, M. Varavin, J. Varju, V. Weinzettl, J. Zajac, and the COMPASS Team. Current status of the compass tokamak and characterization of the first H-mode. *Plasma Phys. Contr. Fusion - Invited talk at EPS Conference on Plasma Physics*, (I2.107), 2015. Status: To Be Submitted.

[80] J. Mlynar, O. Ficker, M. Vlainic, V. Weinzettl, M. Imrisek, R. Paprok, M. Rabinski, M. Jakubowski, M. Tomes, M. Peterka, R. Pánek1, and the COMPASS Team. Effects of plasma control on runaway electrons in the COMPASS tokamak. In *42nd EPS Conference on Plasma Physics*, number P4.102, 2015.

[81] L.L. Lao, H. St. John, R.D. Stambaugh, A.G. Kellman, and W. Pfeiffer. Reconstruction of current profile parameters and plasma shapes in tokamaks. *Nucl. Fusion*, 25(11), 1985.

[82] L.C. Appel, G.T.A. Huysmans, L.L. Lao, P.J. McCarthy, D.G. Muir, E.R. Solano, J. Storrs, D. Taylor, W. Zwingmann, contributors to the EFDA Integrated Tokamak Modelling (ITM) Task Force, and JET-EFDA contributors. A unified approach to equilibrium reconstruction. In *33rd EPS Conference on Plasma Physics*, number P2.184, 2006.

[83] V.B. Berestetskii and E.M. Lifshitz. *Quantum Electrodynamics.* Elsevier, 1971.

[84] M.E Peskin and D.V Schroeder. *An Introduction To Quantum Field Theory.* Elsevier, 2005.

Appendix A

Definition of the four momentum

The four momentum describes the normalized energy and normalized momentum. The definition is

$$\mathbf{P} \equiv \gamma(\mathbf{1}, \frac{\mathbf{v}}{\mathbf{c}}), \tag{A.1}$$

where the normalization is m_0c^2 and m_0c respectively. The scalar product of four vectors is defined as:

$$\mathbf{A} \cdot \mathbf{B} \equiv A_1B_1 - A_2B_2 - A_3B_3 - A_4B_4. \tag{A.2}$$

Using this terminology for the calculations in Sec. 4.1, we get

$$\mathbf{P}_0 \cdot \mathbf{P}_1 = \gamma_0(1, \frac{\mathbf{v_0}}{c}) \cdot \gamma_1(1, \frac{\mathbf{v_1}}{c}) = \gamma_0\gamma_1 - \frac{\gamma_0\gamma_1}{c^2}\mathbf{v_0} \cdot \mathbf{v_1}. \tag{A.3}$$

$$\mathbf{P}_0 \cdot \mathbf{P}_2 = \gamma_0(1, \frac{\mathbf{v_0}}{c}) \cdot \gamma_2(1, \frac{\mathbf{v}_2}{c}) = \gamma_0\gamma_2 - \frac{\gamma_0\gamma_2}{c^2}\mathbf{v}_0 \cdot \mathbf{v_2}, \tag{A.4}$$

$$\mathbf{P}_1 \cdot \mathbf{P}_2 = \gamma_1(1, \frac{\mathbf{v}_1}{c}) \cdot \gamma_2(1, \frac{\mathbf{v}_2}{c}) = \gamma_1\gamma_2 - \frac{\gamma_1\gamma_2}{c^2}\mathbf{v_1} \cdot \mathbf{v_2}. \tag{A.5}$$

In the case of $v_0 \approx 0$ and $\gamma_0 \approx 1$ Eq. A.3 becomes

$$\mathbf{P}_0 \cdot \mathbf{P}_1 = \gamma_1, \tag{A.6}$$

$$\mathbf{P}_0 \cdot \mathbf{P}_2 = \gamma_2, \tag{A.7}$$

$$\mathbf{P}_1 \cdot \mathbf{P}_2 = \gamma_1\gamma_2 - p_1p_2\cos(\theta_2). \tag{A.8}$$

Appendix B

Derivation of scattering angle

We start from the momentum conservation equation (Eq. 4.5):

$$1 + \gamma_0\gamma_1 - \gamma_0\gamma_2 + p_0p_2 sin(\theta_2) - \gamma_1\gamma_2 + p_1p_2\cos(\theta_2) = 0.$$

If $\xi^* = \cos(\theta_2)$ then $sin(\theta_2) = \sqrt{1-\xi^{*2}}$ and we get:

$$1 + \gamma_0\gamma_1 - \gamma_0\gamma_2 + p_0p_2\sqrt{1-\xi^{*2}} - \gamma_1\gamma_2 + p_1p_2\xi^* = 0.$$

We group all the terms not containing ξ^*, so that $\chi = 1 + \gamma_0\gamma_1 - \gamma_0\gamma_2 - \gamma_1\gamma_2$:

$$p_0p_2\sqrt{1-\xi^{*2}} + p_1p_2\xi^* + \chi = 0,$$
$$p_0p_2\sqrt{1-\xi^{*2}} = -p_1p_2\xi^* - \chi.$$

Squaring both sides leads to

$$(p_0p_2)^2(1-\xi^{*2}) = (-p_1p_2\xi^* - \chi)^2 = (p_1p_2\xi^*)^2 + \chi^2 + 2p_1p_2\xi^*\chi,$$

$$(1-\xi^{*2}) = \frac{(p_1p_2\xi^*)^2}{(p_0p_2)^2} + \frac{\chi^2}{(p_0p_2)^2} + \frac{2p_1p_2\xi^*\chi}{(p_0p_2)^2} \implies \xi^{*2} + \frac{2p_1p_2\xi^*\chi}{\left(1+\frac{p_1^2}{p_0^2}\right)(p_0p_2)^2} = \frac{1-\frac{\chi^2}{(p_0p_2)^2}}{\left(1+\frac{p_1^2}{p_0^2}\right)},$$

$$\left(\xi^* + \frac{p_1p_2\chi}{\left(1+\frac{p_1^2}{p_0^2}\right)(p_0p_2)^2}\right)^2 = \frac{1-\frac{\chi^2}{(p_0p_2)^2}}{\left(1+\frac{p_1^2}{p_0^2}\right)} + \left(\frac{p_1p_2\chi}{\left(1+\frac{p_1^2}{p_0^2}\right)(p_0p_2)^2}\right)^2,$$

$$\xi^* = \pm\sqrt{\frac{1-\frac{\chi^2}{(p_0p_2)^2}}{\left(1+\frac{p_1^2}{p_0^2}\right)} + \left(\frac{p_1p_2\chi}{\left(1+\frac{p_1^2}{p_0^2}\right)(p_0p_2)^2}\right)^2} - \frac{p_1p_2\chi}{\left(1+\frac{p_1^2}{p_0^2}\right)(p_0p_2)^2}.$$

Which leads to:

$$\xi^* = \pm\sqrt{\frac{p_0^2 - \frac{(1+\gamma_0\gamma_1-\gamma_0\gamma_2-\gamma_1\gamma_2)^2}{p_2^2}}{p_0^2+p_1^2} + \left(\frac{(1+\gamma_0\gamma_1-\gamma_0\gamma_2-\gamma_1\gamma_2)p_1}{p_2(p_0^2+p_1^2)}\right)^2} - \frac{(1+\gamma_0\gamma_1-\gamma_0\gamma_2-\gamma_1\gamma_2)p_1}{p_2(p_0^2+p_1^2)},$$

which may also be expressed as

$$\xi^* = \pm\sqrt{\frac{p_0^2}{p_0^2+p_1^2} + \frac{(1+\gamma_0\gamma_1-\gamma_0\gamma_2-\gamma_1\gamma_2)^2}{p_2^2(p_0^2+p_1^2)}\left(\frac{p_1^2}{p_0^2+p_1^2}-1\right)} - \frac{(1+\gamma_0\gamma_1-\gamma_0\gamma_2-\gamma_1\gamma_2)p_1}{p_2(p_0^2+p_1^2)}.$$

Appendix C

Ellipse of momentum conservation

In Sec. 4.1 we arrived at the momentum conservation equation:

$$1 + \gamma_1 - \gamma_2 - \gamma_1\gamma_2 + p_1 p_2 \xi^* = 0, \tag{C.1}$$

where $\xi^* = \cos(\theta_2) = p_{2||}/p_2$. We also have $\gamma_2^2 = 1 + p_{2||}^2 + p_{2\perp}^2$. Therefore, Eq. C.1 becomes

$$(1 + \gamma_1)(1 - \gamma_2) = -p_1 p_2 \xi^*, \tag{C.2}$$

$$(1 - \gamma_2) = -\frac{p_1 p_2 \xi^*}{(1 + \gamma_1)}, \tag{C.3}$$

$$\gamma_2^2 = \left(1 + \frac{p_1 p_2 \xi^*}{(1 + \gamma_1)}\right)^2, \tag{C.4}$$

$$\gamma_2^2 = \left(1 + \frac{p_1 p_{2||}}{(1 + \gamma_1)}\right)^2, \tag{C.5}$$

$$1 + p_{2||}^2 + p_{2\perp}^2 = \left(1 + \frac{p_1 p_{2||}}{(1 + \gamma_1)}\right)^2, \tag{C.6}$$

$$1 + p_{2||}^2 + p_{2\perp}^2 = \left(\frac{p_1}{1 + \gamma_1}\right)^2 p_{2||}^2 + 2\frac{p_1 p_{2||}}{1 + \gamma_1} + 1, \tag{C.7}$$

$$\left(\frac{\gamma_1^2 - 1 - (1 + \gamma_1)^2}{(1 + \gamma_1)^2}\right) p_{2||}^2 + 2\frac{p_1 p_{2||}}{1 + \gamma_1} - p_{2\perp}^2 = 0, \tag{C.8}$$

$$\left(\frac{2(1 + \gamma_1)}{(1 + \gamma_1)^2}\right) p_{2||}^2 - 2\frac{\sqrt{\gamma_1^2 - 1} p_{2||}}{1 + \gamma_1} + p_{2\perp}^2 = 0, \tag{C.9}$$

$$\left(\frac{2}{1 + \gamma_1}\right) p_{2||}^2 - 2\frac{\sqrt{\gamma_1^2 - 1} p_{2||}}{1 + \gamma_1} + p_{2\perp}^2 = 0. \tag{C.10}$$

By multiplying this expression with $1/(2(\gamma_1 - 1))$ we obtain

$$\left(\frac{1}{(\gamma_1^2 - 1)}\right) p_{2||}^2 - \frac{p_{2||}}{\sqrt{\gamma_1^2 - 1}} + \frac{p_{2\perp}^2}{2(\gamma_1 - 1)} = 0. \tag{C.11}$$

We complete the square and arrive at an elliptic equation:

$$\left(\frac{p_{2||}}{\sqrt{\gamma_1^2 - 1}} - \frac{1}{2}\right)^2 + \frac{p_{2\perp}^2}{2(\gamma_1 - 1)} = \frac{1}{4}. \tag{C.12}$$

Appendix D

Derivation of the electron-electron differential cross section

For demonstration, the main steps of the quantum electro dynamic (QED) derivation of the electron electron differential cross section are presented, further details can be found in [83]. The Minkowski metric tensor definition chosen for the calculations through this section is

$$g_{\mu\nu} = \begin{bmatrix} 1 & 0 & 0 & 0 \\ 0 & -1 & 0 & 0 \\ 0 & 0 & -1 & 0 \\ 0 & 0 & 0 & -1 \end{bmatrix}.$$

Let us consider the scattering of an electron with 4-momenta p_1 by an electron with 4-momenta p_2 which result in two electrons ($p_1^{'}$ and $p_2^{'}$). The 4-momentum $p_a = (\varepsilon_a, \mathbf{p}_a)$ where the first element is the energy and the second the 3-momentum. The conservation of 4-momenta is expressed as

$$p_1 + p_2 = p_1^{'} + p_2^{'}. \tag{D.1}$$

In theoretical physics, the Mandelstam variables [84] are numerical quantities that encode the energy and momentum of particles in a scattering process of two particles to two particles. Mandelstam variables, also called kinetic invariants since they are equal in all reference systems [84]. Using that $p_a^2 = m_a^2$, they are expressed as:

$$s = (p_1 + p_2)^2 = p_1^2 + p_2^2 + 2p_1p_2 = 2(m^2 + p_1p_2), \tag{D.2}$$

$$t = (p_1 - p_1^{'})^2 = 2(m^2 - p_1p_1^{'}), \tag{D.3}$$

$$u = (p_1 - p_2^{'})^2 = 2(m^2 - p_1p_2^{'}), \tag{D.4}$$

which leads to

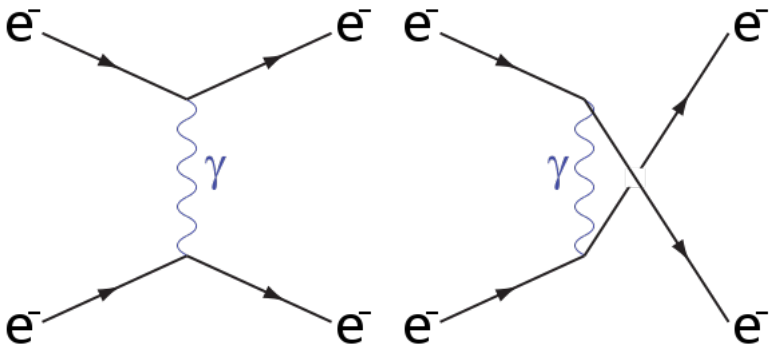
$$s + t + u = 6m^2 + 2p_1(p_2 - p_1^{'} - p_2^{'}) = 4m^2, \tag{D.5}$$

where m is the electron mass. The cross section in the center of mass system is expressed according to Ref. [83]:

$$d\sigma = \frac{1}{64\pi}|M_{fi}|^2\frac{dt}{I^2}, \tag{D.6}$$

where

$$I^2 = \frac{1}{4}(s - (m_1 + m_2)^2)(s - (m_1 - m_2)^2) = \frac{1}{4}s(s - 4m^2),$$



(a) t-channel (b) u-channel.

Figure D.1: Feynman diagrams.

since all the particles are electrons. M_{fi} is the amplitude of the two Feynman diagrams corresponding to the electron electron scattering process, one in the t-channel and one in the u-channel (Fig. D.1). The matrix element of the operator M for transition from initial state i to final state f is $\langle f|M|i\rangle$ or M_{fi}. We write down the amplitude using the Feynman rules of QED.

The calculation of the differential scattering cross section consists of the following steps:

1. drawing the Feynman diagrams
2. writing $-iM_{fi}$ using the Feynman rules
3. squaring M_{fi} and using the Casimir trick to get traces
4. evaluate the traces
5. apply kinematics of the chosen frame

As an example, for the t-channel diagram, the matrix element is built by following fermion lines with a factor for each propagator ($\bar{u}(p_a)$ for outgoing fermion ($\bar{u}$ is the complex conjugate of u), $u(p_b)$ for incoming fermion, $-ig_{\mu\nu}/(p_a - p_b)^2$ for propagating photon) and vertex ($ie\gamma^\nu$), see Fig. D.2. $g_{\mu\nu}$ is the Minkowski metric tensor and γ^ν denotes the Dirac matrices $(\gamma^0, \gamma^1, \gamma^2, \gamma^3)$ in the original Dirac representation. Here $u_a^{'}$ and u_a is the Dirac spinor related to a plane-wave (with wave vector p) for each electron before and after the interaction. Note that u without index is one of the Mandelstam variables in Eq. D.4. Writing $-iM_{fi}$ using the Feynman rules gives

$$-iM_{fi} = (\bar{u}_2^{'} ie\gamma^\nu u_2)(\frac{-ig_{\mu\nu}}{(p_2 - p_2^{'})^2})(\bar{u}_1^{'} ie\gamma_\mu u_1) = ie^2 \frac{1}{t}(\bar{u}_2^{'}\gamma^\mu u_2)(\bar{u}_1^{'}\gamma_\mu u_1).$$

The same method is used for the term from the u-channel diagram. The two terms represent the two possible Feynman diagrams of the process:

$$M_{fi} = -4\pi e^2(\frac{1}{t}(\bar{u}_2^{'}\gamma^\mu u_2)(\bar{u}_1^{'}\gamma_\mu u_1) - \frac{1}{u}(\bar{u}_1^{'}\gamma^\nu u_2)(\bar{u}_2^{'}\gamma_\nu u_1)). \tag{D.7}$$

Exchanging the two initial or the two final particles ($s \to s$, $t \to u$, $u \to t$) should change the sign of the scattering amplitude, and expression D.7 indeed fulfills this criterion.

The state polarization (spins) of the electrons in the reaction must be taken into account, by summation over initial (σ_1, σ_2) and final (σ_3, σ_4) polarization:

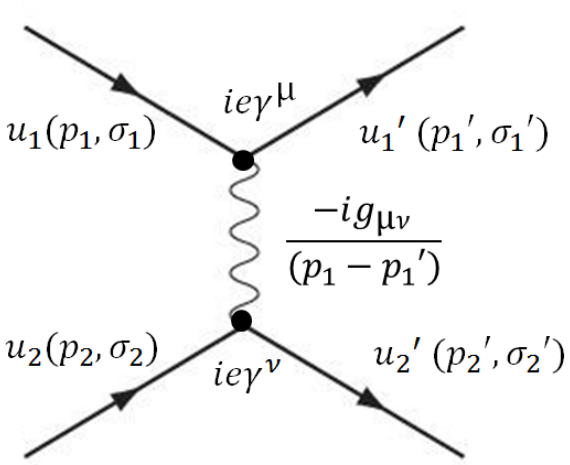


Figure D.2: t-channel Feynman diagram with Feynmann rules.

$$|\bar{M}|^2_{fi} = \sum_{\sigma_1,\sigma_2}\sum_{\sigma_3,\sigma_4}|M_{fi}|^2.$$

In the calculation of $|M_{fi}|^2 = M^*_{fi}M_{fi}$, the following identity is needed:

$$[\bar{u}\gamma^{\mu}v]^* = [u^{\dagger}\gamma^0\gamma^{\mu}v]^{\dagger} = v^{\dagger}\gamma^{\mu\dagger}\gamma^0 u = [\bar{v}\gamma^{\mu}u].$$

Thus,

$$\begin{aligned}|\bar{M}_{fi}|^2 \quad = \tfrac{e^4}{4}\Big(\quad & \frac{1}{t^2}\sum_{\sigma_{1,2,3,4}}(\bar{u}_2^{'}\gamma^{\mu}u_2)(\bar{u}_1^{'}\gamma_{\mu}u_1)(\bar{u}_2\gamma^{\mu}u_2^{'})(\bar{u}_1\gamma_{\mu}u_1^{'}) + \\ & + \frac{1}{u^2}\sum_{\sigma_{1,2,3,4}}(...) - \frac{1}{tu}\sum_{\sigma_{1,2,3,4}}(...) - \frac{1}{tu}\sum_{\sigma_{1,2,3,4}}(...)\Big).\end{aligned}$$

Sums over polarizations are performed using the following manipulation, known as the Casimir trick. It turns the summation over the electron spins into traces. First we write $\sum(\bar{u}_1^{'}\gamma_{\mu}u_1)(\bar{u}_1\gamma_{\mu}u_1^{'})$ with explicit spinor indices $\alpha,\beta,\gamma,\delta = 1,2,3,4$:

$$\sum_{\sigma_1,\sigma_2}(\bar{u}_{1\alpha}^{'}\gamma_{\mu\alpha\beta}u_{1\beta})(\bar{u}_{1\gamma}\gamma_{\mu\gamma\delta}u_{1\delta}^{'}). \tag{D.8}$$

We can now move $u_{1\delta}^{'}$ to the front (it is just a number, an element of $u_1^{'}$ vector, so it commutes with everything), and then use a relation, known as the completeness relation:

$$\sum_{\sigma_1}u_{1\delta}^{'}\bar{u}_{1\alpha}^{'} = (\gamma p_1^{'} + m)_{\delta\alpha}$$

and

$$\sum_{\sigma_2}u_{1\beta}\bar{u}_{1\gamma} = (\gamma p_1 + m)_{\beta\gamma},$$

which turns a sum like D.8 into a trace:

$$(\gamma p_1^{'} + m)_{\delta\alpha}\gamma^{\mu}_{\alpha\beta}(\gamma p_1 + m)_{\beta\gamma}\gamma^{\nu}_{\gamma\delta} = Tr((\gamma p_1^{'} + m)\gamma^{\mu}(\gamma p_1 + m)\gamma^{\nu})$$

Thus all the spinors are eliminated and only with traces of Dirac matrices remain. M_{fi} is squared and the summation over initial and final polarization is done with Casimir's trick, where $\rho = \frac{1}{2}(\gamma p + m)$ is the density matrix, not taking polarization into account (because we have averaged over the polarization). The full expression becomes:

$$\begin{aligned} |M_{fi}|^2 &= M_{fi}^* M_{fi} = 16\pi^2 e^4 (\frac{1}{t^2} Tr(\rho_2^{'} \gamma^\mu \rho_2 \gamma^\nu) Tr(\rho_1^{'} \gamma_\mu \rho_1 \gamma_\nu) + \\ &+ \frac{1}{u^2} Tr(\rho_1^{'} \gamma^\mu \rho_2 \gamma^\nu) Tr(\rho_2^{'} \gamma_\mu \rho_1 \gamma_\nu) - \\ &- \frac{1}{tu} Tr(\rho_2^{'} \gamma^\mu \rho_2 \gamma^\nu \rho_1^{'} \gamma_\mu \rho_1 \gamma_\nu) - \frac{1}{tu} Tr(\rho_1^{'} \gamma^\mu \rho_2 \gamma^\nu \rho_2^{'} \gamma_\mu \rho_1 \gamma_\nu)). \end{aligned} \tag{D.9}$$

The evaluation of the traces are and summation over the indices μ and ν are performed with help of the FeynCalc package [1] in Mathematica, and in agreement with [83] the cross section becomes:

$$d\sigma = r_e^2 \frac{4\pi m^2 dt}{s(s-4m^2)} \times$$

$$\left\{ \frac{1}{t^2} \left[\frac{1}{2}(s^2+u^2) + 4m^2(t-m^2) \right] + \frac{1}{u^2} \left[\frac{1}{2}(s^2+t^2) + 4m^2(u-m^2) \right] + \frac{4}{tu}(\frac{1}{2}s - m^2)(\frac{1}{2}s - 3m^2) \right\}$$

where $r_e = e^2/m$. In the laboratory system where one of the electrons have zero parallel momentum before the collision (say electron number 2), the cross section can be expressed in terms of energy gained by the target electron:

$$\Delta = \frac{\varepsilon_1 - \varepsilon_1^{'}}{m} = \frac{\varepsilon_2 - \varepsilon_2^{'}}{m} = \gamma_2 - \gamma_2^{'}. \tag{D.10}$$

The Mandelstam variables expressed in energy transfer are:

$$s = 2(m^2 + \varepsilon_1 \varepsilon_2 - \mathbf{p}_1 \cdot \mathbf{p}_2) \approx 2(m^2 + \varepsilon_1 \varepsilon_2), \tag{D.11}$$

$$t = -2m^2 \Delta, \tag{D.12}$$

$$u = -2(\varepsilon_1 \varepsilon_2 - m^2 - m^2 \Delta). \tag{D.13}$$

Where $\varepsilon = m\gamma$. Substituting the variables into the above cross section equation yields:

$$d\sigma = 2\pi r_e d\Delta \frac{\left(\Delta^4 + \Delta^3(2 - 2\gamma_0\gamma_1) + 3\Delta^2 \gamma_0^2 \gamma_1^2 + \Delta\left(-2\gamma_0^3\gamma_1^3 + 3\gamma_0\gamma_1 - 1\right) + \gamma_0^2\gamma_1^2(\gamma_0\gamma_1 - 1)^2\right)}{\Delta^2\left(\gamma_0^2\gamma_1^2 - 1\right)(\Delta - \gamma_0\gamma_1 + 1)^2}.$$

If we did not ignore the parallel momentum of the target particle the expression is:

[1] http://www.feyncalc.org/

$$d\sigma = 2\pi r_e d\Delta((2\Delta^4 m^4 - 4\Delta^3(-1+\gamma_0\gamma_1)m^4 - 2\Delta(-1+\gamma_0\gamma_1)m^2 \times$$
$$\times\left(\left(-1+2\gamma_0\gamma_1+2\gamma_0^2\gamma_1^2\right)m^2 - 4\sqrt{-1+\gamma_1^2}\mathrm{p}_{0\|}\right) +$$
$$+\Delta^2\left(6\gamma_0^2\gamma_1^2 m^4 - 8\sqrt{-1+\gamma_1^2}m^2\mathrm{p}_{0\|}\right) + (-1+\gamma_0\gamma_1)^2 \times$$
$$\times\left(2\gamma_0^2\gamma_1^2 m^4 - 2\gamma_0\gamma_1\sqrt{-1+\gamma_1^2}m^2\mathrm{p}_{0\|} + \mathrm{p}_{0\|}\left(-2\sqrt{-1+\gamma_1^2}m^2 + \left(-1+\gamma_1^2\right)\mathrm{p}_{0\|}\right)\right) /$$
$$/\left(2\Delta^2(1+\Delta-\gamma_0\gamma_1)^2\left(\left(-1+{\gamma_0}^2{\gamma_1}^2\right)m^4 - 2\gamma_0\gamma_1\sqrt{-1+{\gamma_1}^2}m^2\mathrm{p}_{0\|} + \left(-1+{\gamma_1}^2\right){\mathrm{p}_{0\|}}^2\right)\right))).$$

This reduces to D.18 for $\gamma_0 = 1$. In the limit $\gamma_1 \to \infty$.

If the secondary electron is assumed to initially be at rest the energy transfer and Mandelstam variables become:

$$\Delta = \frac{\varepsilon_1 - \varepsilon_1^{'}}{m} = \frac{\varepsilon_2 - m}{m} = \gamma_2 - 1, \tag{D.14}$$

and

$$s = 2(m^2 + \varepsilon_1\varepsilon_2) = \{\varepsilon_2 \to m\} = 2m(m+\varepsilon_1), \tag{D.15}$$

$$t = -2m^2\Delta, \tag{D.16}$$

$$u = -2(\varepsilon_1 m - m^2 - m^2\Delta) = -2m(\varepsilon_1 - m - m\Delta). \tag{D.17}$$

Substituting the variables into the above cross section equation yields:

$$d\sigma = 2\pi r_e d\Delta \frac{\left(\Delta^4 - 2\Delta^3(\gamma_1-1) + 3\Delta^2{\gamma_1}^2 + \Delta\left(-2{\gamma_1}^3 + 3\gamma_1 - 1\right) + (\gamma_1-1)^2\gamma_1^2\right)}{\Delta^2\left({\gamma_1}^2-1\right)(\Delta-\gamma_1+1)^2}, \tag{D.18}$$

or

$$d\sigma = 2\pi r_e^2 \frac{d\Delta}{\gamma_1^2-1}\left[\frac{(\gamma_1-1)^2\gamma_1^2}{\Delta^2(\gamma_1-1-\Delta)^2} - \frac{2\gamma_1^2+2\gamma_1-1}{\Delta(\gamma_1-1-\Delta)} + 1\right]. \tag{D.19}$$

The kinetic energies of the two electrons after the collision will be Δ and $\gamma - 1 - \Delta$. The cross section expressed in $\gamma_1 = \gamma$ and $\gamma_2 = \Delta + 1$ becomes:

$$\begin{aligned} d\sigma &= 2\pi r_e^2 \frac{\gamma_1^2}{(\gamma_1^2-1)(\gamma_2-1)^2(\gamma_1-\gamma_2)^2} \times \\ &\quad \left\{(\gamma_1-1)^2 - \frac{(\gamma_2-1)(\gamma_1-\gamma_2)}{\gamma_1^2}\cdot\left[2\gamma_1^2+2\gamma_1-1-(\gamma_2-1)(\gamma_1-\gamma_2)\right]\right\}d\gamma_2. \end{aligned}$$

which is the Møller expression [32]. In the limit $\gamma_1 \to \infty$ the differential cross section becomes $d\sigma = 2\pi r_e^2 \frac{d\Delta}{(\gamma_2-\gamma_0)^2}$ and for $\gamma_0 = 1$, this corresponds to the differential cross section used in [5].

Appendix E

Particle motion in magnetic field

The particle motion along the magnetic field lines exhibits a constant of the motion, the energy (or the total momentum p), and an adiabatic invariant, the magnetic moment μ. They are given by the following equations:

$$p^2 = p_{||}^2 + p_{\perp}^2, \tag{E.1}$$

$$\mu = \frac{p_{\perp}^2}{2m_e B} \tag{E.2}$$

such that, as a function of the moment component $(p_{||0}, p_{\perp 0})$ at the location θ_0 at minimum B-field, we have

$$p_{||0}^2 + p_{\perp 0}^2 = p_{||}^2 + p_{\perp,}^2 \tag{E.3}$$

$$\frac{p_{\perp 0}^2}{B_0(\psi)} = \frac{p_{\perp}^2}{B(\psi,\theta)}. \tag{E.4}$$

The transformation from $(p_{||}, p_{\perp})$ to (p, ξ) is given by

$$p = \sqrt{p_{||}^2 + p_{\perp}^2} \tag{E.5}$$

and

$$\xi = \frac{p_{||}}{\sqrt{p_{||}^2 + p_{\perp}^2}}. \tag{E.6}$$

We invert this to:

$$p_{||} = p\xi, \tag{E.7}$$

$$p_{\perp} = p\sqrt{1-\xi^2}. \tag{E.8}$$

Thus Eq. E.4 can be written as:

$$p_0^2 = p^2 \tag{E.9}$$

$$\frac{1-\xi_0^2}{B_0(\psi)} = \frac{1-\xi^2}{B(\psi,\theta)} \tag{E.10}$$

which leads to an expression for ξ:

$$\xi(\psi,\theta,\xi_0) = \sigma\sqrt{1-\Psi(\psi,\theta)(1-\xi_0^2)} \tag{E.11}$$

where $\Psi(\psi,\theta) = B(\psi,\theta)/B_0(\psi)$ and $\sigma = sign(v_{||}) = sign(\xi_0)$ indicates the direction of acceleration for the runaway electrons.

Appendix F

Flux surface average of avalanche operator

This section describes how a flux surface averaged avalanche operator could look like. The general relation for flux surface averaging is:

$$< \Phi >_V (\psi) = \frac{\int \int_{dV} \Phi(\psi, \theta) dV}{\int \int_{dV} dV}. \tag{F.1}$$

In order to obtain a flux surface dependent avalanche operator it can be flux surface averaged accordingly. Here p_{min} and p_{max} corresponds to the runaway threshold p_c and the upper momentum boundary of the integration domain of the Fokker-Planck equation.

$$\begin{aligned} < \bar{\mathbf{S}} >_V (\psi) &= \frac{2\pi}{\hat{q}} \int_0^{2\pi} \frac{d\theta}{2\pi} \frac{1}{|\hat{\psi} \cdot \hat{r}|} \frac{r}{R_p} \frac{B_0(\psi)}{B_P} \int_{p_{min}}^{p_{max}} 2\pi p^2 dp \int_{-1}^{+1} \bar{S}(\psi, p, \xi) d\xi, \\ &= \frac{2\pi}{\hat{q}} \int_0^{2\pi} \frac{d\theta}{2\pi} \frac{1}{|\hat{\psi} \cdot \hat{r}|} \frac{r}{R_p} \frac{B_0(\psi)}{B_P} \int_{p_{min}}^{p_{max}} 2\pi p^2 \bar{S}^* dp \int_{-1}^{+1} \delta(\xi - \xi^*) d\xi. \end{aligned} \tag{F.2}$$

Since $\int_{-1}^{+1} \delta(\xi - \xi^*) d\xi = 1$ and $\hat{q} = \int_0^{2\pi} \frac{d\theta}{2\pi} \frac{1}{|\hat{\psi} \cdot \hat{r}|} \frac{r}{R_p} \frac{B_0}{B_P}$ the expression simplifies to:

$$< \bar{\mathbf{S}} >_V (\psi) = 4\pi^2 \int_{p_{min}}^{p_{max}} p^2 dp \bar{\mathbf{S}}^*(\psi, p) = \frac{\pi}{\ln \Lambda^\dagger} \bar{n}_e \bar{n}_R \left[\frac{1}{1 - \sqrt{1 + \beta_{th}^{\dagger 2} \bar{p}^2}} \right]_{\bar{p}_{min}}^{\bar{p}_{max}}. \tag{F.3}$$

Which in the limit $\beta_{th}^\dagger p_{max}^2 \gg 1$ simplifies to:

$$< \bar{\mathbf{S}} >_V (\psi) = \frac{\pi}{\ln \Lambda^\dagger} \bar{n}_e \bar{n}_R(t) \frac{1}{\sqrt{1 + \beta_{th}^{\dagger 2} \bar{p}_{min}^2} - 1}. \tag{F.4}$$

Appendix G

Publications

IOP Publishing Plasma Physics and Controlled Fusion

Plasma Phys. Control. Fusion **57** (2015) 095006 (11pp) doi:10.1088/0741-3335/57/9/095006

Kinetic modelling of runaway electron avalanches in tokamak plasmas

E Nilsson[1], J Decker[2], Y Peysson[1], R S Granetz[3], F Saint-Laurent[1] and M Vlainic[4,5]

[1] CEA, IRFM, F-13108 Saint-Paul-lez-Durance, France
[2] Ecole Polytechnique Fédérale de Lausanne (EPFL), Centre de Recherches en Physique des Plasmas (CRPP), CH-1015 Lausanne, Switzerland
[3] MIT Plasma Science and Fusion Center, Cambridge, MA 02139, USA
[4] Department of Applied Physics, Ghent University, B-9000 Ghent, Belgium
[5] Institute of Plasma Physics AS CR, 18200 Prague, Czech Republic

E-mail: emelie.nilsson@cea.fr

Received 13 March 2015, revised 8 June 2015
Accepted for publication 7 July 2015
Published 30 July 2015



Abstract

Runaway electrons can be generated in tokamak plasmas if the accelerating force from the toroidal electric field exceeds the collisional drag force owing to Coulomb collisions with the background plasma. In ITER, disruptions are expected to generate runaway electrons mainly through knock-on collisions (Hender *et al* 2007 *Nucl. Fusion* **47** S128–202), where enough momentum can be transferred from existing runaways to slow electrons to transport the latter beyond a critical momentum, setting off an avalanche of runaway electrons. Since knock-on runaways are usually scattered off with a significant perpendicular component of the momentum with respect to the local magnetic field direction, these particles are highly magnetized. Consequently, the momentum dynamics require a full 3D kinetic description, since these electrons are highly sensitive to the magnetic non-uniformity of a toroidal configuration. For this purpose, a bounce-averaged knock-on source term is derived. The generation of runaway electrons from the combined effect of Dreicer mechanism and knock-on collision process is studied with the code LUKE, a solver of the 3D linearized bounce-averaged relativistic electron Fokker–Planck equation (Decker and Peysson 2004 DKE: a fast numerical solver for the 3D drift kinetic equation *Report* EUR-CEA-FC-1736, Euratom-CEA), through the calculation of the response of the electron distribution function to a constant parallel electric field. The model, which has been successfully benchmarked against the standard Dreicer runaway theory now describes the runaway generation by knock-on collisions as proposed by Rosenbluth (Rosenbluth and Putvinski 1997 *Nucl. Fusion* **37** 1355–62). This paper shows that the avalanche effect can be important even in non-disruptive scenarios. Runaway formation through knock-on collisions is found to be strongly reduced when taking place off the magnetic axis, since trapped electrons can not contribute to the runaway electron population. Finally, the relative importance of the avalanche mechanism is investigated as a function of the key parameters for runaway electron formation, namely the plasma temperature and the electric field strength. In agreement with theoretical predictions, the LUKE simulations show that in low temperature and electric field the knock-on collisions becomes the dominant source of runaway electrons and can play a significant role for runaway electron generation, including in non-disruptive tokamak scenarios.

Keywords: plasma physics, runaway electrons, knock-on collisions, tokamak, Fokker–Planck, runaway avalanches

(Some figures may appear in colour only in the online journal)

 © 2015 EURATOM Printed in the UK

1. Introduction

Runaway electrons have been observed in magnetic confinement fusion experiments during tokamak operation [1, 4]. They are also encountered in nature in solar flares and electric discharges associated with thunderstorms [5]. Collisional friction forces acting on the electrons reach a global maximum at the thermal velocity (v_{th}) and decrease for higher velocities. In the presence of a strong toroidal electric field (E) collisional drag may consequently be too weak to counteract the acceleration of electrons, which results in continuously accelerated electrons, known as runaway electrons. If no other loss mechanisms than the collisional drag are present [6], runaway electrons may be generated if the electric field exceeds the critical field [7]

$$E_{\mathrm{c}} = \frac{n_{\mathrm{e}} e^3 \ln \Lambda}{4\pi\varepsilon_0^2 m_0 c^2}, \tag{1}$$

where n_{e} is the electron density, m_0 is the electron rest mass, c is the speed of light, e is the elementary charge, and $\ln \Lambda$ is the Coulomb logarithm. The acceleration by a DC field of electrons that diffuse via small angle collisions beyond the critical momentum (p_{c}), defined as the minimum momentum for which collisions are too weak to prevent acceleration of the electrons by the electric field to even higher energies, is referred to as the Dreicer mechanism [7]. In addition, these relativistic electrons can undergo close collisions with bulk electrons and transfer part of their momentum so that also the target electrons may get kicked into the runaway momentum region, while the momentum of the primary electrons remains above the critical momentum. These knock-on collisions lead to multiplication of the number of runaway electrons, commonly referred to as runaway avalanche [3].

Various methods to mitigate the formation of runaway electrons in tokamak plasmas are based on either increasing the plasma density and thereby E_{c} by so-called massive gas injection (MGI) [8], or on deconfining the runaway electrons before they can reach too high an energy, by the means of resonant magnetic perturbations (RMP) [9]. Even though such mitigation methods have been demonstrated in present tokamak experiments, they might not provide a solution for runaways during disruptions in large tokamaks like ITER [10]. Therefore the formation of the runaway electron population is a topic in urgent need of investigation.

Disruptions are interesting but complex processes for studying the birth of runaway electrons, since they include magnetohydrodynamic (MHD) instabilities, anomalous transport and complex evolution of the magnetic field topology [11]. However, the generation of runaway electrons does not necessarily require the extreme conditions found in disruptions. In low density plasmas, the electric field can exceed the critical electric field also during the current flattop in a quiescent plasma [12], free of equilibrium transients, or during current ramp up or ramp down. An advantage of studying runaway formation in these so called non-disruptive scenarios is that the key parameters for the runaway electron mechanisms, mainly the electric field strength, electron density and temperature, can be better diagnosed than during disruptions. Runaway electrons have been detected in non-disruptive scenarios in several of the existing tokamaks [12, 13]. In this work the formation of runaway electrons generated from the combined effect of Dreicer and knock-on collision mechanisms is studied with the code LUKE, a solver of the 3D (one spatial and two momentum dimensions) linearized bounce-averaged relativistic electron Fokker–Planck equation [2]. The code LUKE handles arbitrary shapes of the flux surfaces, but in this work the magnetic flux surfaces are assumed to remain circular and concentric as in the Tore Supra tokamak. They are assumed to remain intact throughout the runaway formation process, an assumption that would be too restrictive for the thermal quench in disruptive scenarios.

Modelling the evolution of the temperature and electric field in disruptions would require a proper description of the thermal quench including radiative or convective loss mechanisms and MHD instabilities. The coupling of a kinetic code capable of handling 3D magnetic topologies and open field lines with a fluid code such as JOREK [14] would be necessary for such a purpose, but is beyond the scope of this work. The kinetic modelling of the formation of runaway electrons is therefore done for non-disruptive scenarios as found in the current flattop with constant electric field and plasma temperature. With the restrictions of disruption modelling in mind, the objective of this work is to study the formation of runaway electrons in non-disruptive scenarios owing to the combined effect of Dreicer and knock-on collisions with a fast solver for the electron distribution function, in order to make predictions for the birth of runaway electrons in tokamak experiments.

The LUKE code has previously been used for current drive and Dreicer runaway calculations. The model uses a relativistic collision operator for small angle collisions and a recently added description of the large angle (knock-on) collisions leading to the avalanche effect, which enables a description of the full 2D momentum dynamics of the runaway population. Runaway electrons generated via knock-on collisions are typically scattered off with a significant perpendicular component of the momentum with respect to the local magnetic field direction. In a non-uniform magnetic field configuration, highly magnetized electrons could be subject to magnetic trapping effects resulting in reduced runaway electron growth rate off the magnetic axis in comparison to estimates obtained for a cylindric geometry. Such toroidicity effects are studied by implementing a 2D kinetic description of the knock-on momentum dynamics, including the momentum dynamics both perpendicular and parallel to the magnetic field lines.

Knock-on collisions are included in the kinetic equation through a source term from [3], implemented along with a sink term to ensure a particle conserving form of the process. The bounce-averaged knock-on source term is presented in section 2. In section 3 the effect of magnetic field non-uniformity is investigated. The role played by the magnetic mirror force on the runaway population off the magnetic axis, owing to a reduction in Dreicer growth rate as well as the high magnetization of the knock-on electrons, is described. Finally, in section 4, the relative importance of the avalanche effect compared to the Dreicer mechanism is quantified as

a function of plasma temperature and toroidal electric field strength. The parametric dependencies of the relative importance of the avalanche effect obtained from the numerical modelling are related to both analytic predictions and experimental data from runaway observations in non-disruptive scenarios from several tokamaks. The comparison includes a low density flattop pulse from the Tore Supra tokamak, during which suprathermal electrons are observed. The analysis of this scenario supports recently published results [13], showing that runaway electron formation requires lower density than expected from collisional theory, which suggests the existence of additional runaway electron loss mechanisms.

2. Knock-on collisions model

A knock-on collision between an existing runaway electron and a slower electron is considered. This paper follows the model from [3] in which the target electron is assumed to be at rest whereas the initial runaway travels at the speed of light in the direction of the magnetic field. This approximation will be justified later in this section. The target electron gains a momentum p from the close collision. As both energy and momentum must be conserved in the collision process, the secondary electron is scattered with a pitch-angle with respect to the direction of the incoming electron, which cosine ξ^* is given by the relation

$$\xi^* = \sqrt{\frac{\gamma - 1}{\gamma + 1}}, \tag{2}$$

where $\gamma = \sqrt{1 + p^2}$ is the relativistic factor and the momentum p is normalized to $m_0 c$.

The relativistic electron electron differential cross section derived by Møller [15] yields

$$\frac{\mathrm{d}\sigma}{\mathrm{d}\Omega} = r_e^2 \frac{1}{p\gamma(\gamma - 1)^2} \delta(\xi - \xi^*(p)), \tag{3}$$

where $r_e = e^2/(4\pi\varepsilon_0 m_e c^2)$ is the classical electron radius. As $\mathrm{d}\sigma/\mathrm{d}\Omega$ decrease rapidly with momentum, a large fraction of secondary electrons have a moderate kinetic energy with $\gamma - 1 \ll 1$ and are thus scattered with a large pitch-angle characterized by $\xi^* \ll 1$. Hence it is necessary to properly account for the 2D guiding-center momentum dynamics in non-uniform magnetic field geometries, where the electrons are influenced by the magnetic trapping effect.

The source term originally formulated in [3] is proportional to both the target population, i.e. the bulk electron density n_e and the existing runaway electron population n_r

$$\begin{aligned} \mathbf{S}(\psi, p, \xi) &= n_e(\psi) n_r(\psi) c \frac{\mathrm{d}\sigma}{\mathrm{d}\Omega}(p, \xi) \\ &= \frac{n_r}{4\pi\tau \ln\Lambda} \frac{1}{p^2} \frac{\mathrm{d}}{\mathrm{d}p} \left[\frac{1}{1 - \sqrt{1 + p^2}} \right] \delta(\xi - \xi^*(p)), \end{aligned} \tag{4}$$

where ψ is the poloidal magnetic flux surface coordinate. In the expression above, the collision time for relativistic electrons

$$\tau = \frac{4\pi\varepsilon_0^2 m_e^2 c^3}{n_e e^4 \ln\Lambda}, \tag{5}$$

has been introduced.

An analytic estimate of the avalanche growth rate is obtained from integration of the knock-on source term in equation (4) over the runaway region $p > p_c$ in momentum space, as done in the work by Rosenbluth, which yields the following expression for $E > E_c$ [3]

$$\frac{1}{n_r} \frac{\partial n_r}{\partial t} = \frac{1}{2\tau \ln\Lambda} \left(\frac{E}{E_c} - 1 \right). \tag{6}$$

2.1. Implementation of knock-on collisions in the LUKE code

The Rosenbluth model (equation (4)) for the runaway generation through knock-on collisions is implemented in the code LUKE. Electrons with a momentum larger than $p_{re} \equiv \max[p_c; p(E_k = 1\ \mathrm{MeV})]$ are accounted for in the population n_r of primary runaways for the knock-on collision process. The numerical momentum grid boundary p_{max} must be chosen to be larger or equal to p_{re} and electrons leaving the domain through the boundary remain accounted for in n_r.

To be valid, the Rosenbluth approximation requires that: (a) primary runaways in the knock-on collision process have a velocity near the speed of light, and (b) primary electrons have a momentum much larger than target electrons. The condition (a) is ensured by the 1 MeV minimum condition in p_{re}, which corresponds to $v/c \geqslant 0.94$, whereas the condition (b) is guaranteed by restricting the model to plasmas with $T_e \ll 1$ MeV. The Rosenbluth approximation is further justified by the weak dependence of the knock-on source term upon the incident electron energy in the energy range 1–100 MeV [16].

The bulk electron density is defined as the integral of the bulk electron distribution in momentum space:

$$\int_0^{p_{re}} f(r, p) \mathrm{d}^3 p = n_e(r). \tag{7}$$

The bulk and the runaway region, corresponding to $p < p_{re}$ and $p > p_{re}$ respectively, are shown in figure 1. The runaway electron population is the integral over both Dreicer and knock-on runaway fluxes

$$n_r(t) = \int_0^t \left(\gamma_D + \int_{p_{re}}^{p_{max}} S \ \mathrm{d}^3 p \right) \mathrm{d}t,$$

where $\gamma_D = \int\int \mathbf{S_p}(\psi, p, \xi) \cdot \mathrm{d}\mathbf{S}$ is the integral of the particle flux through the surface $p = p_{re}$. In order to ensure conservation of number of particles in LUKE, a sink term is implemented to compensate for the knock-on source term

$$\mathbf{S} = \mathbf{S}_+ - <\mathbf{S}_+> \frac{f_M}{<f_M>}, \tag{8}$$

where f_M is the bulk distribution, assumed to be Maxwellian and $< ... >= \int_0^{p_{max}} ... \ \mathrm{d}^3 p$. The source and sink terms ensure that the number of electrons $n_e + n_r = n_{tot}$ is conserved.

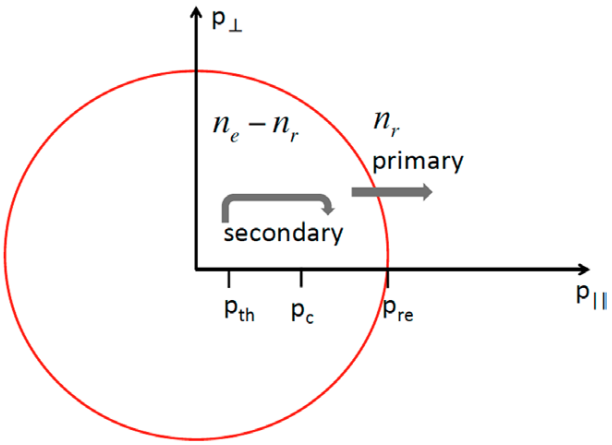


Figure 1. The LUKE momentum space is divided into two separate populations: the bulk electrons with momentum $p < p_{re}$ and the runaway electrons $p > p_{re}$. The knock-on collisions between the populations n_r and n_e can lead to secondary runaway electrons. Electrons that escape the domain $p < p_{re}$ by diffusion through p_{re} contribute to the runaway electron population n_r.

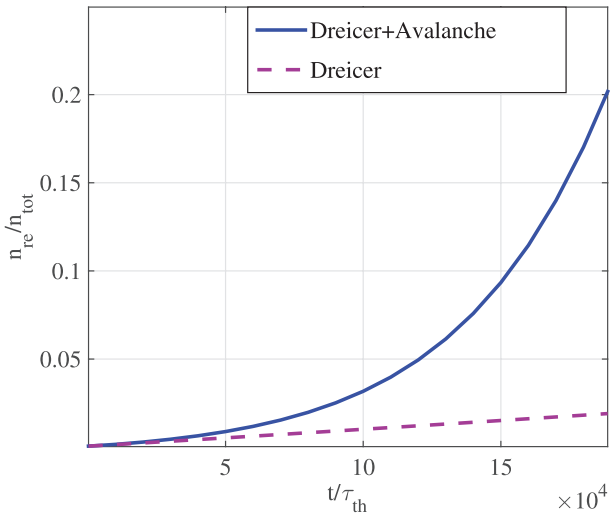


Figure 2. The fraction of runaway electrons ($E/E_c = 30$, $T_e = 0.5$ keV and $n_{tot} = 2 \cdot 10^{19}$ m^{-3}) as a function of time normalized to thermal collision time (here $\tau_{th} \approx 3.5 \cdot 10^{-6}$ s), with and without the avalanche effect due to the knock-on collisions.

2.2. Runaway electron growth rate

The runaway electron dynamics implemented in LUKE captures the combined effect of Dreicer and knock-on processes. The evolution of the runaway electron population under the influence of a constant electric field is calculated. Figure 2 shows the evolution of a runaway electron fraction with and without knock-on collisions. At first, there are very few runaway electrons, the knock-on contribution becomes significant only when a primary runaway electron population has been built up by the Dreicer effect. Then, an exponential growth of the runaway electron population is observed—describing the avalanche effect—and quickly becomes dominant over the Dreicer generation.

The avalanche mechanism is proportional to the bulk density $n_e = n_{tot} - n_r$, such that the runaway production rate can be expressed in the generic form

$$\frac{\partial n_r}{\partial t} = n_e(\gamma_D + \gamma_A) \rightarrow \frac{1}{(n_{tot} - n_r)}\frac{\partial n_r}{\partial t} = \gamma_D + \gamma_A. \quad (9)$$

To quantify the avalanche growth rate, the avalanche term may be expressed as $\gamma_A = n_r\bar{\gamma}_A$, where $\bar{\gamma}_A$ is an avalanche multiplication factor. Thus, equation (9) becomes:

$$\frac{1}{(n_{tot} - n_r)}\frac{\partial n_r}{\partial t} = \gamma_D + n_r\bar{\gamma}_A. \quad (10)$$

Equation (10) is an affine function of $n_r(t)$, where the constant term is the Dreicer growth rate and the avalanche multiplication factor is given by the slope. In figure 3 the growth rate given by equation (9) is illustrated for $E/E_c = 60$, $T_e = 0.5$ keV and $n_e = 2 \cdot 10^{19}$ m^{-3}. The growth rates from the LUKE calculations are evaluated numerically, the Dreicer as a constant value (γ_D) and the avalanche multiplication factor ($\bar{\gamma}_A$) from the slope of the curve. The Dreicer growth rate calculated by LUKE agrees well with predictions from Kulsrud [17] where the Fokker–Planck equation is solved numerically. The avalanche multiplication factor $\bar{\gamma}_A$ characterizes the tendency of a runaway avalanche to develop, for a given magnetic equilibrium and parallel electric field. The actual runaway production due to avalanche is however time dependent since it is a product of the avalanche multiplication factor $\bar{\gamma}_A$ and the time dependent runaway electron density n_r. For example, $\bar{\gamma}_A$ can be non-zero, even though the number of runaway electrons born from knock-on collisions is negligible until a seed of primary electrons is established.

For the sake of simplicity, the Rosenbluth model in [3] considers only secondary electrons born with a momentum larger than p_c. However, electrons accelerated via a knock-on collision to an intermediate momentum $p_{th} < p < p_c$ could contribute to the runaway growth rate indirectly by populating the suprathermal region and thereby modifying the Dreicer flux. Numerically, three thresholds must be defined when implementing the Rosenbluth model (4): the minimum and maximum values for the secondary electron momentum, and the minimum value p_{re} above which runaways are counted as primary electrons in the knock-on process. In order to determine these parameters, the lower threshold above which knock-on collisions are included is varied and the results are shown in figure 4 for electric field $E/E_c = 2$ and $E/E_c = 5$ ($T_e = 5$ keV). We can see that the indirect contribution of knock-on collisions to suprathermal energies $p_{th} < p < p_c$ is negligible, such that it is appropriate to set the lower threshold for secondary electron momentum at p_c. Energy conservation imposes that the higher threshold for secondary electron momentum is lower than p_{re}. We see that setting $p_{re} = 4p_c$ is sufficient to account for more than 80% of knock-on collisions while ensuring energy conservation.

2.3. Bounce-averaged knock-on source term

Since knock-on accelerated electrons emerge with high perpendicular momentum [3], it is necessary to properly account for the guiding-center dynamics in non-uniform magnetic

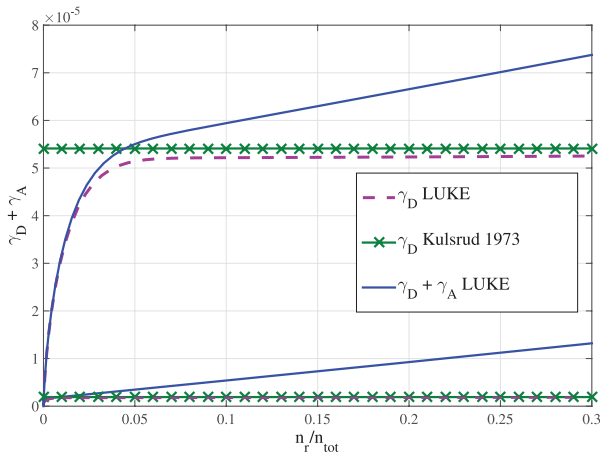


Figure 3. The growth rate in constant electric field in $T_e = 0.5$ keV and $n_{tot} = 2 \cdot 10^{19}$ m^{-3} for $E/E_c = 60$ i.e. $E/E_D = 0.06$ as a function of the runaway electron density, with and without the avalanche effect. For $n_r/n_{tot} < 0.05$ ($t \lesssim 2400\tau_{th} \approx 8$ ms) the growth rate has yet to reach its asymptotic value. The Dreicer contribution is in good agreement with Kulsrud's theory in the asymptotic limit [17]. The growth rates are normalized to the thermal collision frequency ($\nu_{th} = 1/\tau(v_{th}) \approx 2.9 \cdot 10^5$ s^{-1}).

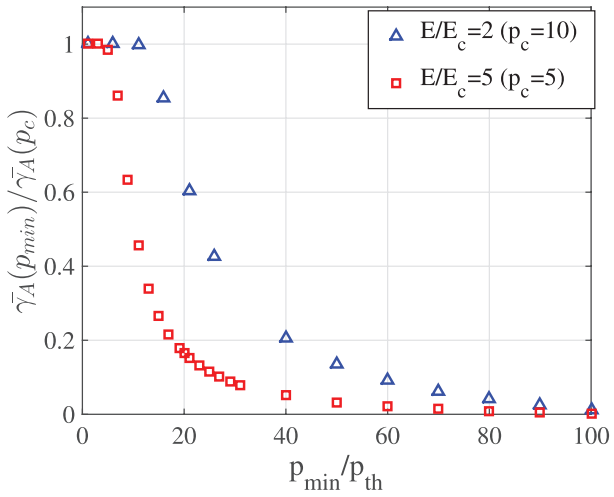


Figure 4. Avalanche multiplication factor as a function of the lower momentum cut off p_{min}/p_{th} for $T_e = 5$ keV, normalized to the avalanche factor at $p_{min} = p_c$.

field geometry and treat the full 2D momentum electron dynamics. In a non-uniform magnetic field, the magnetic moment is an adiabatic invariant such that the guiding center parallel velocity varies along the electron trajectory. The pitch angle coordinate ξ in equation (4) can be expressed as a function of (ξ_0, ψ, θ) where ξ_0 is the pitch angle measured at the poloidal position θ_0 of the minimum magnetic field $B_0(\psi)$ on a magnetic flux surface. When the collisional time is longer than the bounce period [2], the rapid poloidal motion ensures that the electron distribution $f(\psi, p, \xi_0)$ is independent of the poloidal angle θ. The poloidal angle dependence can thus be averaged out of the kinetic equation by bounce-averaging, defined as

$$\{\mathbf{S}\}(\psi, p, \xi_0) = \frac{1}{\lambda\tilde{q}}\left[\frac{1}{2}\sum_{\sigma}\right]_T \int_{\theta_{min}}^{\theta_{max}} \frac{d\theta}{2\pi}\frac{1}{|\hat{\psi}\cdot\hat{r}|}\frac{r}{R_p}\frac{B}{B_p}\frac{\xi_0}{\xi}\mathbf{S}(\psi, p, \xi), \tag{11}$$

where R_p is the major radius, θ_{min} and θ_{max} are the poloidal turning points for the trapped electrons, B_p is the poloidal component of the magnetic field B and the sum over σ applies to trapped particles (T) only. The normalized bounce time is

$$\lambda(\psi) = \frac{1}{\tilde{q}(\psi)}\int_{\theta_{min}}^{\theta_{max}} \frac{d\theta}{2\pi}\frac{1}{|\hat{\psi}\cdot\hat{r}|}\frac{r}{R_p}\frac{\xi_0}{\xi}\frac{B}{B_p}, \tag{12}$$

with

$$\tilde{q}(\psi) \equiv \int_0^{2\pi} \frac{d\theta}{2\pi}\frac{1}{|\hat{\psi}\cdot\hat{r}|}\frac{r}{R_p}\frac{B}{B_p}. \tag{13}$$

In the code LUKE, the electron distribution is normalized to a reference density $n_e^\dagger$ and the time evolution is normalized to the reference thermal collision frequency $\nu_{coll}^\dagger = 1/\tau(v_{th})$, so that the resulting source term is $\bar{\mathbf{S}} = \mathbf{S}/\mathbf{S}^\dagger$ where $\mathbf{S}$ is from equation (4) and $\mathbf{S}^\dagger = n_e^\dagger \nu_{coll}^\dagger$ Momentum is normalized to the thermal momentum $\bar{p} = p/p_{th}$. The knock-on source term is decomposed as $\bar{\mathbf{S}}(\mathrm{p}, \psi, \xi, \theta) = \bar{\mathbf{S}}^* \delta(\xi - \xi^*(\bar{\mathrm{p}}))$ where

$$\bar{\mathbf{S}}^* = \frac{1}{4\pi}\frac{\beta_{th}^{\dagger 2}}{\ln\Lambda^\dagger}\bar{n}_e\bar{n}_r\frac{1}{\bar{p}\gamma(\gamma-1)^2}, \tag{14}$$

is independent of θ, so that $\{\bar{\mathbf{S}}\} = \bar{\mathbf{S}}^*\{\delta(\xi - \xi^*(\bar{p}))\}$, where $\beta_{th}^\dagger = v_{th}^\dagger/c$ and ξ is the pitch angle cosine at the poloidal angle position θ

$$\xi(\xi_0, \psi, \theta) = \sigma\sqrt{1 - \Psi(\psi, \theta)(1 - \xi_0^2)}. \tag{15}$$

Here $\Psi(\psi, \theta) = B(\psi, \theta)/B_0(\psi)$ and $\sigma = \mathrm{sign}(v_\parallel) = \mathrm{sign}(\xi_0)$ indicates the direction of the electrons along the magnetic field line. Using the general relation for Dirac's delta function $\delta(g(x)) = \sum_k \delta(x - x_k)/|g'(x_k)|$ where x_k are the zeros of the function $g(x)$ and $g'(x) = \mathrm{d}g/\mathrm{d}x$ provided that $g(x)$ is a continuously differentiable function and $g'(x)$ is non-zero:

$$\delta(\xi - \xi^*) = \sum_k \frac{2\delta(\theta - \theta_k^*)|\xi^*|}{|\Psi'(\psi, \theta_k^*)|(1 - \xi_0^2)}, \tag{16}$$

where θ_k^* is the poloidal angle at which the secondary electron emerges. From equation (15) θ_k^* is given by

$$\sigma\sqrt{1 - \Psi(\psi, \theta_k^*)(1 - \xi_0^2)} - \xi^* = 0, \tag{17}$$

or

$$\Psi(\psi, \theta_k^*) = \frac{B_{\theta_k^*}}{B_0} = \frac{1 - \xi^{*2}}{1 - \xi_0^2} = \frac{2}{(1 - \xi_0^2)(\gamma + 1)}. \tag{18}$$

Using equation (16), the delta function can be expressed as

$$\{\delta(\xi - \xi^*)\} = \frac{1}{\lambda\tilde{q}}\frac{1}{\pi}\sum_k \frac{1}{|\hat{\psi}\cdot\hat{r}|_{\theta_k^*}}\frac{r_{\theta_k^*}}{R_p}\frac{B_{\theta_k^*}}{B_{p,\theta_k^*}}\frac{\xi_0}{\xi_{\theta_k^*}}\frac{|\xi^*|}{|\Psi'(\psi, \theta_k^*)|(1 - \xi_0^2)}.$$

and since $B_{\theta_k^*} = (1-\xi^{*2})/(1-\xi_0^2)B_0$ with $\xi_{\theta_k^*} = \xi^*$

$$\{\delta(\xi-\xi^*)\} = \frac{1}{\lambda\tilde{q}}\frac{1}{\pi}\sum_k \frac{1}{|\hat{\psi}\cdot\hat{r}|_{\theta_k^*}}\frac{r_{\theta_k^*}}{R_p}\frac{B_0}{B_{p,\theta_k^*}}|\xi_0| \times \frac{(1-\xi^{*2})}{|\Psi'(\psi,\theta_k^*)|(1-\xi_0^2)^2}, \tag{19}$$

and the normalized, bounce-averaged avalanche operator becomes

$$\{\bar{\mathbf{S}}(p,\psi,\xi_0)\} = \frac{1}{2\pi^2}\frac{1}{\ln\Lambda}\bar{n}_e\bar{n}_r \times \frac{1}{\bar{p}^3\gamma(\gamma-1)}\frac{B_0}{\lambda\tilde{q}}\frac{|\xi_0|}{(1-\xi_0^2)^2}\sum_k\left[\frac{1}{|\hat{\psi}\cdot\hat{r}|}\frac{r}{B_p}\frac{1}{|\Psi'|}\right]_{\theta_k^*}, \tag{20}$$

using the relation $p^2 = (\gamma^2-1) = (\gamma-1)(\gamma+1)$ and $p = \bar{p}\beta_{\text{th}}$.

3. Effect of toroidicity

The reduction of the Dreicer runaway rate away from the magnetic axis has been identified in previous work [18] including with the code LUKE, which solves the bounce-averaged kinetic equation [2]. The poloidal dependence of the electric field is accounted for and the input value is the flux-surface averaged elecric field. At least three effects contribute to reduce the growth rate: the overall effect of the electric field on trapped electrons cancels out over one bounce period; the acceleration of passing electrons is also reduced as their pitch angle increases towards the high field side; the existence of a magnetic trapping cone creates larger pitch-angle gradients in the circulating region, thereby increasing the effect of pitch-angle scattering.

As discussed in section 2, secondary electrons emerging from the knock-on collisions are typically highly magnetized. Since the trapping effect increases off the magnetic axis in a non-uniform magnetic field configuration, the further away from the magnetic axis the electrons appear, the more they tend to be born trapped [3].

To quantify the tendency of magnetic trapping, the evolution of the runaway population is calculated in a scenario with circular plasma cross section and magnetic non-uniformity, with the inverse aspect ratio ranging from $\epsilon = 0$ to $\epsilon = a/R = 1$. The inverse aspect ratio of the Tore Supra tokamak is $\epsilon \approx 0.3$. The calculations in figure 5 reveal that the runaway electron population grows significantly slower off the magnetic axis than in the center.

In order to study the trapping effects on the runaway population, the Dreicer growth rate γ_D and the avalanche multiplication factor $\bar{\gamma}_A$ are calculated with the bounce-averaged code LUKE and quantified separately. The Dreicer growth rate is found to be strongly affected by the non-uniformity of the magnetic field, as shown in figure 6. A fit of the numerical results gives an analytic expression of the Dreicer growth rate $\gamma_D/\gamma_{D,\text{cyl}} = 1-\sqrt{2\epsilon/(1+\epsilon)}$. The results indicate that

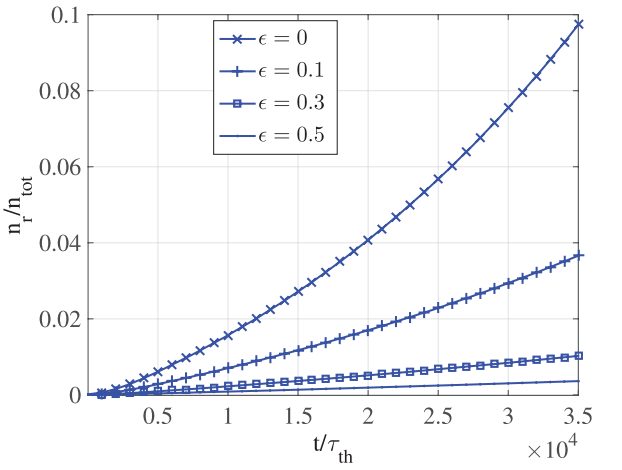


Figure 5. The evolution of the runaway electron population, including the avalanche effect owing to knock-on collisions, depends strongly on the radial position in a non-uniform magnetic field configuration, where $\epsilon = r/R$ is the inverse aspect ratio coordinate. $E/E_c = 40$, $T_e = 0.5$ keV, $n_e = 2\cdot 10^{19}$ m^{-3} and the time t is normalized to the thermal collision time $\tau_{th} \approx 3.5\cdot 10^{-6}$ s.

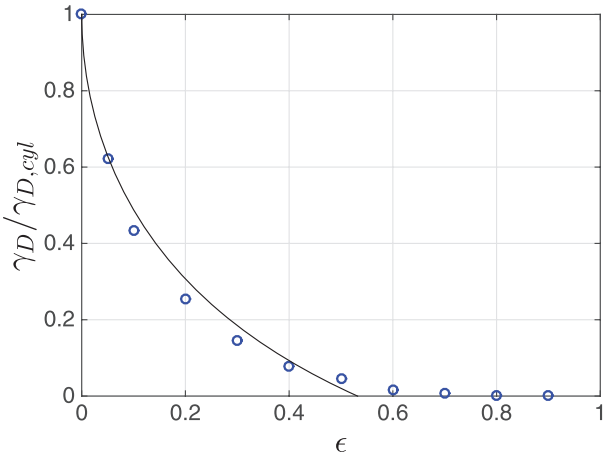


Figure 6. Radial dependence of Dreicer growth rate, normalized to the growth rate for cylindrical case $\epsilon = 0$ and a fit $\gamma_D/\gamma_{D,\text{cyl}} = 1 - 1.2\sqrt{2\epsilon/(1+\epsilon)}$.

for $\epsilon > 0.5$ runaway generation from Dreicer acceleration vanishes.

A reduction of $\bar{\gamma}_A$ away from the magnetic axis is observed in figure 7, with an avalanche multiplication factor that decreases with the inverse aspect ratio. In order to derive an analytical estimate for the avalanche growth rate including the effect of magnetic trapping owing to a non uniform magnetic configuration, it is assumed that all electrons with momentum $p > p_c$ will contribute to the runaway population (as in [3]), except the secondary electrons that appear in the trapped momentum region $p < p_T$. The magnetic trapping criterion on the momentum p_T of secondary electrons born via knock on collisions is

$$\frac{B(\theta)}{B_{\max}} > \frac{2}{\sqrt{1+p_T^2}+1}, \tag{21}$$

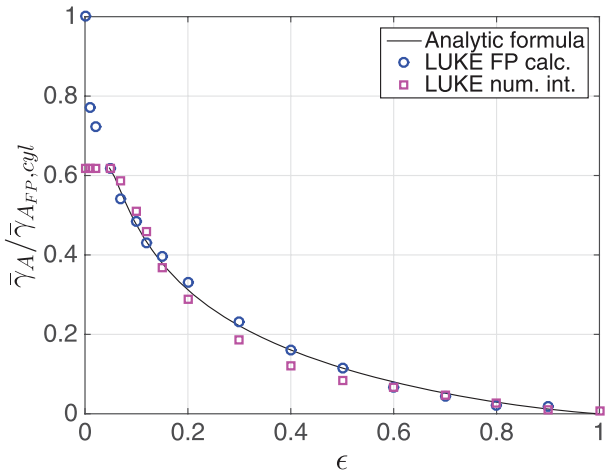


Figure 7. Radial dependence of the avalanche multiplication factor from bounce-averaged LUKE calculations (circles), normalized to to the avalanche multiplication factor for the cylindrical case $\epsilon = 0$. The numerical integration over the knock-on source term in equation (4) with the toroidal dependence in the momentum integration boundary is plotted in squares. The solid line shows the analytic estimate of the growth rate off the magnetic axis from equation (A.4).

where $B_{max}/B(\theta) = (1 + \epsilon\ \cos\ \theta)/(1 - \epsilon)$ in a circular concentric magnetic configuration. Electrons will run away if their momentum exceeds both the critical momentum and the trapping condition in equation (21). The lower integration limit p_{min} for the analytical estimate of the avalanche growth rate is thus given by $\max(p_c, p_T)$. An analytical expression for the inverse aspect ratio dependent avalanche growth rate is obtained by integrating the source term from over momentum space from p_{min} to $p_{max} = \infty$, which results in a locally modified, inverse aspect ratio dependent avalanche growth rate

$$\begin{aligned}\frac{\mathrm{d}n_r}{\mathrm{d}t_n}(\theta,\epsilon) &= \frac{1}{2}\frac{1}{\ln\,\Lambda^\dagger}\bar{n}_e\bar{n}_r\frac{1}{\sqrt{1+p_{min}^2}-1}\\ &= \frac{1}{2}\frac{1}{\ln\,\Lambda^\dagger}\bar{n}_e\bar{n}_r\,\min\left(\frac{E}{E_c},\frac{(1-\epsilon)^2}{2\epsilon(1+\cos\theta)}\right).\end{aligned} \tag{22}$$

The flux surface averaged growth rate is derived in appendix A. For $\epsilon E/E_c \gg 1$, $\theta_b \to \pi$, the growth rate is reduced by a factor $(1-\epsilon)^2/\left(\pi\sqrt{\epsilon E/E_c}\right)$. The inverse aspect ratio dependence of the estimated avalanche growth rate obtained from equation (22) is compared to numerical results. In addition, a numerical integration of the source term is also performed, with the same criterion on the lower integration boundary in momentum space p_{min} as the analytic estimate in equation (A.4). The analytic result is also compared to avalanche growth rate from Fokker–Planck calculations with the LUKE code. In that case, the trapping conditions are the same as in the analytic result, except for that the critical momentum is pitch angle dependent $p_c^2 = E_c/(E\xi)$. The LUKE calculated avalanche multiplication factor and the analytical estimate show good agreement (figure 7).

Figure 7 shows the reduced growth rate for $E/E_c = 5$, relative to a cylindric plasma, equivalent to the growth rate on the magnetic axis ($\epsilon = 0$). Numerical integration of the source term shows good agreement with the analytic result (equation (A.4)). Close to the center, at low inverse aspect ratio, the effect of trapping is not visible, since the critical momentum is higher than the trapped momentum over the whole flux surface. This effect decreases with increasing E/E_c as the critical momentum p_c decreases and becomes less restrictive compared to the trapping condition p_T, which explains the flat top seen in figure 7. However, for the FP calculations the magnetic trapping effect influences the growth rate also close to the magnetic axis. A possible explanation is pitch angle collisions that couple the dynamics between the trapped and the passing region.

The growth rate obtained from bounce-averaged calculations suggest that the formation of runaway electrons is slower the further away from the magnetic axis they appear. In other words, the time scale of the local growth rate could be longer than suggested by collisional theory [3, 17]. Potential loss mechanisms, such as transport of fast electrons due to magnetic field perturbations [19] could therefore act more efficiently on the runaway electrons formed off the magnetic axis than the ones formed on axis which could lead to well confined runaway electrons at the center of the plasma.

4. The relative importance of the avalanche effect

The results presented in section 2.2 (see figure 2) have shown that the runaway electron distribution can be significantly modified by including the effect of knock-on collisions. In order to understand the mechanisms that govern the runaway electron generation processes a parametric study is performed with the aim to investigate which runaway formation process, Dreicer or avalanche, dominates in non-disruptive tokamak experiments.

The relative importance of the avalanche mechanism to the Dreicer mechanism can be estimated by comparing the analytic avalanche growth rate in equation (6) and the Dreicer generation that is derived in [6]:

$$\left(\frac{\partial n_r}{\partial t}\right)_D \sim \frac{2}{\sqrt{\pi}}n_e\nu(v_{th})\left(\frac{E}{E_D}\right)^{1/2}\exp\left(-\frac{E_D}{4E}-\left(\frac{2E_D}{E}\right)^{1/2}\right),$$

where $E_D = (c/v_{th})^2 E_c$ is the electric field at which even thermal electrons will run away, known as the Dreicer field. The ratio of the two growth rates is

$$\frac{\gamma_A}{\gamma_D} \sim \frac{\sqrt{\pi}}{4}\frac{n_r}{n_e}\frac{1}{\ln\Lambda}\left(\frac{v_{th}}{c}\right)^3\left(\frac{E}{E_c}-1\right)\left(\frac{E}{E_D}\right)^{-1/2}\exp\left(\frac{E_D}{4E}+\sqrt{\frac{2E_D}{E}}\right). \tag{23}$$

By letting a small fraction of electrons run away in LUKE, the relative importance of the avalanche effect as a function of plasma temperature and electric field strength can be evaluated numerically from the fraction of the runaway electrons that originate from Dreicer and knock-on collisions. In figure 8 the fraction of runaway electrons born from knock-on collisions is shown, when 1% of the initial electron population has run away in a cylindrical magnetic configuration with constant electric field, density and temperature. The fraction of

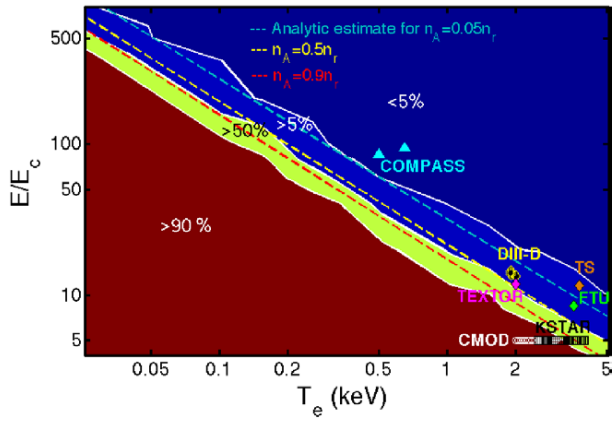


Figure 8. The fraction of runaways originating from knock-on collisions (n_A/n_r) as modelled in LUKE. The analytic estimate of when 5% (cyan line), 50% (yellow line) and 90% (red line) of the runaways come from avalanche is obtained from equation (23). Non-disruptive scenarios where runaway electrons were generated in several tokamaks are taken from [13] except for the Tore Supra (TS) point (discharge #40719) and COMPASS points (discharge #8555 and #8630).

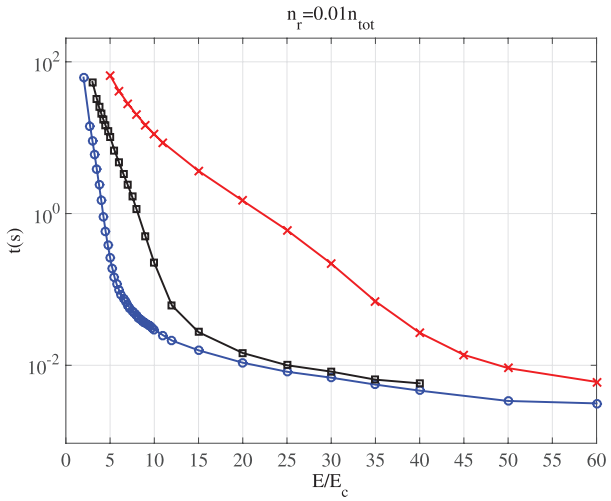


Figure 9. The time required for 1% of the Maxwellian electrons to run away, for the electron temperature $T_e = 0.5$ keV (dashed line), 2 keV (solid line and squares) and 5 keV (solid line and circles).

runaway electrons has to be small enough for the equilibrium parameters to remain constant. The relative importance of secondary runaway electrons grows at lower temperature and electric field, as the slower primary generation in high collisionality (low temperature) allows for runaway avalanches to take off. The time required to reach the runaway fraction varies strongly in the parameter space presented in figure 8. The time required for 1% of the electrons to run away is illustrated for various electron temperatures ($T_e = 0.05, 0.5, 2$ and 5 keV) in figure 9. The formation of runaway electrons slows down as the collisionality increases at lower bulk temperature.

The numerical results are compared with the analytical estimate from equation (23) with $n_r/n_e = 0.01$. The condition for the dominance of the avalanche effect $\gamma_A/\gamma_D > 1$ is plotted in figure 8 along with the boundaries for which $n_A/n_r = 5\%$ and 90%.

In order to relate the study to experimental tokamak scenarios, it must be noted that the simulations are performed for constant electric field and temperature. Consequently, the study is restricted to non-disruptive scenarios with well-diagnosed and quiescent conditions from several tokamaks, where runaway electrons have been observed in the current flattop with the relevant plasma parameters maintained essentially constant. Results from scenarios with reproducible measurements of electron density, loop voltage and plasma temperature at the runaway electron onset from DIII-D, FTU, TEXTOR, Alcator C-Mod and KSTAR were recently published in [13]. From this study the threshold electric field normalized to the critical field is found to be significantly higher than predicted by collisional theory where the birth of runaway electrons is predicted at $E/E_c > 1$, provided that no additional runaway electron loss mechanisms are present [17]. However, the condition for runaway onset in collisional theory does not take the time required to generate runaway electrons into account. Estimations from LUKE calculations in figure 9 shows that this time scale can be unrealistically large as compared to the tokamak discharge duration. The time to generate a small fraction of runaway electrons from a Maxwellian distribution is finite for $E/E_c > 1$ but as $E/E_c \to 1$, the required time to generate runaway electrons $t \to \infty$. However, it is not the only explanation since the study in [13] found that the E/E_c threshold for suppression is also well above unity.

Runaway electrons have been generated in the Tore Supra (TS) tokamak in low density discharges ($n_e < 10^{19}$ m^{-3}). The TS pulses #40719 and #40721 are performed after a boronization and suprathermal electrons are observed in the former discharge but not in the latter. Both are ohmic discharges at $I_p = 0.6$ MA in the current flattop. A possible signature of suprathermal electrons is observed in #40719 by the ECE edge chords at current ramp-up and ramp-down, when the density is low ($< n_e > = 0.4 \cdot 10^{19}$ m^{-3}), see figure 10(a). The uniform E-field, estimated as the time derivative of the resistive flux [20], is $E_\parallel = 0.038 \pm 0.003$ V m^{-1} and the core temperature is 3.8 keV. The determination of the magnetic flux at the plasma boundary is described in [21]. No suprathermal electrons are detected by electron cyclotron emission (ECE) in the following pulse #40721 at a higher electron density, see figure 10(b). Similar result is found from HXR measurements from the vertical camera detecting emission of 20–200 keV (figure 11). A peak of photo-neutrons is observed at the plasma termination for the lower density shot (#40719) but not for the higher density shot (#40721). It must be noted that the ECE signal alone is not a definite signature of runaway electrons, as its interpretation depends on the optical thickness of the plasma. However, it is from the combined observations on ECE, HXR and photo-neutron measurements, that the presence of relativistic electrons during the ramp-down of #40719 is identified. During the current flattop of #40719, the electron density is $< n_e > = 0.64 \cdot 10^{19}\, m^{-3}$, corresponding to $E/E_c \approx 8$ or $E/E_D \approx 0.06$, but there is no sign of suprathermals until $E/E_c \approx 11$. The suprathermal generation in #40719 is added to the $(E/E_c, T_e)$ scan (see figure 8) and lands in the region where Dreicer generation is dominant. In the higher density pulse

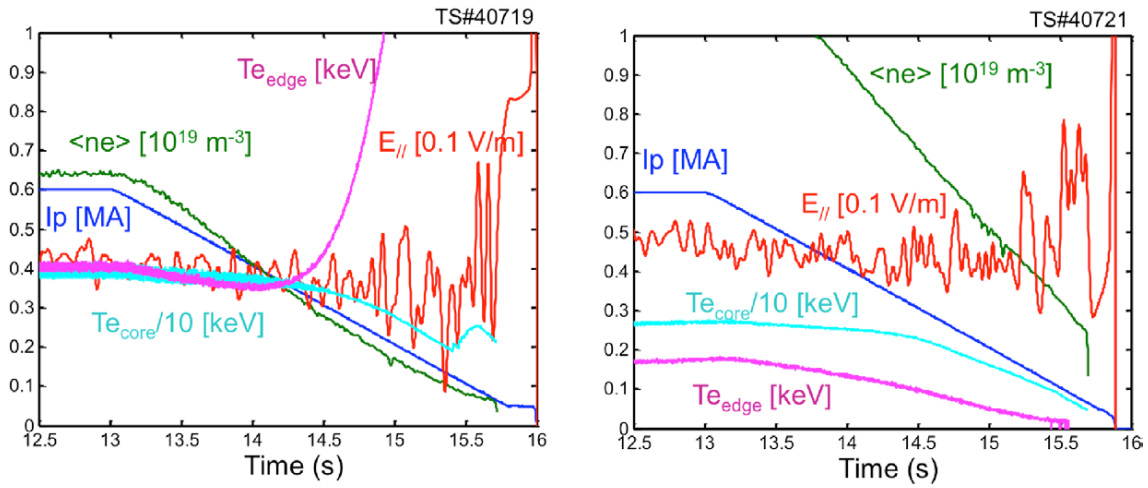


Figure 10. Possible signature of suprathermal electrons on the edge ECE chord ($T_{e,edge}$) at around $t = 14.5$ s are seen in the Tore Supra discharge 40719 (left). In a following discharge, with higher density (right), there is no sign of suprathermal electrons on the ECE measurements. E_l is the electric field strength, $<n_e>$is the line averaged density and l_p is the plasma current.

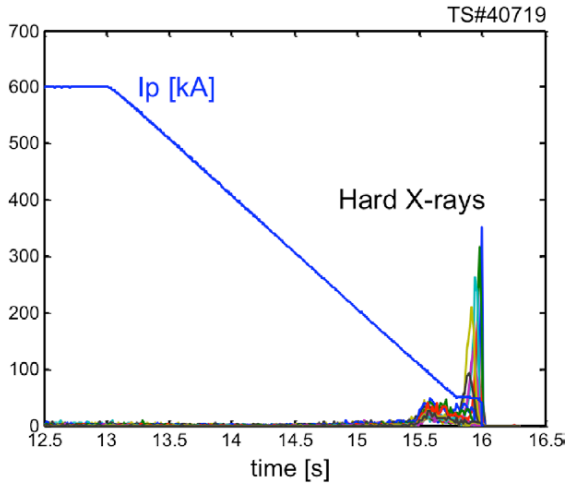


Figure 11. HXR data from the vertical camera (channels 1–21) in the energy range $E_{HXR} = 20$–200 keV. The HXR emission produced in the current ramp down in 40719 is a signature of suprathermal electrons, whereas in the higher density discharge 40721 no HXR emission is detected.

(#40721) $E/E_c \approx 4$ or $E/E_D = 0.02$ during the current flattop and no suprathermal electrons are detected. These results are in line with those of [13] where $E/E_c \sim 3$–12 is required to generate a detectable population of runaway electrons in the various tokamaks.

Relating the data from the experiments in [13] and the TS discharge #40719 to the parameter scan done in LUKE (figure 8) reveals that the scenarios fall in or close to the region where the avalanche mechanism becomes significant for the runaway electron growth rate (figure 8). Data from two COMPASS discharges where runaways were observed (#8555 and #8630) fall in the region where the Dreicer effect is dominant [22]. Runaway electrons are commonly produced in the current ramp-up phase of the COMPASS tokamak, due to the relatively high E/E_c ratio (20–200). The circular 130 kA discharge #8555 was part of the flattop line averaged electron density $< n_e >$ scan from $1–4 \cdot 10^{19}$ m^{-3}, where $< n_e >$ for this particular shot was $2 \cdot 10^{19}$ m^{-3} during the flattop. The rise in runaway activity was observed with HXR NaI(Tl) scintillator and photoneutron detector as the $< n_e >$ decreased from discharge to discharge, while Parail–Pogutse instability appeared for all discharges with $< n_e >$ lower than in the discharge #8555. D-shaped 160 kA discharge #8630 was done for the purpose of the sawteeth-runaway correlation studies with the electron density $< n_e > = 9 \cdot 10^{19}$ m^{-3}. Even though the discharge had relatively high $< n_e >$, the runaway activity correlated with the sawteeth instability was visible in HXR and photoneutron signals. These two COMPASS discharges #8555 and #8630 are plotted on figure 8, where E/E_c at the ramp-up phase were 85 and 94, respectively. The electron density at the time of the runaway detection is $1.1 \cdot 10^{19}$ and $0.80 \cdot 10^{19}$ m^{-3}. In COMPASS, interferometry is used for the line averaged electron density $< n_e >$ measurements, while Thomson scattering is used for electron temperature T_e and electron density n_e profile measurements.

These observations suggest that knock-on collisions may contribute to the formation of runaway electron generation in tokamak plasmas, even in non-disruptive scenarios. The study predicts that avalanches can play an important role during current flattop. A self consistent electric field and equilibrium solver would be necessary to study avalanches with LUKE in disruptions, but is beyond the scope of the current work.

5. Conclusion

In this work the growth of runaway electron populations through the combined effect of Dreicer and knock-on collision mechanisms is studied. The Rosenbluth [3] model is extended to non-uniform magnetic field configurations and implemented as a bounce-averaged conservative source/sink term within the kinetic equation in the 3D Fokker–Planck solver LUKE. Dependencies of key parameters such as electric field

strength, electron temperature, and density are investigated. In addition, magnetic trapping effects are quantified in a non-uniform magnetic equilibrium, resulting in a reduced runaway population off the magnetic axis for both the Dreicer and the avalanche mechanism.

The kinetic modelling of the formation of runaway electrons is restricted to non-disruptive scenarios as found in the current flattop with non-transient electric field and plasma temperature. Modelling the rapidly varying temperature and electric field found in disruptions would require a proper description of the thermal quench with implemented radiative or convective loss mechanisms of the plasma energy, including MHD instabilities. The extension of the kinetic code LUKE to 3D magnetic configuration and its coupling with a fluid code such as JOREK [14] would be necessary for such a purpose and is beyond the scope of this work. In the present paper, runaways are confined to the flux-surface where they are generated, such that the growth rate derived herein should be considered as upper estimates.

Since knock-on accelerated electrons emerge with high perpendicular momentum, the full 2D guiding-center momentum dynamics is taken into account via a bounce-averaged description. The effect of magnetic trapping of the electrons in a non-uniform magnetic field configuration, known as the magnetic mirror effect, has been investigated, revealing reduction of both Dreicer and avalanche mechanisms off the magnetic axis. An analytical expression for avalanche growth rate accounting for magnetic trapping is derived. It is in agreement with numerical simulations and shows that a significant proportion of secondary electrons are knocked into the trapped region off the magnetic axis. The reduction of the off axis growth rate implies that the time scale of runaway formation is longer at the edge than close to the center, which means that potential loss mechanisms such as radial electron transport could compete with the acceleration of runaway electrons at the edge.

Moreover, quantifying the relative importance of avalanche generation as a function of plasma temperature and electric field strength, the simulations reveal that runaway electrons originating from knock-on collisions dominate at low temperature and electric field strength and likely play a significant role in runaway generation processes in several tokamaks with data from non-disruptive scenarios that are presented in [13]. The onset of runaway electrons found in these experiments is related to LUKE simulations of corresponding electric field and temperature in order to evaluate the importance of the avalanche effect, revealing that knock-on collisions may play a significant role also in non-disruptive scenarios. The LUKE calculations predict runaway electron generation also in a near critical field, in agreement with collisional theory if no other runaway electron loss mechanisms than collisional damping are present. However, the time to generate runaway electrons can be significantly greater compared to the duration of the phase in which $E/E_c > 1$ in experiments. In addition, the required time for runaway electron formation is very sensitive to the bulk electron temperature. The lack of runaway electron signatures near the critical electric field could therefore be explained by the long time scale required for their formation. To understand this discrepancy between observations and theory, the existence of additional loss mechanisms that dominate during the current flattop must be addressed. One possible candidate is transport of fast electrons due to magnetic field perturbations [19]. Once such additional runaway electron loss mechanisms have been identified, the LUKE code may form an excellent test bed for quantifying these effects, which will be the objective of future work.

Acknowledgments

This work has been carried out within the framework of the EUROfusion Consortium and has received funding from the Euratom research and training programme 2014-2018 under grant agreement No 633053. The views and opinions expressed herein do not necessarily reflect those of the European Commission.

Appendix A. Derivation of toroidicity dependent avalanche growth rate

As described in section 3, the avalanche growth rate is evaluated by the flux surface averaged knock-on source term in equation (4) where the lower integration boundary is set by the maximum of the critical momentum p_c and the momentum defining the boundary of a passing and a trapped electron p_T, given by the trapping condition in equation (21). For finite E/E_c, the critical momentum $p_c > 0$. As the growth rate is averaged over the poloidal angle, $p_{min} \to p_c$ as the high field side is approached ($p_T \to 0$ as $\theta \to \pi$). The growth rate becomes:

$$\frac{dn_r}{dt_n}(\theta,\epsilon) = \frac{1}{2}\frac{1}{\ln\Lambda^\dagger}\bar{n}_e\bar{n}_r\frac{1}{\sqrt{1+p_{min}^2}-1} \tag{A.1}$$

$$= \frac{1}{2}\frac{1}{\ln\Lambda^\dagger}\bar{n}_e\bar{n}_r \min\left(\frac{E}{E_c}, \frac{(1-\epsilon)^2}{2\epsilon(1+\cos\theta)}\right). \tag{A.2}$$

The poloidal angle θ_{bound} where $p_c = p_T$ constitutes the boundary between the region where the avalanche rate is limited either by the drag force or by the magnetic trapping effect. This angle is obtained from the condition $p_c = p_T$:

$$1+\cos\,\theta_{bound} = (1-\epsilon)^2/\left(2\epsilon\frac{E}{E_c}\right) \to$$

$$\theta_{bound} = \pm\arccos\left((1-\epsilon)^2/\left(2\epsilon\frac{E}{E_c}\right)-1\right).$$

If $\epsilon E/(E_c(1-\epsilon)^2) < 1/4$, p_c is the lower integration limit p_{min} and if $\epsilon E/(E_c(1-\epsilon)^2) > 1/4$, $p_{min} = p_T(\theta)$. Averaged over the flux surface according to volumic flux surface average the growth rate is:

$$< \frac{\mathrm{d}n_\mathrm{r}}{\mathrm{d}t_n} >_V (\epsilon) = \frac{1}{\hat{q}}\left(\frac{1}{\pi}\int_0^{\theta_\mathrm{bound}} \epsilon \frac{B_0(\epsilon)}{B_P}\frac{\mathrm{d}n_\mathrm{r}}{\mathrm{d}t_n}(p_\mathrm{T}(\theta))\mathrm{d}\theta + \frac{1}{\pi}\int_{\theta_\mathrm{bound}}^{\pi} \epsilon \frac{B_0(\epsilon)}{B_P}\frac{\mathrm{d}n_\mathrm{r}}{\mathrm{d}t_n}(p_\mathrm{c})\mathrm{d}\theta\right) = \frac{1}{2}\frac{1}{\ln\Lambda^\dagger}\bar{n}_\mathrm{e}\bar{n}_\mathrm{r} \times\left((1+\epsilon)\frac{B_p}{B}\frac{1}{\pi}\int_0^{\theta_\mathrm{bound}} \frac{B_0(\epsilon)}{B_P}\frac{(1-\epsilon)^2}{2\epsilon(1+\cos\theta)}\mathrm{d}\theta + (1+\epsilon)\frac{E}{E_\mathrm{c}}\frac{1}{\pi}\int_{\theta_\mathrm{bound}}^{\pi}\frac{(1+\epsilon\,\cos(\theta))}{1+\epsilon}\mathrm{d}\theta\right). \tag{A.3}$$

In the above calculation circular concentric flux surfaces are considered so that $|\widehat{\psi}\cdot\hat{r}|= 1$, $r/R_p = \epsilon$ and

$$\hat{q} = \int_0^{2\pi}\frac{\mathrm{d}\theta}{2\pi}\epsilon\frac{B_0}{B_p} = \int_0^{2\pi}\frac{\mathrm{d}\theta}{2\pi}\epsilon\frac{(1+\epsilon\,\cos(\theta))}{(1+\epsilon)}\frac{B}{B_p} = \frac{\epsilon}{(1+\epsilon)}\frac{B}{B_p}.$$

The flux surface averaged growth rate takes the form:

$$< \frac{\mathrm{d}n_\mathrm{r}}{\mathrm{d}t_n} >_V(\epsilon) = \frac{1}{2\,\ln\Lambda^\dagger}\bar{n}_\mathrm{e}\bar{n}_\mathrm{r}\frac{E}{E_\mathrm{c}} \times\left(1-\frac{\theta_\mathrm{bound}}{\pi}-\frac{\epsilon}{\pi}\sin(\theta_\mathrm{bound})\right) + (1-\epsilon)^2\frac{1}{2\epsilon\pi}((1-\epsilon)\tan(\theta_\mathrm{bound}/2)+\epsilon\theta_\mathrm{bound}) = \frac{1}{2\,\ln\Lambda^\dagger}\bar{n}_\mathrm{e}\bar{n}_\mathrm{r}\frac{E}{E_\mathrm{c}}\times\left(1-\frac{\theta_\mathrm{bound}}{\pi}-\frac{\epsilon}{\pi}\sin(\theta_\mathrm{bound}) + \frac{(1-\epsilon)^2E_\mathrm{c}}{2\epsilon\pi E}\left(\sqrt{1-\epsilon}\,\sqrt{4\epsilon E/E_\mathrm{c}-(1-\epsilon)}+\epsilon\theta_\mathrm{bound}\right)\right), \tag{A.4}$$

where

$$\tan(\theta_\mathrm{bound}/2) = \frac{\sin(\theta_\mathrm{bound})}{1+\cos(\theta_\mathrm{bound})} = \frac{\sqrt{4\epsilon E/E_\mathrm{c}-(1-\epsilon)}}{\sqrt{1-\epsilon}}.$$

For $\epsilon E/E_\mathrm{c} \gg 1$, $\theta_b \to \pi$ and the growth rate is reduced by a factor $(1-\epsilon)^2/\left(\pi\sqrt{\epsilon E/E_\mathrm{c}}\right)$.

References

[1] Hender T C *et al* 2007 MHD stability, operational limits and disruptions *Nucl. Fusion* **47** S128–202

[2] Decker J and Peysson Y 2004 DKE: a fast numerical solver for the 3D drift kinetic equation *Report* EUR-CEA-FC-1736, Euratom-CEA

[3] Rosenbluth M N and Putvinski S V 1997 Theory for avalanche of runaway electrons in tokamaks *Nucl. Fusion* **37** 1355–62

[4] Wesson J A *et al* 1989 Disruptions in JET *Nucl. Fusion* **29** 641–66

[5] Tavani M *et al* 2011 Terrestrial gamma-ray flashes as powerful particle accelerators *Phys. Rev. Lett.* **106** 018501

[6] Connor J W and Hastie R J 1975 Relativistic limitations on runaway electrons *Nucl. Fusion* **15** 415–24

[7] Dreicer H 1959 Electron and ion runaway in a fully ionized gas. I *Phys. Rev.* **115** 238–49

[8] Lehnen M *et al* 2011 Disruption mitigation by massive gas injection in JET *Nucl. Fusion* **51** 123010

[9] Lehnen M *et al* 2009 Runaway generation during disruptions in JET and TEXTOR *J. Nucl. Mater.* **390–1** 740–6

[10] Hollmann E M *et al* 2015 Status of research toward the ITER disruption mitigation system *Phys. Plasmas* **22** 021802

[11] Nedospasov A V 2008 Thermal quench in tokamaks *Nucl. Fusion* **48** 032002

[12] Jaspers R, Finken K H, Mank G, Hoenen F, Boedo J A, Cardazo N J L and Schuller F C 1993 Experimental investigation of runaway electron generation in textor *Nucl. Fusion* **33** 1775

[13] Granetz R S, Esposito B, Kim J H, Koslowski R, Lehnen M, Martin-Solis J R, Paz-Soldan C, Rhee T, Wesley J C and Zeng L 2014 An ITPA joint experiment to study runaway electron generation and suppression *Phys. Plasmas* **21** 072506

[14] Huysmans G T A and Czarny O 2007 MHD stability in x-point geometry: simulation of ELMs *Nucl. Fusion* **47** 659–66

[15] Møller C 1932 *Ann. Phys.* **14** 531–85

[16] Chiu S C, Rosenbluth M N, Harvey R W and Chan V S 1998 Fokker-planck simulations of knock-on electron runaway avalanche and bursts in tokamaks *Nucl. Fusion* **38** 1711–21

[17] Kulsrud R M, Sun Y-C, Winsor N K and Fallon H A 1973 Runaway electrons in a plasma *Phys. Rev. Lett.* **31** 690–3

[18] Eriksson L G and Helander P 2003 Simulation of runaway electrons during tokamak disruptions *Comput. Phys. Commun.* **154** 175–96

[19] Zeng L *et al* 2013 Experimental observation of a magnetic-turbulence threshold for runaway-electron generation in the TEXTOR tokamak *Phys. Rev. Lett.* **110** 235003

[20] Ejima S, Callis R W, Luxon J L, Stambaugh R D, Taylor T S and Wesley J C 1982 Volt-second analysis and consumption in Doublet III plasmas *Nucl. Fusion* **22** 1313

[21] Wijnands T and Martin G 1997 An advanced plasma control system for Tore Supra *Fusion Technol.* **32** 471–86

[22] Vlainic M, Mlynar J, Cavalier J, Weinzettl V, Paprok R, Imrisek M, Ficker O, Noterdaeme J-M and the COMPASS Team 2015 Post-disruptive runaway electron beam in COMPASS tokamak *J. Plasma Phys.* Accepted

CrossMark

J. Plasma Physics (2015), *vol.* 81, 475810403 © Cambridge University Press 2015
doi:10.1017/S0022377815000446

Trapped-electron runaway effect

E. Nilsson[1]†, J. Decker[2], N. J. Fisch[3] and Y. Peysson[1]

[1]CEA, IRFM, F-13108 Saint-Paul-lez-Durance, France
[2]Ecole Polytechnique Fédérale de Lausanne (EPFL), Centre de Recherches en Physique des Plasmas (CRPP), CH-1015 Lausanne, Switzerland
[3]Princeton Plasma Physics Laboratory, Princeton University, Princeton, NJ 08543, USA

(Received 1 March 2015; revised 27 March 2015; accepted 31 March 2015; first published online 28 April 2015)

In a tokamak, trapped electrons subject to a strong electric field cannot run away immediately, because their parallel velocity does not increase over a bounce period. However, they do pinch toward the tokamak center. As they pinch toward the center, the trapping cone becomes more narrow, so eventually they can be detrapped and run away. When they run away, trapped electrons will have a very different signature from circulating electrons subject to the Dreicer mechanism. The characteristics of what are called *trapped-electron runaways* are identified and quantified, including their distinguishable perpendicular velocity spectrum and radial extent.

1. Introduction

Under acceleration by a constant toroidal electric field, circulating electrons in tokamaks run away when their velocity parallel to the magnetic field is so large that the frictional collision forces become too small to impede acceleration by the electric field. The runaway velocity is the demarcation velocity: the electric field cannot prevent electrons slower than this velocity from slowing down further due to collisions; collisions are too weak to prevent electrons faster than this velocity from undergoing acceleration by the electric field to even higher energies. This demarcation velocity is called the critical velocity (Dreicer 1959). However, since collisions are random events, it is not quite precisely put to term an electron as a runaway or not. A more precise description would be to assign to each electron a probability of running away, based on its initial set of coordinates (Fisch 1986; Karney and Fisch 1986). To the extent that this probability is a sharp function of velocity, the notion of a critical velocity then becomes useful.

Runaway electrons are sensitive, in addition to collisions, to other energy loss mechanisms such as the synchrotron radiation reaction force (Stahl et al. 2013). They are also sensitive to perturbation of the magnetic field, which lead to enhanced transport (Zeng et al. 2013). In addition, the runaway population that would arise in a tokamak magnetic field configuration is diminished owing to magnetic trapping effects in a non-uniform magnetic field, since trapped electrons cannot immediately contribute to the runaway electron population (Nilsson et al. 2015). The fate of the suprathermal electrons, whether trapped or circulating, is determined from the balance of the accelerating electric field and various radiative, convective and diffusive loss mechanisms.

† Email address for correspondence: emelie.nilsson@cea.fr

Runaway populations can be quite deleterious to the operation of a tokamak. In the case of a disruption, the loop voltage spikes, so that large numbers of runaway electrons reach relativistic velocities and damage the tokamak wall. Various means of mitigating the runaway damage have been suggested, since concerns are increasing as tokamaks become larger and carry more current, like in ITER (Hender et al. 2007; Izzo et al. 2011; Paz-Soldan et al. 2014). It is clearly important to understand the behavior of the runaway electrons in order to optimize a runaway electron mitigation strategy.

The runaway electron population in tokamaks typically arises from the acceleration of electrons with large parallel velocities, on the order of the critical velocity, and average perpendicular velocities, on the order of the thermal velocity. These electrons born via the Dreicer mechanism are circulating. In addition, a knock-on collision between an existing runaway and slow electrons can result in two runaway electrons. This secondary runaway generation process can generate an avalanche of runaway production and dominate the Dreicer effect, in particular during disruptions. These large angle collisions between runaways and slow electrons can result in electrons with perpendicular energies on the order of the parallel energies. When the knock-on runaways are created near the magnetic axis, trapped particle effects are not important (Rosenbluth and Putvinski 1997; Parks et al. 1999; Eriksson and Helander 2003). However, these electrons will be trapped if they are created far enough away from the magnetic axis. In fact, since circulating runaway electrons tend to move substantially radially outwards as they are accelerated by the electric field (Guan et al. 2010), the secondary electrons generated via collision with these runaways may not be near the magnetic axis at all and could be trapped. Alternatively, a significant population of suprathermal trapped electrons can be generated via interaction with electron cyclotron waves.

The present paper focuses on electrons with a large enough parallel velocity to run away in a tokamak, but are magnetically trapped because of their large perpendicular velocity, and therefore incapable of running away. These trapped electrons drift radially inwards due to the Ware pinch (Ware 1970). Nearer the magnetic axis the trapping cone contracts such that these electrons could be detrapped and run away. When they run away, they will have a distinct signature, which is identified in this work.

The paper is organized as follows: In Sec. 2, we describe how trapped runaways are generated and provide their phase-space characteristics. In Sec. 3, we discuss collisional effects on the trapped runaways. In Sec. 4, we offer perspectives on runaway positrons and runaway interaction with RF current drive.

2. Signature of trapped runaways

Let us describe more precisely the expected signature of the trapped runaways. As opposed to circulating electrons, trapped electrons cannot run away while they remain on the same flux surface, because their interaction with the electric field results in no net gain in parallel velocity over a bounce period. However, according to the conservation of canonical angular momentum, they pinch toward the tokamak center. As they pinch toward the center, the trapping condition changes such that eventually they do run away. We call this the *trapped-electron runaway effect*, by which we refer to electrons that were initially trapped, before running away. However, when they do run away, trapped electrons will have a very different signature from the circulating electrons that run away in several ways.

First, the initially-trapped runaway electrons will run away closer to the magnetic axis of the tokamak than they were initially. Second, the trapped electron runaways will have a distinct pitch angle corresponding to the detrapping condition at the radial location where they run away, which implies a high-perpendicular velocity on the order of the critical velocity. In addition, upon application of a DC electric field these initially trapped electrons first need to undergo the Ware pinch and associated detrapping before running away. This process creates a delay in the runaway generation process, which can occur only if not disrupted by collisions or other mechanisms in the meantime.

For an initially Maxwellian distribution function, the fraction of trapped-electron runaways compared to Dreicer runaways would be small, although it increases with the effective charge. However, the relative importance of trapped-electron runaways might increase significantly for three reasons: first, the usual runaways may not be well confined, whereas, the trapped-electron runaways, since born nearer the magnetic axis, are very well confined; second, knock-on collisions between existing runaways and thermal electrons produce a non-thermal population of secondary runaways of which a significant number may be trapped due to their high-perpendicular velocities (Nilsson et al. 2015). Third, tokamak plasmas are typically non-Maxwellian, and a significant population of suprathermal electrons with high-perpendicular momentum can be created, for instance, via resonant interaction with electron cyclotron waves.

Assuming a circular plasma and neglecting the radial excursion of electron orbits, the unperturbed motion of an electron guiding center can be characterized by its radial position r, its momentum p, and the value ξ_0 of its pitch angle cosine $\xi = p_\parallel/p$ on the outboard midplane where $\theta = 0$ and the magnetic field is at a minimum. Here $p_\parallel$ is the momentum projected in the direction of the magnetic field. Electron trapping derives from the adiabatic invariance of the magnetic moment $\mu = p^2(1-\xi^2)/(2mB)$ along the particle orbit, such that electrons in a non-uniform magnetic field $B(r,\theta) = B_0(r)/(1+\epsilon\cos\theta)$ are trapped if $|\xi_0| < \xi_T(r)$ with

$$\xi_T(r) = \sqrt{\frac{2\epsilon}{1+\epsilon}},$$

where $\epsilon = r/R_0$ is the local inverse aspect ratio.

Due to the conservation of toroidal canonical momentum in an axisymmetric configuration, all trapped particles orbits subject to a toroidal electric field E_ϕ drift toward the plasma center according to the Ware pinch (Ware 1970)

$$\frac{dr}{dt} = -\frac{E_\phi}{B_\theta}, \tag{2.1}$$

where B_θ is the poloidal magnetic field. An otherwise unperturbed electron initially trapped on the flux surface r with $|\xi_0| < \xi_T(r)$ will drift inwards to the surface r' where $\xi_T(r') = |\xi_0|$. There, it will be detrapped and can run away if its parallel velocity is above the critical value. The electron will thus become circulating at the radial location ϵ' with

$$\epsilon' = \frac{\xi_0^2}{2-\xi_0^2}. \tag{2.2}$$

Figure 1 shows the required displacement $\Delta\epsilon = \epsilon - \epsilon'$ and Fig. 2 shows the radial position ($\epsilon' = r/R$) where the electrons can detrap and run away.

Runaway electrons born at a given radial location via this detrapping process driven by the Ware pinch will have a specific pitch-angle according to the local trapping

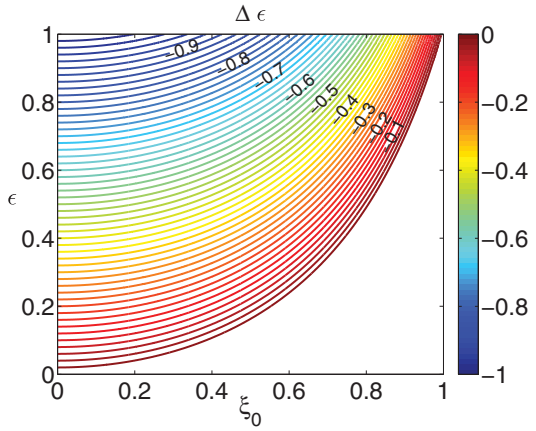


FIGURE 1. The inward radial displacement ($\Delta\epsilon$) required for trapped electron initially at radial position ϵ and pitch angle ξ_0 to become circulating.

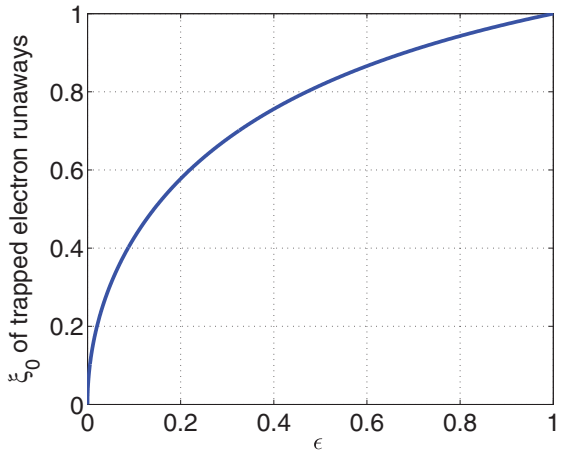


FIGURE 2. The trapped-electron runaways will appear with a distinct pitch angle (ξ_0) in the radial direction.

condition. The minimum perpendicular velocity of the trapped electron runaways is presented in Fig. 3, normalized to $v_c(\xi_0 = 1)$. The time it takes for these initially trapped electrons to become runaways is derived from the Ware pinch velocity and radial displacement until detrapping occurs

$$dt_W = \frac{B_\theta}{E_\phi} R \left(\epsilon - \frac{\xi_0^2}{2 - \xi_0^2} \right). \tag{2.3}$$

For an equilibrium with $B_\theta = 0.05\,\mathrm{T}$ and $E_\phi = 0.8\,\mathrm{Vm}^{-1}$. The time required for a trapped electron to become passing is shown in Fig. 4.

In a disruption in an ITER-like scenario the toroidal electric field can be much stronger; around $38\,\mathrm{Vm}^{-1}$ has been predicted (Hender et al. 2007). In that case, the Ware pinch detrapping time scale would be much shorter; see Fig. 5.

Corrections to the detrapping radius and detrapping time due to the Shafranov shift, non-circular plasma shape, grad-B and curvature drifts are beyond the scope of this paper. It is important to note that very near the magnetic axis the approximations made in this paper break down.

Although the poloidal magnetic field B_θ has little effect on the detrapping condition, it does have a strong effect on the detrapping time. For simplicity, we took the E_ϕ/B_θ

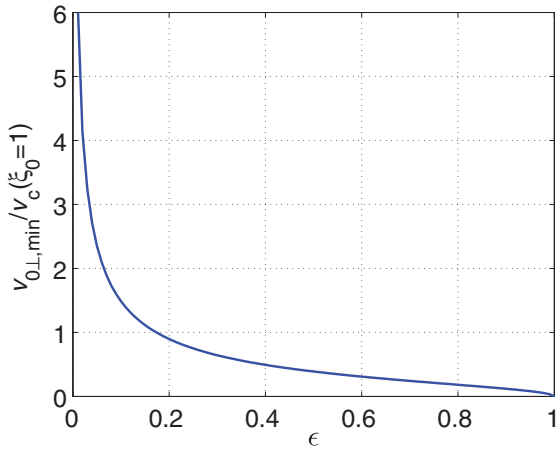


FIGURE 3. The radial distribution of the minimum perpendicular velocity of the trapped electron runaways, normalized to the critical velocity for $\xi_0 = 1$.

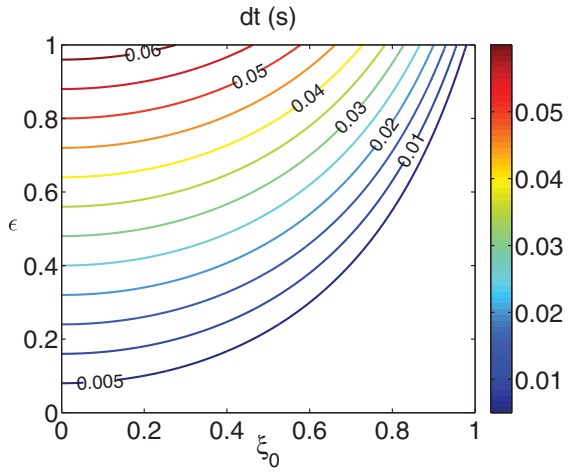


FIGURE 4. Time (s) for trapped electrons at (ξ_0, ϵ) to reach the radial position where they become passing electrons, for $B_\theta = 0.05\,\mathrm{T}$, $E_\phi = 0.8\,\mathrm{Vm}^{-1}$ and $R = 1\,\mathrm{m}$.

velocity to be constant. In fact, as the electron pinches inward, the poloidal field decreases, thereby speeding up the drift. Thus, a more precise formulation of (2.3) would account for the E_ϕ/B_θ dependence upon r.

3. Limitations of the collisionless approach

The collisionless approximation used in Sec. 2 is valid if the pinch time is small compared to both the collisional slowing down and detrapping times of runaway electrons. If the pinch time is longer than the slowing-down time, the electron may slow down such that it may not have the energy required to run away when it finally detraps. If the electron undergoes significant pitch-angle scattering during the pinch time, it may be detrapped at a different radial location.

Since the collision time increases with velocity, the validity condition for the collisionless approach must be evaluated from the pitch angle dependent critical momentum (Rosenbluth and Putvinski 1997)

$$p_c^2 \approx \frac{2}{1+\xi_0}\frac{E_c}{E}, \tag{3.1}$$

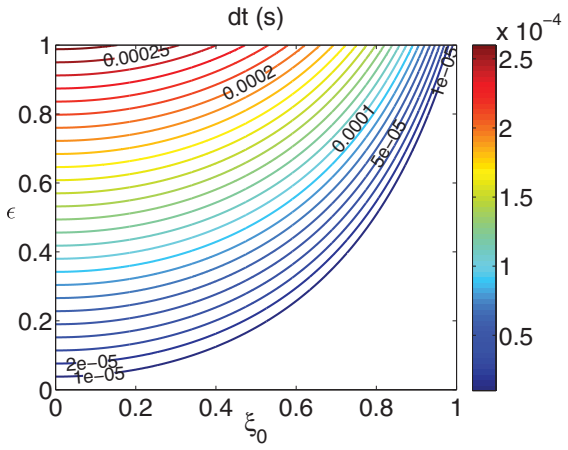


FIGURE 5. Time (s) for trapped electrons at (ξ_0, ϵ) to reach the radial position where they become passing electrons, for $B_\theta = 0.01$ T, $E_\phi = 38$ V m^{-1} and $R = 1$ m.

where the critical field E_c is proportional to the plasma density. The slowing-down time for electrons with velocity $v_c/c = p_c/\gamma_c$ is

$$\tau_c = \frac{4\pi\epsilon_0^2 m_e^2 v_c^3}{q^4 n_e \ln\Lambda}.$$

Slowing-down can thus be neglected if $dt_W \ll \tau_c$.

Collisional detrapping via pitch-angle scattering occurs over a shorter time than the collision time that is proportional to the square of the width ξ_T of the trapping region and can be estimated as

$$\tau_{dt} \sim \frac{\epsilon\tau_c}{1 + Z_{\text{eff}}}.$$

If the condition $dt_W \ll \tau_{dt}$ is not satisfied, trapped-electron runaways will still be generated, but the detrapping radial distribution will be different.

The collisionless condition is shown in Fig. 6 for ITER-like parameters and various values of the electric field. The density is $n_e = 10^{20}$ m^{-3}. The magnetic field is calculated from a current density profile, peaked on-axis and with a total plasma current of $I_p = 15$ MA. With the current profile assumed in this calculation, the maximum of the poloidal magnetic field is located inward from the plasma edge, which explains the maximum in the energy condition. The radial dependence of the density and the electric field strength are not taken into account.

The minimum energy required for the collision time to be longer than the Ware pinch time is on the order of MeV for ITER-like parameters during a disruption. Considering that runaway electrons have many tens of MeV, it can be expected that runaways produced from knock-on collisions should be in the range where collisions can be neglected. For trapped electron runaways with lower energy, collisions must be accounted for. That regime is left for a future study.

Just like the collisional slowing down, the synchrotron reaction force (Pauli 1958) limits the energy of the particle.

The relativistic characteristic time for the radiation reaction force is

$$\tau_r = \frac{6\pi\varepsilon_0\gamma(m_0c)^3}{q^4B^2} \approx 5.2\frac{\gamma}{Z^4B^2}. \tag{3.2}$$

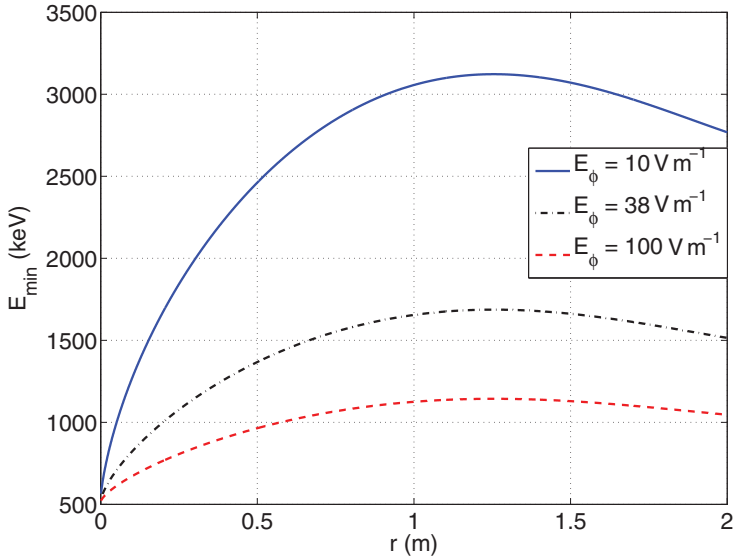


FIGURE 6. The minimum energy needed for the Ware pinch to be faster than the collision time, for the parameters $E_\phi = 10\,\mathrm{Vm}^{-1}$, $38\,\mathrm{Vm}^{-1}$ and $100\,\mathrm{Vm}^{-1}$, $n_\mathrm{e} = 10^{20}\,\mathrm{m}^{-3}$ and $R = 6.2\,\mathrm{m}$. The poloidal magnetic field is calculated from a current density profile with a total plasma current of $I_\mathrm{p} = 15\,\mathrm{MA}$.

In addition the synchrotron reaction force limits the pitch angle $\theta = \arccos(\xi)$ (Helander et al. 2002)

$$F_{\mathrm{rad},\,\xi} = -\frac{p\xi\sqrt{1-\xi^2}}{\gamma\tau_\mathrm{r}}. \tag{3.3}$$

This force could affect the trapped electron runaways in the Ware pinch process, as electrons would detrap faster, i.e. at a larger radius than predicted in Sec. 2, if $p_\perp/p_\parallel$ decreases.

Limitations of the collisionless theory was discussed previously in this section and a regime was identified where the Ware pinch detraps trapped runaways fast enough for the collisions to be negligible ($dt_W \ll \tau_\mathrm{c}$). A similar condition can be set for the radiation loss time $dt_W \ll \tau_\mathrm{r}$. We compare the time scale of collisional damping with the one of the radiation damping

$$\frac{\tau_\mathrm{c}}{\tau_\mathrm{r}} = \frac{2\epsilon_0}{3m_\mathrm{e}n_\mathrm{e}\ln\Lambda}\gamma\left(\frac{v}{c}\right)^3 Z^4B^2 \approx \frac{\gamma}{n_{\mathrm{e},19}}\left(\frac{v}{c}\right)^3 Z^4B_{[5\mathrm{T}]}^2, \tag{3.4}$$

where $n_{e,19}$ is the electron density in the unit $10^{19}\,\mathrm{m}^{-3}$ and $B_{[5T]}$ in units of 5 T. For relevant plasma parameters, the condition $\tau_\mathrm{c} \ll \tau_\mathrm{r}$ is fulfilled unless γ gets very large. From the minimum energy defined in Fig. 6, where the Lorentz factor γ is in the range of 1–6, for higher γ the time scale of the synchrotron reaction force may be short enough to change the pitch before the detrapping radius is reached, if the product B^2Z^4/n_e becomes large. Since this effect would speed up the detrapping process, the prediction in Sec. 2 can be considered as an upper estimate of the detrapping time and lower estimate of the detrapping radius. To properly account for the combined effect of synchrotron reaction and collisional drag on the trapped-electron runaway distribution during the Ware pinch would require further investigation by numerical studies.

4. Discussion

This paper describes how initially trapped electrons may become runaway electrons if their parallel velocity is above the critical runaway velocity as they become detrapped following the inward Ware pinch. These runaway electrons are born nearer the magnetic axis as compared to their initial location, and with a high-perpendicular velocity corresponding to the trapped/circulating boundary. That will distinguish the trapped runaways from the passing runaways, which have average perpendicular energies. They will produce a relatively more intense synchrotron radiation than Dreicer runaways. The production dynamics of the trapped-electron runaways is determined by the Ware pinch time. There will be a turn-on time for the electrons to reach the radial detrapping position and only then to begin to run away. The presence of trapped-electron runaways may affect the radial profile of runaway electrons since they are concentrated near the magnetic axis. Even in the case where primary generation would be small in the center, for example for very peaked density, one could still expect a centrally concentrated runaway electron population under some circumstances. This would be the case if the avalanche growth rate from knock-on collisions decays strongly off-axis owing to magnetic trapping effects as found for toroidal geometries (Nilsson et al. 2015). At the same time, the trapped-electron runaways are concentrated near the center, as found in the previous section.

In other words, the radial dependence of the growth rate of runaways depends on various effects, where the avalanche effect and the trapped-electron runaway effect would weigh the runaway distribution toward the center. Quantitative predictions of the radial profile of runaway electrons are left to future studies. All these signatures should be most prominent during a disruption, where the electric field is large, and might be used to provide information on plasma conditions. The combination of high synchrotron emission and specific dynamics could make it possible to identify the signature of trapped-runaway electrons during disruptions when a large number of energetic trapped electrons is generated via knock-on collisions.

The large perpendicular energies of the trapped-electron runaways also suggest that they may be easier to control than conventional Dreicer runaways, as they can be deconfined through interactions with ripple fields (Laurent and Rax 1990; Rax et al. 1993), coherent wave instabilities (Fülöp et al. 2006; Fülöp and Newton 2014) or magnetic perturbations (Papp et al. 2011). In all of these processes, the strength of the interaction increases with perpendicular momentum.

Recently, there has been interest in the creation of runaway positrons in tokamaks, and the information that might be obtained from them upon annihilation (Helander and Ward 2003; Fülöp and Papp 2012; Liu et al. 2014). When large tokamaks disrupt, large electron–positron pair production is expected to occur. The positron runaways behave just like electron runaways, only they run away in the opposite direction. Just as there are circulating positron runaways, there will be trapped positron runaways. These trapped positron runaways will pinch toward the tokamak magnetic axis just like the trapped electron runaways. Except that they will travel in the opposite toroidal direction, which will affect the Doppler shift of the synchrotron radiation, the trapped positron runaways will have a completely analogous signature to the trapped electron runaways. Moreover, since the positrons would only be produced in large numbers through the avalanche effect involving very high energy runaways, there will be relatively more of the trapped positron runaways (compared to the usual positron runaways) than there would be trapped electron runaways (compared to the usual electron runaways). This effect would be enhanced to the extent that the

most energetic runaways – and those most capable of the pair production – would be found near the low field side of the tokamak (Guan et al. 2010), where the trapping effect is also most significant.

Note that the trapped-electron runaway effect that we discuss is for runaway electrons that run away eventually in the direction in which they support the plasma current. The same is true for the runaway positrons. When the tokamak current is maintained by a DC electric field, it is after all the thermal electrons that carry the toroidal current, and the runaway electrons carry current in the same direction, only they are accelerated to far higher energies. This would also be true during start-up of the tokamak (Mueller 2013), if the start-up relies on an inductive current. In such a case, there is also danger from runaway electrons, since the plasma may not be so dense as to hold back the runaways. Moreover, in the case of RF-assisted start-up of the current, such as through electron cyclotron heating, there might be more electrons produced at higher energies, which could then run away in the direction in which the runaways support the current.

Whether or not the runaways are in a direction to support the plasma current is an important distinction that comes into play in non-inductive start-up of the tokamak current. In the case of non-inductive current drive, for example by RF waves (Fisch 1987), there is the opportunity to start up the tokamak or to recharge the transformer (Fisch 2010). In such a case, the loop voltage is driven negative; in other words, as the RF-current is increased, a loop voltage is induced which opposes the RF-driven current. This DC electric field also produces runaway electrons, only now they are so-called *backwards runaways*, which are runaway electrons that carry current counter to the toroidal current (Fisch 1986; Karney and Fisch 1986). It is also important to note that the trapped-electron runaways are not a concern in the case of backward runaways. In this case, which may occur during the startup or flattop phases in the presence of strong RF current drive (Karney et al. 1985; Fisch 1987, 2010; Ding et al. 2012; Li et al. 2012), the electric field opposes the plasma current such that the pinch is directed outward where the trapping cone widens. Hence, in the case of RF ramp-up, while circulating backwards runaways are produced, there is no production whatsoever of backwards trapped-electron runaways (or, for the same reason, backwards trapped-positron runaways). Thus, in vigorous RF ramp-up regimes, while the circulating backwards runaways might be of some concern, at least the trapped-electron runaways do not add to that concern.

A recurring question is to what extent RF current drive generates runaway electrons. This question should also be posed for the trapped-electron runaways. In the case of RF current drive, if the current drive effect relies on RF wave interactions with suprathermal electrons, there is risk of producing runaway electrons. It is particularly the case for lower hybrid current drive (Fisch 1978), where a suprathermal electron tail is formed at high parallel velocities that could supply more runaway electrons than could a Maxwellian distribution. It is also the case for electron cyclotron current drive (Fisch and Boozer 1980), where heating in perpendicular velocity makes electrons collide less frequently and become more likely to run away. In these cases, the RF heating of passing electrons enhances the runaway current through the usual runaway effect. However, there is also a trapped particle runaway effect when the RF current drive affects trapped electrons. Consider first waves that provide parallel momentum to energetic trapped electrons, such as low parallel-phase-velocity waves (Wort 1971). Since the particles remain trapped, there is an RF-pinch effect similar to the Ware pinch effect (Fisch and Karney 1981). If the wave momentum is in the direction supportive of the total current, then as with the Ware pinch effect,

the pinch will be inwards. Moreover, as with the Ware pinch, the trapped electrons experience less stringent trapping conditions when they pinch, so they can eventually run away like a trapped runaway. One important difference is that, as opposed to the Ware pinch effect where the electric field pinches the electron, without increasing its energy, in the case of the RF-pinch effect, the RF waves pinch the electron, while increasing its energy. As a result, the trapped runaways become detrapped sooner, and so run away at larger radii. It must be pointed out that the RF pinch may only occur if the wave-particle resonance is present continuously through the pinching process, i.e. if the spatial distribution of the waves has sufficient radial extent. In any event, in inputting parallel momentum with waves that would be supportive of the toroidal current, whereas targeting electrons with higher parallel velocity can increase the number of runaway electrons, targeting electrons with low parallel velocity can increase the number of trapped runaways.

In contrast, in the case of perpendicular heating rather than parallel heating of trapped electrons, such as by electron cyclotron waves, there is no pinch effect bringing electrons to less stringent trapping conditions. In fact, the perpendicular heating causes the electrons to be more deeply trapped. Hence, there is no trapped-particle runaway effect for heating by electron cyclotron waves.

5. Summary

To sum up, we identified the trapped-electron runaway effect. We calculated the key parameters that distinguish these runaways, namely the large perpendicular energy, the dependency of the perpendicular energy on radius, and the turn-on time for the appearance of the runaways. We identified when these effects might be expected (in the case of positrons) and when they would be absent (in the case of RF ramp-up). Possible observables would therefore be based on signals sensitive to perpendicular energy, such as synchrotron radiation. Similarly, the degree of manipulation by waves or magnetic perturbations is also sensitive to perpendicular energy. Thus, we hope that these observations and calculations will assist in formulating methods of controlling those runaways or in utilizing measurements of their behavior for informing on other processes in the plasma.

Acknowledgements

This work has been carried out within the framework of the EUROfusion Consortium and has received funding from the Euratom research and training programme 2014–2018 under grant agreement No. 633053. The views and opinions expressed herein do not necessarily reflect those of the European Commission. The authors appreciate the hospitality of the Chalmers University of Technology, where, at a meeting organized by Professor Tünde Fülöp, these ideas were initially conceived. The authors are grateful to Eero Hirvijoki, Isztvan Pusztai and Adam Stahl for fruitful discussions. One of us (NJF) acknowledges support, in part, from DOE Contract No. DE-AC02-09CH11466.

REFERENCES

Ding, B. J. et al. 2012 Current ramp-up with lower hybrid current drive in EAST. *Phys. Plasmas* **19**(12), 122 507.

Dreicer, H. 1959 Electron and ion runaway in a fully ionized gas. I. *Phys. Rev.* **115**(2), 238–249.

Eriksson, L. G. and Helander, P. 2003 Simulation of runaway electrons during tokamak disruptions. *Comput. Phys. Commun.* **154**, 175–196.

Fisch, N. J. 1978 Confining a tokamak plasma with RF-driven currents. *Phys. Rev. Lett.* **41**(13), 873–876.

Fisch, N. J. 1986 Transport in driven plasmas. *Phys. Fluids* **29**(1), 172–179.

Fisch, N. J. 1987 Theory of current drive in plasmas. *Rev. Mod. Phys.* **59**(1), 175–234.

Fisch, N. J. 2010 Transformer recharging with alpha channeling in tokamaks. *J. Plasma Phys.* **76**(3-4), 627–634.

Fisch, N. J. and Boozer, A. H. 1980 Creating an asymmetric plasma resistivity with waves. *Phys. Rev. Lett.* **45**(9), 720–722.

Fisch, N. J. and Karney, C. F. F. 1981 Current generation with low-frequency waves. *Phys. Fluids* **24**(1), 27–39.

Fülöp, T. and Newton, S. 2014 Alfvenic instabilities driven by runaways in fusion plasmas. *Phys. Plasmas* **21**(8), 080 702.

Fülöp, T. and Papp, G. 2012 Runaway positrons in fusion plasmas. *Phys. Rev. Lett.* **108**(21), 225 003.

Fülöp, T., Pokol, G., Helander, P. and Lisak, M. 2006 Destabilization of magnetosonic-whistler waves by a relativistic runaway beam. *Phys. Plasmas* **13**(6), 062 506.

Guan, X., Qin, H., and Fisch, N. J. 2010 Phase-space dynamics of runaway electrons in tokamaks. *Phys. Plasmas* **17**, 092 502.

Helander, P., Eriksson, L.-G. and Andersson, F. 2002 Runaway acceleration during magnetic reconnection in tokamaks. *Plasma Phys. Control. Fusion* **44B**, 247–262.

Helander, P. and Ward, D. J. 2003 Positron creation and annihilation in tokamak plasmas with runaway electrons. *Phys. Rev. Lett.* **90**(13), 135 004.

Hender, T. C. et al. 2007 MHD stability, operational limits and disruptions. *Nuclear Fusion* **47**, S128–S202.

Izzo, V. A. et al. 2011 Runaway electron confinement modelling for rapid shutdown scenarios in DIII-D, Alcator C-Mod and ITER. *Nuclear Fusion* **51**, 063 032.

Karney, C. F. F. and Fisch, N. J. 1986 Current in wave-driven plasmas. *Phys. Fluids* **29**(1), 180–192.

Karney, C. F. F., Fisch, N. J. and Jobes, F. C. 1985 Comparison of the theory and the practice of lower-hybrid current drive. *Phys. Rev.* A **32**(4), 2554–2556.

Laurent, L. and Rax, J. M. 1990 Stochastic-instability of runaway electrons in tokamaks. *Europhys. Lett.* **11**(3), 219–224.

Li, M., Ding, B., Li, W., Kong, E., Shan, J., Liu, F., Wang, M. and Xu, H. 2012 Investigation of LHCD efficiency and transformer recharging in the EAST tokamak. *Plasma Sci. Technol.* **14**(3), 201–206.

Liu, J., Qin, H., Fisch, N. J., Teng, Q. and Wang, X. 2014 What is the fate of runaway positrons in tokamaks? *Phys. Plasmas* **21**, 064 503.

Mueller, D. 2013 The physics of tokamak start-up. *Phys. Plasmas* **20**(5), 058 101.

Nilsson, E., Decker, J., Peysson, Y., Granetz, R. S., Saint-Laurent, F. and Vlainic, M. 2015 Kinetic modelling of runaway electron avalanches in tokamak plasmas. *Plasma Phys. Control. Fusion.* Sumbitted For Publication.

Papp, G., Drevlak, M., Fülöp, T., Helander, P. and Pokol, G. I. 2011 Runaway electron losses caused by resonant magnetic perturbations in ITER. *Plasma Phys. Control. Fusion* **53**(9), 095 004.

Parks, P. B., Rosenbluth, M. N. and Putvinski, S. V. 1999 Avalanche runaway growth rate from a momentum-space orbit analysis. *Phys. Plasmas* **6**(6), 2523–2528.

Pauli, W. 1958 *Theory of Relativity*. New York: Dover Publications.

Paz-Soldan, C. et al. 2014 Growth and decay of runaway electrons above the critical electric field under quiescent conditions. *Phys. Plasmas* **21**(2), 022 514.

Rax, J. M., Fisch, N. J. and Laurent, L. 1993 Fast particle resonances in tokamaks. *Plasma Phys. Control. Fusion* **35**(B), B129–B140.

Rosenbluth, M. N. and Putvinski, S. V. 1997 Theory for avalanche of runaway electrons in tokamaks. *Nuclear Fusion* **37**(10), 1355–1362.

Stahl, A., Landreman, M., Papp, G., Hollmann, E. and Fülöp, T. 2013 Synchrotron radiation from a runaway electron distribution in tokamaks. *Phys. Plasmas* **20**, 093 302.

Ware, A. A. 1970 Pinch effect for trapped particles in a tokamak. *Phys. Rev. Lett*. **25**(1), 15–17.

Wort, D. J. H. 1971 The peristaltic tokamak. *Plasma Phys.* **13**(3), 258–262.

Zeng, L. et al. and the TEXTOR team 2013 Experimental observation of a magnetic-turbulence threshold for runaway-electron generation in the TEXTOR tokamak. *Phys. Rev. Lett*. **110**, 235 003.